Dissertation

submitted to the

Combined Faculty of Mathematics, Engineering and Natural Sciences

of Heidelberg University, Germany

for the degree of

Doctor of Natural Sciences

Put forward by

Daniel Tobias Unger

born in Heidelberg

Oral examination: 29 October 2025

High-Resolution X-ray Spectroscopy of Light Muonic Atoms

Dissertation

High-Resolution X-ray Spectroscopy of Light Muonic Atoms

Daniel Tobias Unger

August 2025

Referees: apl. Prof. Dr. Loredana Gastaldo
Prof. Dr. André Schöning

Abstract

The low-lying energy levels of muonic atoms are highly sensitive to nuclear structure due to the strong overlap of the muon wavefunction with the nucleus. The energy of the muonic $2p$–$1s$ transition allows the determination of the nuclear charge radius, an essential quantity for establishing reliable nuclear models. The QUARTET collaboration aims to achieve an improvement by more than an order of magnitude in the precision of nuclear charge radii for light atoms from Li to Ne. This thesis focuses on the detector development within QUARTET for high-resolution X-ray spectroscopy of muonic atoms. A dedicated MMC-based detector array was designed, fabricated, and characterized. A cryostat sidearm was designed and assembled, a precise ADC calibration was established, and a data analysis library was developed. Two successful muon-beam measurements using Li, Be, and B as target materials were conducted. The results demonstrate the feasibility of QUARTET for significantly improving the accuracy of nuclear charge radii for light nuclei.

Zusammenfassung

Die tief liegenden Energieniveaus myonischer Atome sind aufgrund der starken Überlappung der Wellenfunktion des Myons mit dem Kern besonders empfindlich gegenüber der Kernstruktur. Die Energie des myonischen $2p$–$1s$ Übergangs ermöglicht die Bestimmung des Kernladungsradiusses, einer grundlegenden Größe für die Entwicklung zuverlässiger Kernmodelle. Die QUARTET-Kollaboration hat sich das Ziel gesetzt, die Präzision der Ladungsradien leichter Atome von Li bis Ne um mehr als eine Größenordnung zu verbessern. Diese Arbeit konzentriert sich auf die Detektorentwicklung innerhalb von QUARTET für die hochauflösende Röntgenspektroskopie myonischer Atome. Ein MMC-basiertes Detektorarray wurde entworfen, hergestellt und charakterisiert. Ein Kryostat-Seitenarm wurde konstruiert und aufgebaut, eine ADC-Kalibrierung etabliert sowie eine Bibliothek zur Datenanalyse entwickelt. Zwei erfolgreiche Myonenstrahlmessungen mit Li, Be und B als Targetmaterialien wurden durchgeführt. Die Ergebnisse zeigen die Machbarkeit von QUARTET zur deutlichen Verbesserung der Genauigkeit der Kernladungsradien leichter Kerne.

Publications

During this work, several publications, both published and unpublished, were prepared and are listed below. In addition, bachelor and master theses were supervised, some of which provided results presented in this thesis. A few figures are also adapted from the corresponding publications.
As first author, or as one of two first authors, publications were prepared on the characterization of an MMC-based detector setup for IAXO [1], the preparation of the test run of QUARTET [2], the results of an ^{225}Ac measurement for medical research [3], and the open-source *Python* library *fitfiles* [4].

[1] D. Unger et al., "High-resolution for IAXO: MMC-based X-ray detectors", J. Instrum. **16**, P06006 (2021) 10.1088/1748-0221/16/06/P06006.

[2] D. Unger et al., "MMC array to study X-ray transitions in muonic atoms", J. Low Temp. Phys. **216**, 344–351 (2024) 10.1007/s10909-024-03141-x.

[3] K. Maurer et al., "Towards cancer theragnostic–probing the ^{225}Ac decay chain with ultra-high-resolution MMC-based detectors", under review.

[4] D. Unger et al., "fitfiles", https://github.com/unger-daniel/fitfiles.

Several works were prepared as coauthor, including publications on QUARTET covering its theoretical considerations [5], a letter of intent [6], a research proposal [7], and a beamtime request [8]. Further contributions were made to multichannel MMC readout [9], and to a large-area MMC detector [10]. In the context of IAXO, contributions include detector development towards BabyIAXO [11], and the advantages of MMCs [12]. In addition, a manual with its experiment were prepared for the advanced physics lab course for physicists [13].

[5] B. Ohayon et al., "Towards precision muonic X-ray measurements of charge radii of light nuclei", Physics **6**, 206–215 (2024) 10.3390/physics6010015.

[6] A. Fleischmann et al. (QUARTET Collaboration), "Quantum interactions with exotic atoms", Letter of Intent, 2023.

[7] A. Abeln et al. (QUARTET Collaboration), "Measurement of charge radii from lithium to neon", Quartet Reasearch Proposal for BVR 55, 2024.

[8] A. Abeln et al. (QUARTET Collaboration), "Measurement of charge radii from lithium to neon", Quartet Progress Report and Beamtime Request for BVR 56, 2025.

[9] F. Mantegazzini et al., "Multichannel read-out for arrays of metallic magnetic calorimeters", J. Instrum. **16**, P08003 (2021) 10.1088/1748-0221/16/08/P08003.

[10] A. P. Jadhav et al., "Large area photon detector for the search of $0\nu\beta\beta$ using scintillators", in preparation.

[11] A. Abeln et al. (IAXO Collaboration), "Conceptual design of BabyIAXO, the intermediate stage towards the international axion observatory", J. High Energy Phys. **2021**, 137 (2021) 10.1007/JHEP05(2021)137.

[12] L. Gastaldo, D. Hengstler, and D. Unger, "High energy resolution x-ray detectors for IAXO: advantages in pre- and post-discovery phases", PoS **COSMICWISPers**, 038 (2024) 10.22323/1.454.0038.

[13] C. Ständer and D. Unger, "F98: SQUIDs and noise thermometers", https://physi.uni-heidelberg.de/Einrichtungen/FP/anleitungen/F98.pdf, Advanced Physics Lab for Physicists, Mar. 2022.

Several theses were supervised, some related to QUARTET [14, 15], others to a large-area detector [16], to the SQUID readout of MMCs [17, 18], and to the ECHo experiment [19, 20].

[14] P. L. Wiedemann, "Characterisation of thermal properties of an MMC array designed for X-ray spectroscopy of muonic atoms", Master's thesis (Heidelberg University, 2025).

[15] I. G. N. W. Saor, „Simulationsbasierter Vergleich von Algorithmen zur Datenreduzierung für die hochauflösende Röntgenspektroskopie", Bachelor's Thesis (Heidelberg University, 2025).

[16] A. P. Jadhav, "Design and fabrication of a large area photon detector for the search of $0\nu\beta\beta$ using scintillators", Master's thesis (Heidelberg University, 2024).

[17] D. Behrend-Uriarte, "Assembly and characterization of a SQUID amplifier module for IAXO and automation of SQUID tuning", Bachelor's Thesis (Heidelberg University, 2021).

[18] S. Hilscher, "Addressing noise in SQUID-based MMC-readout: investigating lossy input coils and automated SQUID-tuning", Bachelor's Thesis (Heidelberg University, 2024).

[19] D. L. Klumpp, "Spectral shape analysis with the kernal density estimation for the ECHo-experiment", Bachelor's Thesis (Heidelberg University, 2022).

[20] I.-A. Nitu, "Calorimetric measurement of the ^{193}Pt electron capture spectrum", Bachelor's Thesis (Heidelberg University, 2022).

Acknowledgements

This thesis represents a long journey and I sincerely thank all who contributed, directly or indirectly, along the way.

I am deeply grateful to my supervisor *apl. Prof. Dr. Loredana Gastaldo* for her continuous guidance and invaluable support throughout this work. I would also like to thank my second referee *Prof. Dr. André Schöning* as well as my third and fourth examiners *Prof. Dr. Peter Fischer* and *PD Dr. Zoltán Harman* for their time, patience, and interest in this work. I am grateful to my secondary supervisor *Prof. Dr. Christian Enss* for leading the *F345* low-temperature research group at KIP, and I would like to thank the group for the opportunity to contribute over several years to detector development and applications. I am also grateful to the *QUARTET* collaboration for preparing and carrying out two successful beamtime measurements at PSI.

In particular, I thank *Katharina von Schoeler* for working closely with me on the preparation of the two runs at PSI and for her invaluable contributions. I am grateful to *Peter Lukas Wiedemann* for his assistance during the preparation of the data run and the characterization of a *maXs 30-56-14* detector, and to *Ashish Pradeep Jadhav* for his help in preparing for the test run. I also thank *Prof. Dr. Ben Ohayon* for his advice and lecture notes on the theory of muonic atoms. I would like to thank *Dr. Andreas Fleischmann* for leading the detector development and *Dr. Andreas Reifenberger* for leading the cleanroom fabrication. I am grateful to *Dr. Andreas Reifenberger*, *Dr. Daniel Hengstler*, *Daniel Kreuzberger*, *Andreas Abeln*, *Axel Brunold*, and *Alexander Stoll* for their help with detector fabrication. I would also like to thank *Prof. Dr. Sebastian Kempf*, *Dr. Fabienne Bauer*, *Dr. Daniel Richter*, and *Dr. Mathias Wegner* for the development and fabrication of the SQUID chips used in this work.

I am grateful to *Daniel Kreuzberger* and *Andreas Abeln* for testing two *maXs 30-56-14* detectors at low temperatures. I also thank *Dr. Daniel Hengstler* for the development and improvement of *PAQS*, *Dr. Matthew Herbst* for developing the detector and sensor simulations, and *Dr. Arnulf Barth* for developing *DARQ* and initiating data analysis with *Python*. I am grateful to *Dr. Anna Ferring-Siebert* for her expertise in SQUID tuning and operation, and to *Dr. Steffen Allgeier* for his advice regarding the cryostat sidearm. I also thank *Andreas Abeln* for developing the adapter PCB used for the cryostat sidearm, and *Lukas Münch* and *Daniel Kreuzberger* for taking the presented SEM images.

I also thank *Daniel Behrend-Uriarte* and *Sebastian Hilscher* for their contributions to developing the automatic SQUID tuning and characterization, *Rasmus Jeske* for his help developing the

pulse generator in *fitfiles*, and *I Gusti Ngurah Wishnu Saor* for assistance with verifying fits in *fitfiles*. I thank *Julian Wendel* and *Adrian Alexander Striebel* for the initial operation of the electronics for the ADC calibration. I would also like to thank the students *Ashish Pradeep Jadhav*, *Peter Lukas Wiedemann*, *Daniel Behrend-Uriarte*, *Ioana-Alexandra Nitu*, *Domenic Lucas Klumpp*, *Sebastian Hilscher*, and *I Gusti Ngurah Wishnu Saor*, whom I had the opportunity to supervise.

I would like to thank the KIP staff for their support, including sample preparation, helium liquefaction, IT services, administrative assistance, and electronics. I am especially grateful to *Rudolf Eitel*, *Beatrice Schwöbel*, and *Thomas Wolf*. I also thank the precision workshop of KIP, especially *Werner Lamade*, *Julia Bing*, *David Jansen*, and *Sascha Braun*, for the fabrication of the cryostat sidearm. I am additionally grateful to the precision workshop of MPIK, particularly *Thorsten Spranz* and *Michael Lamade*, for their assistance with the same.

I would like to thank the research training group *HighRR* for the exchange with other detector physicists and for their substantial support in funding this research. I also thank the graduate school *HGSFP* for providing teaching opportunities.

Finally, I would like to thank *apl. Prof. Dr. Loredana Gastaldo*, *Prof. Dr. Ben Ohayon*, *Ashish Pradeep Jadhav*, *Lukas Münch*, *Katharina von Schoeler*, and *Alexander Stoll* for taking the time to read this work and for providing comments.

Contents

List of Figures

List of Tables

List of Acronyms

ADC analog-to-digital converter. i, vi, xii, 2, 24, 89, 96–107, 111–113, 117, 118, 122, 123, 128, 135, 141, 142, 145, 146, 150, 156–158, 163, 168

eVP electronic vacuum polarization. 6, 11, 12, 14–16

FLL flux-locked loop. xi, 59–62, 64, 96

FNS finite nuclear size. 6, 13–16, 21, 22

FOM figure of merit. xi, 51, 74, 75, 98, 99, 104, 114, 115, 123, 126, 150, 165, 168

FS fine structure. 6, 8, 11, 14, 15

FWHM full width at half maximum. 5, 16, 17, 21, 45, 46, 54, 65, 67, 68, 72–74, 124, 156

HDSQ Heidelberg SQUID. 59, 63, 64, 90–92, 173–176

HPGe high-purity germanium. 2, 16, 17, 19, 20

INL integral non-linearity. xii, 100–104

KIP Kirchhoff-Institute for Physics. v, vi, 65, 82, 90, 105, 151, 163

maXs microcalorimeter array for X-ray spectroscopy. 65, 69

MMC metallic magnetic calorimeter. i, iii, iv, xi, 2, 3, 19, 21, 22, 24–27, 30, 34, 38–45, 47–51, 53–58, 64–68, 75, 76, 89, 96, 97, 104, 105, 107–109, 111, 122, 129, 147, 152–154, 164, 167, 168

NEP noise equivalent power. 45–47, 53, 54, 56, 72, 124, 125, 140, 150, 152, 158, 169

OFHC oxygen-free high-conductivity copper. 90, 92, 93

PCB printed circuit board. v, 90–92

ppm parts per million. 32, 34

PSD power spectral density. 41, 42, 44–46, 51, 53, 57, 113, 116, 120

PSI Paul Scherrer Institute. v, xii, 2, 4, 19, 22, 24, 89, 105, 114, 147, 156, 167, 169

QED quantum electrodynamics. 1, 6, 11, 16

QUARTET QUAntum inteRacTions with Exotic aToms. i, iii, iv, xi, xv, 2, 3, 19, 21–24, 65, 66, 68, 75, 78, 89, 90, 96, 102, 104, 105, 111, 112, 127, 142, 147, 150, 151, 154, 158, 161, 164, 167, 168, 173

RIE reactive-ion etching. 82, 84

RKKY Ruderman-Kittel-Kasuya-Yosida. 35, 36

RMS root mean square. 1, 2, 12, 14, 19, 45, 46, 54, 72, 124

RRR residual resistivity ratio. 28, 31, 71

SEM scanning electron microscope. v, 86, 87

SM standard model. 1, 25

SNR signal-to-noise ratio. 46, 119

SQUID superconducting quantum interference device. iv, v, xi, xii, 2, 26, 43, 44, 47–51, 53, 54, 56–64, 66, 68, 69, 71, 76, 79, 80, 89–92, 96–100, 105, 107, 122, 127, 128, 131, 141, 149, 152, 153, 156, 158, 168, 173–176

TSV through-silicon via. 67, 71, 82

Chapter 1.

Introduction

Physics experiments are essential for probing the laws of nature and deepening our understanding of the fundamental interactions. Theoretical models that describe these interactions depend on physical quantities derived from precise measurements. As theoretical predictions have become more accurate, high-precision measurements have become indispensable in modern physics. These measurements make it possible to evaluate theoretical models, establish benchmarks for *ab initio* theories, and determine fundamental constants [21]. Furthermore, inconsistencies between experimental results and theoretical predictions may reveal limitations in existing models or hint at physics beyond the standard model (SM). Physical constants that characterize nuclei are among the quantities studied to verify or rule out theoretical models and to search for new physics [22]. One prominent example is the *proton radius puzzle*, in which spectroscopy of muonic hydrogen revealed a proton charge radius that was significantly smaller than the value obtained from electronic hydrogen [23, 24]. This unexpected result has motivated a wide range of experimental and theoretical investigations.

Muonic atoms are particularly suitable systems for studying nuclear properties. Formed when a negative muon is bound by the electric field of a nucleus from an ordinary atom, muonic atoms have a much smaller Bohr radius than electronic atoms due to the muon mass being roughly 200 times that of the electron. This results in a significantly greater overlap of the muon wavefunction with the nucleus, enhancing the sensitivity of the muonic energy levels to nuclear structure. In particular, the low-lying $2p$–$1s$ transitions exhibit a measurable energy shift due to the finite nuclear size. The sensitivity to this effect scales roughly with the fourth power of the atomic number (Z^4) and is enhanced for muonic atoms by roughly $200^3 \approx 10^7$ compared to electronic atoms [25]. In addition to the finite nuclear size, these transitions are also sensitive to relativistic bound-state quantum electrodynamics (QED) contributions, nuclear polarizability, and possible short-range interactions [26]. By accurately measuring the energy of low-lying muonic transitions, a fundamental nuclear property that can be extracted is the root mean square (RMS) nuclear charge radius, which characterizes the spatial distribution of the nuclear electric charge.

Precise knowledge of the nuclear charge radius is essential for developing accurate nuclear models, interpreting isotope shifts, and calculating nuclear corrections [5]. The most precise

absolute nuclear charge radii have been obtained through muonic laser spectroscopy, elastic scattering, and X-ray spectroscopy of muonic atoms [27]. Muonic laser spectroscopy provides the most accurate nuclear charge radii for the lightest elements ($Z \leq 2$) with sub-permille uncertainties [24, 28, 29], but this approach is difficult to extend to heavier elements. For heavy elements ($11 \leq Z$), high-purity germanium (HPGe) X-ray detectors are used and yield precise results [30, 31], but their limited energy resolution prevents accurate measurements for light elements ($7 \leq Z \leq 10$). Crystal spectrometers have achieved high precision for carbon ($Z = 6$) due to their high resolving power [32, 33], but their low efficiency and narrow bandwidth make them impractical for systematic studies. For light elements ($3 \leq Z \leq 5$, $Z = 7$), elastic electron and pion scattering provide nuclear charge radii with intermediate precision and are limited by systematic uncertainties. Consequently, a precision gap remains for light nuclei, which are of particular interest as they are probed by recent *ab initio* theories. These theories still lack accurate experimental data for evaluation [34, 35].

The QUAntum inteRacTions with Exotic aToms (QUARTET) collaboration aims to close this gap by performing high-resolution X-ray spectroscopy of light, stable muonic atoms from lithium to neon ($3 \leq Z \leq 10$) at the Paul Scherrer Institute (PSI) [6]. By using low-temperature detectors based on metallic magnetic calorimeters (MMCs), the collaboration seeks to enhance the precision of RMS nuclear charge radii by up to 20 [5]. Operating at mK temperatures, these detectors combine excellent resolving power, high quantum efficiency, high linearity, and broad coverage in the relevant energy range of the corresponding $2p$–$1s$ transitions at 18.7 keV-207 keV. Their good energy resolution and reliable energy calibration make them particularly advantageous for measuring X-ray transitions of light muonic atoms with unprecedented precision [2].

The work presented in this thesis was carried out within the QUARTET collaboration and focuses on the development and application of MMC-based detectors for high-resolution X-ray spectroscopy of light muonic atoms. A dedicated detector setup was prepared, including the design of a custom-built cryostat sidearm [2], the preparation of its two-stage superconducting quantum interference device (SQUID) readout, and the development of a precise analog-to-digital converter (ADC) calibration. To obtain high-resolution energy spectra, a general-purpose open-source analysis package was developed for online processing, data reduction, and offline analysis [4]. With the developed detector setup, two successful beamtime measurements were conducted at PSI, including an initial test run and a dedicated data run with lithium, beryllium, and boron ($3 \leq Z \leq 5$) [7]. A new detector optimized for muonic X-ray spectroscopy was designed, fabricated, and characterized for measurements up to 60 keV. The results represent the first successful application of MMCs for high-precision X-ray spectroscopy of exotic atoms and demonstrate the feasibility of QUARTET for significantly improving the accuracy of nuclear charge radii for light nuclei [8].

Chapter 2.

Muonic Atoms

Exotic atoms are bound systems that do not exclusively contain protons, neutrons, and electrons, but include at least one exotic particle. Among these, muonic atoms are formed when a negative muon is bound by the electric field of the nucleus of an ordinary atom. Since the muon mass is about $m_\mu/m_e \approx 200$ times greater than that of the electron, its binding energy is roughly 200 times greater, and its orbital radius roughly 200 times smaller. This leads to a significantly larger overlap of the muon wavefunction with the nucleus by about $200^3 \approx 10^7$, greatly enhancing the sensitivity of muonic atoms to nuclear structure [25]. Consequently, muonic atoms are particularly well-suited for studying nuclear properties [26]. The physics of muonic atoms is discussed in detail in dedicated literature [36, 37].

This chapter presents the theoretical basis for high-resolution X-ray spectroscopy of light muonic atoms using MMC-based detectors to determine their nuclear charge radii. It covers the formation of muonic atoms, their energy levels including leading-order corrections, and the determination of nuclear charge radii from their $2p$–$1s$ transition. The chapter concludes with a summary of nuclear charge radii of light atoms and the expected sensitivity of the QUARTET experiment.

2.1. Formation of Muonic Atoms

For X-ray spectroscopy of muonic atoms, a muon beam is produced at an accelerator facility and stopped in a target material, where muonic atoms are formed. The bound muons undergo a cascade to lower energy levels, releasing Auger electrons and emitting characteristic muonic X-rays. The muon ultimately decays or is captured by the nucleus. High-resolution spectroscopy of these characteristic X-rays allows the determination of nuclear charge radii.

2.1.1. Muon Production

The production of muonic atoms in large quantities requires a high-intensity, low-momentum muon beam. Muons are produced by directing high-energy protons onto a low-Z target, such

as graphite, where Z is the atomic number. These protons p undergo strong interactions with nucleons. One possible interaction is with a neutron n in the nucleus, given by

$$\mathrm{p} + \mathrm{n} \rightarrow \mathrm{p} + \mathrm{p} + \pi^- \tag{2.1}$$

producing negative pions π^-. Other processes can produce positive or neutral pions. The negative pions subsequently decay into a muon μ^- and a muon-antineutrino $\bar{\nu}_\mu$ according to

$$\pi^- \rightarrow \mu^- + \bar{\nu}_\mu \tag{2.2}$$

and the resulting muons are collected, momentum selected, and collimated into a beam. The muon beam is directed at a macroscopic target to be investigated, in which the muons lose energy via ionization and are eventually stopped. Once the energy of a muon is on the order of the electron binding energy, it is bound by the electric field of a nucleus, forming a muonic atom of the target material.

At PSI, a proton beam is generated by ionizing hydrogen gas, which is pre-accelerated using a Cockcroft–Walton generator and further accelerated by two cyclotrons to 590 MeV with currents of up to 2.4 mA [38]. The high-energy proton beam is directed onto a graphite target, where negative pions are produced and decay in flight to muons. The high-intensity $\pi E1$ beamline can produce a continuous negative muon beam with a momentum of 25 MeV c^{-1} at a rate of approximately 10 kHz, depending on the selected momentum up to about 40 MeV c^{-1} [39]. Such a low-momentum muon beam, with a corresponding kinetic energy of about 3 MeV, can be stopped within approximately 1 mm of a low-Z target material on a timescale of roughly 100 ps. This continuous muon beam provides the highest intensity currently available and is well suited for muonic X-ray spectroscopy using detectors with long response times.

2.1.2. Muon Cascade

A bound muon is initially in a high-energy state ($n \approx 14$), corresponding to an orbital radius slightly smaller than the electron orbital radii, where the muon experiences the nearly unscreened nuclear electric field [36]. The muon de-excites through a cascade of transitions towards its ground state ($1s$). Initially, the muonic transition energies are on the same order of magnitude as the electronic binding energies, and the emission of Auger electrons is dominant if bound electrons are still present. At lower energy levels ($n \leq 5$), the de-excitation is dominated by the emission of characteristic muonic X-rays. A statistical initial population for the cascade is assumed to be proportional to the spin degeneracy $P(n, l, j) \propto (2j + 1)$. The most probable transitions are those with $\Delta n = -1$, $\Delta l = -1$, and $l = n - 1$, for example $4f$–$3d$, $3d$–$2p$, and $2p$–$1s$, but transitions with $\Delta n \geq 2$ also occur with reduced intensity [37].

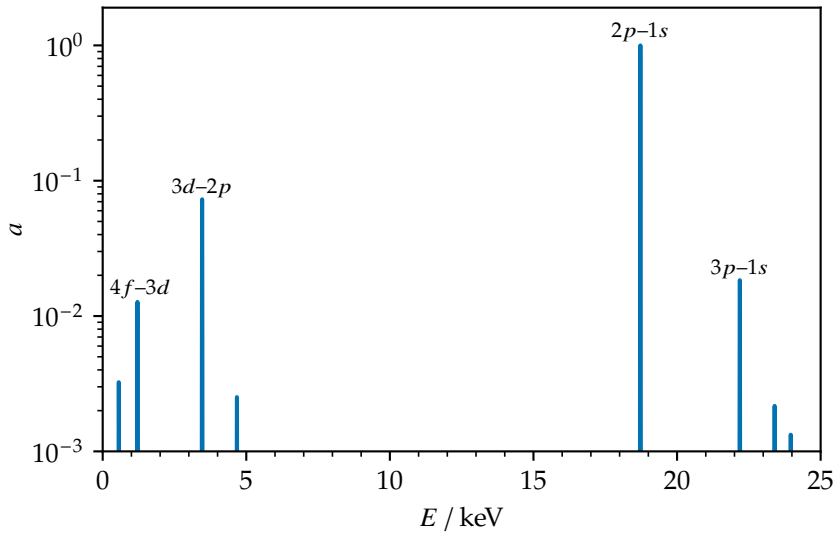

Figure 2.1.: Simulated X-ray spectrum from the muon cascade of muonic lithium (^{7}Li). Muonic X-ray transition rates and energies are simulated using *MuDirac* [40, 41]. The cascade is separately calculated from the transition rates for a statistical initial population of $P(n, l, j) \propto (2j + 1)$ with $5 \leq n \leq 8$, providing a rough estimate and omitting Auger electrons. The spectrum is calculated for a detector with an FWHM energy resolution of $E_{\mathrm{FWHM}} = 10\,\mathrm{eV}$ and the amplitude a is normalized to the $2p$–$1s$ line.

The spectrum of characteristic muonic X-rays from the cascade can be simulated based on transition rates and energies, and assuming an initial population of states. By simulating the muonic X-ray transition rates and energies using *MuDirac* [40, 41], the expected X-ray spectrum of the cascade of muonic lithium (^{7}Li) is calculated separately, as an approximation neglecting Auger electrons, shown in Figure 2.1. According to this estimation, roughly 80 % of the bound muons undergo the $2p$–$1s$ transition.

The muon either decays as a free muon or is captured by a proton from the nucleus. The free muon decay, known as Michel decay [42], has a lifetime of about 2.2 µs via the weak interaction

$$\mu^- \rightarrow e^- + \bar{\nu}_e + \nu_\mu \tag{2.3}$$

which produces an electron e^-, known as the Michel electron, together with an electron-antineutrino $\bar{\nu}_e$, and a muon-neutrino ν_μ. The resulting Michel electrons appear as a background with a continuous energy spectrum, peaking at approximately 35 MeV and reaching a maximum energy of 53 MeV [42]. For heavier nuclei ($10 \leq Z$), low-lying muons have a higher probability of being within the nucleus, and muon capture by a proton of the nucleus becomes the dominant process. Muon capture significantly reduces the muon lifetime via the weak interaction

$$\mu^- + p \rightarrow n + \nu_\mu \tag{2.4}$$

which converts a proton of the nucleus into a neutron, produces a muon-neutrino, and leaves the daughter nucleus in an excited state.

For low-Z atoms, the muon cascade to the ground state $(1s)$ occurs on a timescale of about 1 ns, while for high-Z atoms it is around 1 ps [36]. For muonic lithium $(Z = 3)$, the muon lifetime is similar to that of a free muon, whereas for high-Z atoms it is reduced to less than 100 ns due to nuclear capture [37]. Since the cascade is significantly faster than muon decay, nearly all muons reach the ground state $(1s)$ before decaying.

2.2. Muonic Energy Levels

During the de-excitation of the bound muon, characteristic muonic X-rays are emitted. To evaluate the energy shifts induced by the nuclear structure, the muonic energy levels and corresponding transition energies must be calculated with high precision. The energy levels can be estimated in the same way as for the electronic hydrogen atom. Solving the time-independent Schrödinger equation for a non-relativistic muon in the Coulomb field of a point-like nucleus yields hydrogen-like energy levels, also referred to as Bohr levels. The leading-order corrections to these levels include the fine structure (FS), the electronic vacuum polarization (eVP), and the finite nuclear size (FNS).

While this discussion considers only leading-order corrections, a precise determination of the muonic energy levels requires the calculation of higher-order corrections as well. These account for higher-order QED contributions such as self-energy and nuclear polarization effects arising from virtual excitations, hyperfine structure due to magnetic dipole and electric quadrupole interactions, and nuclear recoil corrections beyond the leading-order reduced-mass approximation.

2.2.1. Bohr Levels

A hydrogen-like system of a non-relativistic muon bound in the Coulomb field of a point-like nucleus can be described by the Hamiltonian $\hat{H}_0$, given in natural units $(\hbar = c = 1)$ by

$$\hat{H}_0 = -\frac{\nabla^2}{2\,\mu} - \frac{Z\,\alpha}{r} \tag{2.5}$$

where μ is the reduced mass, Z is the atomic number, and $\alpha \approx 1/137$ is the fine-structure constant. The first term $-\nabla^2/(2\,\mu)$ represents the non-relativistic kinetic energy, while the second term $V_\mathrm{p} = -Z\,\alpha/r$ is the Coulomb potential of a point-like nucleus. The reduced mass μ is given by

$$\mu = \frac{m_\mu\, m_n}{m_\mu + m_n} \tag{2.6}$$

where m_μ is the muon mass and m_n is the mass of the nucleus. The nuclear mass m_n can be calculated by summing the masses of all protons and neutrons in the nucleus and subtracting the nuclear binding energy as reported in the literature [43].

The energy levels appear as the eigenvalues of the time-independent Schrödinger equation

$$\hat{H}_0 \, \psi(\mathbf{r}) = E \, \psi(\mathbf{r}) \tag{2.7}$$

where the wavefunction $\psi(\mathbf{r})$, expressed in spherical coordinates, can be separated into a radial part $R_{nl}(r)$ and an angular part $Y_l^m(\vartheta, \varphi)$. The general solution is a set of orthogonal wavefunctions $\psi_{nlm}(r, \vartheta, \varphi)$ given by

$$\psi_{nlm}(r, \vartheta, \varphi) = R_{nl}(r) \, Y_l^m(\vartheta, \varphi) \tag{2.8}$$

with the principal quantum number n, the orbital angular momentum quantum number l, and the magnetic quantum number m, with $1 \leq n$, $0 \leq l \leq n - 1$, and $-l \leq m \leq +l$. In spectroscopic notation, states are labeled by n and l as nl, for example $1s$ for $n = 1$, $l = 0$ and $2p$ for $n = 2$, $l = 1$, where for l the conventional spectroscopic letters s $(l = 0)$, p $(l = 1)$, d $(l = 2)$, f $(l = 3)$, and so on, are used.

The angular part $Y_l^m(\vartheta, \varphi)$ is given by the spherical harmonics

$$Y_l^m(\vartheta, \varphi) = \sqrt{\frac{2l + 1}{4\pi} \, \frac{(l - m)!}{(l + m)!}} \, P_l^m(\cos \vartheta) \, e^{im\varphi} \tag{2.9}$$

with the associated Legendre polynomials $P_l^m(x)$. The radial functions $R_{nl}(r)$ are given by

$$R_{nl}(r) = \sqrt{\frac{(n - l - 1)!}{(n + l)!}} \, \frac{2^{l+1}}{n^2} \, r^{3/2} \left(\frac{r}{n\,a}\right)^l \, e^{-r/(n\,a)} \, L_{n-l-1}^{2l+1}\left(\frac{2\,r}{n\,a}\right) \tag{2.10}$$

where $L_{n-l-1}^{2\,l+1}(x)$ are the associated Laguerre polynomials, and r is the radial coordinate, expressed in units of the Bohr radius $a = 1/(Z\,\alpha\,\mu)$, which corresponds to the characteristic radii r with $n = 1$, given below.

The eigenvalues are the quantized Bohr energy levels E_B given by

$$E_\mathrm{B} = -\frac{1}{2} \, \frac{(Z\,\alpha)^2}{n^2} \, \mu \tag{2.11}$$

and the characteristic radii r are given by

$$r = \frac{n^2}{Z\,\alpha\,\mu} \tag{2.12}$$

which correspond to the most probable radial distance for s-states ($l = 0$). These results are identical to those of the well-known semi-classical Bohr model. The energy levels are degenerate with respect to the orbital angular momentum l and magnetic quantum number m, as the Coulomb potential is spherically symmetric.

The Bohr energy levels E_B scale with the reduced mass μ, while the characteristic orbital radii r scale inversely with the reduced mass μ. The mass ratio of the muon to the electron $m_\mu/m_e \approx 200$ thus roughly sets the scaling factor between energy level and radii in electronic and muonic atoms. The Bohr energy of the ground state $1s$ ($n = 1$, $l = 0$) of electronic hydrogen ($Z = 1$) is the well-known $E_\mathrm{B} \approx -13.6\,\mathrm{eV}$, whereas for muonic hydrogen it is $-2.53\,\mathrm{keV}$, significantly higher in absolute energy and within the X-ray range. The Bohr radius for electronic hydrogen is $a = 53\,\mathrm{pm}$, while in muonic hydrogen it is 280 fm, which is significantly closer to the nucleus.

For muonic ^{7}Li ($Z = 3$, $A = 7$), the ground-state $1s$ energy is $-24.9\,\mathrm{keV}$, while the first excited states $2p$ and $2s$ have an energy of $-6.23\,\mathrm{keV}$. The corresponding Bohr radius $a = 87$ fm is very close to the nucleus, with a nuclear charge radius of about 2.4 fm, as listed later in Table 2.1. The resulting $2p$–$1s$ transition energy is $\Delta E_{2p-1s} = 18.7\,\mathrm{keV}$, which lies within the X-ray energy range.

2.2.2. Fine Structure

The fine structure (FS) accounts for the muon being a relativistic Dirac particle with an intrinsic spin-1/2. It combines three corrections, namely the leading-order relativistic correction to the kinetic energy, the spin–orbit coupling, and the Darwin term. The FS correction scales with $(Z\,\alpha)^4\,\mu$ and lifts the degeneracy of the energy levels derived from the non-relativistic Schrödinger equation. In the following, the correction is derived under the assumption of an infinitely heavy nucleus, which also applies to the corresponding wavefunctions ψ. Nuclear recoil effects originating from the finite nuclear mass are therefore neglected.

Relativistic Correction

The kinetic energy of the muon must be treated relativistically in this correction. For a muon with momentum much smaller than its rest mass ($\hat{p}/m_\mu \ll 1$), the relativistic free-particle Hamiltonian $\hat{H}$ can be expanded in powers of the Laplace operator ∇ as

$$\hat{H} = \sqrt{-\nabla^2 + m_\mu^2} \tag{2.13}$$

$$= m_\mu - \frac{\nabla^2}{2m_\mu} - \frac{\nabla^4}{8\,m_\mu^3} + O\left(\nabla^6\right) \tag{2.14}$$

where the first term m_μ corresponds to the rest mass energy of the muon, the second term $-\nabla^2/(2m_\mu)$ represents the non-relativistic kinetic energy, and the third term $-\nabla^4/(8\,m_\mu^3)$ provides the leading-order relativistic correction. The corresponding Hamiltonian $\hat{H}_\mathrm{R}$ given by

$$\hat{H}_\mathrm{R} = -\frac{\nabla^4}{8\,m_\mu^3} \tag{2.15}$$

can be treated as a perturbation. Its expectation value with respect to the unperturbed hydrogen-like wavefunctions

$$\begin{aligned} \delta E_\mathrm{R} &= \langle\psi|\hat{H}_\mathrm{R}|\psi\rangle && (2.16)\\ &= (Z\,\alpha)^4\,m_\mu\left(\frac{3}{8\,n^4} - \frac{1}{(2\,l+1)\,n^3}\right) && (2.17)\end{aligned}$$

yields the relativistic energy correction δE_R.

Spin–Orbit Coupling

The spin–orbit coupling describes the interaction between the intrinsic magnetic moment of the muon, associated with its spin angular momentum $\mathbf{S}$, and the magnetic field generated by its orbital motion in the rest frame of the muon. The intrinsic magnetic moment of the muon μ_μ is given by

$$\mu_\mu = -\frac{g\,e}{2\,m_\mu}\,\mathbf{S} \tag{2.18}$$

where $g \approx 2$ is the Landé g-factor of the muon, and e is the elementary charge. The interaction with the magnetic field generated by its orbital motion leads to the spin–orbit Hamiltonian $\hat{H}_\mathrm{SO}$ given by

$$\begin{aligned} \hat{H}_\mathrm{SO} &= \frac{(g-1)}{2\,m_\mu^2}\,\frac{1}{r}\,\frac{\mathrm{d}V_\mathrm{p}}{\mathrm{d}r}\,\mathbf{L}\cdot\mathbf{S} && (2.19)\\ &= (Z\,\alpha)\,\frac{(g-1)}{2\,m_\mu^2}\,\frac{1}{r^3}\,\mathbf{L}\cdot\mathbf{S} && (2.20)\end{aligned}$$

where $V_\mathrm{p} = -Z\,\alpha/r$ is the point-like Coulomb potential, and $\mathbf{L}\cdot\mathbf{S}$ represents the spin–orbit alignment. The resulting spin–orbit energy correction δE_SO is given by

$$\begin{aligned} \delta E_\mathrm{SO} &= \langle\psi|\hat{H}_\mathrm{SO}|\psi\rangle && (2.21)\\ &= -(Z\,\alpha)^4\,m_\mu\,\frac{(g-1)}{n^3}\,\frac{\langle\mathbf{L}\cdot\mathbf{S}\rangle}{l\,(l+1)\,(2\,l+1)} && (2.22)\end{aligned}$$

where the expectation value of the spin–orbit alignment is given by

$$\langle \mathbf{L} \cdot \mathbf{S} \rangle = \frac{1}{2} \left[j\,(j+1) - l\,(l+1) - s\,(s+1) \right] \tag{2.23}$$

with the spin quantum number $s = 1/2$, and the total angular momentum quantum number $j = l \pm s$. The spin–orbit energy correction δE_{SO} vanishes for $l = 0$ states.

Darwin Term

The Darwin term arises from the intrinsic quantum fluctuations in the position of the muon. It can be understood as the result of interference between the positive- and negative-energy components of the Dirac spinor, which effectively spread out the muon position. The Darwin Hamiltonian $\hat{H}_{\mathrm{D}}$ for this correction is given by

$$\hat{H}_{\mathrm{D}} = \frac{1}{8\,m_{\mu}^2}\,\nabla^2 V_{\mathrm{p}} \tag{2.24}$$

$$= \frac{\pi}{2\,m_{\mu}^2}\,(Z\,\alpha)\,\delta^3(\mathbf{r}) \tag{2.25}$$

where $\delta^3(\mathbf{r})$ is the three-dimensional delta function. The corresponding Darwin energy correction δE_{D} is

$$\delta E_{\mathrm{D}} = \langle \psi | \hat{H}_{\mathrm{D}} | \psi \rangle \tag{2.26}$$

$$= \frac{\pi}{2\,m_{\mu}^2}\,(Z\,\alpha)\,\left\langle \delta^3(\mathbf{r}) \right\rangle \tag{2.27}$$

$$= (Z\,\alpha)^4\,m_{\mu}\,\frac{1}{2\,n^3}\,\delta_{l0} \tag{2.28}$$

which follows from the expectation value of the delta function, which selects the probability density at the origin. Assuming an infinitely heavy nucleus, it is given by

$$\left\langle \delta^3(\mathbf{r}) \right\rangle = |\psi_{nlm}(0)|^2 \tag{2.29}$$

$$= (Z\,\alpha)^3\,m_{\mu}^3\,\frac{1}{\pi\,n^3}\,\delta_{l0} \tag{2.30}$$

and is non-zero only for s-states ($l = 0$).

Combined Correction

The combined energy correction of the FS δE_{FS}, neglecting nuclear recoil, is given by the sum of the individual corrections

$$\delta E_{\mathrm{FS}} = \delta E_{\mathrm{R}} + \delta E_{\mathrm{SO}} + \delta E_{\mathrm{D}} \tag{2.31}$$

$$= (Z\,\alpha)^4\, m_{\mu} \left[\frac{3}{8\,n^4} - \frac{1}{(2l+1)\,n^3} - \frac{(g-1)}{n^3} \frac{\langle \mathbf{L}\cdot\mathbf{S}\rangle}{l(l+1)(2l+1)} + \frac{1}{2\,n^3}\,\delta_{l0} \right] \tag{2.32}$$

which can be simplified to

$$\delta E_{\mathrm{FS}} = (Z\,\alpha)^4\, m_{\mu} \left(\frac{3}{8\,n^4} - \frac{1}{(2\,j+1)\,n^3} \right) \tag{2.33}$$

using $g \approx 2$ as predicted by the Dirac theory. The corresponding energy levels including the FS correction are commonly denoted in spectroscopic notation as nl_j, for example $1s_{1/2}$ for $n = 1$, $l = 0$, $j = 1/2$ and $2p_{3/2}$ for $n = 2$, $l = 1$, $j = 3/2$, where j is the total angular momentum. The leading-order FS energy correction including nuclear recoil can be calculated using the Breit Hamiltonian, as described in the literature [44].

For muonic Li, the fine-structure correction to the ground state $1s_{1/2}$ is $\delta E_{\mathrm{FS}} = -3.0\,\mathrm{eV}$, while for $2p_{1/2}$ and $2p_{3/2}$ the corrections are $-0.9\,\mathrm{eV}$ and $-0.2\,\mathrm{eV}$, respectively. The resulting fine-structure energy shifts of the $2p$–$1s$ transitions are $\delta E_{2p_{1/2}-1s_{1/2}} = 2.1\,\mathrm{eV}$ and $\delta E_{2p_{3/2}-1s_{1/2}} = 2.8\,\mathrm{eV}$. For the targeted precision, both the fine-structure splitting and the relative peak intensities must be evaluated in order to accurately model the observed spectrum.

2.2.3. Lamb Shift

The Lamb shift originates from QED effects beyond the static Coulomb interaction. These effects arise from the presence of virtual particles and include self-energy and electronic vacuum polarization (eVP) corrections. In muonic atoms, the leading-order contribution is due to eVP, which modifies the Coulomb potential at short distances through the screening caused by virtual electron–positron pairs. This differs from electronic atoms, where the dominant contribution to the Lamb shift arises from the electron self-energy.

The leading-order correction from the eVP is described by the Uehling potential V_{U} [45] as a perturbative correction to the point-like Coulomb potential V_{p}, given by

$$V_{\mathrm{U}} = -\frac{Z\,\alpha}{r}\,\frac{\alpha}{3\,\pi} \int_1^{\infty} e^{-2\,m_{\mu}\,r\,\zeta} \left(1 + \frac{1}{2\,\zeta^2}\right) \frac{\sqrt{\zeta^2-1}}{\zeta^2}\,\mathrm{d}\zeta \tag{2.34}$$

where ζ is a dimensionless variable, parameterizing the scaled momentum in the loop. The leading-order energy correction δE_L is given by

$$\delta E_\mathrm{L} = \langle \psi | V_\mathrm{U} | \psi \rangle \tag{2.35}$$

which generally requires numerical evaluation due to the integral form of the Uehling potential. The leading-order correction δE_L from the eVP scales approximately as $\alpha\,(Z\,\alpha)^2\,\mu$.

The leading-order Lamb shift from eVP δE_L can be evaluated non-perturbatively using *MuDirac* by solving the Dirac equation numerically with a modified binding potential [40, 41]. For muonic ^{7}Li, the correction of the $1s_{1/2}$ state is $\delta E_\mathrm{L} = -61.4\,\mathrm{eV}$, while for $2p_{1/2}$ and $2p_{3/2}$ it is $-2.1\,\mathrm{eV}$. The corresponding correction of the $2p$–$1s$ transition is $\delta E_{2p-1s} = 59.3\,\mathrm{eV}$. In contrast to electronic atoms, this correction is significantly larger than the fine-structure correction. For an accurate evaluation, this means that recoil effects and other higher-order contributions of the Lamb shift must be taken into account.

2.2.4. Finite Nuclear Size

The finite size of the nucleus modifies the Coulomb field near the origin. This leads to a measurable energy shift for states with non-zero probability density at the nucleus, making these states sensitive to the nuclear charge distribution.

Assuming a uniformly charged spherical nucleus with radius r_s, the Coulomb potential V_s is given by

$$V_\mathrm{s} = \begin{cases} -\dfrac{Z\,\alpha}{r} & \text{for } r \geq r_\mathrm{s} \\ -\dfrac{Z\,\alpha}{2\,r_\mathrm{s}} \left[3 - \left(\dfrac{r}{r_\mathrm{s}} \right)^2 \right] & \text{for } r \leq r_\mathrm{s} \end{cases} \tag{2.36}$$

as shown in Figure 2.2. The corresponding RMS nuclear charge radius r_c is given by

$$r_\mathrm{c}^2 = \frac{1}{Ze} \int \rho(\mathbf{r})\, r^2 \, \mathrm{d}^3 r \tag{2.37}$$

$$= \frac{3}{5}\, r_\mathrm{s}^2 \tag{2.38}$$

where ρ is the charge density. The potential V_s can be used to define a perturbative correction $V_\mathrm{s} - V_\mathrm{p}$ to the point-like Coulomb potential V_p.

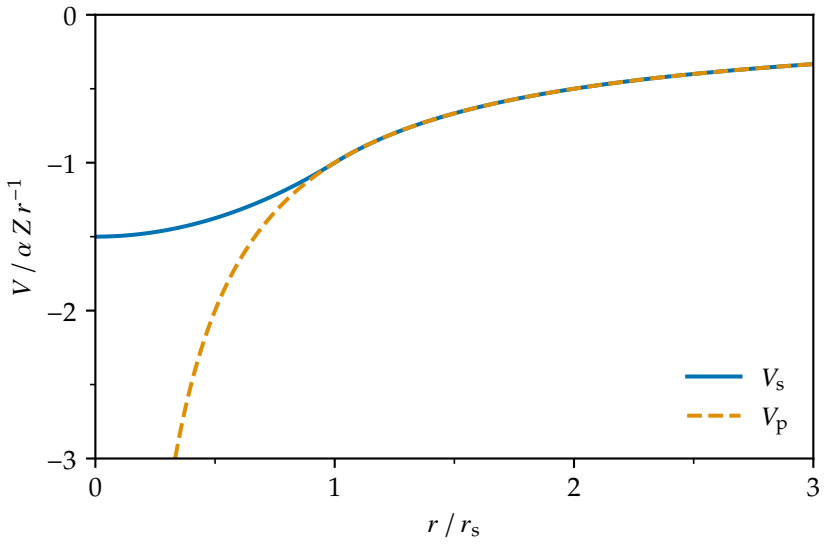

Figure 2.2.: Dimensionless Coulomb potential of a uniformly charged sphere V_s compared to the potential of a point-like nucleus V_p. The finite-size correction lifts the singularity at the origin and raises the potential at small radii within the nucleus.

The corresponding leading-order energy correction due to the finite nuclear size (FNS) δE_FNS is given by

$$\delta E_\mathrm{FNS} = \langle\psi|V_\mathrm{s} - V_\mathrm{p}|\psi\rangle \tag{2.39}$$

$$\approx \frac{2\,\pi}{3}\,(Z\,\alpha)\,\left\langle\delta^3(\mathbf{r})\right\rangle\,r_\mathrm{c}^2 \tag{2.40}$$

$$= \frac{2}{3}\,(Z\,\alpha)^4\,\mu^3\,\frac{1}{n^3}\,r_\mathrm{c}^2\,\delta_{l0} \tag{2.41}$$

which contributes only to s-states ($l = 0$). First, the approximation $r_\mathrm{c} \ll a$ was applied, and then the delta function was evaluated

$$\left\langle\delta^3(\mathbf{r})\right\rangle = (Z\,\alpha)^3\,\mu^3\,\frac{1}{\pi\,n^3}\,\delta_{l0} \tag{2.42}$$

using a finite nuclear mass, similar to equation (2.30). The leading-order correction is independent of the charge distribution. The scaling of $(Z\,\alpha)^4\,\mu^3$ results in a significant enhancement of approximately $(m_\mu/m_\mathrm{e})^3 \approx 10^7$ for muonic atoms compared to electronic atoms.

For muonic ^{7}Li with $r_\mathrm{c} = 2.449(41)$ fm, as listed later in Table 2.1, the FNS energy correction for the ground state $1s_{1/2}$ is $\delta E_\mathrm{FNS} = 26.5\,\mathrm{eV}$. Since only s-states are affected in this approximation, the energy correction to the $2p$–$1s$ transition is therefore $\delta E_{2p-1s} = -26.5\,\mathrm{eV}$. The sensitivity of the $2p$–$1s$ transition to the nuclear charge radius is $\mathrm{d}r_\mathrm{c}/\mathrm{d}E \approx 48\,\mathrm{am\,eV}^{-1}$. To improve the current accuracy of the nuclear charge radius of ^{7}Li, its muonic $2p$–$1s$ transition

energy must be measured with an energy precision of at least 0.9 eV, based on the sensitivity to the nuclear charge radius $\mathrm{d}r_\mathrm{c}/\mathrm{d}E_\mathrm{FNS} \approx 48\,\mathrm{am\,eV}^{-1}$ and the current uncertainty of the radius $\sigma_{r_\mathrm{c}} = 41\,\mathrm{am}$. This corresponds to about 50 ppm, which requires high-resolution X-ray detectors.

2.2.5. Level Scheme

The Bohr energy levels derived from the non-relativistic Schrödinger equation, along with their leading-order corrections from FS, Lamb shift from eVP, and FNS, given by

$$E = E_\mathrm{B} + \delta E_\mathrm{FS} + \delta E_\mathrm{L} + \delta E_\mathrm{FNS} \tag{2.43}$$

are shown in Figure 2.3 for muonic ^{7}Li and principal quantum numbers $n \leq 3$.

Among these corrections, the FNS introduces a large energy shift to the $1s$ ground state due to the strong overlap between its wavefunction and the nuclear charge distribution. Consequently, the $2p$–$1s$ transition is highly sensitive to the nuclear charge radius. For muonic ^{7}Li, the leading-order corrected transition energies are $\delta E_{2p_{1/2}\text{–}1s_{1/2}} = 18\,723.0\,\mathrm{eV}$ and $\delta E_{2p_{3/2}\text{–}1s_{1/2}} = 18\,723.8\,\mathrm{eV}$, each with an uncertainty of about 1 eV, dominated by the current uncertainty in r_c.

2.3. Nuclear Charge Radius

The nuclear charge radius r_c, defined as the RMS radius of the nuclear charge distribution, is a fundamental property that characterizes the spatial distribution of the nuclear electric charge. The nuclear charge radius and its shift between different isotopes can be determined by several experimental methods. Among these, the most relevant are elastic electron scattering, laser spectroscopy of electronic atoms, muonic laser spectroscopy, and X-ray spectroscopy of muonic atoms.

2.3.1. Muonic X-ray Spectroscopy

The derived muonic energy levels provide the theoretical basis for extracting nuclear charge radii from X-ray spectroscopy of muonic atoms. Higher-order corrections of order $\alpha\,(\alpha\,Z)^4$, as well as corrections for recoil effects beyond the leading-order reduced-mass approximation, allow for accurate predictions of transition energies and line shapes for a given nuclear charge radius r_c. A general approach with higher-order corrections yields for the energy of a muonic transition the sum of contributions

$$\Delta E = \Delta E_\mathrm{D} + \delta E_\mathrm{QED} + \delta E_\mathrm{FNS} + \delta E_\mathrm{NP} \tag{2.44}$$

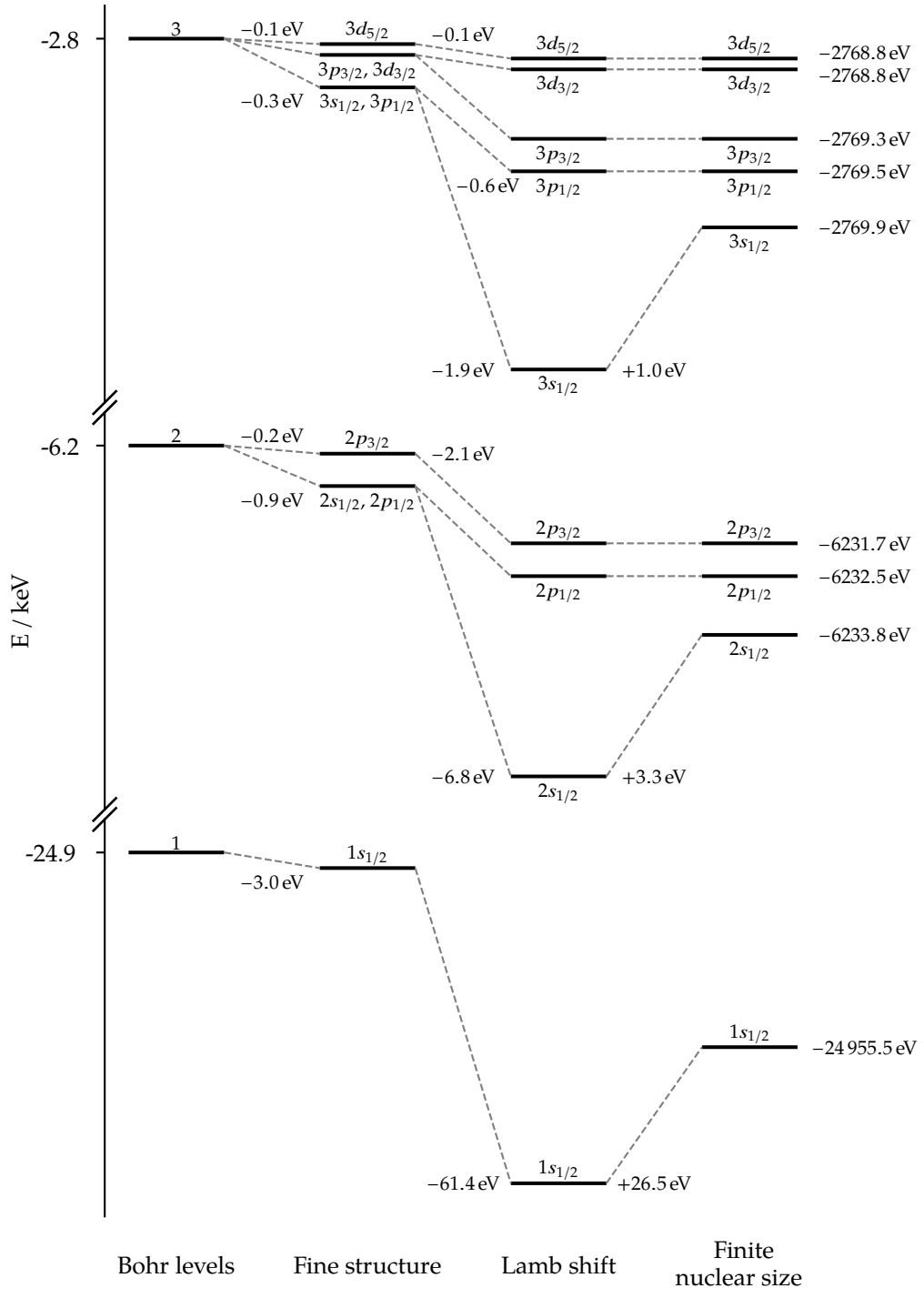

Figure 2.3.: Bohr energy levels and their leading-order corrections from FS, leading-order Lamb shift from eVP, and FNS, for muonic ^{7}Li. The diagrams for different principal quantum numbers n are plotted with different vertical energy scales.

where ΔE_{D} is the Dirac energy for a point-like nucleus, corresponding to the Bohr energy with higher-order corrections for the muon being a relativistic Dirac particle with intrinsic spin-1/2, δE_{QED} are QED effects such as eVP and self-energy, δE_{FNS} is the correction for the FNS, and δE_{NP} corrects for nuclear polarization effects arising from virtual excitations [5]. By precisely measuring the energy of a muonic transition sensitive to the nuclear charge radius and accurately evaluating each of the corrections, the nuclear charge radius is extracted from the FNS contribution δE_{FNS}. This enables precise determination of the nuclear charge radius r_{c}, provided all other contributions are well understood and accurately calculated. For X-ray spectroscopy of muonic atoms, crystal spectrometers and HPGe detectors are used.

Crystal Spectrometers

Crystal spectrometers are high-resolution detectors that determine X-ray energies via Bragg diffraction in crystals. When X-rays impinge on a crystal with lattice spacing d, constructive interference occurs at specific angles θ, according to Bragg's law

$$n\,\lambda = 2\,d\,\sin\theta, \tag{2.45}$$

where λ is the X-ray wavelength and n is the diffraction order. By measuring the Bragg angle θ, the X-ray wavelength λ and thus its energy can be determined with high accuracy. The resolution can be further enhanced by using multiple crystals in series.

Although crystal spectrometers provide excellent energy resolution, with resolving powers $E/\Delta E_{\mathrm{FWHM}}$ of several thousand, they are limited by low detection efficiency and a narrow spectral bandwidth. For example, the crystal spectrometer used to measure the muonic $2p$–$1s$ transitions of ^{12}C and ^{13}C at 75 keV employed two crystals, achieving a full width at half maximum (FWHM) energy resolution of 70 eV and covering a bandwidth below 500 eV [33, 46].

High-Purity Germanium Detectors

High-purity germanium (HPGe) detectors are semiconductor detectors widely used for X-ray and γ-ray spectroscopy. They are based on ultrapure germanium crystals across which a bias voltage of several kV is applied to fully deplete it of free charge carriers and establish a uniform electric field. To suppress thermally generated charge carriers, the detectors are typically cooled to 77 K using liquid nitrogen. When X-rays interact with the crystal, they deposit energy, creating electron–hole pairs, with about 3 eV required to form each pair. These charge carriers drift in the electric field and are collected at electrodes, generating an electric signal proportional to the X-ray energy.

HPGe detectors combine high detection efficiency with broad energy coverage, extending up to several MeV. They are therefore well suited for broadband X-ray and γ-ray spectroscopy, though they feature only a moderate energy resolution, with resolving powers ranging from a few hundred at low energies to several thousand at high energies. For example, an HPGe detector with a FWHM energy resolution of approximately 1 keV at 300 keV was used to measure the muonic $2p$–$1s$ transitions of multiple elements, with $8 \leq Z \leq 14$ in the energy range from 130 keV to 400 keV [30].

2.3.2. Experimental Methods

In addition to X-ray spectroscopy of muonic atoms, several other experimental techniques have been employed to determine nuclear charge radii. The most relevant methods are elastic electron scattering, laser spectroscopy of electronic atoms, and muonic laser spectroscopy. A detailed discussion can be found in the literature [31].

Elastic Electron Scattering

Elastic electron scattering is a direct method for determining nuclear charge radii. A high-energy electron beam is elastically scattered from a nuclear target, and the angular distribution of the scattered electrons is measured. The measured differential cross section deviates from that of a point-like nucleus due to the extended nuclear charge distribution and is related to the nuclear form factor $F(q)$ by

$$\left(\frac{\partial\sigma}{\partial\Omega}\right)_{\text{exp}} = \left(\frac{\partial\sigma}{\partial\Omega}\right)_{\text{Mott}} |F(q)|^2 \tag{2.46}$$

where $(\partial\sigma/\partial\Omega)_{\text{Mott}}$ is the Mott cross section for a point-like nucleus, and q is the momentum transfer. The form factor $F(q)$ is the Fourier transform of the nuclear charge density and encodes the spatial distribution of the nuclear charge. To extract the nuclear charge radius, $F(q)$ is obtained from measurements at different scattering angles and fitted using model-independent parameterizations or phenomenological models.

This method provides nuclear charge radii with intermediate precision, as its accuracy is limited by systematic uncertainties. Elastic electron and pion scattering currently yields the most accurate results for light elements, with $3 \leq Z \leq 5$ and $Z = 7$.

Laser Spectroscopy

Precision laser spectroscopy can resolve isotope shifts as differences in the resonant frequencies of atomic transitions. The frequency shift $\delta\nu_{AA'}$ of an atomic transition

$$\delta\nu_{AA'} = \nu_{A'} - \nu_A \tag{2.47}$$

between two isotopes with mass numbers A and A' results from two primary contributions, a mass shift due to the change in the reduced mass and a field shift caused by differences in the nuclear charge distribution between the isotopes. The total isotope shift can be approximated as

$$\delta\nu_{AA'} \approx M\,\frac{A' - A}{AA'} + F\,\delta r_{\mathrm{c}}^2 \tag{2.48}$$

where M and F are the mass and field shift constants, respectively, and δr_{c}^2 is the difference in mean-square nuclear charge radii. Accurate atomic structure calculations are required to determine the constants M and F with sufficient precision to extract the difference in the nuclear charge radii.

Since this method yields only relative changes in nuclear charge radii of isotope chains, a reference isotope with a known absolute radius is required to establish an absolute scale. The method can also be applied to small sample quantities of material and to radioactive isotopes, making it particularly suitable for studies of rare and short-lived nuclei. Combined with absolute measurements from other methods, laser spectroscopy provides the most precise nuclear charge radii for several isotopes [47, 48].

Muonic Laser Spectroscopy

The $2s$–$2p$ transition in very light muonic atoms can be driven with a tunable infrared laser. A small fraction of muonic atoms populate the metastable $2s$ state during the cascade, which has a lifetime of about 1 μs. This state can be excited with an infrared laser to the $2p$ state, which has a short lifetime and undergoes the $2p$–$1s$ transition, emitting an X-ray. By scanning the laser frequency while detecting $2p$–$1s$ X-rays in delayed coincidence, the $2s$–$2p$ transition energy can be measured with high precision. Similar to X-ray spectroscopy of the $2p$–$1s$ transition, the $2s$–$2p$ transition energy is also sensitive to the finite spatial distribution of the nuclear charge and allows the extraction of the nuclear charge radius.

This method provides the most precise absolute charge radii for H and He, with $Z \leq 2$ [24, 29]. However, it is difficult to extend this approach to heavier elements, as this requires an initial narrow frequency scan range and a tunable laser operating at the wavelength corresponding to the muonic $2s$–$2p$ transition.

2.3.3. Overview

An overview of nuclear charge radii r_c for selected light, stable nuclei is given in Table 2.1, and later visualized in Figure 2.4. For the lightest nuclei with $Z \leq 2$, laser spectroscopy of muonic atoms provides precise absolute values. However, this technique is currently infeasible for heavier nuclei due to technological limitations. For nuclei with $11 \leq Z$, X-ray spectroscopy of muonic atoms using HPGe detectors yields accurate nuclear charge radii, but the precision is limited for lighter nuclei due to their reduced energy resolution. In the case of ^{12}C with $Z = 6$, X-ray spectroscopy using a crystal spectrometer provided an accurate absolute value, though the low efficiency and narrow bandwidth of crystal spectrometers make them unsuitable for systematic studies. For nuclei with $3 \leq Z \leq 5$ and for ^{15}N with $Z = 7$, elastic electron and pion scattering provides charge radii with intermediate precision. Additionally, laser spectroscopy yields relative isotope shifts for many isotopes, but depends on accurate absolute reference measurements. As a result, a precision gap remains for light nuclei with $3 \leq Z \leq 10$, especially for Li, Be, and B with $3 \leq Z \leq 5$.

2.4. QUARTET

The QUAntum inteRacTions with Exotic aToms (QUARTET) collaboration aims to close the precision gap in determining RMS nuclear charge radii for light nuclei by performing high-resolution X-ray spectroscopy of light muonic atoms from Li to Ne, with $3 \leq Z \leq 10$ [5]. The absolute values of the nuclear charge radii r_c are extracted from the characteristic $2p$–$1s$ muonic X-rays, in the energy range from 19 keV for muonic Li to 207 keV for muonic Ne. The collaboration aims to improve the precision of the nuclear charge radii by up to a factor of nearly 30 and to determine isotope shifts between stable isotopes with high accuracy [5].

2.4.1. Experimental Method

The QUARTET experiment employs MMCs-based detector arrays for high-resolution X-ray spectroscopy [2]. These low-temperature detectors, operated at mK temperatures, determine the energy of incident particles by measuring the temperature rise caused by their energy deposition. Their excellent resolving power of several thousand, broad energy coverage, and reliable energy calibration make them particularly well suited for high-resolution spectroscopy of muonic X-rays [2].

Measurements are performed at the continuous low-energy muon beamline $\pi E1$ at PSI [39]. A beam of negative muons, with a rate of approximately 10 kHz, is directed onto isotopically enriched macroscopic targets. About 60 % of the muons are stopped in the target material, where they form muonic atoms. Approximately 20 % are stopped in the collimator before

Table 2.1.: Nuclear charge radii r_c, relative uncertainties $\sigma_{r_c} r_c^{-1}$, and the dominant determination method for selected light, stable nuclei. This table is based on a table of charge radii for light nuclei [5] and a review on charge radii [27]. The methods refer to the experimental technique: μ^-*-atom laser spec.* for laser spectroscopy of muonic atoms, *IS* for isotope shift from laser spectroscopy, *el.* e^- *scat.* and *el.* π^+ *scat.* for elastic electron and pion scattering, respectively, and μ^-*-atom X-ray spec.* for X-ray spectroscopy of muonic atoms, where the value for ^{12}C was obtained with a crystal spectrometer, while the other values were obtained with HPGe detectors.

Nucleus	r_c / fm	$\sigma_{r_c} r_c^{-1}$ / 10^{-3}	Method
^{1}H	0.840 60(39)	0.46	μ^--atom laser spec.
^{2}H	2.127 75(17)	0.08	$r_c(^{1}\mathrm{H})$ + IS
^{3}He	1.970 07(94)	0.48	μ^--atom laser spec.
^{4}He	1.6786(12)	0.71	μ^--atom laser spec.
^{6}Li	2.589(39)	15	el. e^- scat.
^{7}Li	2.449(41)	17	$r_c(^{6}\mathrm{Li})$ + IS
^{9}Be	2.519(32)	13	el. e^- scat.
^{10}B	2.531(38)	15	$r_c(^{11}\mathrm{B})$ + IS
^{11}B	2.411(21)	8.7	$r_c(^{12}\mathrm{C})$ + el. π^+ scat.
^{12}C	2.483(2)	0.8	μ^--atom X-ray spec.
^{13}C	2.458(2)	0.8	$r_c(^{12}\mathrm{C})$ + IS
^{14}N	2.556(9)	3.5	μ^--atom X-ray spec.
^{15}N	2.612(9)	3.4	el. e^- scat.
^{16}O	2.701(4)	1.5	μ^--atom X-ray spec.
^{18}O	2.775(7)	2.5	$r_c(^{16}\mathrm{O})$ + IS
^{19}F	2.902(5)	1.7	μ^--atom X-ray spec.
^{20}Ne	3.001(6)	2.0	μ^--atom X-ray spec.
^{22}Ne	2.948(6)	2.0	$r_c(^{20}\mathrm{Ne})$ + IS
^{23}Na	2.992(6)	2.0	μ^--atom X-ray spec.
^{24}Mg	3.056(3)	1.0	μ^--atom X-ray spec.
^{26}Mg	3.030(3)	1.0	μ^--atom X-ray spec.

the target, and the remaining 20 % pass through the target without stopping. The bound muons rapidly cascade to the ground state, emitting characteristic X-rays, and eventually decay. Approximately 80 % of the stopped muons undergo the $2p$–$1s$ transition, which is highly sensitive to the nuclear charge radius.

An MMC-based detector array with an active area of 16 mm^2 is mounted inside a sidearm of a dilution refrigerator and positioned approximately 135 mm from the target, covering a fraction of about 7×10^{-5} of the full solid angle. Depending on the energy-dependent quantum efficiency of the detector, this results in an event rate of up to 0.3 Hz on the detector for muonic $2p$–$1s$ X-rays, which are identified by coincidence with the muon signal from the entrance scintillator located in the beamline before the target. The continuous muon beam enables the use of a detector with a relatively long response time, while its high intensity compensates for the limited solid angle covered by the compact detector, which is optimized for high energy resolution. The detector is continuously calibrated during the measurement using external radioactive X-ray and γ-ray sources, as well as an X-ray tube with fluorescence targets.

2.4.2. Projected Sensitivity

The projected sensitivity of the QUARTET experiment is estimated from the expected experimental uncertainty σ_{E} in measuring the energy of the $2p$–$1s$ transition, the theoretical uncertainty σ_{T} in extracting the corresponding energy shift due to the FNS δE_{FNS}, and converting it to an uncertainty on the nuclear charge radius σ_{r_c}, as summarized in Table 2.2. The experimental uncertainty σ_{E} of the line position is given by the combined statistical and calibration uncertainty of the detector. A relative accuracy of up to 2 ppm is targeted, and the final experimental uncertainty is estimated as $\sigma_{\mathrm{E}} \approx 2\,\mathrm{ppm} \cdot \Delta E_{2p-1s}$, based on the respective transition energy. This projection assumes a high-resolution detector optimized for the specific energy range, where the uncertainty is expected to be dominated by the energy calibration. Furthermore, this requires multiple calibration lines, known with sufficiently high accuracy, in the vicinity of the transition. For F and Ne, with $9 \leq Z \leq 10$, the fabrication of a suitable detector with both sufficient energy resolution and quantum efficiency at around 200 keV remains to be demonstrated.

For Li, achieving the required statistical precision for the targeted 2 ppm accuracy corresponds to several days of measurement time. This estimate assumes a FWHM energy resolution of $\Delta E_{\mathrm{FWHM}} \approx 8\,\mathrm{eV}$, a quantum efficiency of 97 % at $\Delta E_{2p-1s} = 18.7\,\mathrm{keV}$, and a muonic $2p$–$1s$ X-ray rate of 0.15 Hz on the detector for each of the stable isotopes ^{6}Li and ^{7}Li, while simultaneously recording multiple calibration lines with sufficient statistics.

The nuclear charge radii are determined from the $2p$–$1s$ transition energy according to equation (2.44). The theoretical uncertainty σ_{T} in determining the FNS correction δE_{FNS} is

Table 2.2.: The $2p$–$1s$ transition energies ΔE_{2p-1s}, the projected experimental, theoretical, and FNS energy uncertainties σ_{E}, σ_{T}, and σ_{FNS}, respectively, the sensitivity to the nuclear charge radius $\mathrm{d}r_{\mathrm{c}}/\mathrm{d}E_{\mathrm{FNS}}$ and the projected uncertainty $\sigma_{r_{\mathrm{c}}}$ on nuclear charge radii for the QUARTET experiment.

Nucleus	ΔE_{2p-1s} / keV	σ_{E} / eV	σ_{T} / eV	σ_{FNS} / eV	$\mathrm{d}r_{\mathrm{c}}/\mathrm{d}E_{\mathrm{FNS}}$ / am eV^{-1}	$\sigma_{r_{\mathrm{c}}}$ / am
^{6}Li, ^{7}Li	18.7	0.04	0.02	0.04	48	1.9
^{9}Be	33.4	0.07	0.04	0.08	15	1.2
^{10}B, ^{11}B	52.3	0.10	0.1	0.14	6.4	0.90
^{12}C, ^{13}C	75.3	0.15	0.2	0.25	3.1	0.77
^{14}N, ^{15}N	102	0.20	0.4	0.45	1.6	0.72
^{16}O, ^{18}O	134	0.27	0.8	0.84	0.91	0.76
^{19}F	168	0.34	1.2	1.2	0.55	0.66
^{20}Ne, ^{22}Ne	207	0.41	1.6	1.7	0.35	0.59

expected to be dominated by the uncertainty from nuclear polarization σ_{NP} [5]. It is therefore approximated as $\sigma_{\mathrm{T}} \approx \sigma_{\mathrm{NP}}$, with the corresponding values taken from a recent analysis of nuclear polarization effects [49]. The uncertainty in the FNS correction σ_{FNS} is obtained by quadratically combining the experimental and theoretical uncertainties σ_{E} and σ_{T}, respectively. This is converted into an uncertainty on the nuclear charge radius $\sigma_{r_{\mathrm{c}}}$ using the sensitivity $\mathrm{d}r_{\mathrm{c}}/\mathrm{d}E_{\mathrm{FNS}}$, estimated with *MuDirac* [40, 41]. For light nuclei with $Z \leq 6$, the precision is expected to be limited by both experimental and theoretical uncertainties, while for heavier nuclei with $7 \leq Z$ the theoretical uncertainty begins to dominate. A comparison between the projected and current uncertainties in the nuclear charge radii is shown in Figure 2.4. The projected accuracy indicates that nuclear charge radii of light nuclei can be determined with sub-permille precision, representing a substantial improvement by up to a factor of nearly 30 if the underlying assumptions hold.

2.4.3. Experimental Schedule

The first beamtime request was prepared in 2022 and granted as a proof of principle test run in October 2023 at PSI [2, 5, 6], demonstrating the first successful application of MMCs for high-precision X-ray spectroscopy of exotic atoms. This was followed by a second beamtime request and the first dedicated data run with Li, Be, and B in October 2024 [7]. The results are expected to demonstrate that the accuracy of nuclear charge radii can be improved by employing MMC-based detectors. The next measurement is scheduled for September 2025 and will target C and O [8], while a follow-up measurement with Li and Be is under consideration for 2026.

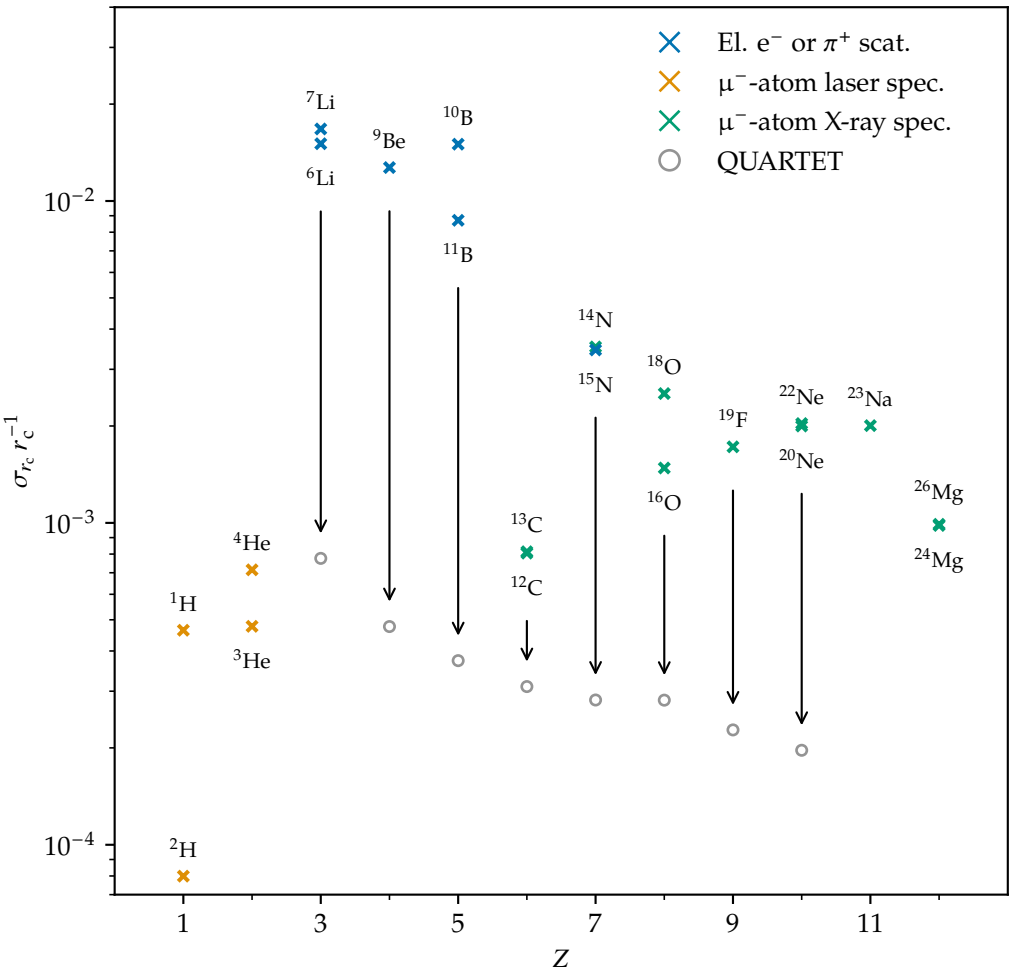

Figure 2.4.: Accuracy of absolute measurements of nuclear charge radii for light, stable nuclei from elastic electron or pion scattering, laser spectroscopy of muonic atoms, and X-ray spectroscopy of muonic atoms, based on Table 2.1, as well as the projected accuracy of the QUARTET experiment based on Table 2.2. This figure is similar to a previously published figure [26].

2.4.4. Detector Development

As part of the QUARTET collaboration, this thesis describes the detector development for QUARTET, as well as the detector preparation for the proof of principle test run and the first dedicated data run at PSI. The targeted relative accuracy of 2 ppm for the line position has not yet been demonstrated with an MMC-based detector array and requires several new developments concerning the detector, detector setup, and data analysis. This 2 ppm goal is very ambitious, although it could in principle be reached with a fully optimized detector setup, it may still be constrained by the limited measurement time or by systematic effects that have not yet been identified. A new high-resolution detector optimized for X-ray spectroscopy of muonic atoms is required, with excellent energy resolution and reliable operation under beamtime conditions. Undesired effects from energy deposition by high-energy Michel electrons produced in muon decays must be suppressed. A dedicated cryostat sidearm is needed to efficiently integrate the detector into the muon beamline and to position it sufficiently close to the muon target. The system must be installed and cooled to mK temperatures directly at the beamline site. The calibration of the ADCs must be precise to suppress non-linearities, and the data analysis must be optimized with a reliable, energy-independent data reduction and data analysis.

The physics of MMCs is discussed in detail in Chapter 3. The detector used for the proof of principle run and dedicated data run, as well as the design and fabrication of a new detector optimized for muonic X-ray spectroscopy, is presented in Chapter 4. The experimental setup, including the cryostat sidearm, preparation of the detector readout, and ADC calibration, is described in Chapter 5. The open-source analysis package developed for preliminary online processing, data reduction, and data analysis is introduced in Chapter 6. The detector-related results of the proof of principle run, the dedicated data run with lithium, beryllium, and boron, and the characterization of the new detector are presented in Chapter 7. The thesis concludes with a summary in Chapter 8.

Chapter 3.

Metallic Magnetic Calorimeter

A metallic magnetic calorimeter (MMC) is a type of microcalorimeter that uses a paramagnetic temperature sensor [50, 51]. Operated at cryogenic temperatures, typically around $T_0 \sim 20\,\mathrm{mK}$ in a dilution refrigerator, an MMC determines the energy of an incident particle by measuring the temperature increase caused by its energy deposition. MMCs offer excellent energy resolution across a broad energy range, combining high linearity, high quantum efficiency, and a fast response time [52]. MMCs can achieve a resolving power $E/\Delta E_{\mathrm{FWHM}}$ of several thousand [53–56], cover an energy range up to 200 keV [57, 58], exhibit less than 1 % non-linearity [56, 59], provide near-perfect quantum efficiency [2, 59], offer a response time of less than 100 ns [57, 59], and have a low intrinsic background [1, 60]. Several reviews cover the physics and applications of MMCs in detail [50–52].

Since their initial experimental demonstration [61, 62] and successful microfabrication [57, 63], MMC-based detectors have been used in a wide range of applications and are being developed for upcoming experiments. In particle physics, MMC-based detectors are used to search for physics beyond the SM. The ECHo (Electron Capture ^{163}Ho) experiment aims to determine the effective electron neutrino mass [64–67], AMoRE (Advanced Mo-based Rare Process Experiment) searches for the neutrinoless double-beta decay in ^{100}Mo [68–70], DELight (Direct Search Experiment for Light Dark Matter) investigates interactions with light dark matter [71], and IAXO (International Axion Observatory) searches for axions and axion-like particles [1, 11, 72]. Beyond particle physics, MMCs are used for high-resolution spectroscopy in atomic and molecular physics. They have been used to study highly charged heavy ions [57, 58, 73], ion–electron collisions [74], molecular fragments from electron–ion interactions [75–77], and low-energy γ-ray spectroscopy [56]. This thesis describes the development and use of MMC-based detectors for X-ray spectroscopy of light muonic atoms to determine their absolute nuclear charge radii [2, 5].

This chapter provides an overview of MMCs and their operating principle. It discusses the materials, response, and noise. The chapter concludes with a description of a common MMC geometry, its optimization, and its low-temperature readout. The focus is on MMC arrays for high-resolution X-ray and γ-ray spectroscopy.

3.1. Operating Principle

An MMC consists of a particle absorber and a paramagnetic temperature sensor. Both components are in good thermal contact and are weakly thermally coupled to a thermal bath at constant temperature T_0. A common MMC geometry is shown later in Figure 3.10.

When an incident particle deposits the energy E in the absorber, the temperature of the MMC rises by ΔT above the thermal bath temperature T_0. The temperature rise ΔT is given by

$$\mathrm{d}E = C \ \mathrm{d}T \tag{3.1}$$

where the temperature-dependent heat capacity C is the sum of the absorber heat capacity C_{abs} and the sensor heat capacity C_{sen}. After the energy is deposited, the MMC thermalizes back to the temperature T_0 of the thermal bath.

The paramagnetic temperature sensor, whose magnetization M is temperature-dependent, resides in an external, weak static magnetic field H. The magnetization change ΔM due to a temperature change ΔT is described by

$$\mathrm{d}M = \frac{\partial M}{\partial T} \ \mathrm{d}T \tag{3.2}$$

where the temperature dependence of the magnetization $\partial M/\partial T$ also varies with temperature. The associated magnetic field change ΔB near the sensor is proportional to the magnetization change ΔM and can be measured using a SQUID, a highly sensitive magnetometer.

The resulting magnetic flux change $\Delta\Phi_{\mathrm{s}}$ from the magnetic field change ΔB can be measured by a SQUID placed near the sensor. Alternatively, a superconducting flux transformer can couple the magnetic flux change $\Delta\Phi_{\mathrm{m}}$ in a pickup coil close to the sensor to the SQUID as a proportional magnetic flux change $\Delta\Phi_{\mathrm{s}}$. Due to magnetic flux conservation in superconducting circuits, screening currents preserve the total magnetic flux. The resulting flux change $\Delta\Phi_{\mathrm{s}}$ is given by

$$\Delta\Phi_{\mathrm{s}} \propto \Delta\Phi_{\mathrm{m}} \propto \Delta B \propto \Delta M \tag{3.3}$$

and is thus proportional to the magnetization change ΔM in the sensor.

For an MMC with a heat capacity $C \approx 20\,\mathrm{pJ\,K^{-1}}$ at a temperature $T_0 \approx 20\,\mathrm{mK}$, a photon with an energy $E = 6\,\mathrm{keV}$ causes a temperature increase $\Delta T \approx 50\,\mu\mathrm{K}$, as shown later in Figure 3.6. This temperature increase ΔT is small compared to the operating temperature T_0. As an approximation, the heat capacity C and the temperature dependence of the magnetization

$\partial M/\partial T$ can be assumed constant within the temperature change ΔT. Equations (3.1) and (3.2) then simplify to

$$\Delta T \approx \frac{E}{C} \tag{3.4}$$

$$\Delta M \approx \frac{\partial M}{\partial T}\,\Delta T \tag{3.5}$$

and the flux change $\Delta\Phi_s$ is given by

$$\Delta\Phi_s \propto \frac{\partial M}{\partial T}\frac{E}{C} \tag{3.6}$$

which, to first order, is proportional to the deposited energy E.

To increase the signal amplitude $\Delta\Phi_s$, the heat capacity C should be minimized, while the temperature dependence of the magnetization $\partial M/\partial T$ should be maximized. These properties should be considered when selecting materials for the absorber and sensor. The heat capacity C can be reduced by minimizing the volume and the operating temperature T_0 of the MMC. Additionally, to suppress non-linearity and reduce sensitivity to thermal fluctuations, the energy and temperature derivatives of the signal amplitude, $\mathrm{d}^2/\mathrm{d}E^2\ \Delta\Phi_s$ and $\mathrm{d}/\mathrm{d}T\ \Delta\Phi_s$, should be minimized. Individual MMCs are typically compact and microfabricated using lithography techniques.

3.2. Particle Absorber

The particle absorber converts the energy E of an incident particle into an increase in temperature ΔT of the MMC. To accurately determine the energy E, the absorber must stop the particle and convert its energy entirely into heat. It must also thermalize quickly and uniformly while maintaining a low heat capacity. The geometry and material of the absorber determine its active area and quantum efficiency and significantly influence both the energy and time resolution. The absorber is optimized for the requirements of a specific experiment or application.

The absorber material should provide high quantum efficiency for effectively stopping incident particles. At low temperatures, the material must have a low specific heat capacity to maximize the signal amplitude. Moreover, high energy resolution requires that the full energy of the incident particle is converted into heat without energy losses. To achieve a position-independent response and high time resolution, the absorber must thermalize rapidly and uniformly. Additionally, the material should be compatible with microfabrication techniques.

Despite its relatively large specific heat capacity at low temperatures, gold is the most common absorber material. Gold (Au), with an atomic number $Z = 79$, has a high quantum

efficiency for photons. As a noble metal, gold is chemically inert and one of the least reactive elements. It has very low intrinsic radioactivity, with ^{197}Au being the only stable and naturally occurring isotope. Gold is widely used in microfabrication and can be deposited by various methods, including sputtering and electrochemical deposition. Electroplated gold films achieve high residual resistivity ratio (RRR) values [78], resulting in high thermal conductivity at low temperatures.

Alternatives, such as superconductors and semiconductors, have a significantly lower specific heat capacity but suffer from slow or incomplete thermalization. In superconductors, the quasiparticles generated by the breaking of Cooper pairs have long relaxation and recombination times [79, 80]. In semiconductors, electron–hole pairs recombine slowly [81]. Energy trapped in long-lived excitations prevents complete thermalization, which can significantly limit energy resolution. Nevertheless, superconductors and semiconductors may offer advantages in specific applications and have been used as absorber materials [16, 82–86].

3.2.1. Specific Heat Capacity

At low temperatures, the specific heat capacity c of a normal-conducting metal consists of two contributions: an electronic term c_e and a phononic term c_p. For temperatures T much lower than the Debye temperature Θ_D of the material, the phononic contribution follows $c_\mathrm{p} = \beta T^3$, where

$$\beta = N_\mathrm{A}\, k_\mathrm{B}\, \frac{12\,\pi^4}{5}\, \frac{1}{\Theta_\mathrm{D}^3} \tag{3.7}$$

is a material-dependent coefficient. The electronic contribution is given by $c_\mathrm{e} = \gamma T$ where γ is the Sommerfeld coefficient. The total specific heat capacity is thus

$$c = c_\mathrm{e} + c_\mathrm{p} \tag{3.8}$$

$$= \gamma T + \beta T^3 \tag{3.9}$$

and is dominated by the electronic term c_e at sufficiently low temperatures T.

The specific heat capacity of gold c, along with its electronic and phononic contributions, is shown in Figure 3.1. It is described by equation (3.9) with $\beta = 0.4504(46)\,\mathrm{mJ\,mol^{-1}\,K^{-4}}$ and $\gamma = 0.729(18)\,\mathrm{mJ\,mol^{-1}\,K^{-2}}$ [87]. Below 100 mK, the phononic contribution c_p is negligible compared to the electronic contribution c_e. At those temperatures, the heat capacity of a gold absorber C_abs can be approximated by $C_\mathrm{abs} \approx V_\mathrm{abs}\,(c_\mathrm{e}/v_\mathrm{Au})$ where V_abs is the absorber volume and $v_\mathrm{Au} = 1.02 \times 10^{-5}\,\mathrm{m^3\,mol^{-1}}$ the molar volume of gold.

For a square gold absorber with side length $a_\mathrm{abs} = 500\,\mu\mathrm{m}$ and thickness $h_\mathrm{abs} = 30\,\mu\mathrm{m}$, the heat capacity is $C_\mathrm{abs} \approx 10\,\mathrm{pJ\,K^{-1}}$ at a temperature of $T \approx 20\,\mathrm{mK}$.

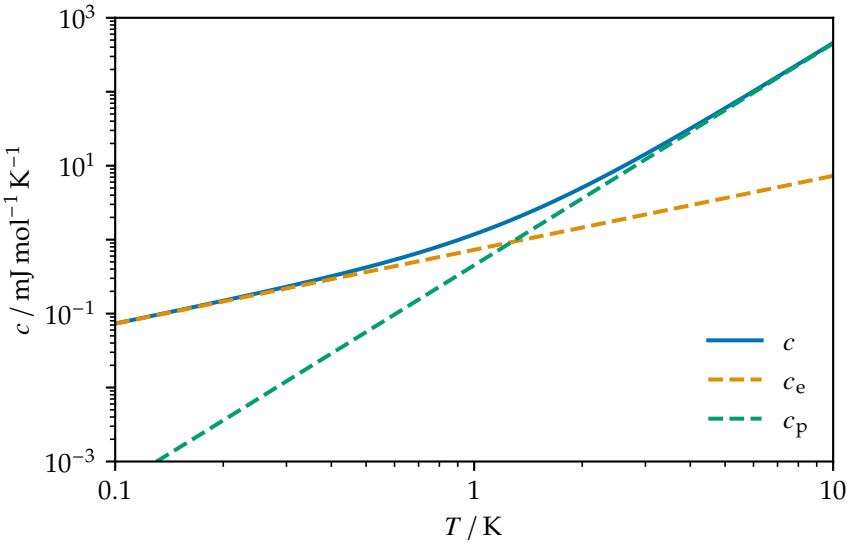

Figure 3.1.: Calculated specific heat capacity of gold c, along with its electronic c_e and phononic c_p contributions [87]. Below 1.3 K, the electronic contribution c_e is larger than the phononic contribution c_p, which is negligible below 100 mK.

3.2.2. Efficiency

For a gold absorber, photoelectric absorption is the dominant interaction mechanism for photons with energies up to $E \approx 400$ keV [88]. The absorption efficiency α can be optimized for a given application by adjusting the absorber thickness h_{abs}. Figure 3.2 shows the photoelectric absorption efficiency α for different gold absorber thicknesses h_{abs}. For photon energies up to about 80 keV, particularly below the K-edge of gold, the efficiency α can be approximated as

$$\alpha = 1 - e^{-\mu h_{abs}} \tag{3.10}$$

where μ is the energy-dependent attenuation coefficient of gold [89]. At higher photon energies, secondary processes, such as fluorescence and Compton scattering, become increasingly important. Photons generated in these processes may escape the absorber, reducing the efficiency α. Simulations are required to accurately account for these processes and determine the efficiency α [90].

3.2.3. Thermalization

The thermalization of metallic absorbers at low temperatures has been extensively studied [80, 91–93]. The energy of an incident particle E is down-converted through a cascade of energy-dependent processes. Initially, an incoming photon primarily interacts via the photoelectric effect with the absorber, ejecting a photoelectron. On a timescale of approximately fs, electron–

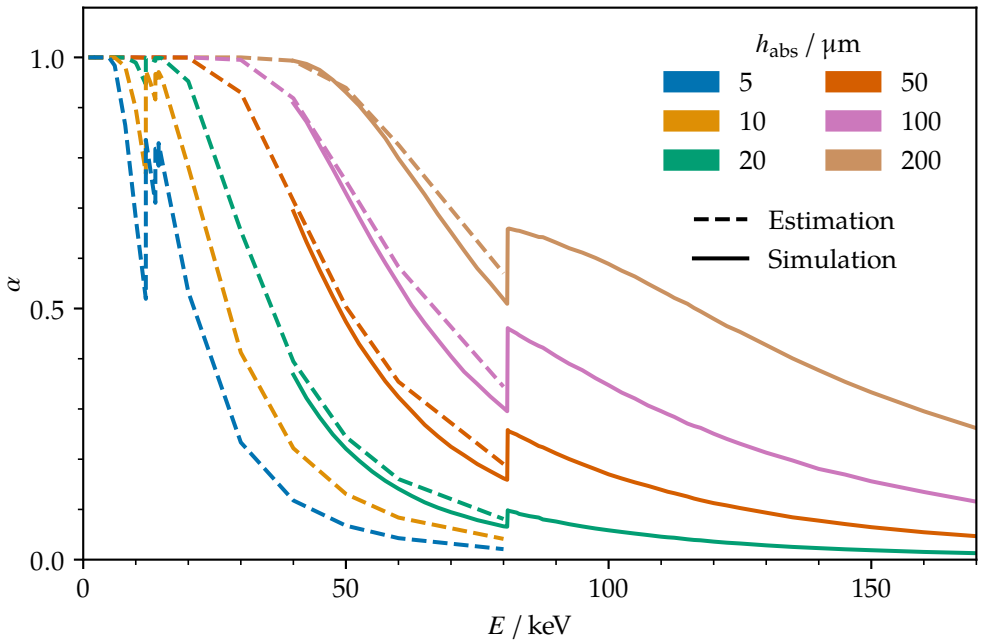

Figure 3.2.: Expected photon absorption efficiency α of gold absorbers with different thicknesses h_{abs}. The estimated values are calculated from mass attenuation coefficients [89], while simulated values are based on EGS5 simulations and include secondary processes [90].

electron interactions dominate, generating secondary high-energy electrons and holes in the conduction band. As the energy of the electrons decreases, electron–phonon interactions become dominant on a timescale of about ps. Energy is then transferred to the phononic system, generating high-frequency, athermal phonons. Finally, on a timescale of about ns, phonon absorption via phonon–electron interactions becomes more efficient than phonon emission, and energy returns to the electronic system. From then on, energy transport is dominated by the thermal diffusion of electronic excitations, limited by electronic conductivity.

Fast thermalization within the absorber is essential to minimize position-dependent variations in the signal. However, since thermalization is inherently position-dependent, it can result in spatial variations in the signal shape if this variation is transferred to the sensor. Introducing a thermal bottleneck between absorber and sensor slows down the temperature change of the sensor, allowing the absorber to thermalize more uniformly beforehand [58]. This method improves the uniformity of the response, especially for large absorbers.

During thermalization, high-frequency athermal phonons may escape the absorber, appearing as partial energy loss and reduced signal amplitude. These event-dependent losses result in low-energy tails in the energy response of MMCs [63, 94]. Implementing a geometric bottleneck between absorber and sensor can suppress energy loss by significantly reducing the probability of athermal phonons escaping [57].

To estimate the thermalization timescale of an absorber τ_{abs}, the initial fast cascade can be neglected. The thermalization time constant τ_{abs} is

$$\tau_{\text{abs}} \approx \frac{l^2}{D} \tag{3.11}$$

where l is a characteristic length scale of the absorber and D is the thermal diffusion coefficient. At low temperatures, the thermal diffusion coefficient D due to electrons is

$$D = \kappa \frac{v}{c_{\text{e}}} \tag{3.12}$$

where v is the molar volume. According to the Wiedemann–Franz law,

$$\frac{\kappa}{\sigma} = L_0 T \tag{3.13}$$

the thermal conductivity κ is related to the electrical conductivity σ and temperature T through the Lorenz number L_0 [95]. Assuming a free electron gas, the material-independent theoretical Lorenz number L_0 is

$$L_0 = \frac{\pi^2}{3} \left(\frac{k_{\text{B}}}{e} \right)^2 \tag{3.14}$$

$$\approx 2.44 \times 10^{-8}\,\text{W}\,\Omega\,\text{K}^{-2} \tag{3.15}$$

where e is the elementary charge [96].

The electrical conductivity σ at low temperatures can be estimated via $\rho = \sigma^{-1}$, where ρ is the electrical resistivity, which is approximated by

$$\rho = \frac{\rho_0}{\text{RRR} - 1} \tag{3.16}$$

where $\text{RRR} = \rho_{300\,\text{K}}/\rho_{0\,\text{K}}$ is the residual resistivity ratio (RRR) of the absorber material and ρ_0 is the reference electrical resistivity at room temperature. This relation assumes the reference material has a much higher RRR than the absorber material.

Combining the above equations, the diffusion coefficient D can be calculated from the thermal conductivity κ. Similarly, the thermal conductance G of a thermal bottleneck is given by

$$G = \kappa \frac{A}{l} \tag{3.17}$$

where A is the cross-sectional area and l is the length of the bottleneck.

Electroplated gold with RRR = 15 at a temperature of $T = 20\,\text{mK}$ has a thermal conductivity $\kappa = 0.28\,\text{W}\,\text{m}^{-1}\,\text{K}^{-1}$, corresponding to a thermal diffusion coefficient $D = 0.20\,\text{mm}^2\,\mu\text{s}^{-1}$. A

square gold absorber with a side length $a_{\mathrm{abs}} = 500\,\mu\mathrm{m}$ and a height $h_{\mathrm{abs}} = 30\,\mu\mathrm{m}$ has a thermalization time constant of $\tau_{\mathrm{abs}} \approx 3\,\mu\mathrm{s}$. For comparison, sputtered gold with RRR = 2.2 has a thermal conductivity of $\kappa = 0.024\,\mathrm{W\,m^{-1}\,K^{-1}}$ at the same temperature. Consequently, absorbers are typically electroplated to achieve a shorter thermalization time.

3.3. Paramagnetic Sensor

The paramagnetic temperature sensor converts the temperature change ΔT into a magnetization change ΔM. Magnetic moments in the sensor material have a temperature-dependent alignment with an external magnetic field H. The sensor should exhibit a strong temperature dependence of the magnetization $\partial M/\partial T$, strong thermal coupling to the magnetic moments, and fast, uniform thermalization, all while maintaining a low heat capacity. The geometry and material properties of the sensor significantly affect the amplitude and shape of the resulting signal. As shown later, the heat capacity of the sensor C_{sen} is usually designed to roughly match the heat capacity of the absorber C_{abs} in order to achieve high energy resolution.

3.3.1. Erbium

The sensor material is a dilute paramagnetic alloy of the rare-earth element erbium (Er) embedded in a metallic host material, commonly silver (Ag) or gold (Au). According to the Korringa relation [97], a metallic host material provides fast electron–spin coupling, faster than 100 ns at low temperatures, which sets a fundamental limit to the signal rise time and is significantly faster than spin–phonon coupling [61, 98]. Erbium concentrations are usually low and in the range of a few hundred parts per million (ppm), with the erbium atoms occupying regular lattice sites in the host material [99].

Each erbium atom donates three electrons to the conduction band, forming an Er^{3+} ion with a permanent magnetic moment due to its partially filled $4f$ shell. According to Hund's rules, the Er^{3+} ion has an orbital angular momentum $L = 6$, a spin $S = 3/2$, a total angular momentum $J = L + S = 15/2$, and a Landé g-factor $g_J = 6/5$ [100]. The diameter of the $4f$ shell is 0.6 Å, which is much smaller than the 2 Å diameter of the $5s$ and $6p$ shells [101]. These outer shells shield the $4f$-shell electrons from the crystal field generated by the conduction electrons, thus reducing their coupling to the electron gas. At temperatures above 100 K, the influence of the crystal field can be neglected [102].

Below 100 K, the crystal field lifts the degeneracy of the $J = 15/2$ ground state, splitting it into five multiplets. The lowest-energy state is a Kramers-Γ_7 doublet [102], which is energetically separated from the next higher multiplet by $\Delta E/k_{\mathrm{B}} = 25\,\mathrm{K}$ for Ag:Er and 17 K for Au:Er [103]. Because of this significant energy separation, only the lowest doublet is thermally populated at low temperatures. The erbium ions behave as two-level systems with spin $S = 1/2$ and

effective Landé factor $g_s = 6.84$ for Ag:Er and $g_s = 6.80$ for Au:Er [100, 104]. At very low erbium concentrations, the magnetic moments can be approximated as independent and non-interacting. At higher concentrations, however, the interactions between the magnetic moments become significant [85]. At sufficiently low temperatures, the material exhibits signatures of a spin-glass transition [105].

3.3.2. Non-Interacting Magnetic Moments

At very low erbium concentrations, the magnetic moments can be approximated as a non-interacting spin system with an effective Landé g-factor g_s and a spin $S = 1/2$. In the presence of a magnetic field B, each spin experiences Zeeman splitting into two energy levels with energies $E_i = m_i \, g_s \, \mu_\mathrm{B} \, B$, where $m_i = \pm 1/2$ and μ_B is the Bohr magneton. The partition function of a single spin is

$$Z = \sum_i \mathrm{e}^{-E_i \,/\, k_\mathrm{B} T} \tag{3.18}$$

$$= 2 \, \cosh\left(\frac{E_\mathrm{Z}}{2 \, k_\mathrm{B} T}\right) \tag{3.19}$$

with Zeeman splitting $E_\mathrm{Z} = E_{+1/2} - E_{-1/2} = g_s \, \mu_\mathrm{B} \, B$ between the two energy levels. The Helmholtz free energy F of an ensemble of N_s spins is given by

$$F = -k_\mathrm{B} T \, \ln\left(Z^{N_\mathrm{s}}\right) \tag{3.20}$$

$$= -N_\mathrm{s} \, k_\mathrm{B} T \, \ln\left[2 \, \cosh\left(\frac{E_\mathrm{Z}}{2 \, k_\mathrm{B} T}\right)\right] \tag{3.21}$$

where Z^{N_s} is the total partition function.

The specific heat capacity of the spin system can be derived from the Helmholtz free energy F by

$$c_\mathrm{s} = -\frac{T}{V} \frac{\partial^2 F}{\partial T^2} \tag{3.22}$$

$$= n_\mathrm{s} \, k_\mathrm{B} \left(\frac{E_\mathrm{Z}}{2 \, k_\mathrm{B} T}\right)^2 \mathrm{sech}^2\left(\frac{E_\mathrm{Z}}{2 \, k_\mathrm{B} T}\right) \tag{3.23}$$

where $n_\mathrm{s} = N_\mathrm{s}/V$ is the spin density. The reduced specific heat capacity c_s is shown in Figure 3.3 (right). It exhibits the characteristic Schottky anomaly with a peak at $k_\mathrm{B} T \approx 0.42 \, E_\mathrm{Z}$, reaching a maximum value of $c_\mathrm{s} \approx 0.44 \, n_\mathrm{s} \, k_\mathrm{B}$. At low temperatures, the heat capacity decreases exponentially with $c_\mathrm{s} \propto \exp(-E_\mathrm{Z} \,/\, k_\mathrm{B} T)$, while at high temperatures it follows the power law $c_\mathrm{s} \propto B^2 \,/\, T^2$.

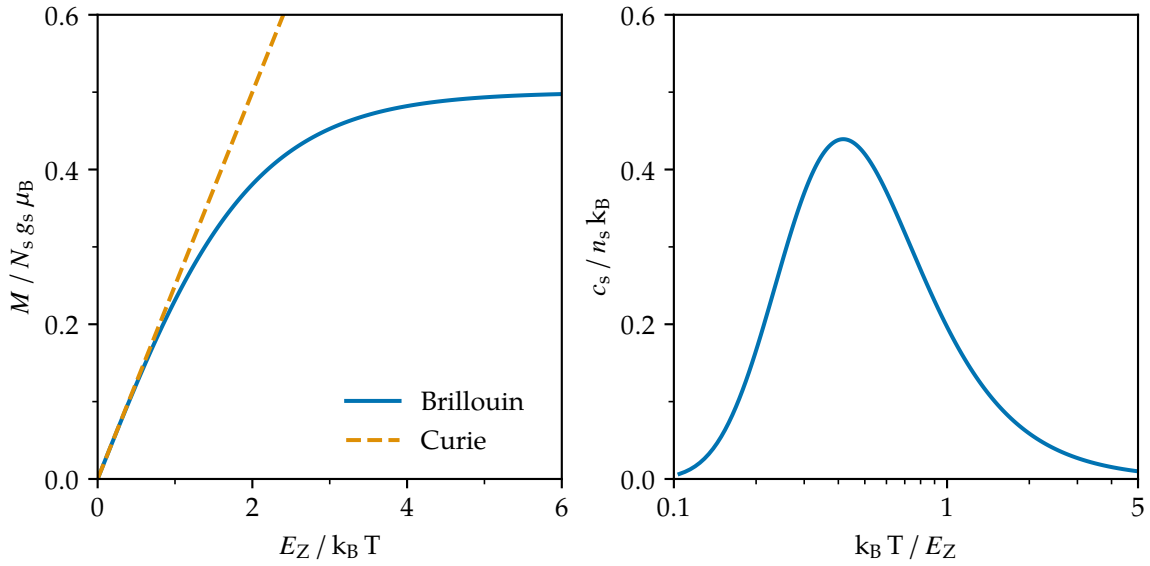

Figure 3.3.: Reduced magnetization $M \,/\, n_\mathrm{s}\, g_\mathrm{s}\, \mu_\mathrm{B}$ (left) and reduced specific heat capacity $c_\mathrm{s} \,/\, n_\mathrm{s}\, \mathrm{k_B}$ (right). The values are calculated for a non-interacting spin-1/2 system with Zeeman splitting E_Z. The magnetization follows the Curie behavior at high temperatures, while the specific heat capacity exhibits the characteristic Schottky peak.

The magnetization M is given by

$$M = -\frac{\partial F}{\partial B} \tag{3.24}$$

$$= N_\mathrm{s}\, \frac{g_s\, \mu_\mathrm{B}}{2}\, \tanh\!\left(\frac{E_\mathrm{Z}}{2\, k_\mathrm{B}\, T}\right) \tag{3.25}$$

as shown in Figure 3.3 (left). At high temperatures, the magnetization M follows the Curie behavior $M \propto B \,/\, T$, while at low temperatures it saturates at $M = N_\mathrm{s}\, g_s\, \mu_\mathrm{B} \,/\, 2$. The temperature dependence of the magnetization $\partial M / \partial T$ is

$$\frac{\partial M}{\partial T} = -\frac{\partial^2 F}{\partial T \partial B} \tag{3.26}$$

$$= -\frac{c_\mathrm{s}}{B} \tag{3.27}$$

and is therefore proportional to the specific heat capacity c_s for non-interacting spins.

3.3.3. Interacting Magnetic Moments

For a typical MMC, with an erbium concentration of several hundred ppm, the interactions between magnetic moments cannot be neglected [106]. Although direct interactions via overlapping $4f$ orbitals are negligible at such low concentrations, long-range interactions

must be considered: the magnetic dipole–dipole interaction and the Ruderman-Kittel-Kasuya-Yosida (RKKY) interaction. Simulations of Ag:Er and Au:Er are discussed in the literature [85, 106–108].

The dipole–dipole interaction between two spins $\mathbf{S}_i$ and $\mathbf{S}_j$ at a distance r_{ij} is described by the anisotropic Hamiltonian

$$H_{ij}^{\mathrm{dd}} = \Gamma_{\mathrm{dd}} \frac{1}{(2\,k_{\mathrm{F}}\,r_{ij})^3} \left[\mathbf{S}_i \cdot \mathbf{S}_j - 3(\mathbf{S}_i \cdot \hat{\mathbf{r}}_{ij})(\mathbf{S}_j \cdot \hat{\mathbf{r}}_{ij})\right] \tag{3.28}$$

where $\hat{\mathbf{r}}_{ij}$ is the unit vector along r_{ij}, and Γ_{dd} is the dipole–dipole interaction strength given by

$$\Gamma_{\mathrm{dd}} = \frac{\mu_0}{4\pi}(g_s\,\mu_{\mathrm{B}})^2(2\,k_{\mathrm{F}})^3 \tag{3.29}$$

where k_{F} is the Fermi wave vector of the host metal.

The RKKY interaction [109–111] describes the indirect interaction of magnetic moments via conduction electrons. The isotropic Hamiltonian is given by

$$H_{ij}^{\mathrm{RKKY}} = \Gamma_{\mathrm{RKKY}} \frac{1}{(2\,k_{\mathrm{F}}\,r_{ij})^3} (\mathbf{S}_i \cdot \mathbf{S}_j) \left[\cos(2\,k_{\mathrm{F}}\,r_{ij}) - \frac{1}{2\,k_{\mathrm{F}}\,r_{ij}} \sin(2\,k_{\mathrm{F}}\,r_{ij})\right] \tag{3.30}$$

which can favor either a parallel or antiparallel orientation, depending on the distance. The RKKY interaction strength Γ_{RKKY} is given by

$$\Gamma_{\mathrm{RKKY}} = I^2 \frac{4\,V_0^2\,m_{\mathrm{e}}^*\,k_{\mathrm{F}}^4}{\hbar^2\,(2\,\pi)^3} \left(\frac{g_s\,(g_s-1)}{g_s}\right)^2 \tag{3.31}$$

where I is the exchange energy between the conduction electrons and magnetic moments, V_0 is the volume of the primitive unit cell, and m_{e}^* is the effective mass of the conduction electrons. Since Γ_{RKKY} depends strongly on the coupling to the conduction electrons, it varies significantly between different host materials.

The relative interaction strength of the dipole–dipole and RKKY interactions can be expressed as

$$\alpha = \Gamma_{\mathrm{RKKY}} \,/\, \Gamma_{\mathrm{dd}} \tag{3.32}$$

since both interactions scale with $\Gamma \propto r_{ij}^{-3}$. For Au:Er, the relative interaction strength is $\alpha \approx 5$ [107], while for Ag:Er it is $\alpha \approx 15$ [112]. Given that the Landé g-factor g_s is similar for Ag:Er and Au:Er, the dipole–dipole interaction is comparable in strength for both host materials. The difference in the relative interaction strength α arises from the different strengths of the RKKY interaction. Both dipole–dipole and RKKY interactions contribute to collective magnetic effects, which significantly influence the properties of the material.

The sensor material can be simulated numerically as a finite lattice of interacting magnetic moments. By constructing a Hamiltonian for a small number of randomly placed erbium ions in an artificial lattice of the host material and applying a magnetic field with a random orientation, microscopic material properties can be derived from the occupation probabilities and expectation values after solving the Hamiltonian. Averaging over many random lattices yields the expected macroscopic properties of the material. The results from different simulations for Au:Er and Ag:Er can accurately predict the respective specific heat capacity c_s, the magnetization M, and the temperature dependence of the magnetization $\partial M/\partial T$ and show good agreement with measurements [85, 106–108].

A previously developed simulation method [85, 108] was used to simulate Ag:Er with an erbium concentration of $x_{Er} = 550\,\text{ppm}$ and a relative interaction strength of $\alpha = 15$ for temperatures T between 10 mK and 500 mK, and magnetic fields B up to 60 mT. The results for magnetic fields up to 10 mT are shown in Figure 3.4. Compared to the non-interacting case, the Schottky peak in the specific heat capacity c_s is lower, broader, and shifted to higher temperatures. The magnetization M saturates at a higher temperature but at a lower value. The temperature dependence of the magnetization $\partial M/\partial T$ is significantly reduced, and it is no longer proportional to the specific heat capacity. The interactions lead to a reduced temperature sensitivity of the magnetization M and a smaller signal amplitude compared to non-interacting magnetic moments.

3.3.4. Nuclear Spin

The nuclear spin of erbium or of the host material can affect the thermodynamic properties of the sensor material. The only stable isotope of gold, ^{197}Au, has a nuclear spin of $I = 3/2$. In Au:Er, the erbium ions locally break the lattice symmetry and cause hyperfine splitting via the nuclear electric quadrupole moment of ^{197}Au [113]. This results in an additional contribution to the heat capacity with a relaxation time of a few hundred microseconds [50]. The associated fast decay component significantly alters the signal shape and degrades the energy resolution. Naturally occurring silver isotopes ^{107}Ag and ^{109}Ag both have a nuclear spin of $I = 1/2$ and therefore have no electric quadrupole moment. Consequently, Ag:Er is typically preferred over Au:Er, despite the much stronger RKKY interaction.

The erbium isotope ^{167}Er has a natural abundance of approximately 23 % and a nuclear spin of $I = 7/2$. This causes hyperfine splitting of the electronic ground state, resulting in an energy separation of $\Delta E/k_B = 140\,\text{mK}$ between the $F = 4$ and $F = 3$ multiplets at zero magnetic field [114]. In a magnetic field, the hyperfine levels split further into 16 states. This hyperfine structure significantly impacts the specific heat capacity c_s and magnetization M, introducing an additional Schottky anomaly at $T \approx 60\,\text{mK}$ [105, 107]. Using enriched ^{168}Er

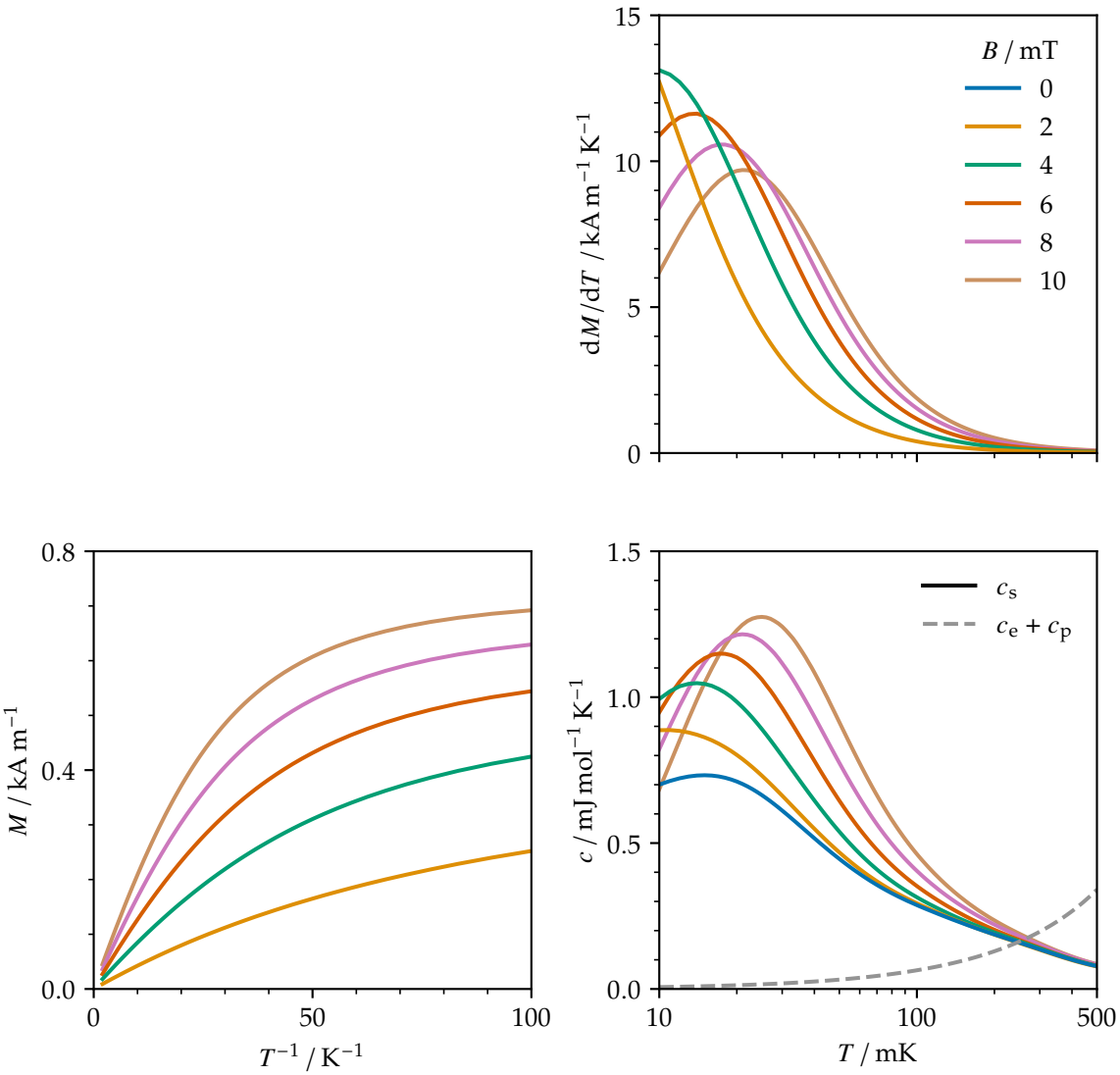

Figure 3.4.: Simulated temperature dependence of the magnetization $\partial M/\partial T$ (top, right), magnetization M (bottom, left), and specific heat capacity c (bottom, right) for Ag:Er with an erbium concentration of $x_\mathrm{Er} = 550\,\mathrm{ppm}$ and a relative interaction strength of $\alpha = 15$. The simulations were carried out with an unpublished simulation package [85]. The specific heat capacity is shown separately for the spin component c_s and the lattice component $c_\mathrm{e} + c_\mathrm{p}$, which is negligible at low temperatures.

with zero nuclear spin as the sensor material, containing only a small residual fraction of ^{167}Er, suppresses the undesired contributions from the nuclear spin of ^{167}Er.

3.3.5. Specific Heat Capacity

The specific heat capacity of the metallic lattice can be described by equation (3.9). The specific heat capacity of silver $c_e + c_p$ is shown in Figure 3.4 (bottom, right) with $\gamma = 0.6396(7)\,\mathrm{mJ\,mol^{-1}\,K^{-2}}$ and $\beta = 0.1670(4)\,\mathrm{mJ\,mol^{-1}\,K^{-4}}$ [115]. At low temperatures, the total specific heat capacity of the sensor is usually dominated by the spin component c_s, and the contribution from the metallic lattice becomes negligible. The heat capacity of an Ag:Er sensor C_{sen} can be approximated as $C_{sen} = V_{sen}\,(c_s/v_{Ag})$ where V_{sen} is the sensor volume and $v_{Ag} = 1.03 \times 10^{-5}\,\mathrm{m^3\,mol^{-1}}$ is the molar volume of silver.

For a square Ag:Er sensor with a side length $a_{sen} = 250\,\mu\mathrm{m}$, a thickness $h_{sen} = 1.6\,\mu\mathrm{m}$, and an erbium concentration of $x_{Er} = 550\,\mathrm{ppm}$, the heat capacity at a temperature of $T \approx 20\,\mathrm{mK}$ and in a magnetic field of $B \approx 5\,\mathrm{mT}$ is $C_{sen} \approx 10\,\mathrm{pJ\,K^{-1}}$.

3.3.6. Thermalization

The thermal conductance is dominated by the thermal diffusion of electrons, and the thermalization time constant of the sensor τ_{sen} can be estimated similarly to that of the absorber. The presence of erbium atoms in the metallic host material decreases the electrical conductivity σ, thereby reducing the thermal conductivity κ according to the Wiedemann–Franz law. At low temperatures, the additional electrical resistivity ρ_{Er} introduced by the erbium atoms is given by

$$\rho_{Er} = x_{Er} \cdot 6.1 \times 10^{-6}\,\Omega\,\mathrm{m} \tag{3.33}$$

where x_{Er} is the erbium concentration [116].

For sputtered Ag:Er with RRR = 2.4 and an erbium concentration of $x_{Er} = 550\,\mathrm{ppm}$, the thermal conductivity is $\kappa = 0.33\,\mathrm{W\,m^{-1}\,K^{-1}}$, corresponding to a thermal diffusion coefficient of $D = 0.027\,\mathrm{mm^2\,\mu s^{-1}}$. A square Ag:Er sensor with a side length of $a_{sen} = 250\,\mu\mathrm{m}$ and a thickness of $h_{sen} = 1.6\,\mu\mathrm{m}$ has a thermalization time constant of $\tau_{sen} \approx 5\,\mu\mathrm{s}$.

3.4. Signal Shape

The signal shape of an MMC is determined by time-dependent heat transport within it. An incident particle causes an energy deposition E in the absorber, leading to a time-dependent temperature change ΔT in the absorber and sensor relative to the thermal bath temperature T_0. The signal from the magnetization change ΔM is proportional to the spin-system temperature T_s of the sensor. To obtain the signal shape, the thermal model of the MMC, described by a

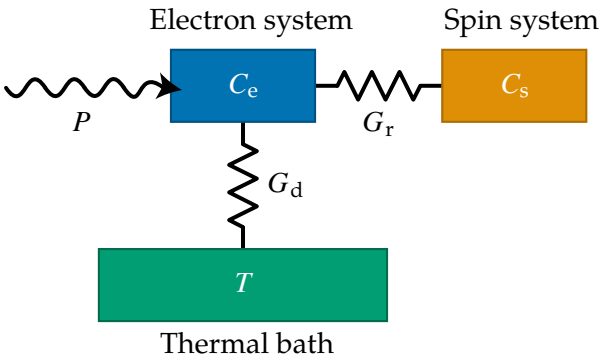

Figure 3.5.: Thermal model of an MMC consisting of an electron system with heat capacity C_e, a spin system with heat capacity C_s, and a thermal bath at constant temperature T_0. The electron system is thermally coupled to the spin system via the thermal conductance G_r and to the bath via the thermal conductance G_d. A particle deposits the energy E at $t = 0$, causing an instantaneous power input $P = E\,\delta(t)$ in the electron system.

set of coupled differential equations, must be solved. MMCs are usually designed to have a well-defined signal shape, independent of the event, to achieve high energy resolution and to identify background events. The signal amplitude and its integral scale with the deposited energy E due to the characteristic shape of the signal.

The thermodynamic system of an MMC can be described by a model with two subsystems, an electron system and a spin system, while neglecting the phonon contribution [51]. As shown in Figure 3.5, the electron system with heat capacity C_e is thermally coupled to a spin system with heat capacity C_s via a thermal conductance G_r and to the thermal bath via a thermal conductance G_d. An incident particle deposits energy E at time $t = 0$, causing an instantaneous power input $P = E\,\delta(t)$ to the electron system. We assume that each subsystem thermalizes internally much faster than energy is exchanged between the subsystems.

For a typical MMC, it is reasonable to approximate $C_e \approx C_{abs}$ and $C_s \approx C_{sen}$, as the absorber heat capacity C_{abs} is dominated by its electronic component and the sensor heat capacity C_{sen} by its spin component. In the literature, the relative heat capacity of the spin system is often defined as $\beta = C_s/C$, but we do not use this notation here for simplicity. The thermal conductance G_d to the thermal bath is much smaller than the thermal conductance G_r, so we assume $G_d \ll G_r$ in the following.

The thermodynamic system can be described by two coupled differential equations:

$$C_e\,\dot{T}_e = G_r\,(T_s - T_e) + G_d\,(T_0 - T_e) + P \tag{3.34}$$

$$C_s\,\dot{T}_s = G_r\,(T_e - T_s) \tag{3.35}$$

where T_e and T_s are the temperatures of the electron and spin systems, respectively. Solving this system with an instantaneous power input $P = E\,\delta(t)$ yields the energy change ΔE_s in the spin system:

$$\Delta E_\mathrm{s} = E\,\frac{C_\mathrm{s}}{C}\left(-\mathrm{e}^{-t/\tau_r} + \mathrm{e}^{-t/\tau_d}\right) \tag{3.36}$$

for $t > 0$, where $C = C_\mathrm{e} + C_\mathrm{s}$ is the total heat capacity. The responsivity p, defined as the signal per input energy, is given by

$$p = \frac{\Delta E_\mathrm{s}}{E} \tag{3.37}$$

$$= \frac{C_\mathrm{s}}{C}\left(-\mathrm{e}^{-t/\tau_r} + \mathrm{e}^{-t/\tau_d}\right) \tag{3.38}$$

expressed in terms of the energy E_s in the sensor.

The signal shape exhibits a fast rise with a time constant τ_r and a slow decay with a time constant τ_d. While the exact solutions for τ_r and τ_d are more complex [51], they reduce to

$$\tau_r \approx \frac{C_\mathrm{s}\,C_\mathrm{e}}{C\,G_\mathrm{r}} \tag{3.39}$$

$$\tau_d \approx \frac{C}{G_\mathrm{d}} \tag{3.40}$$

under the assumption $G_\mathrm{d} \ll G_\mathrm{r}$. The rise time constant τ_r thus depends on the relative heat capacities and the thermal conductance G_r between the two subsystems, while the decay time constant τ_d depends only on the total heat capacity C and the thermal conductance G_d to the thermal bath.

The thermal conductance G_r is fundamentally determined by the electron–spin coupling in the sensor material and is described by the Korringa relation [97]. However, it can be reduced artificially by introducing a thermal bottleneck in the electron system between absorber and sensor. If this bottleneck dominates the rise time, it effectively replaces G_r. The thermodynamic model remains valid as an approximation if the condition $G_\mathrm{d} \ll G_\mathrm{r}$ still holds. Slowing down the signal rise time can suppress position-dependent variations in the signal shape due to a slow thermalization time constant of the absorber τ_abs or the sensor τ_sen.

For an MMC with a heat capacity $C \approx 20\,\mathrm{pJ\,K^{-1}}$ and $C_\mathrm{e} \approx C_\mathrm{s}$, a thermal conductance between the electron and spin systems $G_\mathrm{r} \approx 500\,\mathrm{nW\,K^{-1}}$, and a thermal conductance to the thermal bath $G_\mathrm{d} \approx 20\,\mathrm{nW\,K^{-1}}$, the rise time constant is $\tau_\mathrm{r} \approx 10\,\mu\mathrm{s}$ and the decay time constant is $\tau_\mathrm{d} \approx 1\,\mathrm{ms}$. Figure 3.6 shows the expected signal shape of such an MMC for an incident particle with energy $E = 6\,\mathrm{keV}$.

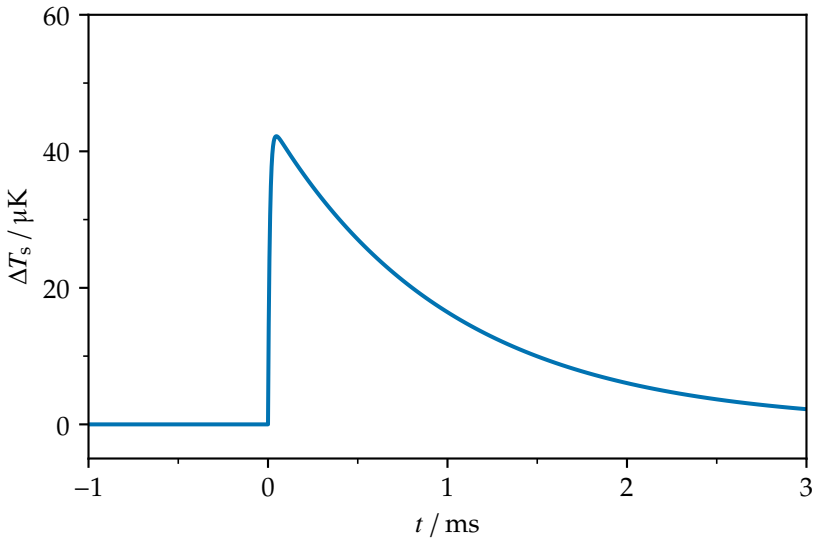

Figure 3.6.: Spin temperature ΔT_s for an incident particle with energy $E = 6\,\mathrm{keV}$. The values are calculated for an MMC with heat capacity $C \approx 20\,\mathrm{pJ\,K^{-1}}$, $C_e \approx C_s$, and time constants $\tau_r = 10\,\mu\mathrm{s}$ and $\tau_d = 1\,\mathrm{ms}$.

3.5. Noise Components

The noise of an MMC is composed of multiple components with different physical origins and frequency dependencies. The combined noise must be estimated and taken into account when optimizing the energy resolution of an MMC. Together with the signal shape, the noise limits the achievable energy resolution and energy threshold. Among the noise sources, the combined thermal energy noise, magnetic flux noise, and readout noise typically dominate across the relevant frequency range, while other noise sources are usually negligible.

3.5.1. Thermal Energy Noise

A fundamental noise contribution originates from thermal energy fluctuations between the thermodynamic subsystems of the MMC [51]. Each thermal conductance G gives rise to a one-sided noise power spectral density (PSD) S, expressed as a power P given by

$$S^{(P)} = 4\,k_B\,T^2\,G \tag{3.41}$$

according to the fluctuation–dissipation theorem. For the previously discussed thermodynamic system shown in Figure 3.5, the two thermal conductances G_r and G_d each generate a

noise PSD S. Assuming thermal equilibrium, the two differential equations (3.34) and (3.35) reduce to

$$\dot{E}_\mathrm{e} = C_\mathrm{e}\,\dot{T}_\mathrm{e} \tag{3.42}$$

$$= G_\mathrm{r}\,(T_\mathrm{s} - T_\mathrm{e}) + G_\mathrm{d}\,(T - T_\mathrm{e}) + P_\mathrm{d} - P_\mathrm{r} \tag{3.43}$$

$$\dot{E}_\mathrm{s} = C_\mathrm{s}\,\dot{T}_\mathrm{s} \tag{3.44}$$

$$= G_\mathrm{r}\,(T_\mathrm{e} - T_\mathrm{s}) + P_\mathrm{r} \tag{3.45}$$

where P_r and P_d are the white-noise power contributions from the thermal conductances G_r and G_d, respectively. If the rise time constant is much smaller than the decay time constant $\tau_\mathrm{r} \ll \tau_\mathrm{d}$ and the heat capacities of the two thermal subsystems are similar $C_\mathrm{e} \sim C_\mathrm{s}$, the PSD of the thermal energy noise S_t, expressed as an equivalent energy noise E_s in the sensor, simplifies to

$$S_\mathrm{t}^{(\mathrm{E_s})} = 4\,k_\mathrm{B}\,T^2\,C_\mathrm{s}\left(\tau_\mathrm{r}\,\frac{C_\mathrm{e}}{C}\,\frac{1}{1+(f/f_\mathrm{r})^2} + \tau_\mathrm{d}\,\frac{C_\mathrm{s}}{C}\,\frac{1}{1+(f/f_\mathrm{d})^2}\right) \tag{3.46}$$

with the two cut-off frequencies $f_\mathrm{r} = (2\,\pi\,\tau_\mathrm{r})^{-1}$ and $f_\mathrm{d} = (2\,\pi\,\tau_\mathrm{d})^{-1}$ [51].

Figure 3.7 (left) shows the thermal energy noise S_t for an MMC at a temperature $T = 20\,\mathrm{mK}$ with a heat capacity $C \approx 20\,\mathrm{pJ\,K^{-1}}$ and $C_\mathrm{e} \approx C_\mathrm{s}$, with time constants $\tau_\mathrm{r} = 10\,\mu\mathrm{s}$ and $\tau_\mathrm{d} = 1\,\mathrm{ms}$. The thermal energy noise S_t has two components, each with a white-noise plateau and a characteristic cut-off frequency defined by its respective time constant.

3.5.2. Magnetic Flux Noise

The magnetic moments in the sensor create another noise source that produces frequency-dependent $1/f$ noise. While its microscopic origin is not yet fully understood, this noise appears to be temperature independent [117] and proportional to the amount of erbium atoms [107, 118]. It is suspected to originate from interactions between clusters of magnetic moments [119, 120].

The magnetic flux noise from a single erbium atom is described by

$$S_\mathrm{Er}^{(\mu_\mathrm{B})} = \alpha\,f^{-\beta} \tag{3.47}$$

with the noise PSD per erbium ion α at 1 Hz and the $1/f$ noise exponent β. Measurements have shown that for Ag:Er, $\alpha = 0.0175(9)\,{\mu_\mathrm{B}}^2\mathrm{Hz}^{-1}$ and $\beta = 0.856(14)$, while for Au:Er, $\alpha = 0.115(6)\,{\mu_\mathrm{B}}^2\mathrm{Hz}^{-1}$ and $\beta = 1.00(3)$ [85, 121]. Figure 3.7 shows the noise S_Er for Ag:Er and Au:Er per erbium atom. In the relevant MMC frequency range, Ag:Er exhibits lower noise per erbium atom up to approximately 500 kHz.

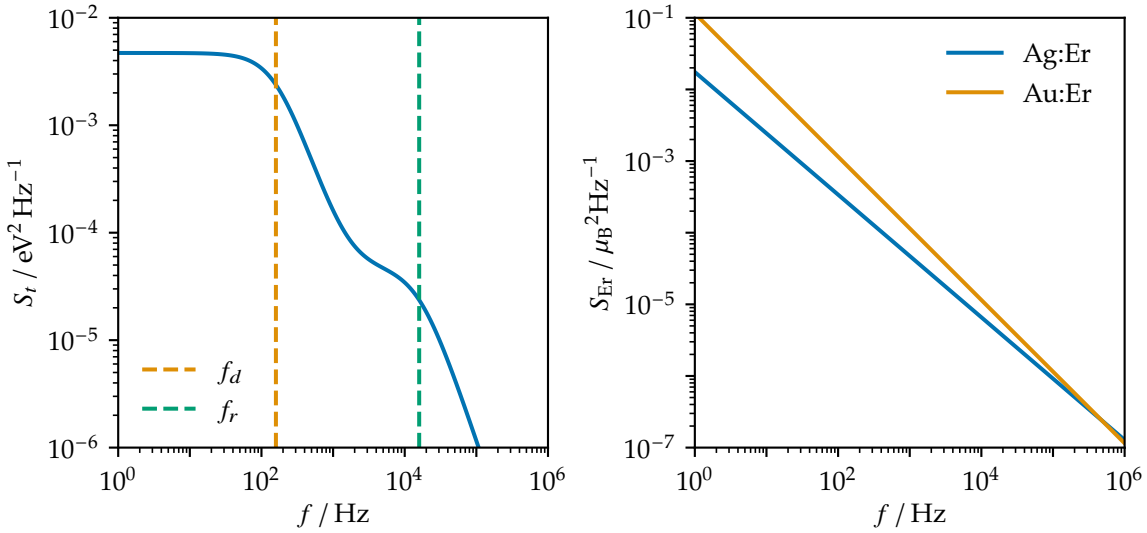

Figure 3.7.: Thermal energy noise S_t expressed as an energy noise E_s in the sensor (left), and the magnetic flux noise S_{Er} for Ag:Er and Au:Er (right). The values are calculated for an MMC at temperature $T = 20\,\mathrm{mK}$, with heat capacity $C \approx 20\,\mathrm{pJ\,K^{-1}}$ and $C_e \approx C_s$, and time constants $\tau_r = 10\,\mu\mathrm{s}$ and $\tau_d = 1\,\mathrm{ms}$.

The resulting magnetic flux noise S_m expressed as a flux noise in a meander is given by

$$S_m^{(\Phi_m)} = \left(\frac{\partial B}{\partial I}\right)^2 N_{Er}\, S_{Er}^{(\mu_B)} \tag{3.48}$$

where N_{Er} is the number of erbium atoms and $\partial B/\partial I$ is the magnetic field per current, representing the coupling of the magnetic moments to a coil.

3.5.3. Readout Noise

The two-stage SQUID readout discussed at the end of this chapter introduces another noise component. The shunt resistances of the SQUIDs, as well as the voltage and current noise on the SQUID bias, contribute significantly to the combined noise [122]. This noise can vary substantially between individual SQUIDs.

The combined readout noise S_r, expressed as an effective magnetic flux Φ_s in the SQUID, is given by

$$S_r^{(\Phi_s)} = \alpha\, f^{-\beta} + \gamma \tag{3.49}$$

with a frequency-dependent $1/f$ noise component α at 1 Hz, the $1/f$ noise exponent β, and a frequency-independent white-noise component γ. The readout has a limited bandwidth with a cut-off frequency f_c, which attenuates both the signal and the noise. A typical two-stage SQUID readout has $\alpha \approx (5.0\,\mu\Phi_0\,\mathrm{Hz}^{-1/2})^2$ for the noise at 1 Hz, a $1/f$ noise exponent $\beta \approx 0.8$,

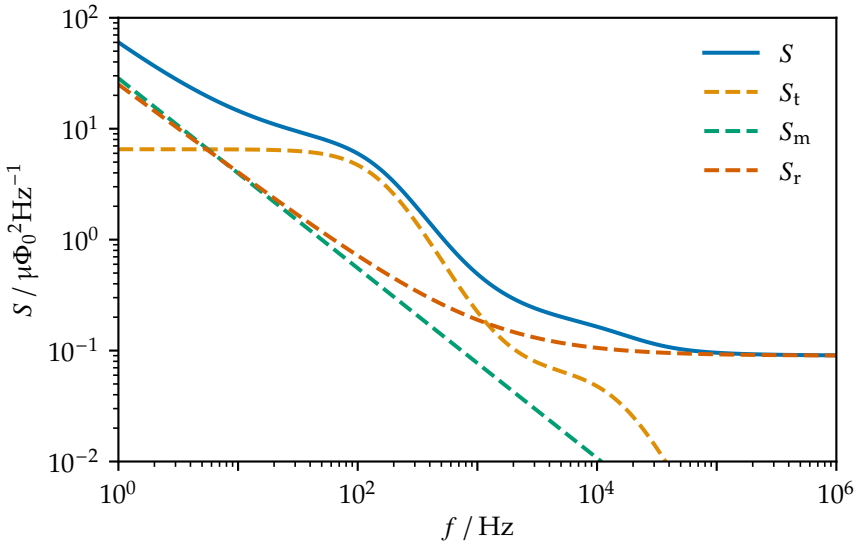

Figure 3.8.: Noise PSD S, expressed as a flux noise Φ_s, with its noise components from thermal energy noise S_t, magnetic flux noise S_m, and readout noise S_r. The values are calculated for an MMC having the double-meander geometry, with a magnetic flux per energy $\partial\Phi_\mathrm{m}/\partial E_\mathrm{s} \approx 0.3\,\Phi_0\,\mathrm{keV}^{-1}$, a flux coupling $\partial\Phi_\mathrm{s}/\partial\Phi_\mathrm{m} \approx 0.04$, a magnetic field per current $\partial B/\partial I \approx 90\,\mu\mathrm{T\,mA}^{-1}$, and a number of erbium atoms $N_\mathrm{Er} \approx 3\times10^{12}$.

and a white-noise component $\gamma \approx (0.3\,\mu\Phi_0\,\mathrm{Hz}^{-1/2})^2$ [9]. The circuit has a typical cut-off frequency $f_\mathrm{c} \approx 1\,\mathrm{MHz}$.

3.5.4. Combined Noise

The combined noise PSD S from an MMC, expressed as an effective flux Φ_s in the SQUID, is given by

$$S^{(\Phi_\mathrm{s})} = S_\mathrm{t}^{(\Phi_\mathrm{s})} + S_\mathrm{m}^{(\Phi_\mathrm{s})} + S_\mathrm{r}^{(\Phi_\mathrm{s})} \tag{3.50}$$

where the individual noise components must be converted using

$$S^{(\Phi_\mathrm{m})} = \left(\frac{\partial\Phi_\mathrm{m}}{\partial E_\mathrm{s}}\right)^2 S^{(E_\mathrm{s})} \tag{3.51}$$

$$S^{(\Phi_\mathrm{s})} = \left(\frac{\partial\Phi_\mathrm{s}}{\partial\Phi_\mathrm{m}}\right)^2 S^{(\Phi_\mathrm{m})} \tag{3.52}$$

where $\partial\Phi_\mathrm{m}/\partial E_\mathrm{s}$ is the magnetic flux in the pickup coil per energy in the sensor, and $\partial\Phi_\mathrm{s}/\partial\Phi_\mathrm{m}$ is the flux coupling between the pickup coil and the SQUID. These properties depend on the MMC geometry, an example of which will be discussed later.

Figure 3.8 shows the combined noise PSD S and its components for an MMC with a magnetic flux per energy $\partial\Phi_\mathrm{m}/\partial E_\mathrm{s} \approx 0.3\,\Phi_0\,\mathrm{keV}^{-1}$ and a flux coupling $\partial\Phi_\mathrm{s}/\partial\Phi_\mathrm{m} \approx 0.04$.

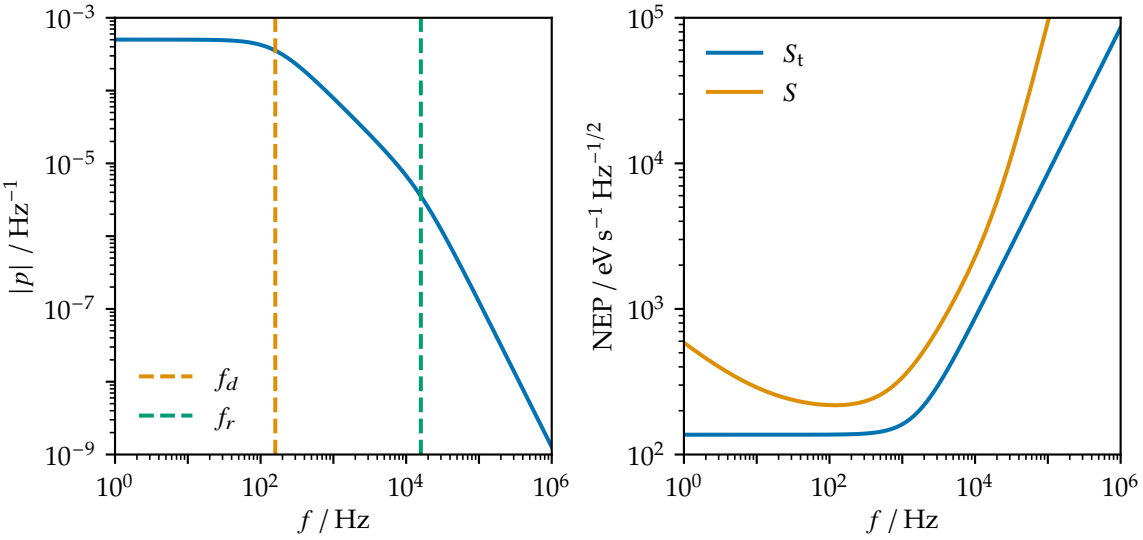

Figure 3.9.: Responsivity $|\tilde{p}|$ (left) and the NEP (right). The values are calculated for an MMC with a heat capacity $C \approx 20\,\mathrm{pJ\,K^{-1}}$ and $C_e \approx C_s$, and time constants $\tau_r = 10\,\mu\mathrm{s}$ and $\tau_d = 1\,\mathrm{ms}$. The NEP is shown for the thermal energy noise S_t only, as in Figure 3.7 (left), and for the PSD S, as in Figure 3.8.

3.6. Energy Resolution

The FWHM energy resolution ΔE_{FWHM} of an MMC can be estimated from its responsivity p and noise S. Assuming the thermodynamic system shown in Figure 3.5, the responsivity p is expressed as an energy in the sensor E_s, as given by equation (3.38). The responsivity p can be transformed into Fourier space $\tilde{p}$, which simplifies to

$$|\tilde{p}| = \frac{C_s}{C} \frac{\tau_d}{\sqrt{1 + (f/f_d)^2}\sqrt{1 + (f/f_r)^2}} \tag{3.53}$$

assuming $\tau_r \ll \tau_d$. The responsivity $|\tilde{p}|$ in Fourier space is shown in Figure 3.9 (left). It has two cut-off frequencies, one each from the rise and decay time constants.

Assuming an instantaneous energy input E, the RMS energy resolution σ_E based on a whitened matched filter is given by

$$\sigma_E = \left(\int_0^\infty \frac{4}{\mathrm{NEP}^2}\, \mathrm{d}f \right)^{-1/2} \tag{3.54}$$

where NEP is the one-sided noise equivalent power (NEP) [123]. The NEP is related to the signal-to-noise ratio (SNR) by SNR = P/NEP and is given by

$$\mathrm{NEP}^2 = \frac{S}{|\tilde{p}|^2} \tag{3.55}$$

where the noise PSD S and the responsivity $\tilde{p}$ in Fourier space must be expressed as effective parameters in the same frame. For high-resolution spectroscopy, the more common form of the energy resolution is

$$\Delta E_{\mathrm{FWHM}} = 2\sqrt{2\,\ln 2}\,\sigma_E \tag{3.56}$$

$$\approx 2.355\,\sigma_E \tag{3.57}$$

the full width at half maximum (FWHM) energy resolution ΔE_{FWHM}. This expression gives the expected energy resolution if the assumptions of the whitened matched filter are valid, with both the response and noise considered stationary.

A fundamental limit on the energy resolution can be calculated by considering only the intrinsic thermal energy noise S_t and neglecting other noise components [107]. The result is geometry-independent because both the responsivity $|\tilde{p}|$ and the thermal energy noise S_t are expressed directly as the energy in the sensor E_s. Using equations (3.53) and (3.46), the NEP can be derived. It simplifies for $\tau_\mathrm{r} \ll \tau_\mathrm{d}$ to

$$\mathrm{NEP} = \sqrt{\frac{4\,k_\mathrm{B}\,T^2\,C}{\tau_\mathrm{d}}\left(1 + \frac{C_\mathrm{e}}{C_\mathrm{s}}\,\frac{\tau_\mathrm{r}}{\tau_\mathrm{d}}\left[1 + \left(\frac{f}{f_\mathrm{d}}\right)^2\right]\right)} \tag{3.58}$$

and is shown in Figure 3.9 (right). The corresponding RMS energy resolution is

$$\Delta E_\mathrm{rms} = \sqrt{4\,k_\mathrm{B}\,T^2\,C}\,\left(\frac{C_\mathrm{e}}{C_\mathrm{s}}\right)^{1/4}\,\left(\frac{\tau_\mathrm{r}}{\tau_\mathrm{d}}\right)^{1/4} \tag{3.59}$$

again assuming $\tau_\mathrm{r} \ll \tau_\mathrm{d}$.

The fundamental energy resolution ΔE_rms is influenced by the temperature T_0, the time constants τ_r and τ_d, and the heat capacities C_e and C_s. The energy resolution scales approximately linearly with temperature $\Delta E_\mathrm{rms} \propto T$ and can be significantly improved by operating at lower T_0. Typically, the electron heat capacity C_e and the rise time τ_r are constrained by the desired absorber geometry and thermalization. For a given electron heat capacity C_e, the energy resolution is minimal when the electron and spin heat capacities match $C_\mathrm{e} = C_\mathrm{s}$, so that $C_\mathrm{e}/C_\mathrm{s} = 1$. For a given rise time τ_r, the ratio $\tau_\mathrm{r}/\tau_\mathrm{d}$ is minimized for a large decay time τ_d. In practice, the noise is not solely dominated by the thermal energy noise S_t, and other noise components are non-negligible. The NEP then deviates significantly from the NEP calculated

with only S_t, as shown in Figure 3.9 (right), and must be used to calculate the expected energy resolution ΔE_{rms} accurately.

For an MMC with heat capacity $C \approx 20\,\mathrm{pJ\,K^{-1}}$ and $C_e \approx C_s$, time constants $\tau_r = 10\,\mu\mathrm{s}$ and $\tau_d = 1\,\mathrm{ms}$, the fundamental limit on the energy resolution is $\Delta E_{FWHM} = 3.2\,\mathrm{eV}$, whereas the expected energy resolution for an MMC with the NEP shown in Figure 3.9 (right) is $\Delta E_{FWHM} = 6.9\,\mathrm{eV}$.

3.7. Detector Geometry

The geometry of an MMC significantly influences its properties. It must efficiently couple the magnetization change ΔM in the paramagnetic temperature sensor to a magnetic flux change $\Delta\Phi_s$ in a SQUID, while also generating a static magnetic field intensity H in the sensor. The geometry should allow for a linear response and a position-independent signal shape, and it should be compatible with reliable and preferably simple microfabrication techniques. While most established MMC geometries are planar and can be fabricated using photolithography, they differ significantly in their magnetic flux coupling $\partial\Phi_m/\partial E_s$ and in the generation of the static magnetic field intensity H.

A highly efficient flux coupling can be achieved using a geometry with integrated SQUID readout, which directly measures the magnetization change of the sensor [124–126]. However, this approach requires a separate coil to generate the magnetic field and has a significantly more complex fabrication process, as MMCs and SQUIDs require different materials and microfabrication steps. Alternatively, a superconducting flux transformer can be used to couple the magnetic flux change $\Delta\Phi_m$ from the pickup coil to a magnetic flux change $\Delta\Phi_s$ in the SQUID. The flux transformer can be split into two parts, enabling the MMCs and the SQUIDs to be fabricated separately, thereby significantly simplifying the fabrication. The separate chips are electrically connected after fabrication via bonding wires that become superconducting at low temperatures. A sensor placed within a superconducting coil of such a flux transformer provides strong indirect flux coupling [16, 57, 127, 128]. This approach offers strong coupling but requires more layers and is more complex to fabricate than other designs.

The so-called double meander geometry, which also uses a superconducting flux transformer, consists of fewer layers [112]. This geometry is widely used in large MMC arrays for high-resolution spectroscopy due to its efficient coverage of a large active area and high fabrication yield. Various other geometries are discussed in the literature [51, 52, 63].

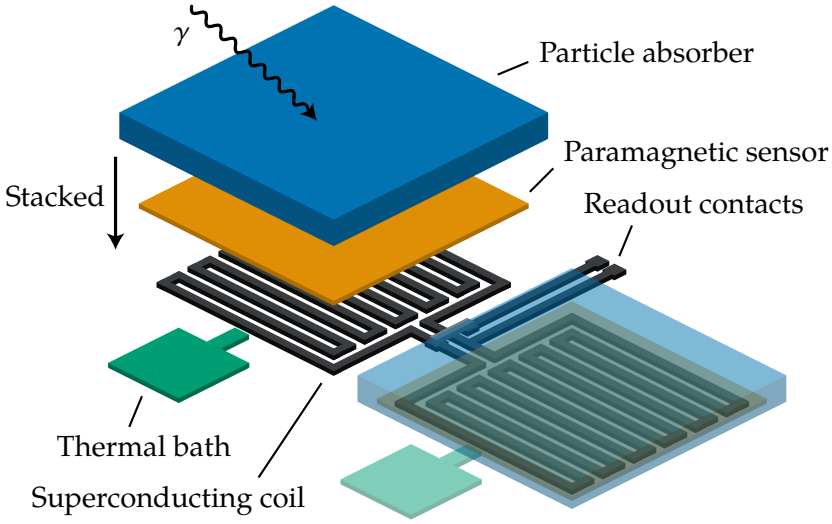

Figure 3.10.: Simplified schematic drawing of the double meander geometry. The planar design features a paramagnetic sensor below a particle absorber, weakly coupled to a thermal bath. A superconducting pickup coil beneath the sensor is connected in parallel to a second coil and to the input coil of a SQUID. A persistent current in the two coils generates the static magnetic field in the sensor.

3.7.1. Double Meander Geometry

A schematic of the double meander geometry is shown in Figure 3.10. A single MMC consists of a planar particle absorber stacked on top of a paramagnetic temperature sensor, which is weakly thermally coupled to a thermal bath. A superconducting meander-shaped coil beneath the sensor serves as the pickup coil, detecting the magnetization change ΔM as a magnetic flux change $\Delta\Phi_\mathrm{m}$. This coil is connected in parallel with another coil and with the readout contacts for the input coil of a SQUID. Together, they form a superconducting flux transformer. A persistent current I_0 in the two coils generates the required magnetic field intensity H. The second coil can either be part of another MMC—acting as a pickup coil—or be a high-impedance coil that only carries the persistent current to enhance the flux coupling $\partial\Phi_\mathrm{m}/\partial E_\mathrm{s}$ between the single MMC and the SQUID.

For a double meander geometry with a single MMC, the signal is, to first order, proportional to the sensor temperature. Slow temperature variations induce a fluctuating offset, while the absorption of an X-ray produces a signal superimposed on that offset. If each coil belongs to a separate, identical MMC, they form a first-order gradiometer. The signal is then the difference between the two MMC signals and becomes proportional to the temperature difference between the two sensors. An X-ray event in either MMC produces a signal with either positive or negative polarity. Temperature drifts that affect both sensors equally cancel out, making the offset insensitive to slow temperature changes. In both cases—whether using a single

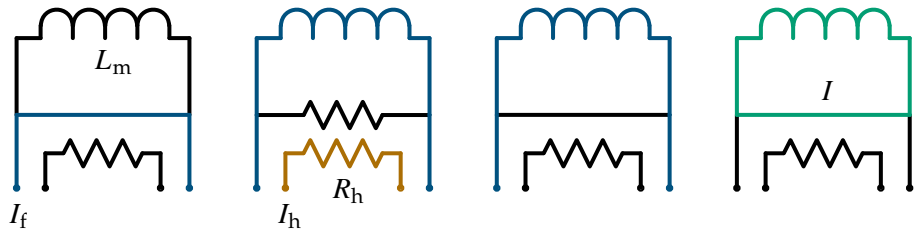

Figure 3.11.: Schematic drawing of the preparation of a persistent current I_0 (green) using a persistent current switch (from left to right). A heater current I_h (orange) through a heater resistance R_h drives a segment of the superconducting loop normal conducting, allowing the field current I_f (blue) to flow through the superconducting coil with inductance L_m. When the heater is turned off, screening currents maintain the magnetic flux, resulting in a persistent current $I_0 \approx I_\mathrm{f}$, assuming negligible parasitic inductance.

asymmetric MMC or two symmetric MMCs—the signal amplitude depends on the MMC temperature. Small temperature variations over time lead to variations in signal amplitude and must be corrected. Slow temperature variations do not affect the offset of symmetric MMCs, which are therefore often operated alongside asymmetric MMCs, whose offsets are used to monitor and correct for temperature variations over time.

Due to the limited number of available readout channels and the implementation of first-order gradiometers to reduce the effect of temperature fluctuations, it is common to read out two MMCs using a single SQUID channel. This configuration enables efficient coverage of large absorber areas with two-dimensional MMC arrays while maintaining high energy resolution. As discussed later in this chapter, a single MMC covering the same area would have approximately twice the heat capacity, typically resulting in poorer energy resolution, even when using a second high-impedance coil to improve the flux coupling $\partial\Phi_\mathrm{m}/\partial E_\mathrm{s}$.

3.7.2. Persistent Current Switch

An MMC requires a static magnetic field intensity H in the sensor, which is usually produced by a persistent current I_0 in a nearby superconducting coil. The preparation of a persistent current I_0 in a closed superconducting circuit, using a persistent current switch, is shown in Figure 3.11. A field current I_f is applied in parallel to the closed superconducting loop. Assuming that the total inductance of the loop is dominated by the inductance of the coil L_m and that parasitic inductances can be neglected, the current initially bypasses the coil. A short heater pulse, applied by a heater current I_h through a heater resistance R_h, temporarily drives a small section of the superconducting loop into the normal-conducting state. This forces the field current I_f through the superconducting coil. After switching off the heater, the heated section returns to the superconducting state. Screening currents maintain the magnetic flux inside the closed loop, thereby sustaining a persistent current $I_0 \approx I_\mathrm{f}$ after I_f is turned off.

In the double meander geometry, a persistent current is established in both meanders, which also serve as part of the superconducting flux transformer that detects the magnetization change ΔM as a flux change $\Delta\Phi_{\mathrm{m}}$. The heater for the persistent current switch is usually located at the junction between the two meanders and the input coil of the SQUID, ensuring that no persistent current is induced in the SQUID input coil.

3.7.3. Detector Fabrication

Placing the SQUIDs for readout on separate chips simplifies the fabrication process and reduces the required number of layers to only those needed for the MMCs. All components of the double meander geometry are planar and compatible with standard microfabrication techniques. Typically, each component can be fabricated using a single layer. Using the same superconducting coils both to pick up the signal and to generate the magnetic field intensity H further reduces complexity. However, this approach requires that the superconducting coils have a sufficiently high critical current I_{c} to sustain the persistent current I_0, which is usually much greater than the MMC signal due to screening currents induced in the superconducting flux transformer. The MMCs are usually fabricated as two-dimensional arrays on silicon (Si) or germanium (Ge) substrates. The geometry requires several distinct layers: at least one superconducting layer for coils and electrical connections, a thermalization layer to couple to the thermal bath, a high-resistance layer for heaters and the persistent current switch, a sensor layer, and an absorber layer, as well as at least one insulating layer beneath the sensor. Additional layers are often introduced to enhance the performance of the MMC and to achieve a more uniform signal shape.

A geometric bottleneck between absorber and sensor can be used to reduce the probability of athermal phonons escaping the absorber without thermalizing [63, 94]. This can be achieved by introducing thermal connections with small cross-sections, so-called stems, which connect the absorber to the sensor thermally only at discrete contact points [57]. Although stems increase fabrication complexity and reduce the mechanical stability of the absorber, they significantly improve the homogeneity of the response. The geometric bottleneck does not necessarily act as a thermal bottleneck and does not necessarily limit the signal rise time. For large absorbers, the thermalization time of the absorber τ_{abs} may exceed the electron–spin coupling time. To prevent position-dependent signal shapes, an additional thermal bottleneck to the spin system C_{s} must be introduced. In the case of stems, a thermal bottleneck can be easily implemented within the sensor layer by introducing a narrow thermal link between the main sensor area and the stem contact region. In this configuration, the time constant of the bottleneck must be longer than both the thermalization time of the absorber τ_{abs} and the thermalization time of the sensor τ_{sen} to suppress position-dependent variations.

3.8. Detector Optimization

The design parameters of an MMC are typically chosen to optimize the energy resolution ΔE_{FWHM} at a given temperature T_0. The heat capacity C_{abs} of the gold absorber is usually determined by the absorber side length a_{abs} and thickness h_{abs} required for a specific experiment or application. In addition to a high energy resolution ΔE_{FWHM}, a low relative non-linearity ζ_E and a low relative temperature sensitivity ζ_T should also be achieved, while fabrication limitations must be taken into account.

During optimization, the responsivity $|p|$ and the noise PSD S are calculated for a given set of design parameters, from which the expected energy resolution ΔE_{FWHM} is derived. The global optimum of ΔE_{FWHM} or the figure of merit (FOM) is determined by repeating the process for many different design parameters. While the parameter space is large, near-optimal energy resolution can often be achieved within a broad range, and trade-offs between different design parameters must be considered. Some parameters are fixed by the MMC layer design, such as the absorber area A_{abs} and sensor area A_{sen}. Others are defined during fabrication, such as absorber thickness h_{abs} and erbium concentration x_{Er}, while parameters like the temperature T_0 and the persistent current I_0 can be tuned during operation. Major steps in the calculation include determining the magnetic field intensity H generated by the persistent current, the magnetic flux in the pickup coil per energy $\partial\Phi_{\mathrm{m}}/\partial E$ from the magnetization change ΔM of the sensor, and the magnetic flux coupling $\partial\Phi_{\mathrm{s}}/\partial\Phi_{\mathrm{m}}$ between the pickup coil and the SQUID.

3.8.1. Magnetic Field

A static magnetic field intensity H is required in the sensor. Figure 3.12 shows a cross-section of the simulated magnetic field per current $\partial B/\partial I$ above a planar superconducting meander-shaped coil. A persistent current I_0 in the coil generates a magnetic field

$$B = \frac{\partial B}{\partial I} I_0 \tag{3.60}$$

which is generally position-dependent. Alternative coil geometries may yield a much more homogeneous magnetic field B. The temperature dependence of the magnetization $\partial M/\partial T$ and the specific heat capacity C_{s} of the spin system depend on B and can be computed from the field distribution in the sensor.

3.8.2. Magnetization Change

A magnetization change ΔM in the sensor couples to the pickup coil in a position-dependent manner. In geometries where the superconducting coil both generates H and detects the

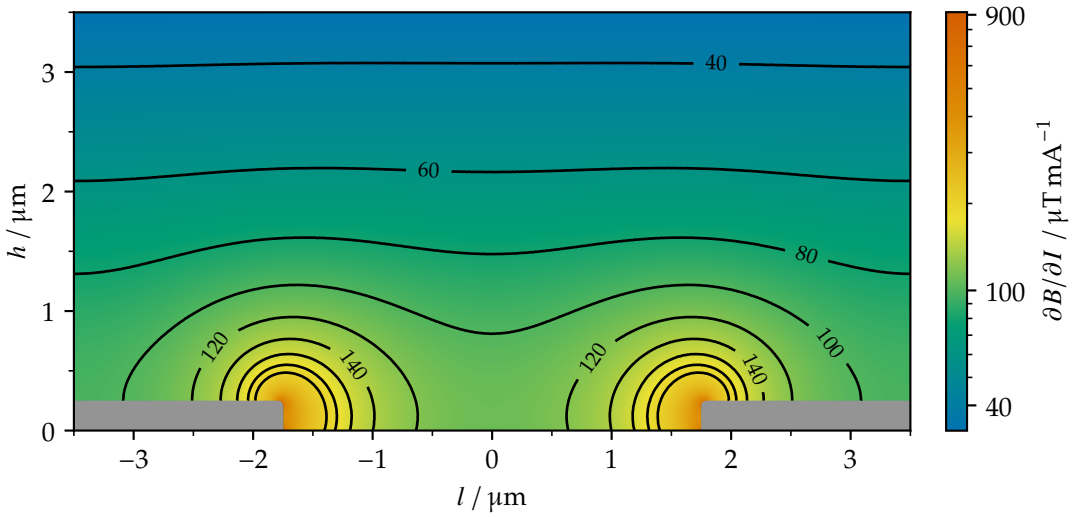

Figure 3.12.: Magnetic field per current $\partial B/\partial I$ in a cross-section above a planar meander-shaped coil (grey). The values are simulated with the program *FEMM* (Finite Element Method Magnetics), assuming a coil of infinite depth with periodic boundary conditions. The coil has a height $h = 250\,\mathrm{nm}$, pitch $p = 7\,\mu\mathrm{m}$, and linewidth $w = p/2$.

resulting flux change $\Delta\Phi_\mathrm{m}$ as a pickup coil, reciprocity ensures that the magnetic field per current $\partial B/\partial I$ describes both the field generation and the flux pickup. Otherwise, the corresponding factor $\partial B/\partial I$ must be separately simulated for the pickup coil.

The magnetic flux in the pickup coil per energy $\partial\Phi_\mathrm{m}/\partial E$ is calculated as the integral over the sensor volume V

$$\frac{\partial\Phi_\mathrm{m}}{\partial E} = \frac{1}{C}\int_V \frac{\partial B}{\partial I}\frac{\partial M}{\partial T}\,\mathrm{d}V \tag{3.61}$$

where the temperature dependence of the magnetization $\partial M/\partial T$ is also position-dependent. This expression simplifies significantly if a constant magnetic field B and constant flux pickup $\partial B/\partial I$ are assumed:

$$\frac{\partial\Phi_\mathrm{m}}{\partial E} = \frac{V}{C}\frac{\partial B}{\partial I}\frac{\partial M}{\partial T} \tag{3.62}$$

where $\partial M/\partial T$ is constant. A geometric factor $G = p/\mu_0\,\partial B/\partial I$ is sometimes introduced in the literature [112], but is not used here for simplicity.

For a given sensor volume V, the coupling $\partial B/\partial I$ can be optimized by maximizing the filling factor η, which describes the fraction of the magnetic field energy contained in the sensor volume:

$$\eta = \frac{\int_V B^2\,\mathrm{d}V}{\int B^2\,\mathrm{d}V} \tag{3.63}$$

with $0 \leq \eta \leq 1$. A sensor embedded in a superconducting coil can reach a very high filling factor $\eta \approx 1$, while a sensor positioned on one side of a planar coil typically achieves a lower value $\eta \approx 1/2$.

3.8.3. Flux Coupling

If the magnetic flux change Φ_m is not directly detected by a SQUID but instead via a superconducting flux transformer that generates a magnetic flux change Φ_s in the SQUID, the flux coupling $\partial\Phi_\mathrm{s}/\partial\Phi_\mathrm{m}$ must be calculated. Using Kirchhoff's rules and magnetic flux conservation in closed superconducting circuits, the flux coupling $\partial\Phi_\mathrm{s}/\partial\Phi_\mathrm{m}$ for the double meander geometry is given by

$$\frac{\partial\Phi_\mathrm{s}}{\partial\Phi_\mathrm{m}} = \frac{M_\mathrm{in}}{L_\mathrm{m} + L_\mathrm{r} + \frac{L_\mathrm{m} L_\mathrm{r}}{L_\mathrm{f}}} \tag{3.64}$$

where M_in is the mutual inductance of the SQUID input coil, L_m is the inductance of the pickup coil, L_f is the coil in parallel that also carries the persistent current, and L_r is the readout inductance. The readout inductance L_r is

$$L_\mathrm{r} = L_\mathrm{in} + L_\mathrm{p} \tag{3.65}$$

with the inductance of the SQUID input coil L_in and a parasitic inductance L_p due to the connection between the MMC and the SQUID, dominated by bonding wires. For the double meander geometry with two gradiometric MMCs, the inductance of both coils is the same $L_\mathrm{f} = L_\mathrm{m}$. For an asymmetric MMC, a large inductance L_f of the field-carrying coil improves the flux coupling.

3.8.4. Energy Resolution

The energy resolution ΔE_FWHM can be calculated from the NEP. The response $|\tilde{p}|$ and noise S must be expressed in the same reference frame, typically as the magnetic flux Φ_s in the SQUID. Following equation (3.53), the response $|\tilde{p}|$ is

$$|\tilde{p}| = \frac{\partial\Phi_\mathrm{s}}{\partial E} \frac{\tau_\mathrm{d}}{\sqrt{1 + (f/f_\mathrm{d})^2}\sqrt{1 + (f/f_\mathrm{r})^2}} \tag{3.66}$$

where the magnetic flux Φ_s in the SQUID per energy is

$$\frac{\partial\Phi_\mathrm{s}}{\partial E} = \frac{\partial\Phi_\mathrm{s}}{\partial\Phi_\mathrm{m}} \frac{\partial\Phi_\mathrm{m}}{\partial E} \tag{3.67}$$

The noise PSD S is

$$S^{(\Phi_\mathrm{s})} = \left(S_\mathrm{t}^{(\Phi_\mathrm{s})} + S_\mathrm{m}^{(\Phi_\mathrm{s})}\right) N_\mathrm{sen} + S_\mathrm{r}^{(\Phi_\mathrm{s})} \tag{3.68}$$

where N_{sen} is the number of sensors. For a gradiometric channel of the double meander geometry with $N_{\text{sen}} = 2$, the thermal and magnetic flux noise of the two MMCs increase the noise relative to an individual readout. The NEP can be calculated using equation (3.55) and subsequently the RMS and FWHM energy resolutions from equations (3.54) and (3.57).

3.8.5. Non-Linearity

The non-linearity of an MMC can be estimated by a Taylor expansion of the flux change $\Delta\Phi_{\text{s}}$ in the SQUID [129]. Upon an energy input E, the flux change $\Delta\Phi_{\text{s}}$ is given by

$$\Delta\Phi_{\text{s}}(E) = \frac{\partial\Phi_{\text{s}}}{\partial E}\,E + \frac{1}{2}\frac{\partial^2\Phi_{\text{s}}}{\partial E^2}\,E^2 + O(E^3) \tag{3.69}$$

where the first term represents the linear response and the second term is the leading-order non-linearity. Higher-order terms $O(E^3)$ in the correction term

$$\delta\Phi_{\text{s}} = \frac{1}{2}\,\frac{\partial^2\Phi_{\text{s}}}{\partial E^2}\,E^2 + O(E^3) \tag{3.70}$$

can be neglected to good approximation. A relative non-linearity ζ_E can be defined by

$$\zeta_E = \frac{\delta\Phi_{\text{s}}}{\frac{\partial\Phi_{\text{s}}}{\partial E}\,E} \tag{3.71}$$

and is evaluated for a given energy E. While non-linearity is corrected during energy calibration, a more reliable calibration is generally achieved when the relative non-linearity ζ_E is minimized.

Assuming a position-independent magnetic field B and magnetic field per current $\partial B/\partial I$, the correction to the signal amplitude $\delta\Phi_{\text{s}}$ at energy E is given by

$$\delta\Phi_{\text{s}} = \frac{1}{2}\,\frac{\partial\Phi_{\text{s}}}{\partial E}\left[\frac{1}{C}\left(\frac{\partial M}{\partial T}\right)^{-1}\frac{\partial^2 M}{\partial T^2} - \frac{1}{C^2}\frac{\partial C}{\partial T}\right]E^2 \tag{3.72}$$

This relation is illustrated in Figure 3.13 for a specific MMC.

3.8.6. Temperature Sensitivity

Temperature fluctuations of the MMC lead to small changes in the signal amplitude. The change in signal amplitude $\delta\Phi_{\text{s}}$ due to a small temperature shift δT from a reference temperature T_0 at a fixed energy E is

$$\delta\Phi_{\text{s}} = \Delta\Phi_{\text{s}}(T + \delta T) - \Delta\Phi_{\text{s}}(T) \tag{3.73}$$

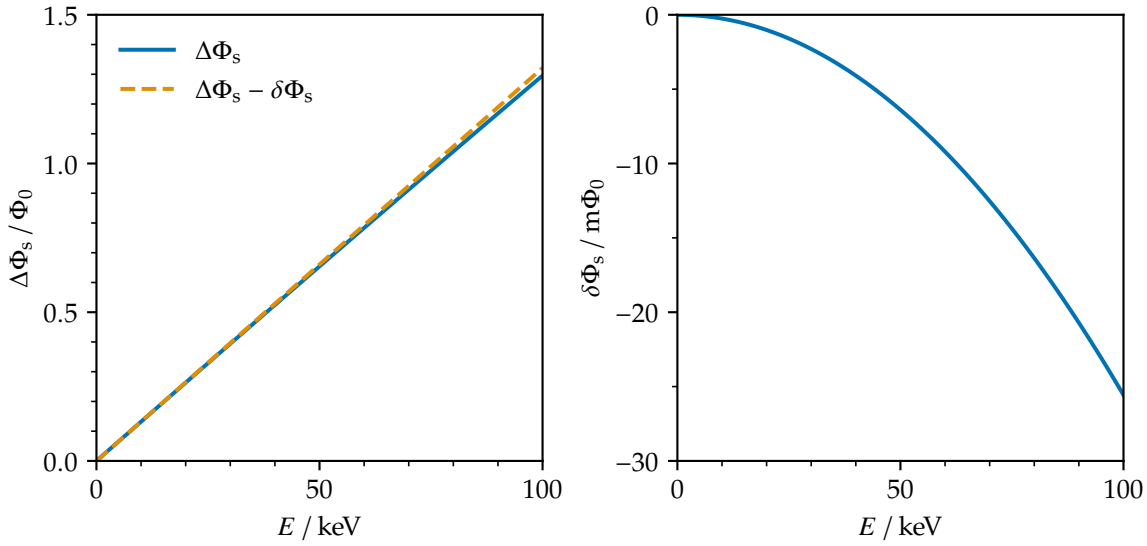

Figure 3.13.: Magnetic flux $\Delta\Phi_s$ (left) and its non-linearity $\delta\Phi_s$ (right) as a function of energy E. The values are calculated for a MMC with a magnetic flux per energy $\partial\Phi_s/\partial E \approx 10\,\mathrm{m}\Phi_0\,\mathrm{keV}^{-1}$, a heat capacity $C \approx 20\,\mathrm{pJ\,K}^{-1}$, its derivative $\partial C/\partial T \approx 400\,\mathrm{pJ\,K}^{-2}$, a temperature dependence of the magnetization $\partial M/\partial T \approx 10\,\mathrm{kA\,m}^{-1}\,\mathrm{K}^{-1}$, and its derivative $\partial^2 M/\partial T^2 \approx -300\,\mathrm{kA\,m}^{-1}\,\mathrm{K}^{-2}$.

Expanding in a Taylor series gives

$$\delta\Phi_s = \left(\frac{\partial^2\Phi_s}{\partial T\,\partial E}\,E + O(E^2)\right)\delta T + O(\delta T^2) \tag{3.74}$$

where higher orders $O(E^2)$ and $O(\delta T^2)$ can be neglected. A relative temperature sensitivity ζ_T can be defined by

$$\zeta_T = \frac{\delta_T\Phi_s}{\frac{\partial\Phi_s}{\partial E}\,E} \tag{3.75}$$

for a small temperature change δ_T. Temperature fluctuations cause amplitude fluctuations that must be corrected using temperature-based corrections. However, uncertainties in the temperature measurement lead to residual amplitude uncertainties, which can exceed the intrinsic energy resolution at higher energies and thus degrade the overall resolution. Minimizing the relative temperature sensitivity reduces this degradation.

Assuming a position-independent magnetic field B and magnetic field per current $\partial B/\partial I$, the change in signal amplitude $\delta\Phi_s$ due to a small temperature shift δT is given by

$$\delta\Phi_s = \frac{\partial\Phi_s}{\partial E}\,E\left[\left(\frac{\partial M}{\partial T}\right)^{-1}\frac{\partial^2 M}{\partial T^2} - \frac{1}{C}\frac{\partial C}{\partial T}\right]\delta T \tag{3.76}$$

which has a similar form to the non-linearity correction $\delta\Phi_s$ for a given energy E.

3.8.7. Example

As an instructive example, an MMC is optimized for X-ray spectroscopy at photon energies around $E \approx 20\,\mathrm{keV}$ and an operating temperature of $T_0 = 20\,\mathrm{mK}$. A gold absorber with a thickness $h_{abs} = 30\,\mu\mathrm{m}$ achieves a quantum efficiency $\alpha > 0.98$ for $E \leq 20\,\mathrm{keV}$ and $\alpha > 0.5$ for $E \leq 40\,\mathrm{keV}$, matching the desired energy range, according to Figure 3.2.

A square absorber with side length $a_{abs} = 500\,\mu\mathrm{m}$ results in a heat capacity $C_{abs} \approx 10\,\mathrm{pJ\,K^{-1}}$ at the given temperature. An electroplated gold absorber with RRR = 15 has a thermalization time constant $\tau_{abs} \approx 3\,\mu\mathrm{s}$. A sensor with comparable heat capacity $C_{sen} \approx 10\,\mathrm{pJ\,K^{-1}}$ can be realized using a square Ag:Er sensor with side length $a_{sen} = 250\,\mu\mathrm{m}$, thickness $h_{sen} = 1.6\,\mu\mathrm{m}$, erbium concentration $x_{Er} = 550\,\mathrm{ppm}$, and a magnetic field $B \approx 5\,\mathrm{mT}$. Such a sputtered sensor, with RRR = 2.4, has a thermalization time constant $\tau_{sen} \approx 5\,\mu\mathrm{s}$. A thermal conductance $G_r \approx 500\,\mathrm{nW\,K^{-1}}$ between absorber and sensor yields a rise time constant $\tau_r = 10\,\mu\mathrm{s}$, which is slower than both τ_{abs} and τ_{sen}, ensuring a position-independent response. The thermal conductance to the thermal bath, $G_d \approx 20\,\mathrm{nW\,K^{-1}}$, results in a decay time constant $\tau_d = 1\,\mathrm{ms}$. The corresponding signal, expressed as the spin temperature ΔT_s from an incident particle with $E = 6\,\mathrm{keV}$, is shown in Figure 3.6.

A planar meander-shaped pickup coil with pitch $p = 7\,\mu\mathrm{m}$, linewidth $w = p/2$, and height $h = 250\,\mathrm{nm}$ underneath the sensor yields a filling factor $\eta = 0.30$ and an inductance $L_m \approx 3\,\mathrm{nH}$. The magnetic field per current $\partial B/\partial I$ is shown in Figure 3.12, and its median value $\partial B/\partial I \approx 90\,\mu\mathrm{T\,mA^{-1}}$ is used in further calculations. The target magnetic field $B \approx 5\,\mathrm{mT}$ can be achieved with a persistent current $I_0 = 60\,\mathrm{mA}$. The temperature dependence of the magnetization $\partial M/\partial T \approx 10\,\mathrm{kA\,m^{-1}\,K^{-1}}$ corresponds to a magnetic flux change in the pickup coil per energy $\partial\Phi_m/\partial E \approx 0.3\,\Phi_0\,\mathrm{keV^{-1}}$. Using the double-meander geometry with two gradiometric MMCs, the flux coupling is $\partial\Phi_s/\partial\Phi_m \approx 0.04$, with the inverse SQUID mutual inductance $M_{in}^{-1} = 8.9\,\mu\mathrm{A}\,{\Phi_0}^{-1}$, SQUID input coil inductance $L_i \approx 1.2\,\mathrm{nH}$, and parasitic inductance $L_w \approx 0.3\,\mathrm{nH}$. This yields a magnetic flux in the SQUID per energy $\partial\Phi_s/\partial E \approx 10\,\mathrm{m}\Phi_0\,\mathrm{keV^{-1}}$.

The resulting response and NEP are shown in Figure 3.9, and the corresponding noise is shown in Figure 3.8. The energy resolution derived from the NEP is $\Delta E_{FWHM} \approx 6.9\,\mathrm{eV}$. The MMC has a relative non-linearity $\zeta_E/E \approx -2{\times}10^{-4}\,\mathrm{keV^{-1}}$ and a relative temperature sensitivity $\zeta_T/T \approx -5 \times 10^{-2}\,\mathrm{mK^{-1}}$, using $\partial C/\partial T \approx 400\,\mathrm{pJ\,K^{-2}}$ and $\partial^2 M/\partial T^2 \approx -300\,\mathrm{kA\,m^{-1}\,K^{-2}}$.

An alternative configuration with a sensor height $h_{sen} = 2.0\,\mu\mathrm{m}$ (25% thicker) yields a comparable energy resolution $\Delta E_{FWHM} \approx 7.0\,\mathrm{eV}$ while reducing ζ_E/E by approximately 10%. A similar resolution can also be achieved without changing the sensor thickness by increasing the persistent current to $I_0 = 75\,\mathrm{mA}$ (25% higher), which reduces both ζ_E/E and ζ_T/T by

about 20%. This design may be preferred due to the significant reduction in non-linearity and temperature sensitivity while maintaining comparable energy resolution, though other factors such as operation at lower temperature must be considered.

These results can be compared to those expected for an asymmetric, single MMC with a high-impedance coil. While the flux coupling only slightly improves to $\partial\Phi_s/\partial\Phi_m \approx 0.05$, the noise PSD S decreases significantly due to the halved thermal and magnetic flux noise with only a single sensor. This improves the energy resolution to $\Delta E_{FWHM} \approx 5.0\,eV$. However, a single MMC with twice the volume to cover the same absorber area as before has a slightly reduced resolution of $\Delta E_{FWHM} \approx 7.5\,eV$ and is more prone to position-dependent effects due to slower thermalization. This demonstrates the advantages of using the double-meander geometry with symmetric MMCs to achieve a large active area. The results deviate from the fundamental limit $\Delta E_{FWHM} \approx 3.2\,eV$, indicating that the combined noise is not solely dominated by thermal energy noise.

3.9. Low Temperature Readout

The readout of MMCs requires highly sensitive magnetometers operating at mK temperatures, with a linear response, broad energy coverage, and low power dissipation. Readout circuits based on superconducting quantum interference devices (SQUIDs) meet these requirements and are widely used for the readout of low-temperature detectors [122, 130]. A SQUID is an extremely sensitive magnetometer, consisting of a superconducting loop interrupted by Josephson junctions [131].

Various readout schemes for MMCs have been developed, employing either dc- or rf-SQUIDs. Readout based on rf-SQUIDs enables frequency-domain multiplexing and has been demonstrated for small numbers of MMCs, showing the potential for scaling to several hundred detectors per radio-frequency readout chain [132–135]. Readout based on dc-SQUIDs achieves very low noise and is particularly well suited for high-resolution measurements with MMC arrays [9, 122].

An MMC can be equipped with an integrated SQUID readout, which directly detects the magnetic flux change near the sensor, or with a SQUID connected via a superconducting flux transformer. Integrated SQUID readout offers excellent flux coupling between sensor and SQUID, but requires complex fabrication and may lead to increased power dissipation near the MMC [124–126]. In contrast, using a superconducting flux transformer allows MMCs and SQUIDs to be fabricated separately. The transformer can be split into two parts, located on separate chips, and connected via bonding wires that become superconducting at cryogenic temperatures. Because MMCs and SQUIDs require different fabrication processes,

this separation simplifies production, enables independent verification of the components, and significantly improves overall yield.

The following introduces the readout of MMCs using a two-stage dc-SQUID circuit, where the input coil of the SQUID is part of a superconducting flux transformer. A detailed overview of SQUIDs, their operating principles, and applications can be found in dedicated literature [136, 137].

3.9.1. SQUID Characteristics

A dc-SQUID consists of a superconducting loop interrupted by two thin insulating barriers, known as Josephson junctions, which are represented by an X in circuit diagrams. These junctions are each shunted by a resistor and can be described by the resistively and capacitively shunted junction (RCSJ) model [138, 139]. The SQUIDs discussed here are practical, non-hysteretic, and optimized for MMC readout, with a modulation parameter $\beta_L \approx 0.7$ and a Stewart–McCumber parameter $\beta_C \approx 0.7$ [140–143].

A simple circuit containing a SQUID biased with a current I_s is shown in Figure 3.15 (left), while the corresponding characteristics are shown in Figure 3.14. The voltage across the SQUID, U_s, depends on both the bias current I_s and the magnetic flux Φ_s in the SQUID. A current ΔI flowing in a coil that is magnetically coupled to the SQUID induces a magnetic flux change $\Delta\Phi_s$ given by

$$\Delta\Phi_s = \Delta I \, M \tag{3.77}$$

where M is the mutual inductance between the coil and the SQUID. This inductance can be expressed as $M = k\sqrt{L_s L}$, where L is the inductance of the coil, L_s is the inductance of the SQUID, and k is the geometric coupling factor, with $0 \leq k \leq 1$.

For small bias currents I_s, Cooper pairs tunnel through the junctions as a supercurrent, resulting in zero voltage U_s across the SQUID. When the current exceeds a critical value I_c, the Cooper pairs alone cannot carry the full current. Some of them break up into quasiparticles, which tunnel through the junctions and contribute to the current, but lead to a non-zero voltage U_s drop. The critical current I_c depends on the magnetic flux Φ_s in the SQUID, which results in a periodic voltage response. The period is one flux quantum Φ_0, defined as

$$\Phi_0 = \frac{h}{2e} \tag{3.78}$$

$$\approx 2.07 \times 10^{-15}\,\mathrm{Wb} \tag{3.79}$$

where h is Planck's constant and e is the elementary charge. For a given bias current I_s, the voltage U_s reaches a maximum when Φ_s equals a half-integer multiple of the flux quantum

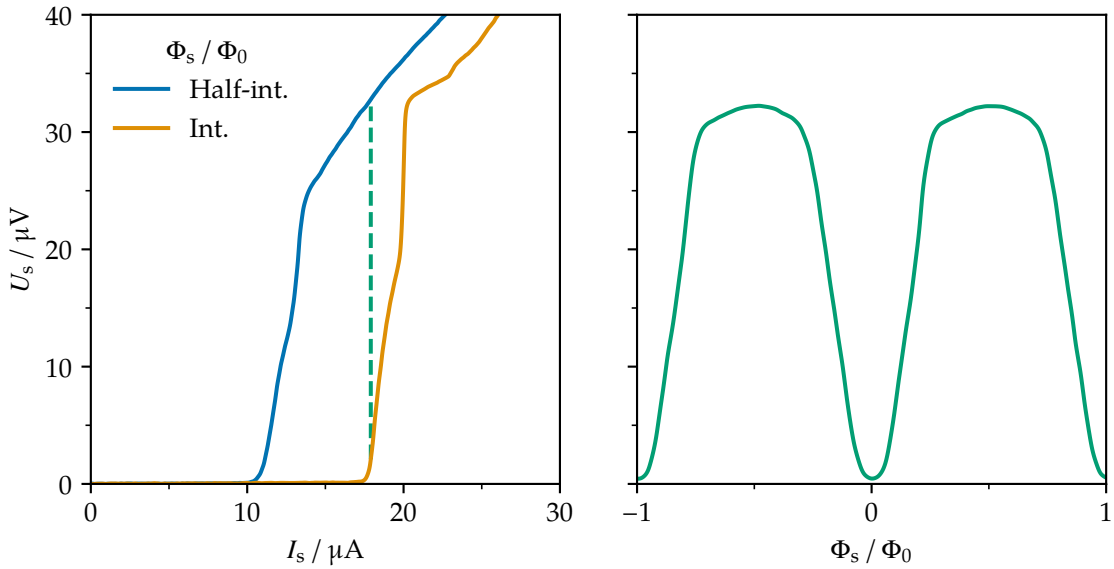

Figure 3.14.: Current–voltage characteristic (left) and flux–voltage characteristic (right) of a dc-SQUID. The characteristics are measured at a few mK in a dilution refrigerator for the SQUID 3A-06 c2 from HDSQ14 w1. The current–voltage curves are shown for magnetic flux values Φ_s at half-integer and integer multiples of the flux quantum Φ_0. The flux–voltage curve is shown for $I_s = 18\,\mu A$, where the voltage modulation $\Delta U_s = 32\,\mu V$ is maximal.

Φ_0 and a minimum at integer multiples. Intermediate values occur for other magnetic flux values. The maximum voltage modulation ΔU_s appears at a specific optimal I_s.

3.9.2. Flux-Locked-Loop Readout

When biased at its maximum voltage modulation, the response of a dc-SQUID is periodic and well defined only within a range of approximately $\Phi_0/2$. A flux-locked loop (FLL) circuit, shown in Figure 3.15, linearizes the response by regulating the magnetic flux Φ_f in the SQUID via feedback to maintain it at a constant value [136]. The SQUID containing the input coil is referred to as the front-end SQUID.

The difference between the voltage across the front-end SQUID, U_f, and the bias voltage U_b is amplified and integrated by room-temperature electronics to produce the output voltage U_{out}, which is then used for feedback. Via a feedback resistor R_{fb}, the output voltage U_{out} is converted to a current flowing through a feedback coil. The total flux change $\Delta\Phi_f$ in the front-end SQUID, induced by both the input and feedback coils, is given by

$$\Delta\Phi_f = \Delta I_{in}\, M_{in} - \frac{\Delta U_{out}}{R_{fb}}\, M_{fb} \tag{3.80}$$

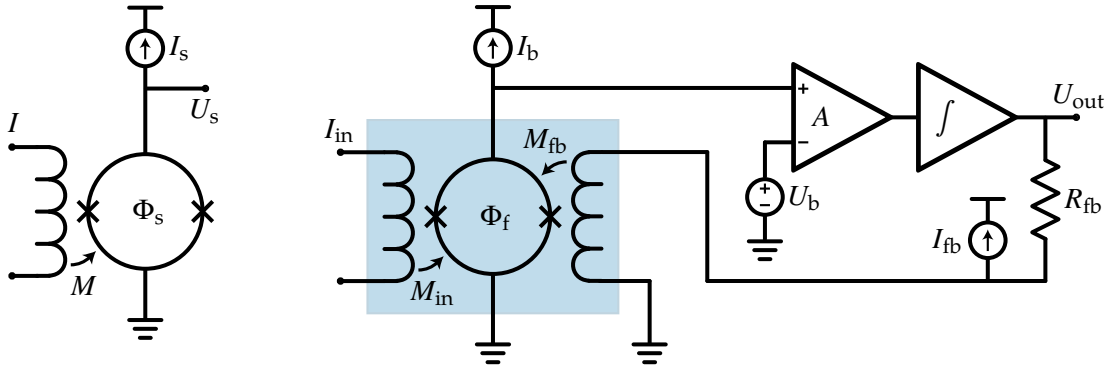

Figure 3.15.: A dc-SQUID biased at a current I_s (left), and a FLL readout circuit using a front-end SQUID (right). The voltage across the front-end SQUID (blue) is amplified and integrated by room-temperature electronics. The resulting output voltage U_{out} is used for feedback through a feedback coil to regulate the magnetic flux Φ_f to remain constant.

where M_{in} and M_{fb} are the mutual inductances of the input and feedback coils, respectively. The output voltage U_{out} remains constant when the integrator input is zero, which occurs when

$$U_f = U_b \tag{3.81}$$

so that the voltage U_f across the SQUID equals the bias voltage U_b. In this condition, the magnetic flux $\Delta\Phi_f = 0$ in the front-end SQUID is regulated, and a flux change from the input coil is compensated by a flux change from the feedback coil. This results in a linear response

$$\Delta U_{out} = -R_{fb} \frac{M_{in}}{M_{fb}} \Delta I_{in} \tag{3.82}$$

where the change in output voltage ΔU_{out} is directly proportional to the input current I_{in}. While M_{in} and M_{fb} are fixed for a given front-end SQUID, the proportionality factor can be adjusted via the feedback resistor R_{fb}.

The front-end SQUID is operated at a fixed point on its voltage–flux characteristic, called the working point, where the voltage across the SQUID equals the bias voltage $U_f = U_b$. Within one flux quantum Φ_0, two working points with opposite slope polarity exist. Depending on the polarity of the feedback loop, one of them is stable while the other is unstable. The working point is set by tuning the bias current I_b and bias voltage U_b. These are usually adjusted to ensure that the voltage per magnetic flux $\partial U_f / \partial \Phi_f$ is maximized, which typically corresponds to a bias current I_b giving the largest voltage modulation ΔU_f and a bias voltage U_b centering the flux–voltage characteristic. Without changing the working point, the offset of the output voltage U_{out} can be tuned via the feedback current I_{fb}.

While the working point does not affect the linear gain of the circuit $\partial U_{\mathrm{out}}/\partial I_{\mathrm{in}}$, it has a significant impact on stability and noise. A working point with high voltage per magnetic flux $\partial U_{\mathrm{f}}/\partial \Phi_{\mathrm{f}}$ yields low noise. However, the bias settings should be further optimized to minimize the noise. For the circuit to remain stable, a working point with $U_{\mathrm{f}} = U_{\mathrm{b}}$ must exist. If the feedback becomes positive, for example due to phase shifts introduced by the feedback delay at high frequencies, the circuit may become unstable. To ensure negative feedback, the bandwidth of the circuit must be limited. The maximum bandwidth is determined by the loop gain and the feedback delay, which also limit the maximal slew rate that the feedback circuit can handle during rapid flux changes. Beyond this rate, the front-end SQUID is only stable for instantaneous magnetic flux changes $\Delta\Phi_{\mathrm{f}}$ up to $\Phi_0/2$, and may otherwise jump to another stable working point separated by a multiple of Φ_0. If the circuit switches to another working point, resetting the integrator of the FLL circuit can help to restore the original one.

3.9.3. Two-Stage Readout

A single-stage FLL readout is limited by the noise of the room-temperature electronics and may suffer from the relatively high power dissipation of the front-end SQUID. A second stage with a large magnetic flux dependence can be introduced to significantly amplify the signal at low temperatures. The overall noise is then no longer dominated by the room-temperature electronics but by the SQUID noise. A schematic of a two-stage FLL readout circuit is shown in Figure 3.16. The circuit has the same response as the single-stage circuit: the magnetic flux Φ_{f} in the front-end SQUID is regulated to be constant, and equation (3.82) remains valid.

The front-end SQUID is operated at constant voltage bias U_{f} using a small gain resistor R_{g} that converts the bias current I into an effective voltage source. Since the gain resistor R_{g} is much smaller than the dynamic resistance of the front-end SQUID, the voltage across the SQUID remains nearly constant. A current source I with a gain resistor R_{g} at cryogenic temperatures is used to avoid thermoelectric voltages and temperature-dependent resistance from the wiring. Voltage biasing the front-end significantly reduces power dissipation near the SQUID input coil.

A magnetic flux change $\Delta\Phi_{\mathrm{f}}$ in the front-end SQUID induces a current change I_{f}, which, through the mutual inductance M_{a}, produces a flux change Φ_{a} in the SQUID array. The second stage consists of N dc-SQUIDs connected in series. If all SQUIDs are identical and experience the same magnetic flux, the SQUID array behaves like a single SQUID with a voltage response U_{a} that is N times larger. The uncorrelated noise of the array scales with $\sqrt{N}$, assuming equal noise contributions from each SQUID. The SQUID array and the gain resistor dissipate considerably more power and can therefore be placed away from the front-end SQUID.

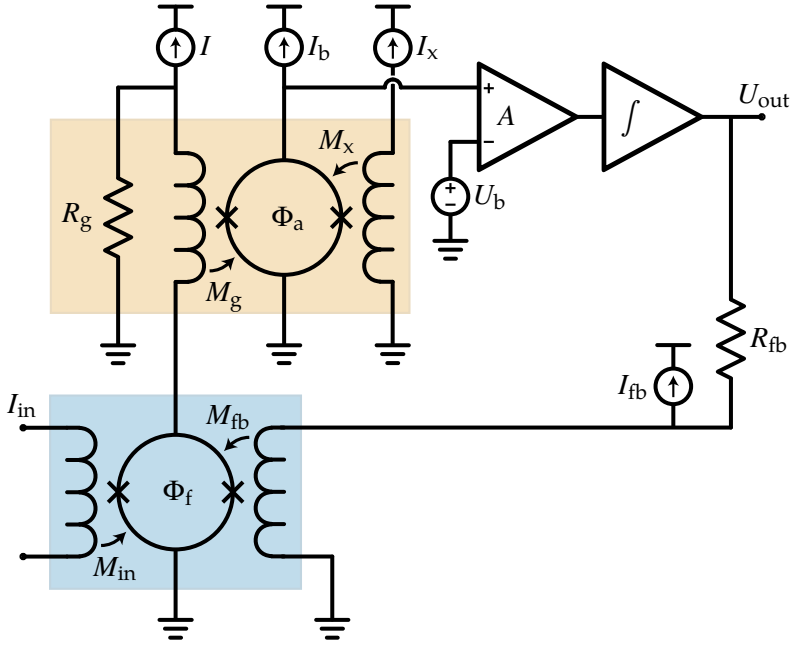

Figure 3.16.: Two-stage FLL readout circuit. The front-end SQUID (blue) is voltage-biased to reduce the power dissipation near the input coil. The second stage is a SQUID array (orange), operated at a constant bias current I_b and having a large magnetic flux dependence.

The working point of the circuit is defined by the parameters I, I_b, I_x, and U_b. These are tuned so that the operating point $U_a = U_b$ maximizes the magnetic flux dependence $\partial U_a/\partial \Phi_f$ across both stages. The flux–voltage characteristics of the front-end SQUID and SQUID array without feedback are shown in Figure 3.17. The SQUID array is biased similarly to a front-end SQUID in a single-stage circuit, where the bias current I_b is chosen to yield the maximum voltage modulation ΔU_a, and the bias voltage U_b is set so that the flux–voltage characteristic is centered at zero.

Subsequently, the current I is adjusted to maximize the current modulation ΔI_f of the front-end, while the phase is tuned via the current I_x to center the flux modulation in the array around zero. The phase between the two stages should be tuned such that only two zero-crossings occur within one flux quantum Φ_0 of magnetic flux change Φ_f in the front-end SQUID—one positive and one negative—with $U_a = U_b$. Otherwise, multiple working points may exist, leading to unstable operation and noise fluctuations due to transitions between working points.

The current modulation ΔI_f must be limited so that the induced flux modulation $\Delta \Phi_a$ in the array does not exceed a flux quantum Φ_0, which would invariably result in multiple working points. If necessary, the bias current I of the front-end SQUID can be reduced to lower the current modulation ΔI_f and thus the power dissipation of the front-end. The mutual

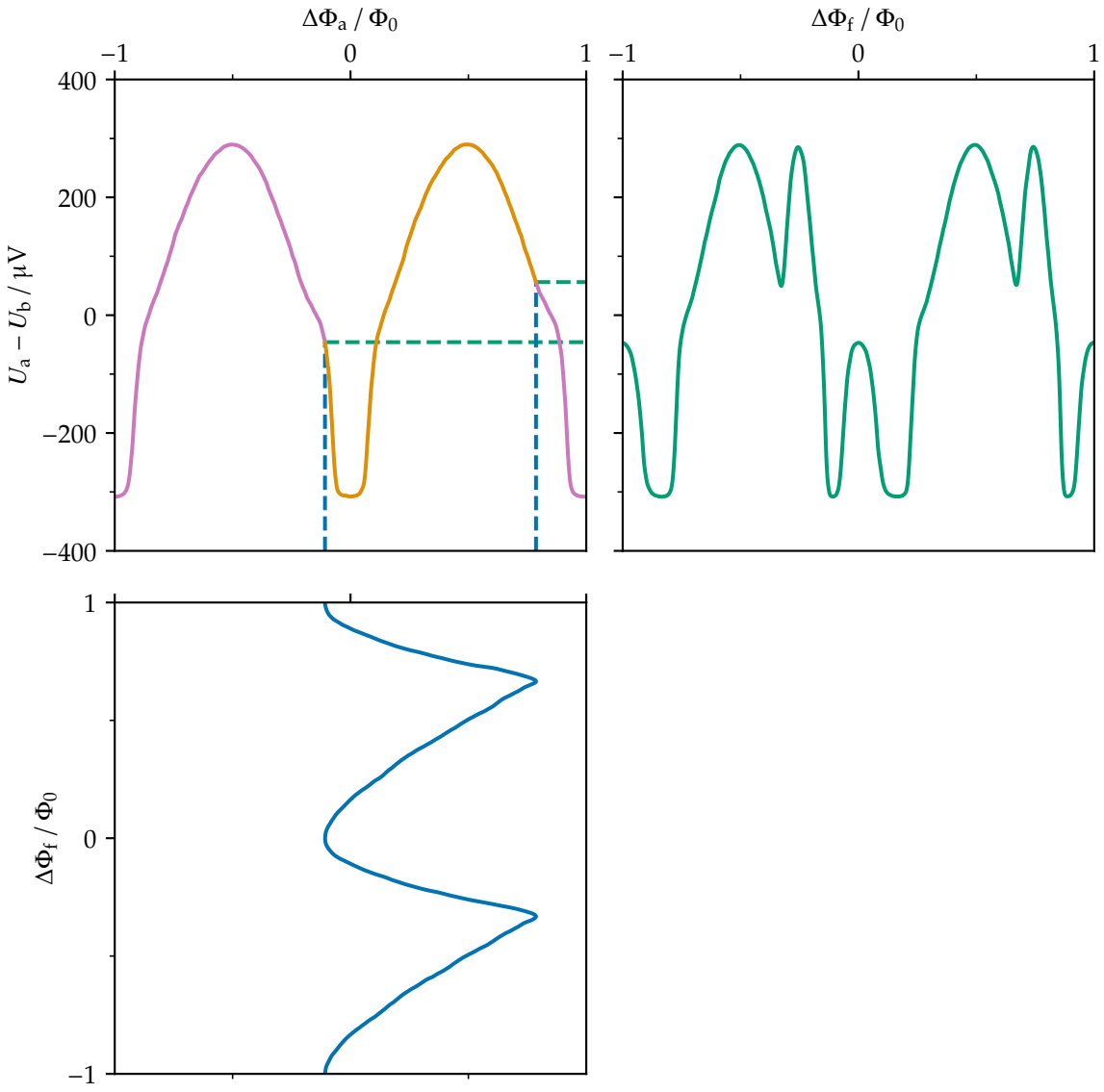

Figure 3.17.: Flux–voltage characteristics of the SQUID array (top, left) and front-end SQUID (top, right) as well as the flux coupling between the two stages (bottom, left), for a two-stage circuit without feedback. Measurements were taken at a few mK in a dilution refrigerator for front-end SQUID 4A-06 c1 and SQUID array 1D-11 ch1 from HDSQ14 w1. The flux coupling between the two stages is reconstructed from the two characteristics. The front-end SQUID induces a flux modulation $\Delta\Phi_a$ in the array slightly below one flux quantum Φ_0. The array has a voltage modulation $\Delta U_a = 600\,\mu V$.

inductance M_a must therefore be matched to the expected current modulation ΔI_f of the front-end SQUID to optimize the coupling between the two stages.

3.9.4. MMC Readout

The available Heidelberg SQUID (HDSQ) SQUIDs, developed and produced in Heidelberg, are specifically optimized for MMC readout [122]. The readout is based on the two-stage FLL circuit, with the front-end SQUID and the SQUID array, together with the gain resistor R_g, fabricated on separate chips to minimize power dissipation near the MMC [140].

The front-end SQUIDs, with 4 readout channels per chip, are designed for low-inductance MMCs. They feature an input coil inductance of $L_{in} = 1.2\,\mathrm{nH}$, an input coil mutual inductance of $M_{in}^{-1} = 8.9\,\mu\mathrm{A}\,{\Phi_0}^{-1}$, and a feedback coil mutual inductance of $M_{fb}^{-1} = 43\,\mu\mathrm{A}\,{\Phi_0}^{-1}$ [140–143]. The second stage consists of SQUID arrays, with 2 readout channels per chip, each containing $N = 16$ dc-SQUIDs in series, and having mutual inductances of $M_a^{-1} = M_x^{-1} = 12\,\mu\mathrm{A}\,{\Phi_0}^{-1}$ [122, 140]. With a feedback resistor of $R_{fb} = 100\,\mathrm{k\Omega}$, the circuit achieves an overall amplification of $\partial U_{out}/\partial \Phi_f \approx 4.3\,\mathrm{V}\,{\Phi_0}^{-1}$, or equivalently $\partial U_{out}/\partial I_{in} \approx 0.48\,\mathrm{V}\,\mu\mathrm{A}^{-1}$. The typical bandwidth is $f_c \approx 500\,\mathrm{kHz}$ with a loop gain of approximately 10 000. Typical bias parameters are $I = 10\,\mu\mathrm{A}$, $I_b = 15\,\mu\mathrm{A}$, and $U_b = 300\,\mu\mathrm{V}$, while I_x depends on the external magnetic flux and I_{fb} is used as an arbitrary voltage offset. The corresponding current modulation of the front-end SQUID is $\Delta I_f = 10\,\mu\mathrm{A}$, while the typical voltage modulation of the SQUID array is $\Delta U_a = 600\,\mu\mathrm{V}$.

Chapter 4.

Detector Development

High-resolution X-ray spectroscopy of muonic atoms with QUARTET requires optimized MMC-based detector arrays. These detectors must provide excellent energy resolution, sufficient quantum efficiency, and reliable energy calibration at the characteristic muonic $2p$–$1s$ transition energies of the various nuclei, in order to determine the transition energies with a targeted accuracy of about 2 ppm. In addition, the detectors must operate reliably in the beamline environment, which is characterized by a high flux of high-energy Michel electrons from muon decays. These electrons pass through the detector and deposit energy via ionization and bremsstrahlung along their paths. Their flux slightly exceeds that of the muonic $2p$–$1s$ X-rays and also affects non-sensitive regions of the detector, particularly by depositing energy in the detector substrate.

Several MMC-based detector arrays have been optimized, designed, fabricated, and characterized at the Kirchhoff-Institute for Physics (KIP) in Heidelberg in recent years. Detectors developed for high-resolution X-ray and γ-ray spectroscopy are referred to as microcalorimeter array for X-ray spectroscopy (maXs)-type detectors and typically consist of two-dimensional arrays of gradiometric MMCs in the double meander geometry [73, 129, 144, 145]. Among these, the *maXs 30-v2b* detector [144, 145] achieves an FWHM energy resolution of up to $\Delta E_{\mathrm{FWHM}} \approx 7\,\mathrm{eV}$ at 6 keV [1, 146], and up to $\Delta E_{\mathrm{FWHM}} \approx 10\,\mathrm{eV}$ at 60 keV [145]. Its absorbers, with a thickness of $h_{\mathrm{abs}} = 20\,\mu\mathrm{m}$, provide sufficient quantum efficiency for measurements of the muonic $2p$–$1s$ transitions in Li, Be, and B [2]. However, new detectors optimized for high-resolution X-ray spectroscopy of muonic atoms, with a chip size and active area comparable to those of the *maXs 30-v2b* detector, are required to meet the accuracy goals of QUARTET. In particular, they must achieve high energy resolution also at higher X-ray energies, operate reliably at increased event rates, and be less susceptible to energy deposition from Michel electrons. Furthermore, they should feature temperature-sensitive channels capable of detecting energy deposited in the detector substrate, in order to identify and discriminate Michel electron-related events.

This chapter presents the detector development for QUARTET. It introduces the *maXs 30-v2b* detector [144, 145] and the detector module [1, 2, 146] used during the first proof of principle run and subsequently in the dedicated data run with Li, Be, and B. A new detector

design is developed and optimized specifically for high-resolution X-ray spectroscopy of muonic atoms, with different absorber heights considered for the various nuclei. For the dedicated data run, three wafers based on this design were fabricated with an absorber height of $h_{\mathrm{abs}} = 25\,\mu\mathrm{m}$, but fabrication-related issues made them unusable for the experiment.

4.1. maXs 30-v2b

The *maXs 30-v2b* detector is based on the design of the *maXs 30* detector. The *maXs 30* is a two-dimensional MMC-based detector array with 64 pixels arranged in an 8×8 layout, optimized for high-resolution X-ray spectroscopy up to 30 keV, and developed for experiments with highly charged ions at the Experimental Storage Ring at the GSI Helmholtzzentrum für Schwerionenforschung [144]. The *maXs 30-v2b* is a further developed version of the *maXs 30* detector, optimized for measuring the isomer energy of ^{229}Th [145]. A detector chip from the same wafer is used in the QUARTET setup [1, 2]. The optimization, design, and fabrication of the *maXs 30* detectors are described in detail in the corresponding works [144, 145].

4.1.1. Detector Parameters

A focus-stacked photograph of the *maXs 30-v2b* detector setup used for QUARTET, with the detector chip visible at the center, is shown in Figure 4.1. The detector has a square outline with a side length of 8 mm and consists of four rotationally symmetric quadrants. All four edges of the chip are equipped with bonding pads for the SQUID readout. The corners include additional bond pads for the field and heater lines of each quadrant, which are used to prepare the persistent current. Each corner also contains bond pads for a test heater that can apply thermal pulses to a pixel in the corresponding quadrant. Four mechanical press pads are located in the corners to enable clamping of the detector chip. At the center, the detector features a square active area, with a side length of 4 mm, featuring 64 pixels arranged in an 8×8 array. Each pixel contains a square gold absorber with a side length of 500 µm and a thickness of 20 µm. Every two pixels form an MMC channel in a double meander geometry, resulting in 32 channels in total. Of these, 28 are symmetric and thus gradiometric, while the 4 channels located at the corners of the array are asymmetric. Each of these four asymmetric channels includes one pixel with a smaller temperature sensor. This causes their signal offsets to become temperature-dependent, allowing them to track the detector temperature. These offsets can be used to correct temperature-induced variations in the pulse height of the other detector pixels. The most relevant parameters of the *maXs 30-v2b* detector, optimized for operation at 25 mK, are summarized in Table 4.1.

The small detector chip uses the full set of the currently available 32 SQUID readout channels [147], while remaining compact and efficiently utilizing the surrounding area for

Table 4.1.: Parameters of the *maXs 30-v2b* detector optimization. The design parameters are based on the corresponding work [145], while other parameters were obtained from new simulations.

General		**Superconducting Coil**	
Temperature	$T_0 = 25\,\mathrm{mK}$	Height	250 nm
Persistent current	$I_0 = 90\,\mathrm{mA}$	Insulation thickness	300 nm
Heat capacity	$C = 21\,\mathrm{pJ\,K^{-1}}$	Pitch	$p = 10\,\mu\mathrm{m}$
Rise time	$\tau_r = 10\,\mu\mathrm{s}$	Line width	$w = 5\,\mu\mathrm{m}$
Decay time	$\tau_d = 3\,\mathrm{ms}$	Inductance	$L_\mathrm{m} \approx 2.5\,\mathrm{nH}$
Particle Absorber		**SQUID Readout**	
Material	Au	Input inductance	$L_\mathrm{in} \approx 1.2\,\mathrm{nH}$
Height	$h_\mathrm{abs} = 20\,\mu\mathrm{m}$	Parasitic inductance	$L_\mathrm{p} \approx 0.3\,\mathrm{nH}$
Side length	$a_\mathrm{abs} = 500\,\mu\mathrm{m}$	**Performance**	
Heat capacity	$C_\mathrm{abs} = 8.9\,\mathrm{pJ\,K^{-1}}$	Flux generation	$\partial\Phi_\mathrm{m}/\partial E \approx 0.30\,\Phi_0\,\mathrm{keV^{-1}}$
Paramagnetic Sensor		Flux coupling	$\partial\Phi_\mathrm{s}/\partial\Phi_\mathrm{m} \approx 42\times10^{-3}$
Material	Ag:Er	Energy resolution	$\Delta E_\mathrm{FWHM} \approx 6.0\,\mathrm{eV}$
Er concentration	$x_\mathrm{Er} = 430\,\mathrm{ppm}$	Temperature sensitivity	$\zeta_T/T \approx -40\times10^{-3}\,\mathrm{mK^{-1}}$
Height	$h_\mathrm{sen} = 1.5\,\mu\mathrm{m}$	Nonlinearity	$\zeta_E/E \approx -0.16\times10^{-3}\,\mathrm{keV^{-1}}$
Side length	$a_\mathrm{sen} = 300\,\mu\mathrm{m}$		
Heat capacity	$C_\mathrm{sen} = 12\,\mathrm{pJ\,K^{-1}}$		

electronic connections. This design results in a reduced cross section for high-energy Michel electrons. The ratio of active area to total chip area is approximately 1/4, which is relatively large compared to other MMC-based detectors. The 20 µm thick absorbers yield detector efficiencies of approximately 97 %, 59 %, and 22 % for the muonic $2p$–$1s$ transitions of Li, Be, and B at 18.7 keV, 33.4 keV, and 52.3 keV, respectively [2]. The detector achieves an excellent FWHM energy resolution of $\Delta E_\mathrm{FWHM} \approx 10\,\mathrm{eV}$ at 60 keV [145].

The thermal design of the detector originally included small thermal vias, also referred to as through-silicon vias (TSVs), which are metallic connections through the wafer intended for thermalization. These metal-filled holes, with a diameter of 70 µm, were designed to couple the thermal bath of each MMC channel to a dedicated thermalization layer with large heat capacity on the backside of the detector chip. However, the *maXs 30-v2b* detector used here does not contain such thermal vias, as their fabrication had not yet been fully developed. As a result, the individual thermal baths have low heat capacity compared to the individual pixels and are also not thermally connected to each other, leading to slow thermalization. First, the two pixels of each pixel pair thermalize with each other on a timescale of about 3 ms, and then with the substrate on a much longer timescale of approximately 300 ms [146]. This long secondary decay time does not directly affect the energy resolution but significantly limits the maximum count rate and makes the detector susceptible to energy deposition in

the substrate. High-energy Michel electrons can deposit energy in the substrate, heating all pixels simultaneously and causing extended dead times across the entire detector.

4.1.2. Detector Module

The detector module used for QUARTET was originally assembled for the *IAXO* experiment to investigate the background rate of an MMC-based detector array in earlier work [1, 146]. A focus-stacked photograph of the module, including the front-end SQUID readout, is shown in Figure 4.1. The detector, along with eight front-end SQUIDs, is glued onto a copper platform. Aluminium bonding wires connect the chips to each another and to polyimide circuit boards, which connect to the second-stage SQUID readout. The module was fully characterized in previous work [1, 146].

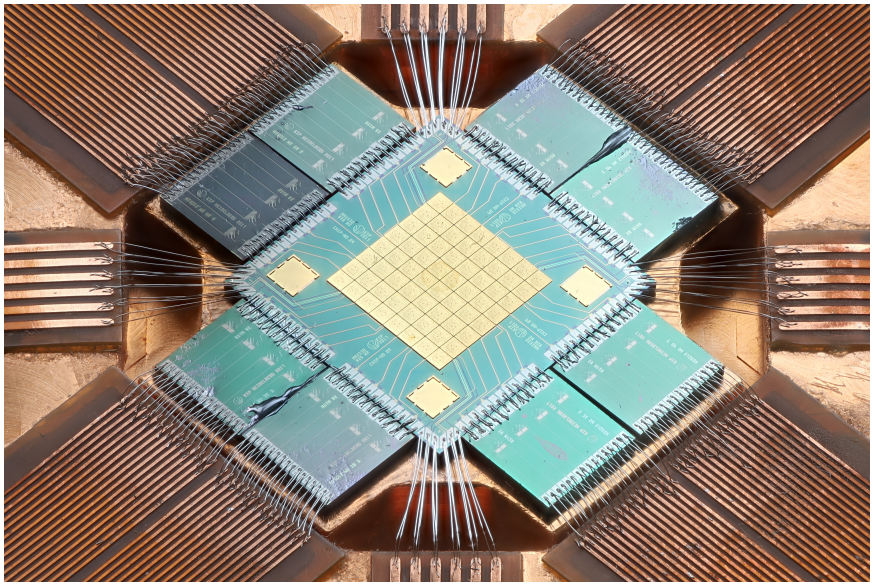

Figure 4.1.: Focus-stacked photograph of the *maXs 30-v2b* detector setup used in the QUARTET experiment. The detector is mounted on a copper platform alongside eight front-end SQUID chips. Electrical connections are made using aluminium bonding wires.

At a detector temperature of approximately 17 mK, an average FWHM energy resolution of $\Delta E_{\mathrm{FWHM}} = 7\,\mathrm{eV}$ was achieved at 6 keV, and approximately $\Delta E_{\mathrm{FWHM}} \approx 20\,\mathrm{eV}$ at 60 keV [1, 146]. Subsequently, as part of this thesis, a FWHM energy resolution of up to $\Delta E_{\mathrm{FWHM}} \approx 12\,\mathrm{eV}$ was achieved at 60 keV using the same setup. Of the 32 detector channels, only one is non-functional due to a damaged front-end SQUID, while the remaining channels are operational, assuming a functional second-stage SQUID readout. A brief description of the detector module used for QUARTET is also provided in a recent publication [2].

4.2. maXs 30-56-14

A new detector design has been developed and optimized specifically for high-resolution X-ray spectroscopy of muonic atoms. Since the *maXs 30* chip geometry already maximizes both the number of available readout channels and the active area on a compact detector chip, the new design retains the same geometry and remains fully compatible with existing *maXs 30* detector platforms. It shares the same chip dimensions, electrical interfaces, active area, and mechanical press pads as previous *maXs 30* detectors. As the detector setup is optimized for lower operating temperatures, it is primarily designed to operate at 20 mK, although its performance at even lower temperatures is also considered.

The detectors fabricated for the first data run with Li, Be, and B are referred to as *maXs 30-56-14*, following the standard maXs naming convention. In this scheme, the first number denotes the energy range in keV, the second the number of pixels used for X-ray spectroscopy, and the third the active area in units of mm^2. According to this naming convention, the *maXs 30-v2b* detector corresponds to *maXs 30-64-16*.

4.2.1. Detector Optimization

The design parameters of the new detector were initially optimized to achieve good energy resolution ΔE_{FWHM} within a parameter region constrained by detector requirements and fabrication limitations. A previously developed simulation script [85], which interpolates and integrates over the sensor volume, was used to scan a broad parameter space and iteratively determine suitable design values.

This script relies on sensor simulations, previously shown in Figure 3.4, which are based on earlier simulation methods [85, 108]. It also requires magnetic field simulations of the meander coil, which were performed using the software *FEMM*. The magnetic field simulations for the chosen design parameters were presented earlier in Figure 3.12, although additional parameter sets were also simulated and evaluated during the optimization process. For calculating the SQUID and erbium noise contributions, the parameters introduced in the previous chapter are used. The final optimized design parameters are summarized in Table 4.2, and are computed using the same procedure described previously.

Optimization Process

For the optimization, an initial Au absorber with a thickness of $h_{\mathrm{abs}} = 20\,\mu\mathrm{m}$ and an operating temperature of $T_0 = 20\,\mathrm{mK}$ are assumed. Together with the requirement to match the geometry of the existing *maXs 30* detectors, this sets the absorber side length to $a_{\mathrm{abs}} = 470\,\mu\mathrm{m}$ in order to maintain the same pixel grid while also accounting for a $30\,\mu\mathrm{m}$ gap between adjacent absorbers. This defines the absorber heat capacity as $C_{\mathrm{abs}} = 6.3\,\mathrm{pJ\,K^{-1}}$.

Table 4.2.: Parameters of the *maXs 30-56-14* detector optimization for achieving the best energy resolution ΔE_{FWHM} at the given temperature T_0. The energy resolution at non-zero energies can be significantly improved by increasing the persistent current I_0.

General	
Temperature	$T_0 = 20\,\mathrm{mK}$
Persistent current	$I_0 = 50\,\mathrm{mA}$
Heat capacity	$C = 14\,\mathrm{pJ\,K^{-1}}$
Rise time	$\tau_r = 15\,\mu\mathrm{s}$
Decay time	$\tau_d = 5\,\mathrm{ms}$
Rise conductance	$G_\mathrm{r} = 230\,\mathrm{nW\,K^{-1}}$
Decay conductance	$G_\mathrm{d} = 2.8\,\mathrm{nW\,K^{-1}}$
Particle Absorber	
Material	Au
Height	$h_\mathrm{abs} = 20\,\mu\mathrm{m}$
Side length	$a_\mathrm{abs} = 470\,\mu\mathrm{m}$
Heat capacity	$C_\mathrm{abs} = 6.3\,\mathrm{pJ\,K^{-1}}$
RRR	≈ 15
Thermalization	$\tau_\mathrm{abs} \approx 2.3\,\mu\mathrm{s}$
Paramagnetic Sensor	
Material	Ag:Er
Concentration	$x_\mathrm{Er} = 550\,\mathrm{ppm}$
Height	$h_\mathrm{sen} = 1.0\,\mu\mathrm{m}$
Side length	$a_\mathrm{sen} = 270\,\mu\mathrm{m}$
Heat capacity	$C_\mathrm{sen} = 7.7\,\mathrm{pJ\,K^{-1}}$
RRR	2.4
Thermalization	$\tau_\mathrm{sen} \approx 5.4\,\mu\mathrm{s}$

Superconducting Coil	
Height	250 nm
Insulation thickness	300 nm
Pitch	$p = 7\,\mu\mathrm{m}$
Line width	$w = 3.5\,\mu\mathrm{m}$
Critical current	$I_\mathrm{c} \approx 100\,\mathrm{mA}$
Inductance	$L_\mathrm{m} \approx 2.9\,\mathrm{nH}$
SQUID Readout	
Input inductance	$L_\mathrm{in} \approx 1.2\,\mathrm{nH}$
Parasitic inductance	$L_\mathrm{p} \approx 0.3\,\mathrm{nH}$
Performance	
Flux generation	$\partial\Phi_\mathrm{m}/\partial E \approx 0.43\,\Phi_0\,\mathrm{keV^{-1}}$
Flux coupling	$\partial\Phi_\mathrm{s}/\partial\Phi_\mathrm{m} \approx 40 \times 10^{-3}$
Energy resolution	$\Delta E_\mathrm{FWHM} \approx 4.0\,\mathrm{eV}$
Temperature sensitivity	$\zeta_T/T \approx -51 \times 10^{-3}\,\mathrm{mK^{-1}}$
Nonlinearity	$\zeta_E/E \approx -0.29 \times 10^{-3}\,\mathrm{keV^{-1}}$

A fabrication constraint is imposed by the available sensor material. At the time of the optimization, Ag:Er with an erbium concentration of $x_{\mathrm{Er}} = 550(20)$ ppm was available, and the detector was therefore designed for this concentration. The sensor must be smaller than the absorber to accommodate the required wiring and persistent current switches beneath it. A sensor side length of $a_{\mathrm{sen}} = 270\,\mu\mathrm{m}$ just provides sufficient space to incorporate thermal vias (TSVs) with a large diameter of 200 µm diagonally between the pixels, which were feasible to fabricate at the time. The sensor width sets the size of the planar coil beneath it. The standard fabrication processes are optimized for a coil height of 250 nm and an insulation thickness of 300 nm above the coil. To match the inductance of the SQUID input coil $L_{\mathrm{in}} \approx 1.2(1)\,\mathrm{nH}$ and the parasitic inductance from wiring and bonding $L_{\mathrm{p}} \approx 0.3(1)\,\mathrm{nH}$ to the two coils of the double meander geometry, a pitch of $p = 7\,\mu\mathrm{m}$ and a line width of $w = 3.5\,\mu\mathrm{m}$ yield a suitable meander inductance of $L_{\mathrm{m}} \approx 2.9(2)\,\mathrm{nH}$. Such a superconducting coil can be reliably fabricated from Nb, and the corresponding critical current is expected to be approximately $I_{\mathrm{c}} \approx 100\,\mathrm{mA}$ for the given line width.

For this parameter set, the sensor height h_{sen} and persistent current I_0 are optimized. A grid search yields $h_{\mathrm{sen}} \approx 1.0\,\mu\mathrm{m}$ and $I_0 \approx 50\,\mathrm{mA}$, which remains well below the expected critical current of the superconducting coil. This fully defines the sensor, which has a heat capacity of $C_{\mathrm{sen}} = 7.7\,\mathrm{pJ\,K^{-1}}$, resulting in a total detector heat capacity of $C = 14\,\mathrm{pJ\,K^{-1}}$. The expected RRR values of the absorber and sensor allow an estimate of their thermalization times. A sputtered Ag:Er sensor with RRR = 2.4 yields a thermalization time constant of $\tau_{\mathrm{sen}} \approx 5.4\,\mu\mathrm{s}$ for the given side length and thickness. An electroplated Au absorber with RRR ≈ 15 yields $\tau_{\mathrm{abs}} \approx 2.3\,\mu\mathrm{s}$. A suitable rise time is $\tau_r = 15\,\mu\mathrm{s}$, approximately three times the sensor thermalization time, and a decay time of $\tau_d = 5\,\mathrm{ms}$ is chosen to be roughly 300 times longer. This requires a thermal conductance between sensor and absorber of $G_{\mathrm{d}} = 2.8\,\mathrm{nW\,K^{-1}}$ and a conductance from the absorber to the thermal bath of $G_{\mathrm{r}} = 230\,\mathrm{nW\,K^{-1}}$.

The now fully defined detector parameters yield a flux generation of $\partial\Phi_{\mathrm{m}}/\partial E \approx 0.43\,\Phi_0\,\mathrm{keV^{-1}}$ and a flux coupling of $\partial\Phi_{\mathrm{s}}/\partial\Phi_{\mathrm{m}} \approx 40 \times 10^{-3}$. The corresponding noise spectrum is shown in Figure 4.2, which, combined with the responsivity, yields an expected energy resolution of approximately $\Delta E_{\mathrm{FWHM}} \approx 4.0\,\mathrm{eV}$. The relative temperature sensitivity $\zeta_T/T \approx -51 \times 10^{-3}\,\mathrm{mK^{-1}}$ and relative nonlinearity $\zeta_E/E \approx -0.29 \times 10^{-3}\,\mathrm{keV^{-1}}$ were not optimized and are considered later. Nevertheless, this detector design achieves an improved energy resolution compared to the *maXs 30-v2b*, though its higher temperature sensitivity is yet expected to limit its performance at higher X-ray energies.

Absorber Thickness

The absorber thickness does not directly influence most of the design parameters. The absorber side length a_{abs} is fixed by the *maXs 30* geometry, while the sensor side length $a_{\mathrm{sen}} = 270\,\mu\mathrm{m}$ is

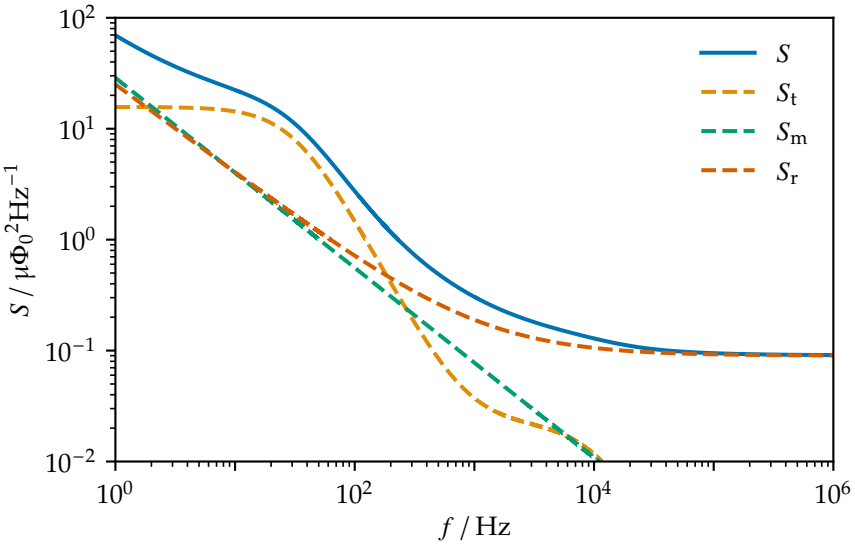

Figure 4.2.: Simulated noise power spectral density S of the *maXs 30-56-14* detector, expressed as flux noise Φ_s with contributions from thermal energy noise S_t, magnetic flux noise S_m, and readout noise S_r.

constrained by the diameter of the thermal vias. A design based on the achieved parameters which is optimized for X-ray spectroscopy of muonic atoms, can be adapted to different energy regions by adjusting the absorber height. Consequently, a suitable sensor height h_sen and persistent current I_0 can be determined to optimize the energy resolution ΔE_FWHM for each absorber height h_abs. The results for different absorber heights are shown in Figure 4.3. Given the relatively small absorber side length, high energy resolution can be achieved even for thick absorbers.

Based on the achievable energy resolution ΔE_FWHM for different absorber heights and the corresponding temperature sensitivity ζ_T/T, the energy resolution at higher energies can be estimated. The FWHM energy resolution is typically given at zero energy and calculated from the NEP. However, uncorrected temperature fluctuations, even after compensating for temperature-induced amplitude variations, introduce an additional energy-dependent uncertainty. The relative amplitude uncertainty ζ_T from temperature fluctuations σ_T contributes quadratically to the total energy resolution,

$$\Delta E_\mathrm{FWHM}(E) = 2\sqrt{2\ln 2}\sqrt{\sigma_E^2 + (\zeta_T\, E)^2} \tag{4.1}$$

where $\sigma_E = \Delta E_\mathrm{FWHM}/(2\sqrt{2\ \ln\ 2})$ is the RMS energy resolution at zero energy. These non-correctable temperature fluctuations limit the energy resolution at higher energies and thus limit the achievable resolving power. Based on previously characterized detectors, a typical un-

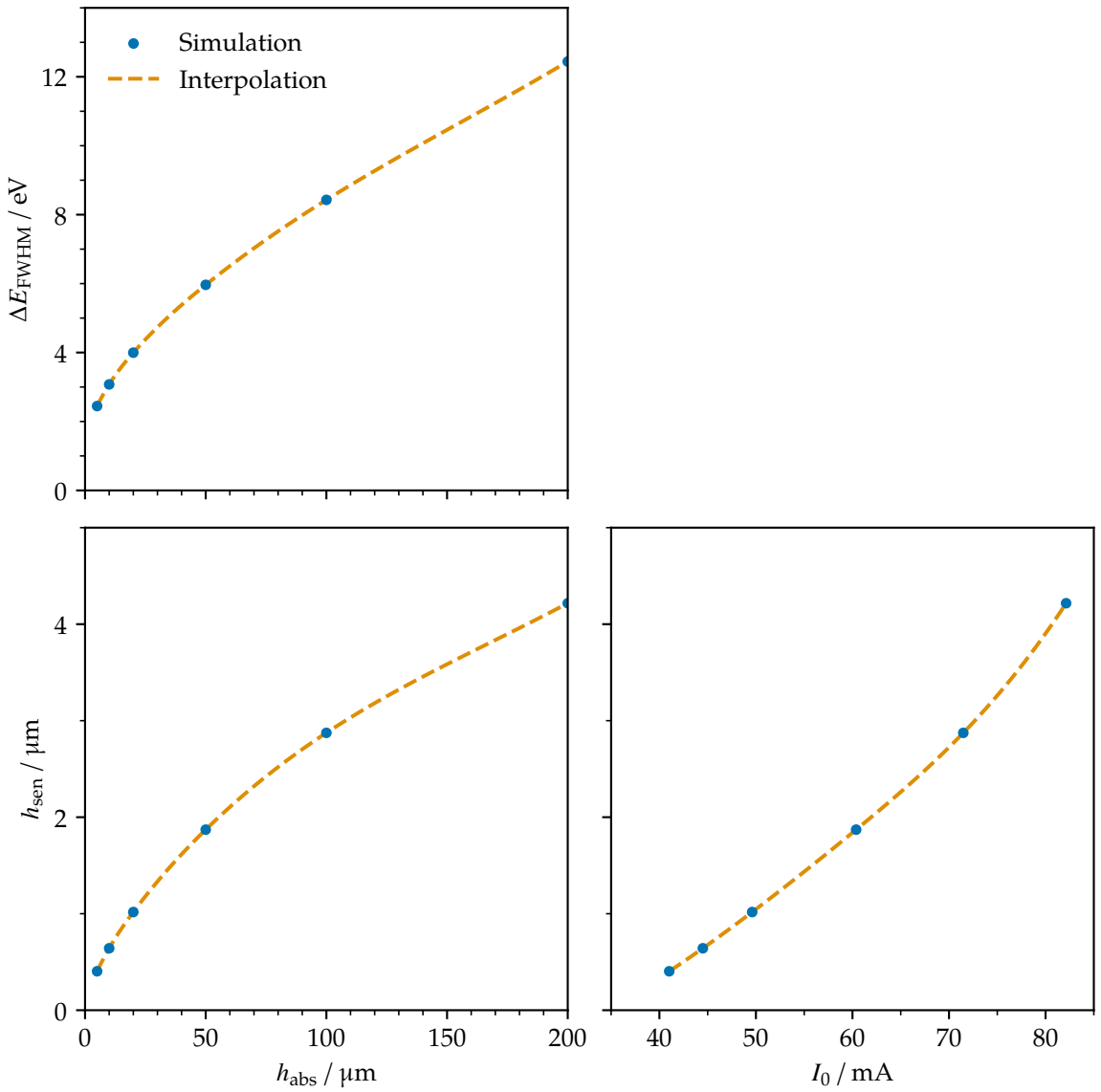

Figure 4.3.: Optimized FWHM energy resolution (top left), the corresponding sensor height h_{sen} (bottom left), and persistent current I_0 (bottom right) for different absorber heights h_{abs}. Each point represents an individually optimized parameter set, while the dashed lines represent interpolations.

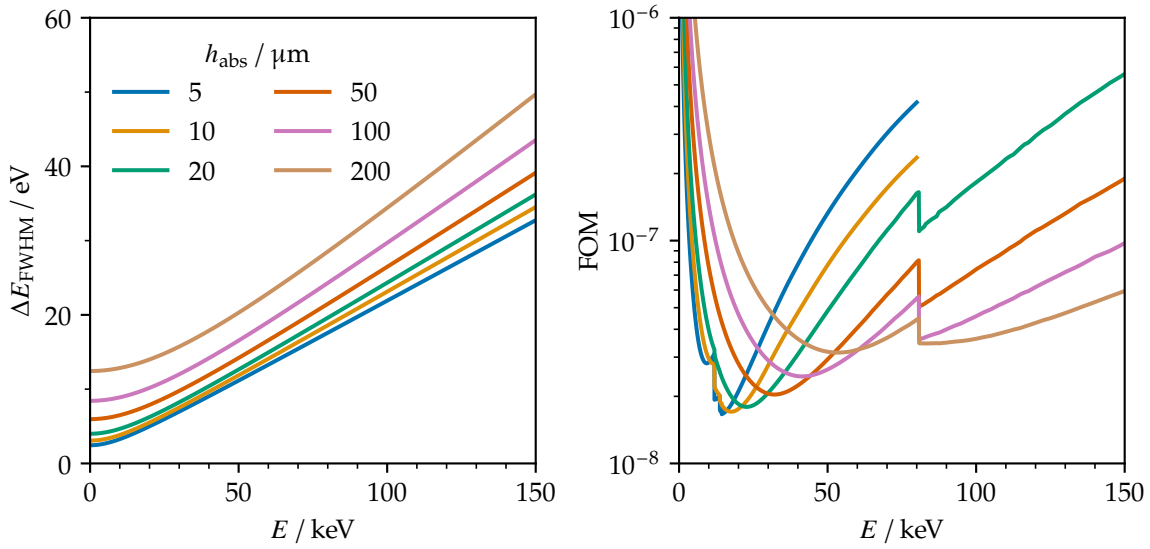

Figure 4.4.: Estimated energy-dependent FWHM energy resolution (left) and the corresponding FOM (right). The FOM accounts for the energy-dependent energy resolution and absorber efficiency for different absorber heights.

corrected temperature fluctuation of $\sigma_T \approx 2\,\mu\text{K}$ is assumed. The resulting energy-dependent resolution under this assumption is shown in Figure 4.4 for different absorber thicknesses. The resolution degrades significantly at higher energies, with all detector variants, each optimized for minimum energy resolution at zero energy, exhibiting approximately the same slope.

Based on the energy-dependent energy resolution ΔE_{FWHM}, a FOM can be defined to evaluate the effectiveness of different absorber heights. Assuming a Gaussian line shape, the statistical uncertainty on the line position for N events and an energy resolution σ_E is $\sigma_E/\sqrt{N}$. Including the desired relative accuracy $\epsilon = \Delta E/E$, which could be the targeted 2 ppm, a suitable figure of merit is given by

$$\text{FOM} = \left(\frac{\sigma_E}{E\sqrt{\alpha}}\right)^2 \tag{4.2}$$

where α is the absorber efficiency, previously shown in Figure 3.2, and the scaling with E accounts for the relative accuracy. The calculated FOM values for different absorber heights are shown in Figure 4.4. The number of events N required to achieve an accuracy ϵ is then given by

$$N = \frac{\text{FOM}}{\epsilon^2} \tag{4.3}$$

which may also serve as a lower limit for non-Gaussian line shapes. Based on these estimations, simulations could yield relative correction factors for different line shapes and energy resolutions.

At an energy of 18.7 keV, corresponding to the $2p$–$1s$ transition in muonic Li, approximately $N \approx 5000$ events are required to achieve a 2 ppm statistical accuracy, assuming a Gaussian line shape, an absorber thickness of $h_{\mathrm{abs}} = 20\,\mu\mathrm{m}$, and an energy resolution of $\Delta E_{\mathrm{FWHM}} = 6.0\,\mathrm{eV}$. The actual number of required events for a line consisting of hyperfine components, each described by a physical Lorentzian line shape and convolved with a Gaussian-like detector response, is expected to differ by more than a factor of two. As a rough, experience-based estimate, approximately four times more events are required to achieve this accuracy.

Based on the calculated FOMs, Table 4.3 summarizes the proposed absorber heights, expected energy resolutions, and absorber efficiencies for the nuclei targeted by QUARTET. Since the MMC-based detector array cannot be exchanged during a data run within a reasonable timeframe, multiple nuclei must be measured with the same detector. Moreover, the development and fabrication of a new detector is highly involved, and suitable configurations must therefore be selected well in advance. As a result, the proposed configurations are not solely based on the FOM, but also take current fabrication constraints into account and prioritize achieving high energy resolution. The FOM could be significantly enhanced by optimizing the energy resolution at the relevant transition energies, which would require improved temperature sensitivity ζ_T/T and reduced non-correctable temperature fluctuations σ_T.

Table 4.3.: Proposed detector configurations for QUARTET, listing the $2p$–$1s$ transition energy ΔE_{2p-1s}, the proposed absorber height h_{abs}, the estimated energy resolution ΔE_{FWHM}, the absorber efficiency α, and the figure of merit FOM.

Nucleus	ΔE_{2p-1s} / keV	h_{abs} / µm	ΔE_{FWHM} / eV	α	FOM / 10^{-9}
^{6}Li, ^{7}Li	18.7	20	6.0	0.97	19
^{9}Be	33.4		9.0	0.55	23
^{10}B, ^{11}B	52.3		13	0.21	54
^{12}C, ^{13}C	75.3	100	23	0.37	46
^{14}N, ^{15}N	102		30	0.34	47
^{16}O, ^{18}O	134		39	0.20	76
^{19}F	168	200	55	0.27	73
^{20}Ne, ^{22}Ne	207		68	0.14	122

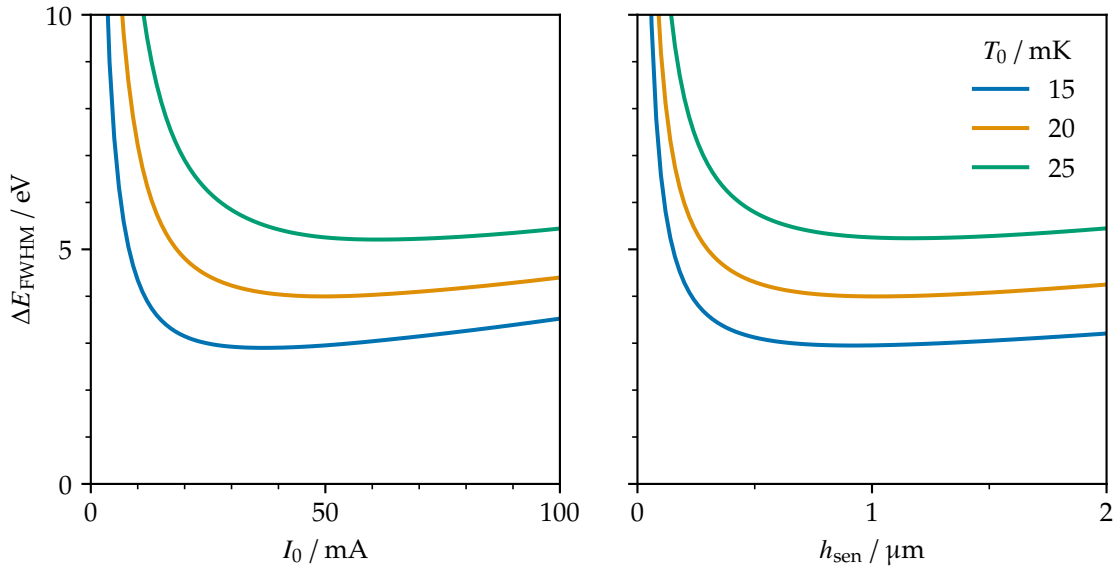

Figure 4.5.: Energy resolution ΔE_{FWHM} for different persistent currents I_0 at a sensor height of $h_{\mathrm{sen}} = 1\,\mu\mathrm{m}$ (left), and for different sensor heights h_{sen} at a persistent current of $I_0 = 50\,\mathrm{mA}$ (right), shown for various operating temperatures T_0. The energy resolution degrades only slightly with increasing sensor height or persistent current beyond the optimal values.

Temperature Sensitivity and Nonlinearity

While MMC-based detectors are typically optimized for high energy resolution ΔE_{FWHM} at zero energy, the resolution may degrades significantly at higher energies. Consequently, the detectors should be optimized to achieve good energy resolution in the relevant energy range. If this degradation is primarily limited by the temperature sensitivity ζ_T/T of the detector and by non-correctable temperature fluctuations σ_T, the design parameters should be chosen to minimize the absolute value of ζ_T/T. A detector design that includes additional temperature-sensitive reference channels could help reduce the impact of non-correctable temperature fluctuations. In addition, the nonlinearity ζ_E/E of the energy response should also be taken into account.

For the design parameters listed in Table 4.2, with an absorber thickness of $h_{\mathrm{abs}} = 20\,\mu\mathrm{m}$, the remaining optimization parameters are the sensor height h_{sen}, the persistent current I_0, and the operating temperature T_0. These must be adjusted not only to achieve good energy resolution, but also to minimize the temperature sensitivity and nonlinearity. In general, a lower operating temperature T_0 leads to improved energy resolution, although the achievable base temperature may vary significantly and is limited by heating from the SQUID readout and by the overall detector setup. Simulation results for the optimal design at $T_0 = 20\,\mathrm{mK}$, with varying sensor height h_{sen} and persistent current I_0, are shown in Figure 4.5 for different

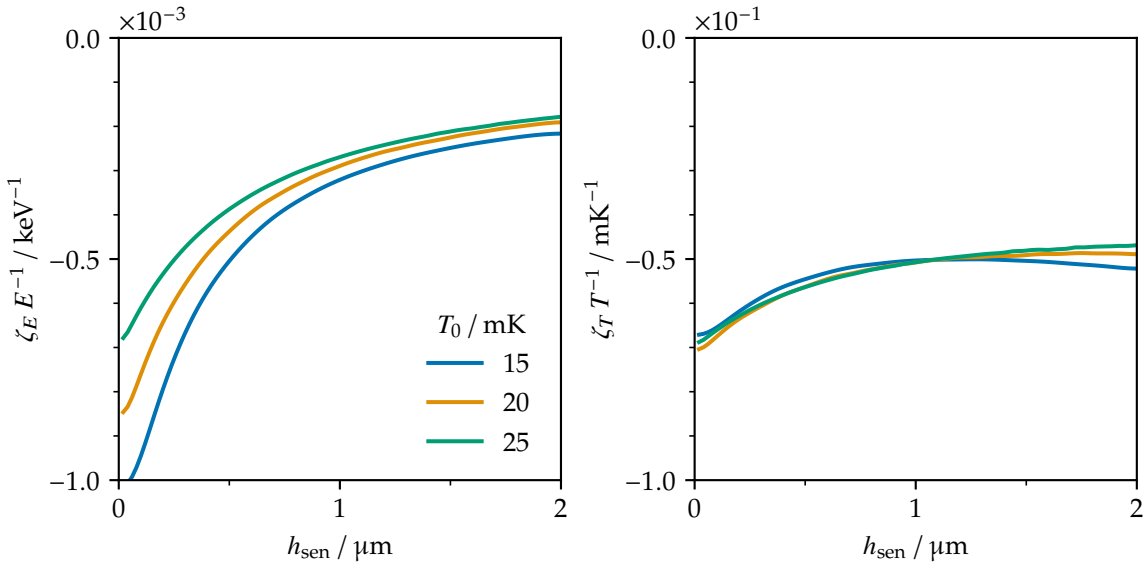

Figure 4.6.: Nonlinearity ζ_E/E (left) and temperature sensitivity ζ_T/T (right) for different sensor heights h_{sen} at a persistent current of $I_0 = 50\,\mathrm{mA}$, shown for various operating temperatures T_0. A higher sensor improves the nonlinearity, while the temperature sensitivity remains nearly unaffected.

temperatures. A high energy resolution requires a minimum sensor height and persistent current, but does not improve significantly beyond the optimal values and remains comparable across different operating temperatures.

The nonlinearity ζ_E/E and temperature sensitivity ζ_T/T for different sensor heights h_{sen} are shown in Figure 4.6. The nonlinearity ζ_E/E can be significantly reduced by increasing the sensor height, as this increases the sensor's heat capacity and thereby decreases the relative temperature change for a given energy deposition. However, the sensor height has little effect on the temperature sensitivity ζ_T/T, since the heat capacity of the sensor does not strongly influence the temperature sensitivity. In contrast, a higher persistent current I_0 substantially reduces both the temperature sensitivity and the nonlinearity. The corresponding dependencies of ζ_E/E and ζ_T/T on the persistent current I_0 are also shown in Figure 4.6. The persistent current modifies the sensor magnetization, and thereby reduces the second derivative $\partial^2 M / \partial T^2$, leading to a smaller absolute value of the temperature sensitivity ζ_T/T.

A two-dimensional grid search over sensor height and persistent current shows that a slightly reduced sensor height combined with the highest feasible persistent current yields the lowest absolute temperature sensitivity ζ_T/T, while also significantly improving the nonlinearity. The same search indicates that the lowest absolute nonlinearity is achieved by increasing both the sensor height and the persistent current. Increasing the persistent current

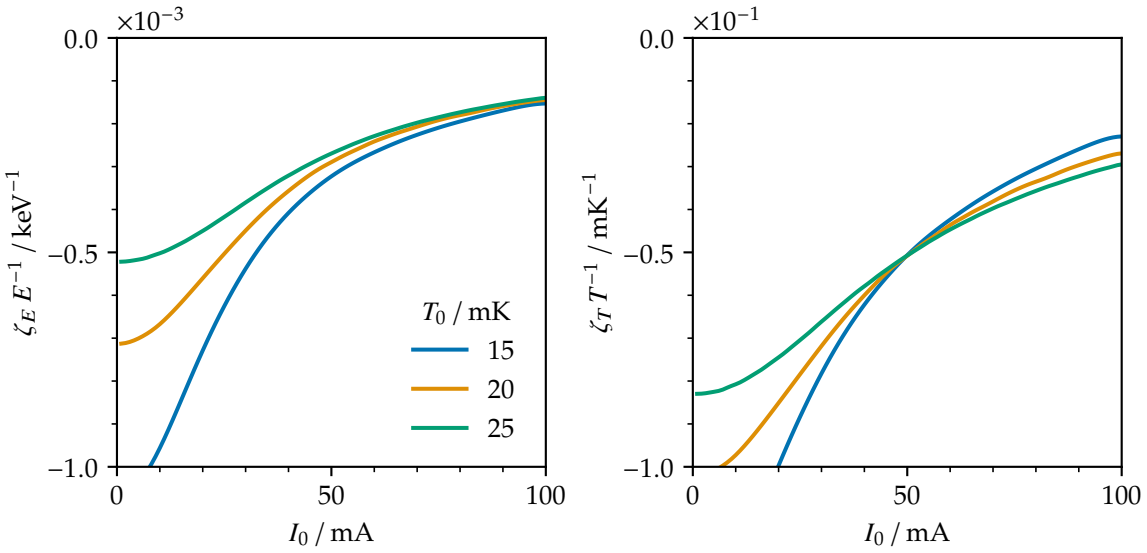

Figure 4.7.: Nonlinearity ζ_E/E (left) and temperature sensitivity ζ_T/T (right) for different persistent currents I_0 at a sensor height of $h_{\text{sen}} = 1\,\mu\text{m}$, shown for various operating temperatures T_0. Increasing the persistent current significantly improves both the nonlinearity and the temperature sensitivity.

I_0 therefore has a strong beneficial effect, making a high critical current of the superconducting pickup coil—well above the optimal operating current—highly desirable.

To achieve high energy resolution at the muonic transition energies for QUARTET, the persistent current can be significantly increased while keeping the sensor height fixed at $h_{\text{sen}} = 1\,\mu\text{m}$. At an operating temperature of $T_0 = 20\,\text{mK}$, a persistent current close to the expected critical current ($I_0 = 100\,\text{mA}$) yields an energy resolution of $\Delta E_{\text{FWHM}} = 4.4\,\text{eV}$, which is slightly worse than the 4.0 eV obtained at $I_0 = 50\,\text{mA}$. However, the temperature sensitivity improves substantially, decreasing from $\zeta_T/T \approx -51 \times 10^{-3}\,\text{mK}^{-1}$ to $\zeta_T/T \approx -27 \times 10^{-3}\,\text{mK}^{-1}$. Assuming an uncorrected temperature fluctuation of $\sigma_T \approx 2\,\mu\text{K}$, the detector with the higher persistent current outperforms the lower-current design above approximately 10 keV, and shows a markedly slower degradation of energy resolution at higher energies. With $\Delta E_{\text{FWHM}} = 4.4\,\text{eV}$ and $\zeta_T/T \approx -27 \times 10^{-3}\,\text{mK}^{-1}$, this design is expected to outperform the *maXs 30-v2b* detector, which exhibits $\Delta E_{\text{FWHM}} = 6.0\,\text{eV}$ and $\zeta_T/T \approx -40 \times 10^{-3}\,\text{mK}^{-1}$.

4.2.2. Detector Design

Based on the parameters determined through the previously described optimization, a new detector was designed using the open-source layout software *KLayout*. While the new design maintains the chip dimensions, electrical connections, and mechanical clamping pads of existing *maXs 30* detectors, it is a complete redesign that implement several modifications,

some of which are expected to significantly enhance the detector performance. In addition to the improved energy resolution and temperature sensitivity resulting from the parameter optimization, the detector features an interconnected thermal bath with thermalization structures on both the front and backside, as well as a dedicated temperature-sensitive pixel without a particle absorber. These changes are expected to substantially improve thermal coupling and the precision of temperature measurements, thereby enabling a higher maximum event rate and reducing the degradation of energy resolution at higher energies.

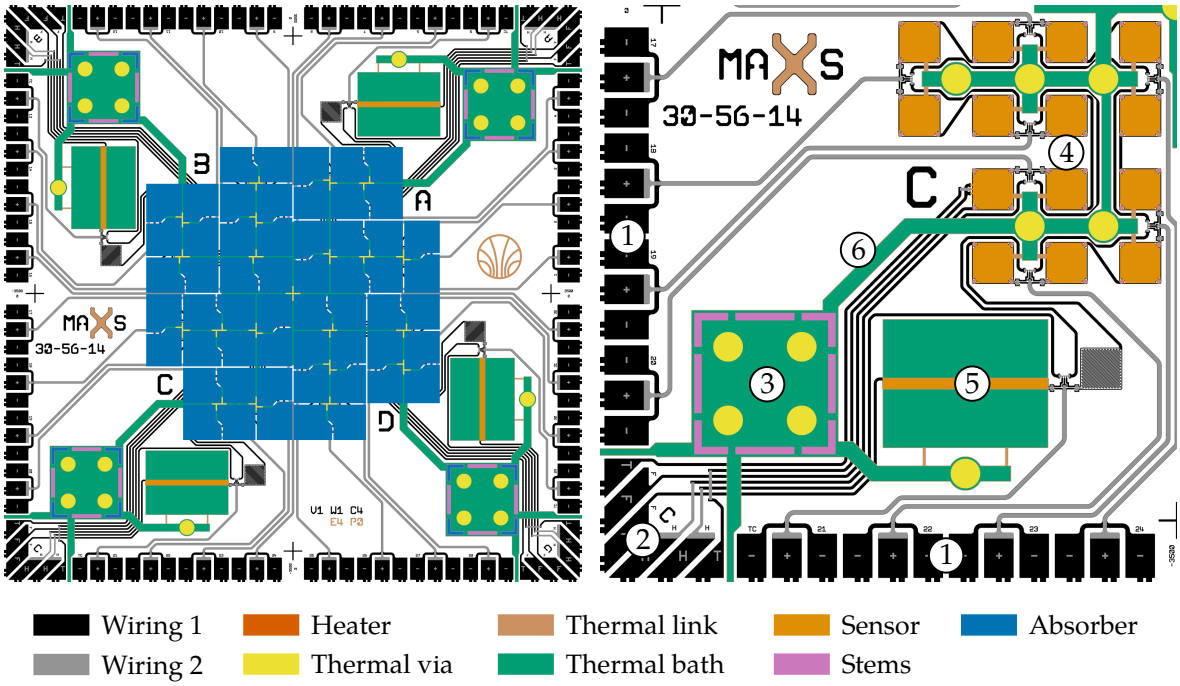

Figure 4.8.: Design of the *maXs 30-56-14* detector (left) and a single quadrant without particle absorbers (right). Isolation layers are omitted for simplicity. The layout preserves the same ① SQUIDs bond pads, ② field and heater bond pads, and ③ mechanical press pads as in other *maXs 30* detectors. Each quadrant contains 14 ④ gradiometric pixels and one ⑤ fully asymmetric temperature-sensitive pixel. All pixels are thermally coupled to a common ⑥ thermal bath, which is connected to a large thermal bath on the backside via multiple thermal vias.

The overall detector layout is shown in Figure 4.8. The detector consists of four rotationally symmetric quadrants that are identical except for their labels. All structures feature rounded corners with radii of several µm, typically matching the line width. This reduces the magnetic field at edges and corners and improves the fabrication reliability, particularly during lift-off processes. The field and heater lines are routed with a line width of 20 µm to fit between the pixel pairs and the thermal bath, while the lines to the SQUID bond pads are 30 µm wide to reduce their parasitic inductance. To achieve a high critical current, the field lines are

routed exclusively in the first wiring layer. The absorbers of each pixel pair are intentionally shaped slightly asymmetrically rather than perfectly square, in order to shield the underlying superconducting structures of the persistent current switches from potential magnetic flux losses due to energy deposition by external radiation.

The thermalization strategy in this design differs significantly from that of previous *maXs 30* detectors. On the front side, all thermal baths are interconnected and connected to the mechanical press pads. In addition, multiple thermal vias provide thermal contact between the front side and a large, electrically isolated backside heat sink located between the pixels. These vias have a significantly larger diameter of 200 µm and are fabricated using a recently developed method [148]. This design enables thermalization both via a metal clamp pressing on the front-side press pads and via direct contact with a metal surface on the backside. Both approaches are expected to lower detector operating temperature and provide a more ideal thermal bath, characterized by a higher heat capacity and a shorter thermalization time constant, thereby improving both energy resolution and temperature sensitivity.

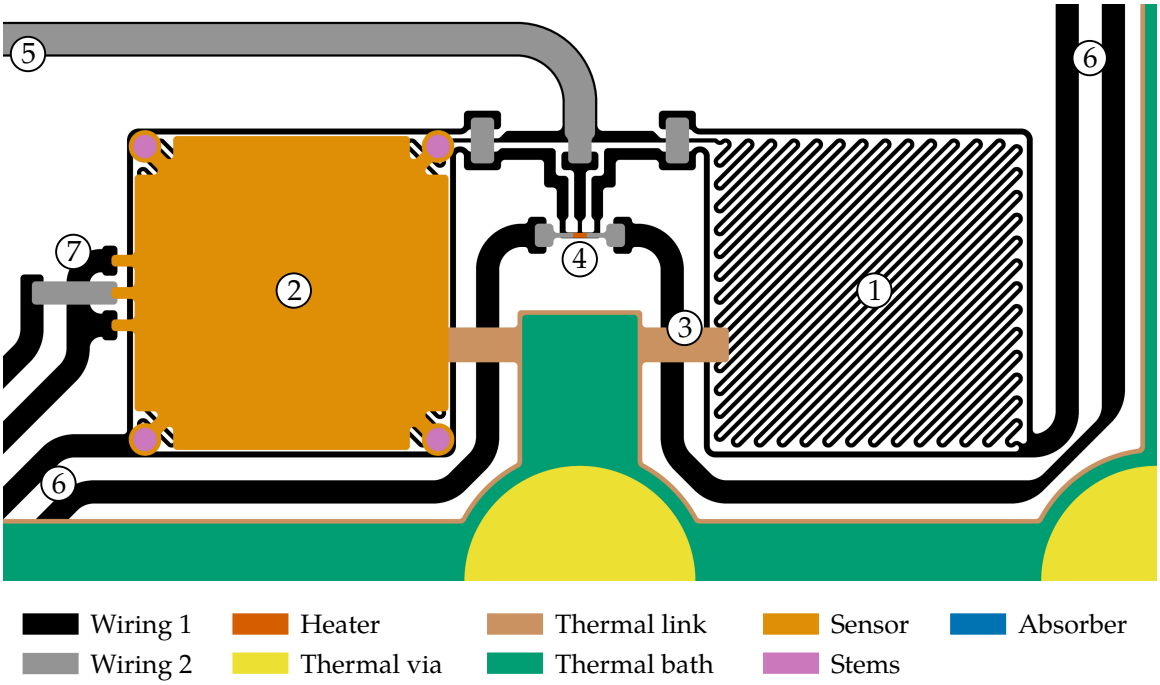

Figure 4.9.: The *maXs 30-56-14* channel design of a gradiometric pixel pair. The right pixel is shown without its sensor and stems. Isolation layers are omitted for simplicity. The ① planar meander-shaped coils lie beneath the ② paramagnetic temperature sensors, each featuring four stems on top for mounting the particle absorber. The sensors are thermally coupled to the thermal bath via ③ thermal links. The persistent current is prepared in the coils via a ④ persistent current switch. The pixel pair is electrically connected via ⑤ SQUID connections and ⑥ field and heater connections. One pixel in each quadrant features a ⑦ test heater for applying heat pulses to the sensor.

The design of a gradiometric channel is shown in Figure 4.9. The dedicated temperature-sensitive pixels were designed based on the results of measurements we performed with a fully asymmetric single-pixel large-area detector [16]. Each pixel pair contains two diagonal meander-shaped pickup coils, enclosed by a surrounding superconducting loop to ensure magnetic flux conservation in the coil. The paramagnetic sensor includes four stems located at its corners, each having a thermal bottleneck to the sensor with a area of approximately one square. These stems, with a diameter of 20 µm, are placed in low-field regions to minimize their signal and reduce their impact on the signal rise time. Thermalization of each pixel is achieved through a thermal link, implemented as a bottleneck of two squares, which connects the sensor to the thermal bath. The thermal bath itself is substantially thicker than the thermal link and is connected to the thermal vias. One pixel in each quadrant includes a test heater, in which a current is applied to the sensor, and the resulting heating generates a controlled thermal pulse.

The temperature-sensitive channels are designed to respond more rapidly and with greater sensitivity to temperature variations, providing more precise information about the thermal bath temperature. These channels are fully asymmetric and function as dedicated temperature pixels. They do not include a particle absorber, but instead feature two large rectangular structures deposited directly onto the substrate that serve as phonon collectors. With a substrate coverage of approximately 1 mm^2, each temperature pixel is particularly sensitive to energy deposited in the substrate. This is achieved using an elongated, narrow meander geometry, and not the square geometry used for gradiometric pixels, while maintaining about the same inductance. The sensor has a heat capacity similar to that of the gradiometric pixels, and the phonon collectors have a heat capacity comparable to that of the absorbers.

To avoid direct energy deposition from incident particles, the temperature pixels are placed at the edges of the chip rather than in the corners of the active area, where they can be shielded by the collimator of the detector module. Two designs exist, one thermally coupled to the bath in the same way as the gradiometric pixels, and one without thermal coupling. Each detector contains four temperature pixels, with different chips across the wafer having different fractions of the two versions, and up to two uncoupled versions per detector. The bath-coupled pixels measure the bath temperature on a timescale of about 5 ms, given by their decay time constant, which is significantly faster than the 300 ms response of the earlier *maXs 30* detectors without thermal vias. The uncoupled pixels are designed to measure only the silicon substrate temperature on a timescale below 100 ms, enabled by their much larger contact area with the substrate.

4.2.3. Detector Fabrication

For the first data run with Li, Be, and B, we fabricated three detector wafers based on the optimized and newly developed design. An absorber height of 25 µm was chosen to ensure sufficient detection efficiency for the $2p$–$1s$ transition in B at 52.3 keV. These wafers are referred to as *maXs 30-56-14*, as introduced previously, and the individual chips are further identified by labels such as *v1w2c16*, where *v* denotes the design version, *w* the wafer number for that version, and *c* the chip number. Each wafer contains 44 chips, including several test chips with dedicated structures for characterizing specific fabrication layers and layer combinations.

An overview of the fabrication layers is provided in Table 4.4. The fabrication process is based on standard processes that have been developed and are continuously optimized in the cleanroom facilities at the KIP in Heidelberg. Typically, thermally oxidized 3 in silicon wafers with a front-side polish are used as substrates. Structures are implemented using photosensitive resist and photolithographic techniques. The resist is spin-coated onto the wafer surface, selectively exposed, and developed to define the desired pattern. Material is deposited either by sputtering or by electroplating onto a metallic seed layer. In some cases, material is selectively removed using reactive-ion etching (RIE) etching.

Table 4.4.: Overview of the *maXs 30-56-14* detector layers, including their layer number, name, material, height h, deposition method, processing technique, and corresponding structures. Thin sticking layers, typically around 1 nm, are not listed. A 150 nm Au protection layer on top of the sensor, serving as an oxidation barrier, is also omitted.

Layer	Name	Material	h / µm	Deposition	Process	Structures
1	Nb1	Nb	0.25	Sputtering	Etching	Wiring, Coils
2	Anod	Nb_2O_5	–	–	Anodization	Isolation
3	Iso1a	SiO_2	0.13	Sputtering	Lift-off	Isolation
4	Iso1b	SiO_2	0.17	Sputtering	Lift-off	Isolation
5	Htr	AuPd	0.16	Sputtering	Lift-off	Heater
6	Nb2	Nb	0.40	Sputtering	Lift-off	Wiring, Vias
7	Etch	–	–	–	–	–
8	Therm	Au	0.30	Sputtering	–	Thermal Link
9	Galv	Au	2.0	Electroplating	Lift-off	Thermal Bath
10	Iso2	SiO_2	0.17	Sputtering	Lift-off	Insulation
11	TSV-Etch	–	–	–	Etching	–
12	TSV-Galv	Cu	380	Electroplating	–	Thermal Vias
13	TSV-Therm	Cu	1.0	Electroplating	–	Thermal Bath
14	Sens	Ag:Er	1.5	Sputtering	Lift-off	Sensors
15	Stem	Au	10	Electroplating	–	Stems
16	Abs	Au	20	Electroplating	Lift-off	Absorbers

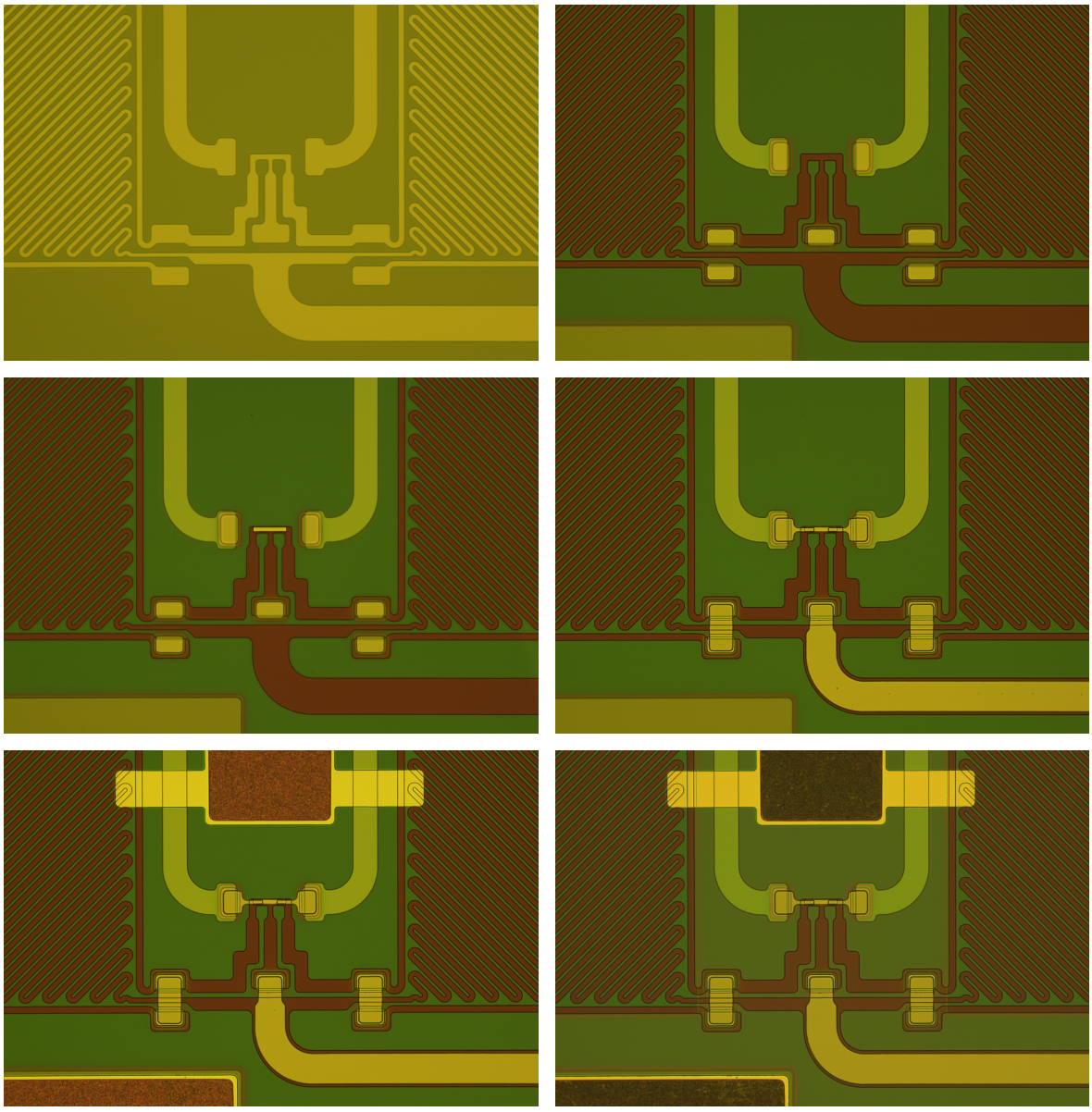

Figure 4.10.: Microscope images of different fabrication steps of a detector channel. Most of the electrical wiring is completed in the first layer (top left). After the fourth layer, only the regions for electrical vias and thermal baths remain without electrical isolation (top right). The heater used to prepare the persistent current is fabricated in the fifth layer (middle left). The sixth layer completes the wiring (middle right). After the ninth layer, the thermal structures are fabricated (bottom left). The tenth layer adds an insulating layer, except in the sensor area (bottom right).

The first layer consists of sputtered Nb with a thickness of 250 nm, structured by resist and reactive ion etching. The majority of the superconducting wiring are within this layer. Electrical insulation is provided by three subsequent layers. First, the exposed Nb is anodized to form a thin Nb_2O_5 oxide layer. This is followed by two sputtered SiO_2 layers deposited sequentially, 130 nm for the lower layer and 170 nm for the upper layer. These insulating layers are patterned by lift-off and serve both as electrical isolation and as stepped structures for electrical vias. These fabrication steps are illustrated by microscope images of a detector channel in Figure 4.10. A layer consisting of 160 nm of AuPd is deposited and patterned by lift-off to form heaters used for preparing the persistent current. A second Nb layer with a thickness of 400 nm completes the superconducting wiring and electrical vias. A photograph of the third wafer after the second wiring layer is shown in Figure 4.11. Subsequently, SiO_2 is selectively etched by RIE to define regions for the thermal structures, which are then fabricated in a two step process. First, a 300 nm sputtered Au layer is deposited, serving both as a thermal bottleneck defining the decay time and as a seed layer for subsequent deposition. Then, a 2.0 µm electroplated Au layer is added to increase thermal conductance and form the thermal bath. Finally, a 170 nm SiO_2 insulation layer is deposited and patterned to protect all areas except the sensor regions and bonding pads.

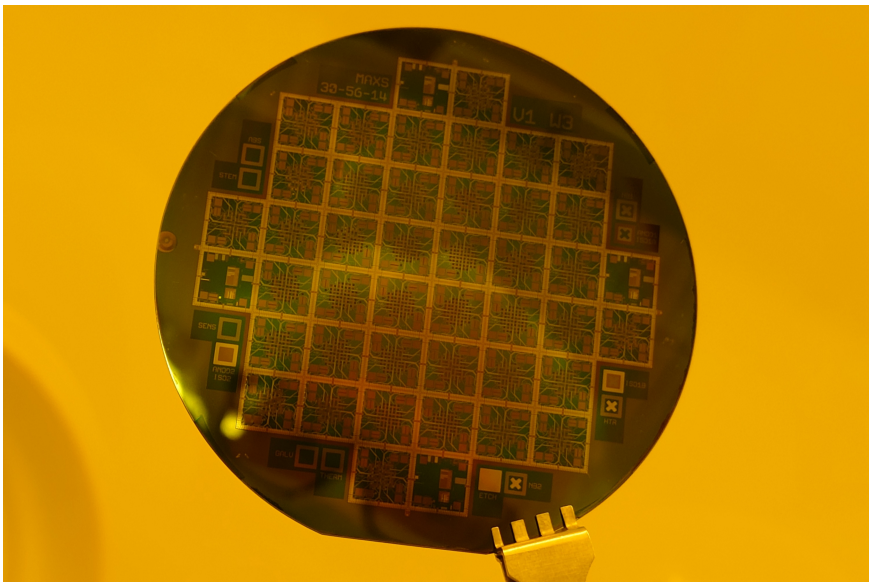

Figure 4.11.: Photograph of the third *maXs 30-56-14* wafer during fabrication in the cleanroom, taken after the completion of the second wiring layer.

Two newly developed fabrication processes were employed. The first is the production of thermal vias, which are metal-filled holes extending from the front to the backside of the wafer. These vias consist of electroplated Cu and an additional 1.0 µm on the backside to form the backside thermal bath and connect all thermal vias. They are expected to improve the

thermalization by providing a fully-connected high heat capacity thermal bath. The second process enables more precise fabrication of the stems and particle absorbers. It reduces the geometric cross section between absorber and sensor, thereby minimizing energy losses from athermal phonons. Both processes are not part of this thesis and are described in detail in the corresponding work [148].

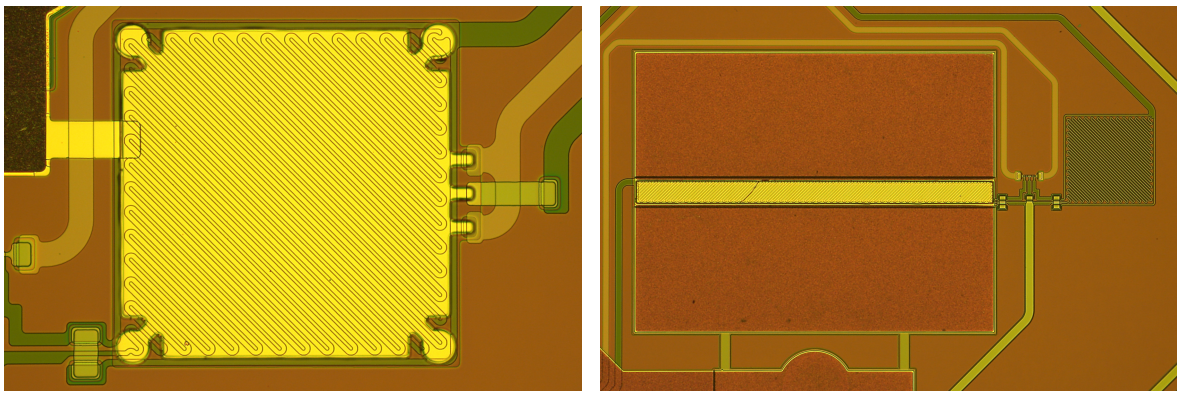

Figure 4.12.: Microscope images after sensor fabrication, showing a sensor of a pixel pair with a test heater (left) and a temperature-sensitive pixel (right).

After fabrication of the thermal vias, the paramagnetic temperature sensors are fabricated from 1.5 µm thick Ag:Er films and patterned by lift-off. Figure 4.12 shows a gradiometric pixel and a temperature-sensitive pixel after the sensor fabrication. The stems and particle absorbers are produced in a two-step electroplating process. First, 10 µm high stems are electroplated onto a metallic seed layer. Then, 20 µm thick Au particle absorbers are deposited by electroplating. Finally, the detector wafer is diced, and the individual chips are sorted and cleaned. A completed detector chip is shown in Figure 4.13 as a focus-stacked photograph.

Fabrication Issues

After the fabrication of the three wafers, several chips were tested at 4 K in liquid helium. On the first wafer, superconducting structures on the test chips exhibited a critical current of only $I_c = 1$ mA for electrical vias, approximately two orders of magnitude below the expected value. Tests with detectors from this wafer also showed that none of the heater lines exhibited electrical connectivity at 4 K. As a result, no persistent current can be prepared in these chips, and all detectors from the first wafer were found to be unusable.

Tests at 4 K on the second wafer showed higher critical currents, with $I_c = 13$ mA for 100 electrical vias and up to 23 mA for a single via, although still about one order of magnitude below the expected value. Measurements on several detectors revealed acceptable heater resistances in some quadrants. However, only two detectors from the second wafer exhibited good electrical connectivity across all quadrants and were subsequently tested at mK

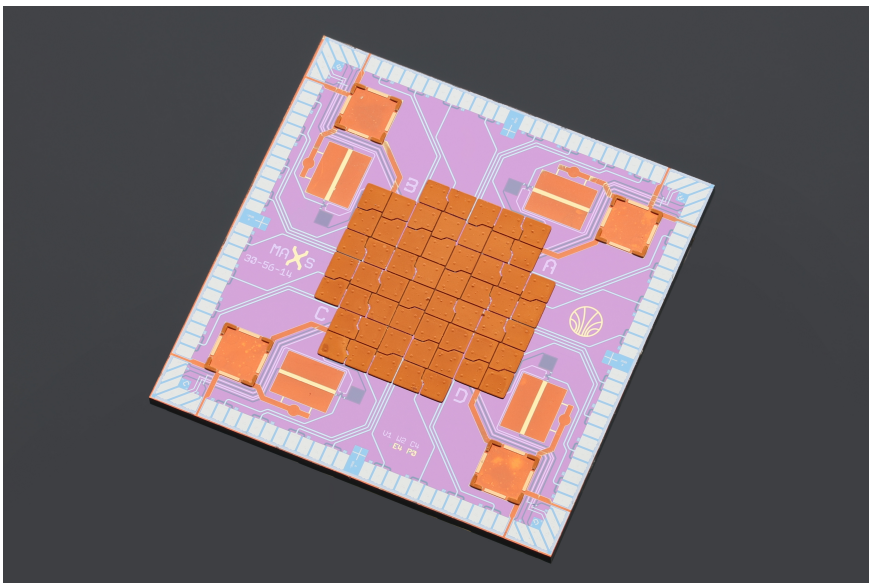

Figure 4.13.: Focus-stacked photograph of the *maXs 30-56-14* detector, optimized for X-ray spectroscopy of muonic atoms. The detector is a complete redesign of the *maXs 30-v2b*, but retains the same chip size, electrical connections, and mechanical clamping pads. The background at the bottom has been edited to hide the mounting structure used to hold the detector during photography.

temperatures in a dilution refrigerator. Preliminary measurements showed a good energy resolution, but only about one-third of the channels were operational, and less than half of the intended persistent current could be prepared in the superconducting meanders. Moreover, the preparation of the persistent current was unreliable. From the third wafer, one chip was tested at mK, which showed a behavior similar to that of the second wafer. Consequently, also for the data run with Li, Be, and B, the previously described *maXs 30-v2b* setup was used instead. The first measurements and results of a detector from the second wafer operated in a dilution refrigerator are presented in Chapter 7. After the data run, we further characterized this detector, assumed to be the best-performing detector of the three wafers, at different temperatures in the dilution refrigerator, and the results are reported in the corresponding work [14].

Subsequent measurements of individual layer thicknesses on test structures from the wafers revealed significant overetching of the first wiring layer. This etching process not only removed the Nb layer but also etched into the underlying SiO_2, which was up to approximately 90 nm for the first wafer, thereby increasing the step height for the second wiring layer. In addition, scanning electron microscope (SEM) images showed that the first wiring layer featured sharp corners, as shown in Figure 4.14, and did not feature a sufficiently gradual step profile. As a result, the second wiring layer is nearly cut off at line crossings and electrical vias, leaving only a small superconducting cross section and is not conected for the first wafer.

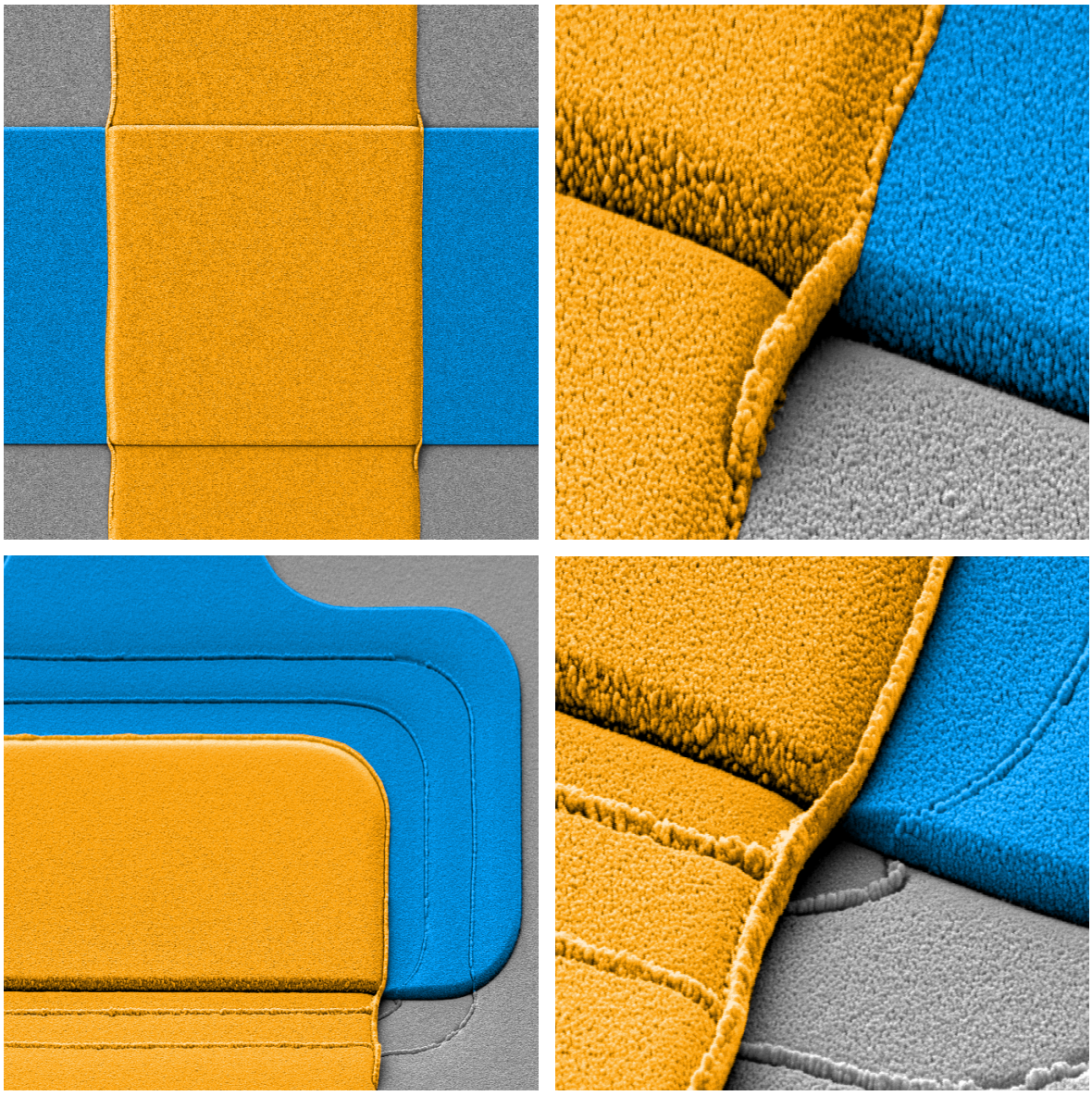

Figure 4.14.: False-color SEM images of the wiring on chip *maXs 30-56-14 v1w2c36*, showing a wiring crossover (top) and an electrical via (bottom), with overview images (left) and zoomed-in, rotated views (right). The bottom etched wiring (blue) exhibits sharp edges, while the top sputtered wiring (orange) appears nearly cut off where it crosses the bottom layer, resulting in a significantly reduced cross section of the electrical connection. The line width is 20 µm. The step profile of the via isolation, with a spacing of 2 µm, is clearly visible.

Chapter 5.

Experimental Methods

The QUARTET experiment imposes not only strict requirements on the MMC-based detector itself, but also on the overall detector setup. The two-stage dc-SQUID readout, consisting of front-end SQUIDs on the detector module and SQUID arrays on the SQUID amplifier module, relies on the characterization and selection of many SQUID chips to ensure low readout noise, minimal heat dissipation, and consequently, high energy resolution. The detector modules and the amplifier module must be assembled and thoroughly characterized. The detector must be operated in a dilution refrigerator at temperatures of about 20 mK and positioned close to the target for the moun beam. For this purpose, the development of a suitable cryostat sidearm is essential to enable efficient placement of the detector. To achieve the targeted measurement accuracy of 2 ppm for the muonic $2p$–$1s$ transition energies, the ADCs used for signal digitization must be precisely calibrated, requiring the development of an appropriate calibration procedure. The entire experimental setup must then be transported to PSI in Villigen, Switzerland, where it is reassembled and optimized in a staging area near the beamline several weeks before the actual measurements. For a measurement at the $\pi E1$ beamline, the cryostat must be disassembled, craned into the experimental area, and then reassembled and cooled down again. The setup must reliably reach mK temperatures and resume full operation quickly to meet the tight run schedule.

This chapter describes the preparation of the detector setup for QUARTET. It covers the assembly of the SQUID amplifier module and the detector modules, as well as the development of the cryostat sidearm. The detector readout system is presented, including the data acquisition, the automatic SQUID characterization, and the calibration of the ADCs. Finally, the experimental setup at PSI is described.

5.1. Detector Setup

The low-temperature detector setup consists of a detector module, which includes a detector chip and eight front-end SQUID chips, as well as an amplifier module equipped with sixteen SQUID array chips. Two amplifier modules were prepared. One amplifier module was equipped with SQUID arrays for the second-stage readout and was characterized and

iteratively improved at mK temperatures until all channels operated reliably with low readout noise. The second amplifier module was configured for the characterization of front-end SQUID chips. This allowed efficient testing and selection of sixteen fully functional front-end SQUID chips to equip two detector modules. Two detector modules were assembled and tested with different detector chips in a newly developed cryostat sidearm, specifically designed for QUARTET. The sidearm provides a large cylindrical experimental volume of up to 8 cm in diameter and height. It is designed to enable rapid mounting, achieve low temperatures, minimize vibrations through a sturdy construction, and provide effective magnetic shielding. This is achieved while maintaining a relatively small distance between the detector and the outer X-ray window of the vacuum shield, despite a temperature difference of approximately four orders of magnitude between them.

5.1.1. Amplifier Module

The design and development of the SQUID amplifier module and the low-temperature readout was developed in previous work [9, 147]. The fully assembled amplifier module for QUARTET, serving as the second-stage readout, is shown in Figure 5.1. An amplifier module contains 36 channels from 18 SQUID array chips, each providing two channels, and can thus fully read out a 32-channel detector module. It consists of three printed circuit boards (PCBs), onto which the SQUID array chips are glued with *GE 7031* and are electrically connected using aluminium bonding wires. Each PCB is inserted into and screwed to a shield made of tin-plated copper. Each shield is composed of two oxygen-free high-conductivity copper (OFHC) copper parts that are plated with tin and welded together with indium. The three assembled modules are then inserted into a cryoperm shield. At low temperatures, the cryoperm shield suppresses external magnetic fields, while the tin and indium of the inner shields become superconducting, expelling magnetic fields and freezing the remaining flux inside. This significantly reduces magnetic field fluctuations and thereby lowers the readout noise. Based on this previously developed design, we prepared two amplifier modules, which is described in more detail in the corresponding work [17].

The amplifier module requires a large number of SQUID chips, 18 chips in total. During its preparation, carried out one year before the QUARTET research proposal, SQUID chips from several SQUID wafers produced at KIP were available. Based on previous measurements, four different HDSQ SQUID wafers were selected: *13w3*, *13w4*, *14w1*, and *15w1*. A total of 18 chips, corresponding to 36 channels, were tested at mK temperatures in a dilution refrigerator from the different wafers. Since the SQUID readout noise is expected to dominate the high-frequency noise spectrum, the SQUIDs were selected based on their white noise performance at high frequencies. Among the tested chips, those from wafers *14w1* and *13w4* exhibited significantly lower white noise than the others. However, only the chips from wafer *14w1* had

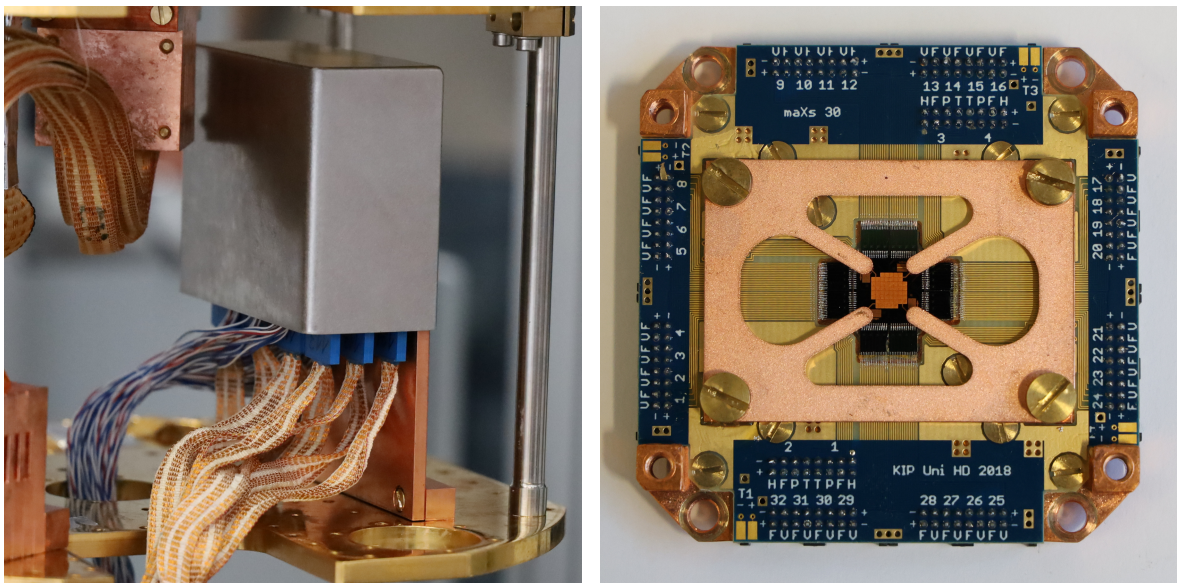

Figure 5.1.: Photograph of the amplifier module (left) and detector module without collimator (right). The amplifier module serves as the second stage of the SQUID readout and is connected to the room-temperature electronics via ribbon cables and to the detector module via 16-pin cables. The detector module contains the front-end SQUID chips and the detector, both glued on the copper platform. The detector is additionally clamped to increase the thermal contact between the copper platform and the thermal bath on the front side.

all channels functioning correctly, while the yield from *13w4* was considerably lower. As a result, chips from wafer *14w1* were used for the amplifier module.

During multiple cooldowns to mK temperatures, SQUID array chips from wafer *14w1*, mounted in the amplifier module, were automatically tuned and characterized using the newly developed automatic SQUID characterization, as described later [17, 18]. For the SQUID characterization, an adapter was used to short-circuit the connection that would normally go to the feedback coil of the front-end SQUID to the input coil of the SQUID array, allowing both the input and feedback coils of the SQUID arrays to be tested simultaneously. During each run, chips that were non-functional, exhibited high noise, had excessive bias parameters, or showed poor resistance values were identified and replaced. After each cooldown, broken bonding wires were repaired, and chips that had become loose were cleaned and re-glued. Each electrical connection between the PCBs and the SQUID chips was made using two bonding wires, ensuring that a single broken bond would not result in the loss of an entire readout channel. The amplifier module was iteratively characterized and adjusted with several cooldowns until all channels operated reliably with low readout noise. The measured characteristics of the SQUIDs arrays from HDSQ wafer *14w1* used in the amplifier module are listed in Table A.3 of the Appendix.

5.1.2. Detector Module

For the first test run and ultimately also for the data run, the *maXs 30-v2b* detector module was used [1, 2, 146]. Since the detector and the front-end SQUID chips were glued using *Araldite RAPID* from *Huntsman Corporation*, an adhesive that is not easily removable, and detaching them would likely have caused damage [146], the detector module was used without modification. The detector and bonding wires were inspected under a microscope before and after both runs, and no damage was observed. For the test run, a new collimator and adapter plate for the sidearm were designed and fabricated. For the data run, the collimator was further modified to enable a broader opening angle, preventing shadowing on the active area of the detector.

For the new detector modules, the existing platform for *maXs*-type detectors was used [73]. A fully assembled detector module with a new *maXs 30-56-14* detector is shown in Figure 5.1. In addition to the detector and the front-end SQUID chips, each module consists of a platform, clamp, and collimator made from tempered OFHC copper, as well as a PCB with connectors. The chips are glued onto the platform, which features thin grooves between the chip positions. These grooves, 0.3 mm wide and 0.4 mm deep, prevent glue from forming thermal bridges between the chips and assist in their alignment during assembly. The detector and SQUID chips must be positioned directly adjacent to each other to minimize the stray inductance of the bonding wires. At the locations of the front-end SQUID chips, a thin niobium layer is sputtered onto the copper platform to suppress magnetic noise that could be detected by the SQUIDs, originating from the Brownian motion of conduction electrons in the copper platform. For the data run, new collimators were designed and fabricated to allow a wider opening angle while still covering the temperature-sensitive pixels of the new detectors. Two detector modules were prepared, characterized, and reassembled with different detectors.

The second prepared amplifier module was used to automatically tune and characterize the required front-end SQUID chips at mK temperatures for the two detector modules. At the time of preparation for the data run following the test run, front-end SQUID chips from the same HDSQ wafer *14w1* as the SQUID arrays were available. These chips are also expected to exhibit low white noise and were ideally suited to be used with the previously prepared amplifier module. As before, an adapter was used to test both the input and feedback coils. Since the front-end SQUID chips provide four channels each, the amplifier module was cooled down twice, each time with a different set of wire-bonded SQUID channels. Of the 18 tested SQUID chips, 16 were fully functional and used for the two detector modules. The measured characteristics of the front-end SQUIDs from HDSQ wafer *14w1*, characterized for the two detector modules, are listed in Tables A.1 and A.2 of the Appendix.

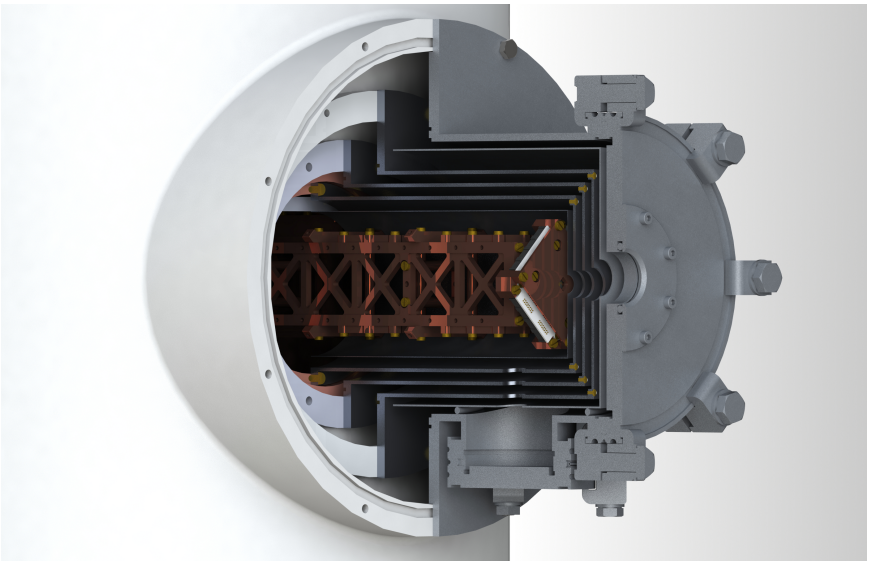

Figure 5.2.: Design of the cryostat sidearm, shown as a cross-section through the thermal and magnetic shields to reveal the internal structure. The shields align precisely with one another upon retraction at low temperatures. The cryostat model was provided by *Bluefors*.

5.1.3. Cryostat Sidearm

To efficiently position the detector close to the muon target, a cryostat sidearm was developed for a commercially available dilution refrigerator from *Bluefors*. The sidearm was designed using *SolidWorks* and is shown in Figure 5.2. It enables a relatively short distance of approximately 5.5 cm between the detector and the outer X-ray window. When the front pillars of the cryostat frame are positioned below of its air damper, the sidearm becomes the outermost component and can be conveniently aligned to external X-ray sources. For the data run, the cryostat was mounted on a frame with wheels and aligned with the target chamber [14]. It was then vertically adjusted to match the beamline height of 1.5 m using height-adjustable feet.

The detector is mounted on an inner copper arm that is attached to the mixing chamber of the cryostat via a dedicated mounting structure, as shown in Figure 5.3. The sidearm is designed to support large experimental volumes, up to a cylindrical shape with a diameter and height of 8 cm. The arm consists of two vertical, truss-structured bars with spacers in between. Each bar includes holes spaced at 2 cm intervals on all sides, enabling the installation of additional support structures for mechanical reinforcement, as well as a niobium shield for magnetic shielding. The copper arm is mounted to the mixing chamber plate using a structure with multiple slotted holes, allowing positional alignment in all directions with a tolerance of up to 3 mm, while the radial position can be freely adjusted. All components are machined from OFHC copper and subsequently tempered. They are designed with large

contact surfaces and assembled using multiple screws and vacuum grease to enhance thermal contact and ensure a low detector temperature. The lightweight yet rigid truss structure minimizes mechanical vibrations. Residual vibrations of the arm are experienced by both the detector and the superconducting niobium shield, and as a result, magnetically induced noise from vibrations is significantly reduced.

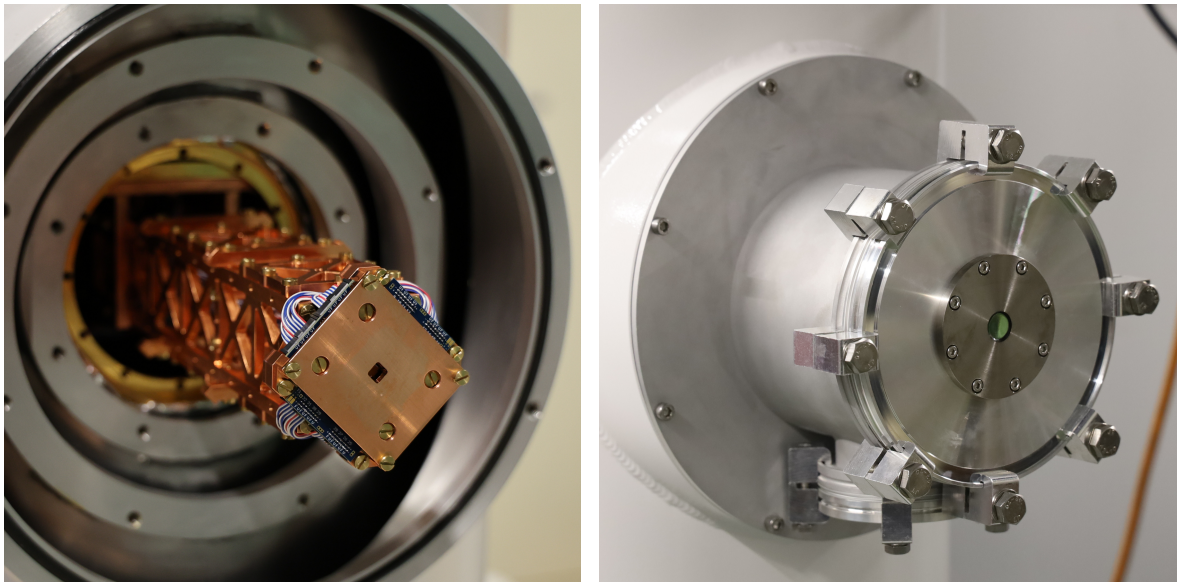

Figure 5.3.: Photographs of the inner copper cryostat arm (left) and the vacuum shield of the fully assembled sidearm (right). The sidearm supports large experimental volumes with a cylindrical geometry of up to 8 cm in diameter and height. The shields are rotatable and include both a radial and a side port.

The sidearm contains three thermal shields located at the 700 mK, 4 K, and 50 K stages of the cryostat, as well as a vacuum shield at room temperature. All shields are made of aluminium and assembled with brass screws, except for the vacuum shield, which is assembled using non-magnetic stainless steel screws to avoid magnetic materials near the detector. The innermost aluminium shield at 700 mK becomes superconducting and provides additional shielding against magnetic field fluctuations. Each shield is equipped with removable lids to enable alignment checks during mounting and to allow manual preparation of the X-ray windows, as discussed later. The vacuum shield includes standard blind flanges that can be connected to external vacuum systems when measuring low-energy X-rays that would otherwise be absorbed in air. Inside the vacuum shield, a μ-metal shield is fixed in place using small NBR (nitrile butadiene rubber) spacers. This shield reduces the internal magnetic field and simultaneously acts as a thermal shield, being only loosely thermally coupled to the vacuum shield. Thermal expansion of the shields are taken into account to ensure proper alignment

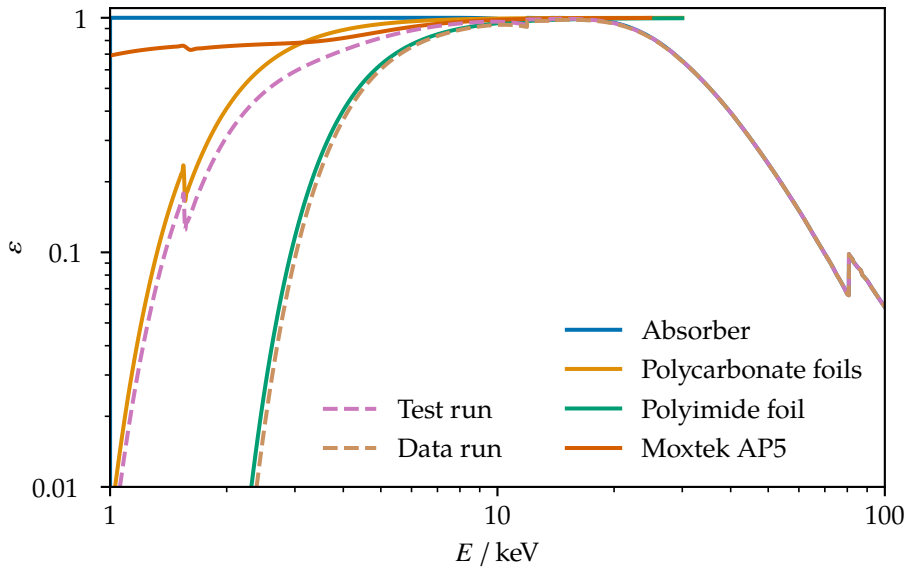

Figure 5.4.: Transmission through the X-ray windows of the cryostat sidearm and absorption efficiency of the detector given by 20 µm gold absorbers, shown in Figure 3.2. For the polycarbonate foils, the transmission through eight foils is shown. For the test run, the *AP5* window from *Moxtek* and six polycarbonate foils was used, while for the data run a polyimide foil with 100 nm sputtered aluminium and eight polycarbonate foils was employed. The transmission of the *AP5* window was provided by *Moxtek*, while the transmission of the other materials are based on attenuation coefficients [149].

at low temperatures. All shields can be rotated in 90° steps, allowing to adjust the side port orientation as needed. The fully assembled sidearm is shown in Figure 5.3.

To mount the sidearm, the amplifier module is first installed on top of the mixing chamber. The cryostat shields are then mounted without their side and bottom plates. In a demanding procedure, the copper arm is inserted from the bottom of the cryostat and must be carefully aligned in all directions so that it is centered within the innermost sidearm shield, which must then also be mounted, with the detector positioned close to the shield lid. Once this alignment is complete, the arm can be removed together with its niobium shield and later reinstalled as a single unit from the bottom of the cryostat, allowing for quick mounting without the need for further adjustment. The sidearm shields provide sufficient clearance and were further adjusted after fabrication to enable rapid installation without realignment. After mounting the sidearm shields, the cables from the detector module are connected to the amplifier module, also from the bottom of the cryostat. Finally, the bottom plates of the cryostat shields are installed, and the cryostat is cooled down.

Except for the niobium shield, each shield of the sidearm requires at least one X-ray window to block thermal radiation. For the thermal shields, eight foils made of 2 µm polycarbonate coated with 20 nm aluminium on both sides are used, of which two are used per shield, located

on either side of the lid. The foils are carefully positioned and attached using aluminium tape. For the vacuum X-ray window, the commercially available *AP5* window from *Moxtek*, with a diameter of 14 mm, was used during the test run. For the data run, the opening angle of the detector was optimized, and a larger, custom-made X-ray window with a diameter of 28 mm was employed. This corresponds to an opening angle of about 30°, limited by the opening in the μ-metal shield. The window was made from a 125 µm polyimide foil with 100 nm sputtered aluminium on one side. The aluminium layer was deposited in five steps, with intermediate oxidation layers serving as diffusion barriers. The efficiency of the different window configurations is shown in Figure 5.4 for both the test and data runs. Above 10 keV, the overall efficiency is primarily limited by detector absorption. The X-ray windows were not optimized for low-energy transmission, as this energy range is not relevant for QUARTET.

5.2. Detector Readout

The two-stage SQUID readout utilizes commercially available room-temperature electronics for the FLL operation of the SQUIDs, followed by ADCs for signal digitization. Both components are briefly introduced. For the characterization and tuning of the SQUIDs, we developed a Python library to automate the process [17, 18]. This library enabled efficient characterization of SQUID chips for the detector and amplifier modules and allowed for rapid tuning of the SQUID readout at the beamline during both runs, significantly reducing the time required to prepare the readout system. The ADCs used for signal digitization were precisely calibrated to achieve the targeted measurement accuracy of 2 ppm. A new calibration procedure was developed, yielding a bit-wise calibration function. This calibration was later applied during the analysis, marking the first time an ADC calibration was used in the evaluation of data from MMC-based detectors.

5.2.1. Data Acquisition

The SQUID readout uses the commercially available *XXF-1* room-temperature SQUID electronics from *MAGNICON*. One FLL unit is used for every three readout channels and is connected on the room-temperature side of the ribbon cables, which are in turn connected at low temperatures to the amplifier module. The FLL units are connected via cables to connector boxes, which provide power for the FLL units, analog output to the ADCs, and an *RS-232* interface to a computer. The readout is typically tuned at the computer connected to the *RS-232* interface and controlled using the *SQUIDViewer* software provided by *MAGNICON*. A detailed description of the readout electronics, their operation, and the *SQUIDViewer* software is available in the corresponding manual [150].

The analog output of the connector boxes is connected to two 16-channel *SIS3316* ADCs from *Struck*. These 16 bit ADCs have a maximum sampling rate of 125 MHz, a voltage range of ±2.6 V and are synchronized via an *LVDS* cable. They are connected via network cables to a computer, on which the data acquisition is performed using *PAQS*, a program specifically developed for MMC-based detectors [144]. *PAQS* controls and configures the ADCs through a graphical user interface, which is used to set the ADC parameters and start measurements. The acquired data is saved to a disk connected to the computer. A detailed description of *PAQS* and its software architecture can be found in the corresponding work [144].

The signals from the MMC-based detector are saved as triggered events. Each channel is triggered individually using a constant-fraction trigger, which exhibits low time walk for individual signals. The ADCs are typically operated at a sampling rate of 100 MHz, and for each signal, $2^{14} = 16384$ samples are saved, of which one quarter, 4096 samples, are recorded before the trigger and the remaining samples after it. The time window is tuned using oversampling, which corresponds to a digital average over several samples. Typical oversampling ratios of 16 or 32 are used to sufficiently resolve the decay of an MMC signal, which is on the order of a few ms. The SQUIDs are usually operated with a feedback resistance of either $R_{\mathrm{fb}} = 100\,\mathrm{k\Omega}$ or $30\,\mathrm{k\Omega}$, depending on the signal amplitude, to produce signals within the ADC voltage range. To reduce the impact of ADC nonlinearity, the SQUID signal is coupled to the ADCs as an ac-signal for gradiometric channels with an offset that is not sensitive to the detector temperature. Temperature-sensitive channels, as well as the muon signal from the entrance window, are configured to be co-triggered whenever any other channel is triggered.

5.2.2. SQUID Characterization

The characterization of SQUIDs is essential to determine whether they operate correctly. Some SQUIDs do not function at all, while others exhibit significantly higher noise or excessive heat dissipation. The characteristics obtained from a SQUID characterization provide important information for evaluating their suitability for use. Once a SQUID has been characterized, it must be re-tuned during every cooldown. The SQUID bias parameters significantly influence the readout noise, its stability, and the heat dissipation near the detector. They must be carefully adjusted to avoid degrading the overall measurement. A manual characterization of a single SQUID channel typically takes about 30 min, while precise tuning for a measurement requires approximately 10 min. Therefore, automating this process is highly desirable. It not only reduces the time and effort required but also yields more accurate, consistent, as well as digitized results compared to manual characterization and tuning.

A first proof of principle for the automatic tuning and characterization of first-stage SQUID setups was provided during the characterization of the SQUID array chips in preparation

for the amplifier module [17]. A further developed version was subsequently used for semi-automatic tuning of the two-stage SQUID readout during the test run, significantly reducing the time required to prepare the SQUID readout at the beamline. Following this, we developed a proof of principle for fully automatic tuning of two-stage setups, in which the SQUIDs were tuned based on a previously defined FOM [18]. This version was also used for the characterization of the front-end SQUID chips [14]. For the data run, the SQUID readout was initially tuned automatically and then manually optimized to reduce heat dissipation. At present, the developed procedure for automatic characterization and tuning of two-stage setups remains a proof of principle. It requires further optimization to improve reliability, and alternative FOMs for tuning need to be evaluated and implemented.

The automatic characterization and tuning library, called *PySQUID*, is implemented in Python and consists of three classes: *MagniconPy* for controlling the SQUID electronics, *OsciPy* for the readout from an oscilloscope or ADC, and the characterization and tuning class itself. Since only a 32-bit Windows DLL (dynamic-link library) is available to control the SQUID electronics, *ctypes* is used to load the library, and *msl.loadlib* is used to create a 32-bit server on which the library runs, allowing it to be executed also on a 64-bit system. This setup enables the creation of either a 32-bit or 64-bit client on the same computer, depending on the operating system. The Python class then gains access to all functions implemented in the library, most of which are provided and documented through wrapper functions. For the readout, a common interface is defined, consisting of a single function that performs a measurement. This interface was implemented for oscilloscopes from *Keysight* as well as for the *Struck* ADCs used in the experiment. As a result, the automatic characterization can be easily extended to support additional devices by implementing this interface.

The tuning class implements several functions that can be used to tune and characterize the SQUID channel. A channel can be fully tuned, fully characterized, or processed step by step. For each measurement, the SQUID settings are configured accordingly, and a measurement is performed. As an example, the optimization of the bias current of the front-end SQUID and the SQUID array is shown in Figure 5.5. A coarse scan through the bias parameters provides the initial values for a Gaussian regression, which is used to determine the maximum voltage or flux swing. Subsequently, the front-end SQUID and SQUID array characteristics can be measured. The combined two-stage characteristic is then calculated from the previously measured front-end and array characteristics for different combinations of the phase current I_x and bias voltage U_b, from which the optimal setting is selected based on a previously defined FOM.

The result is shown in Figure 5.6, which displays the two-stage characteristic of an automatically tuned SQUID channel. In this case, the front-end bias current I was manually reduced further to lower the SQUID heat dissipation. This procedure also reflects how the

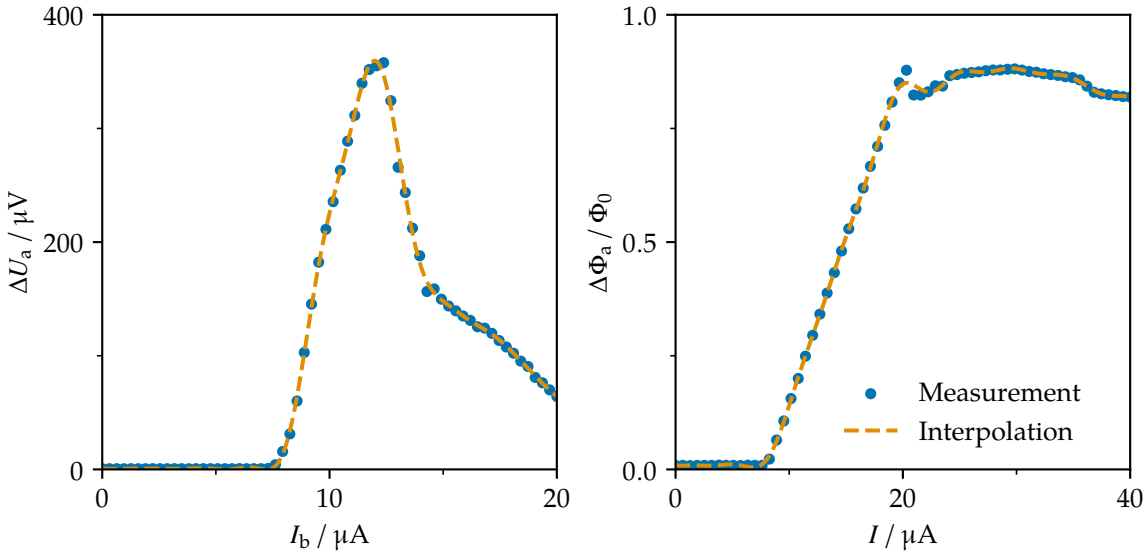

Figure 5.5.: The voltage swing ΔU_a of a SQUID array for different bias currents I_b (left), and the flux swing $\Delta\Phi_a$ of a front-end for different bias currents I (right). Each point represents a measurement, while the dashed lines show the prediction from a Gaussian regression.

SQUID readout was tuned for both runs. The FOM tunes the channel symmetrically, with zero crossings located at one-quarter of a flux quantum Φ_0. This configuration enables stable operation even for instantaneous flux changes of up to half a flux quantum Φ_0. The voltage bias V_b is tuned such that the steepest slope lies on the rising or falling edge at approximately zero voltage. This operating point is expected to exhibit low noise. The resulting characteristic shows one positive and one negative working point per Φ_0 and is roughly centered around zero to ensure stable operation. The front-end bias is manually slightly lowered to reduce heat dissipation near the detector, without significantly decreasing the slope at the operating point.

The Python class used to control the SQUID electronics is not only used during tuning, but also during the measurement. The SQUID electronics include an automatic reset of the integrator, which should be activated when the operating point shifts. This shift is identified by a voltage threshold, typically set to about 3/4 of the voltage corresponding to one Φ_0, in order to prevent the SQUIDs from operating at a different working point. However, this mechanism also prevents the measurement of pulses that exceed the set threshold, as the integrator is automatically reset during the pulse. To enable the measurement of pulses larger than one Φ_0 while still preventing operation at incorrect working points, the automatic SQUID reset of the electronics is configured to the full voltage range of the ADC. In parallel, the SQUIDs are monitored by a Python program, which uses the internal ADC of the SQUID

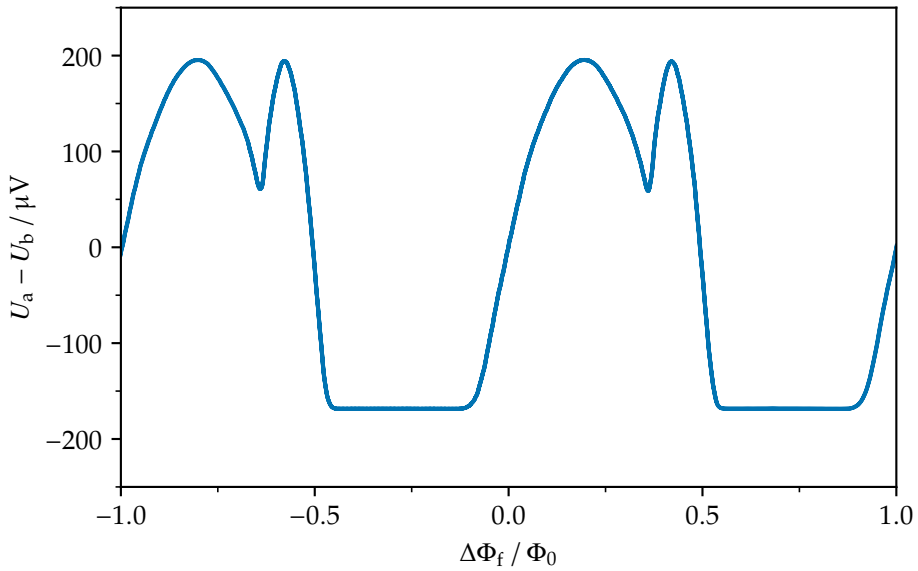

Figure 5.6.: Two-stage SQUID characteristic of a semi-automatically tuned channel. The channel was first tuned automatically, after which the front-end bias was further reduced to decrease heat dissipation. The characteristic corresponds to Figure 5.5, with $I_b = 12.0\,\mu A$ and $I = 16.9\,\mu A$.

electronics to reset individual SQUID channels if the absolute value of the voltage offset remains above a defined threshold for a specified duration.

5.2.3. ADC Calibration

To achieve the targeted measurement accuracy of 2 ppm, the ADCs used for signal digitization must be precisely calibrated. Previous measurements showed an integral non-linearity (INL), defined as the integrated deviation of the ADC response from a linear response, of approximately ±4 bit for the ADCs used in this work. Depending on the pulse height per energy $\partial\Phi_s/\partial E$, one bit typically corresponds to about 2 eV for a feedback resistance of $R_{fb} = 100\,k\Omega$, or about 6 eV for $R_{fb} = 30\,k\Omega$. For the $2p$–$1s$ transition of muonic Li at 18.7 keV, the 2 ppm accuracy target corresponds to a precision of 40 meV, whereas the uncalibrated ADCs exhibit an INL corresponding to approximately ±8 eV for $R_{fb} = 100\,k\Omega$. The INL does not directly translate into an energy uncertainty and can be corrected to some extent by calibrating the energy spectra with a higher-order polynomial. A previous measurement using the same uncalibrated ADCs has shown residuals of the calibration lines below 0.5 eV [145]. However, abrupt jumps in the ADC response cannot be compensated by a polynomial calibration and are expected to fundamentally limit the achievable calibration accuracy. These discontinuities are difficult to characterize and correct, and a dedicated calibration of the ADCs, with signifi-

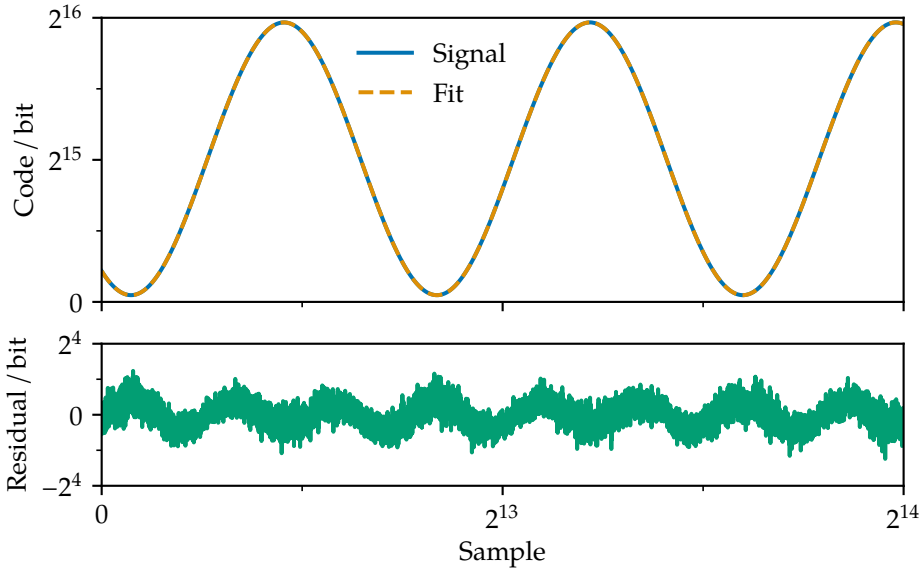

Figure 5.7.: Randomly triggered 1 kHz sinusoidal signal used for the ADC calibration with its sinusoidal fit. The residuals shown for a single trace are dominated by the ADC noise.

cantly improved linearity and explicit correction of the discontinuities, is therefore essential to achieve the targeted 2 ppm accuracy.

The first investigation of the nonlinearity of the used ADC was performed in a previous work using a *2601A* DC voltage source from *Keithley*, in which the general shape of the nonlinearity was measured and found to exceed the specifications of the manufacturer [151]. In a recent work, an *MFLI* lock-in amplifier from *Zurich Instruments* was used to generate a sinusoidal signal, which was digitized by the ADC to evaluate its nonlinearity [152]. This approach was continued in a subsequent work, but employing an ultra-low distortion signal generator to produce a 1 kHz sine wave [153]. In both works, the sinusoidal signals were randomly triggered, phase-aligned, and averaged, and a sinusoidal was fitted at the end to extract the INL, which was then modeled using a spline fit. From the extracted INL, the calibration was estimated to improve linearity by approximately one order of magnitude. However, the resulting ADC calibration was not applied to actual data, and the analysis was performed online without saving the raw traces. In this work, the same hardware was used in combination with a new analysis concept and INL model, resulting in an improvement in the standard deviation of the INL by approximately two orders of magnitude for the calibration. The INL was modeled using a composite model consisting of a bit-flip model and a spline model. Unlike previous approaches, the resulting calibration was applied not only to sinusoidal signals but also to data from both runs, as described in the following chapters.

The same ultra-low distortion signal generator module *EVAL-ADMX1002B* was used in combination with the daughter board *EVAL-ADMX100X-FMCZ* and the controller board *EVAL-SDP-CH1Z* from *Analog Devices*. This generator delivers a 1 kHz sinusoidal signal with a relative total harmonic distortion of −130 dB, corresponding to a nearly ideal sine wave. Signals were randomly triggered using a single channel of the *SIS3316* ADC from *Struck*, controlled by a Python implementation of *PAQS*. The rate of up to approximately 10 Hz was limited by the gigabit bandwidth of the network connection and the Python implementation of *PAQS* requiring that all channels are triggered at once. The signals were acquired and stored per channel as raw data in *brotli*-compressed *parquet* files. For the calibration of the ADCs used in the QUARTET experiment, up to 2^{16} traces per channel were recorded, taking up to approximately 2 h per channel. The same oversampling factor of 16 was applied, along with an active dither to smooth the ADC response, as used during the later measurements. The sinusoidal signal was configured with a voltage swing just below the maximum input range of the ADC. After acquisition, each trace was fitted with a sine function, and the residuals were grouped according to the corresponding ADC code, defined as the digital output of the ADC. A single trace with the fitted sine and the corresponding residuals is shown in Figure 5.7. For each ADC code, the mean, standard deviation, and number of residuals across all traces were calculated. The mean residual represents the INL for that code, while the uncertainty of the INL can be estimated from the standard deviation and the number of occurrences.

Using sinusoidal signals has the advantage of probing nearly the entire ADC code range in a single measurement, while the achievable accuracy is increased by measuring more traces. Assuming a Python implementation of *PAQS* that does not require all channels to be triggered simultaneously, the calibration could be performed within a few minutes, making it well suited to be used directly before and after a run. In contrast, using a DC voltage source to slowly sweep through the ADC code range would take significantly longer and would be heavily affected by both gain fluctuations and the noise of the signal generator, limiting the ability to resolve bit-wise discontinuities in the INL. The implemented approach also differs significantly from the two previous methods using sinusoidal signals, as it does not apply a phase correction before the sinusoidal fit and thus avoids smearing effects. The method is based on the concept of a bit-wise determination of the INL, which enables high accuracy for each bit of the ADC code. Moreover, the trace-wise fit is inherently insensitive to gain fluctuations of the signal generator, as these are corrected by the fit to the sinusoidal waveform itself. This approach is based on the nearly ideal sinusoidal input and presumes that the distortion introduced by the INL is sufficiently small.

The resulting INL curve for a single channel, along with the developed fitted model, is shown in Figure 5.8. The INL exhibits a continuous shape with superimposed discontinuities that occur precisely at multiples of 2^n in the ADC code, clearly indicating their origin within

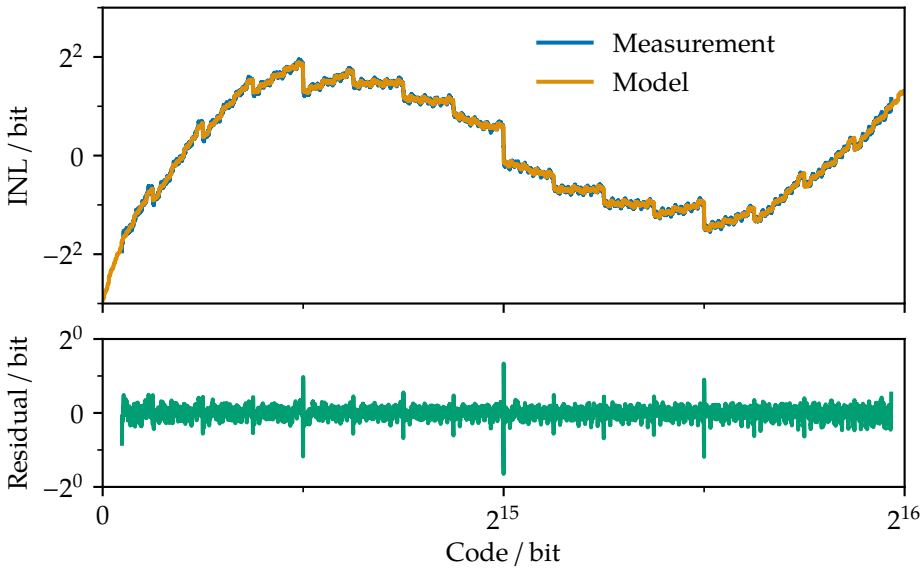

Figure 5.8.: Measured INL from 2^{16} sinusoidal traces, together with the corresponding INL model. The model describes the full ADC code range and provides a pointwise correction for each ADC code, enabling its direct use as a calibration function. The residuals show the smearing effect of the ADC oversampling.

the ADC itself. They have an amplitude of up to about 2 bit and are a significant contribution to the overall INL curve. Consequently, the composite model consists of two components, a bit-flip model and a spline model, fitted using *lmfit*. The discontinuities in the INL are described by a custom-defined bit-flip model

$$f_{\text{bit}}(x) = \sum_n c_n \left(\left\lfloor \frac{x}{2^n} \right\rfloor \bmod 2 \right) \tag{5.1}$$

where n denotes the bit order and c_n are the fit parameters. This model is based on the binary representation of the ADC code and assumes that the discontinuities originate from systematic bit-flips in the digital encoding. Each bit is assumed to contribute identically at every flip, independent of its position in the code range. The remaining, slowly varying component is described by a spline fit. The spline knots are placed such that they do not coincide with the highest order positions of the bit-flip discontinuities, ensuring that the spline does not compensate for the step-like behavior. The fit is performed iteratively, first the spline is fitted to the INL, then the residuals of the spline fit are fitted with the bit-flip model, and finally both components are jointly fitted to the INL as a composite model. During all fitting steps, weights based on the estimated uncertainty of each ADC code are applied. The resulting model describes the full ADC code range and enables a bit-wise correction of the INL, which can be directly applied to measurement data.

The model describes the measurement accurately, but distinct artifacts from the oversampling are visible in the residuals at the discontinuities, as shown in Figure 5.8. The oversampling corresponds to an averaging that is applied at the ADC before the calibration, and its effective range depends on the slope of the input signal. As a result, the intended bit-wise calculated INL becomes an average, and the otherwise sharp steps are smeared out. For the ADCs used in this work, the oversampling cannot be disabled and is also applied during the measurements with the MMC-based detectors. Consequently, the INL model with sharp steps is expected to provide a more accurate description of the true INL than the sinusoidal measurement itself, particularly for arbitrary signals. For the 16 bit ADCs used in this work, the best fit was obtained with a model using 64 spline knots. The highest 13 bit can be modeled with sufficient accuracy, while the lowest 3 bit are smeared out due to the oversampling.

In total, four ADC calibrations for all 32 channels of the two ADCs within approximately one month, before and after the data run, were acquired, each using between 2^{10} and 2^{16} traces per channel. For each dataset, the INL was modeled using the described method, and the corresponding calibration function was extracted. Each calibration was then applied to every calibration dataset to evaluate the INL of the calibrated ADCs. As a FOM, the standard deviation of the filtered INL was calculated. The results from different measurements and channels indicate that, in order to avoid limitations from ADC noise and statistical uncertainties, approximately 2^{16} or more traces should be acquired. A slight time dependence of the calibration was observed, which does not appear to be related to temperature variations. The developed calibration improves the FOM by approximately two orders of magnitude, from about 2 bit to 0.02 bit, for signals similar to those used in the calibration. From the comparison of the different calibration measurements, a calibration using 2^{12} traces recorded directly after the data run was found to be best suited for the run. However, for one channel, the calibration measured before the data run was used instead due to a likely faulty electrical connection during the measurement taken after the data run.

In addition, measurements were performed using sinusoidal signals with an reduced amplitude and an shifted offset to investigate the dependence of the input signal on the INL. These tests showed that, although the corrected INL no longer exhibits visible discontinuities, the FOM improves by only one order of magnitude and shows a quadratic-like shape. This artifact is likely caused by the oversampling of the sinusoidal signal, as the averaging depends on the second derivative of the input. Given that the discontinuities are expected to be corrected by approximately two orders of magnitude, the remaining low-order polynomial residuals introduced by the method with oversampling are expected to be further corrected during the energy calibration during the data analysis. The use of ADCs without oversampling should be considered for future QUARTET measurements, as this may lead to a significant improvement

in ADC calibration using the same developed method. The calibration appears to be fundamentally limited by the oversampling of the ADCs, and a precise evaluation of how accurately the discontinuities are corrected and how large the remaining low-order residuals are is not possible. Nevertheless, compared to previous measurements without ADC calibration, the achieved calibration is expected to be approximately two orders of magnitude better, with the discontinuities corrected accordingly, thereby meeting the QUARTET requirements for reaching the target accuracy of 2 ppm.

5.3. Beamline Measurements

While the development and characterization of the MMC-based detectors was carried out at KIP in Heidelberg, the cryostat with the detector was transported to PSI in Villigen, Switzerland, several weeks prior to each of the scheduled runs at the $\pi E1$ beamline. There, it was reassembled and optimized at a staging area located near the beamline. For the actual measurements, the cryostat was warmed up, disassembled, craned into the experimental area at the $\pi E1$ beamline, reassembled, and cooled down. It was then brought back into full operation as quickly as possible to meet the constraints of the tight run schedule.

5.3.1. Staging Area

To ensure reliable operation of the detector during the run at PSI, the cryostat with the detector was transported approximately one month in advance and reassembled at a staging area adjacent to the beamline, also known as *Tanzboden*, prior to each scheduled run. There, the setup was thoroughly tested and optimized for the subsequent measurements to ensure the best achievable performance and to exclude any potential damage caused during transport. The available time would have allowed for necessary repairs and complete re-optimization at the staging area without impacting the scheduled beamline measurements. The fully assembled setup at the staging area is shown in Figure 5.9.

At the staging area, the setup was thoroughly optimized for the corresponding run to achieve the best possible detector performance for the planned measurements. Initial tests confirmed the general functionality of the detector, and no damage resulting from the transport was found. The SQUID settings were then automatically tuned and manually adjusted to ensure stable operation with low noise and minimal heat dissipation. The heat dissipation behavior of individual SQUIDs was characterized, and channels exhibiting the highest heat dissipation were temporarily disabled to investigate the effect on the pulse height and energy resolution of the remaining channels. However, no significant improvement was observed, and therefore no channels were deactivated during the actual measurements. For different SQUID bias parameters, the resulting energy resolution and overall detector performance were

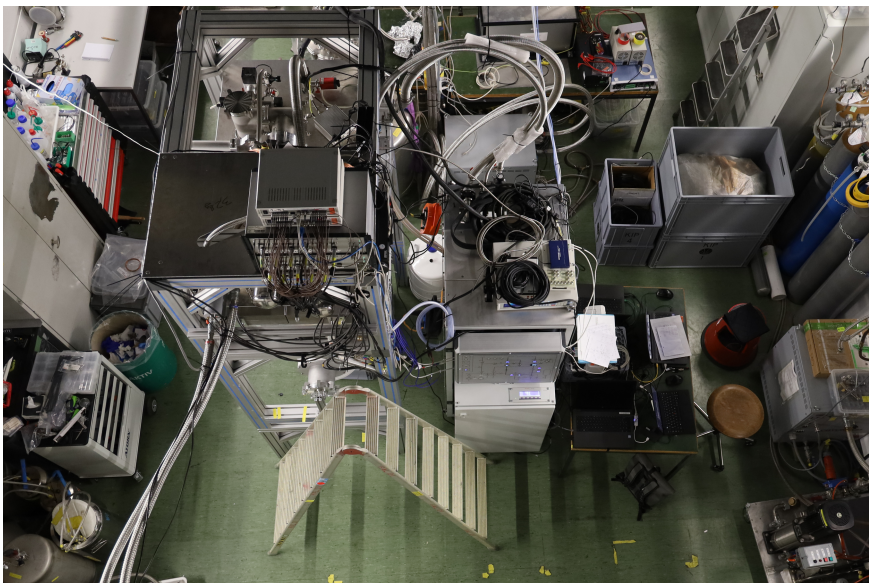

Figure 5.9.: Detector setup at the staging area, known as *Tanzboden*, prior to the test run. The setup was optimized approximately one month in advance to ensure successful operation during the run.

systematically evaluated, and the front-end bias currents were lowered to reduce the detector temperature. For the preparation of a persistent current, the heater pulse was optimized to reliably prepare persistent currents. Subsequently, different persistent currents were prepared, and the resulting performance was evaluated to determine the optimal configuration for achieving the best energy resolution.

The cryostat temperature was stabilized using a PID controller to suppress long-term temperature drifts. Electrical noise contributions from the various electronic components of the setup were investigated, and different grounding schemes were tested to further reduce the overall noise level of the detector system. For the data run, the ADC calibration was performed on site, and the corresponding measurement procedure was optimized. The online analysis was tested in preparation for the run. The opening angle of the detector was evaluated to prevent shadowing effects, and tests with the target chamber were conducted to determine the minimal achievable distance between the detector and the target. Various calibration sources were tested at different activities, and their intensities were adjusted to achieve optimal count rates. Tests with an X-ray tube and different targets were also performed, and the tube parameters were individually optimized for each target to reach the desired event rate at the detector.

5.3.2. Muon Beamline

For the beamline measurement, the cryostat was warmed up, disassembled, and craned in several parts into the beamline area. During craning, the detector and the sidearm remained mounted inside the cryostat to enable a faster cooldown to low temperatures. To support the weight of the mounted cryostat sidearm during craning, rubber spacers were inserted in advance into the sidearm and between the cryostat shields. After craning, the spacers were removed, and the cryostat was reassembled, evacuated, and prepared for cooldown. During the test run, the cryostat was manually aligned with the target chamber and to the beamline height of 1.5 m before its cooldown. For the data run, the cryostat was mounted on a frame with wheels and height-adjustable feet, allowing alignment during cooldown after the beamline and target chamber had been prepared. The cooldown to 4 K took approximately 30 h, followed by an additional 5 h to reach and stabilize at a temperature of 12 mK. The fully assembled experimental setup at the beamline during the test run is shown in Figure 5.10.

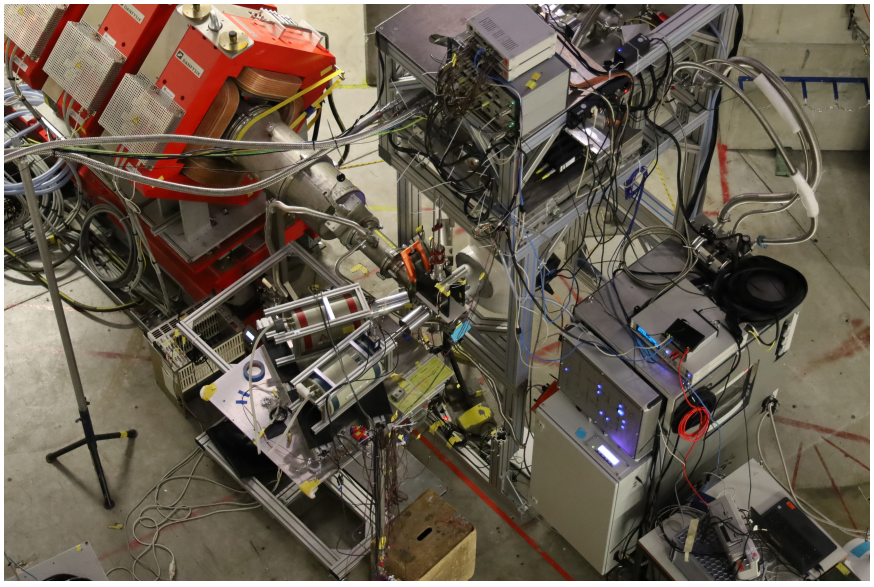

Figure 5.10.: Experimental setup at the $\pi E1$ beamline during the test run. The MMC-based detector is positioned close to the muon target, while two germanium detectors are used on the other side for tuning the muon beam.

During cooldown, the detector readout and automatic SQUID tuning were prepared. For the data run, the ADCs were also calibrated. In parallel, other parts of the setup, including the germanium detectors for tuning the muon beam, the readout of the muon entrance scintillators, and the muon targets were set up. This also included the preparation of the data acquisition system *MIDAS* [154], which was used for metadata recording and for all other detectors than the MMC-based detector. After the cryostat reached a temperature below 1 K, the SQUIDs were automatically retuned and subsequently adjusted manually. The optimized

persistent field current of 80 mA was then prepared, and the cryostat was stabilized at a base temperature of 12 mK. For the data run, the first muonic X-rays were recorded within 36 h of initiating the cooldown of the cryostat.

A photograph of the target chamber during the data run, along with the targets used during the test run, is shown in Figure 5.11. Muons from the beamline pass through an entrance scintillator and are stopped in the target located inside the target chamber, which can be exchanged to a different target on a target ladder without venting the target chamber. The resulting muonic X-rays are detected by both a germanium detector, used for beam tuning, and the MMC-based detector. During the data run, the cryostat sidearm was positioned approximately 2 cm from the target chamber, with the center of the muon target located about 5.5 cm inside the chamber. This resulted in a total distance of approximately 13 cm between the target and the MMC-based detector. For the test run, the distance was about 15 cm, and was subsequently reduced and optimized for the data run, including an increase in the opening angle seen by the detector from about 15° for the test run to about 30° for the data run. An X-ray tube and radioactive calibration sources were used for energy calibration. During the test run, the X-ray tube was mounted to irradiate a target inside the target chamber, so that the target ladder held not only muonic targets but also dedicated targets for X-ray excitation. For the data run, a separate source holder was mounted on the target chamber, positioned between the chamber and the cryostat sidearm, and used to hold both calibration sources and the X-ray tube with its target.

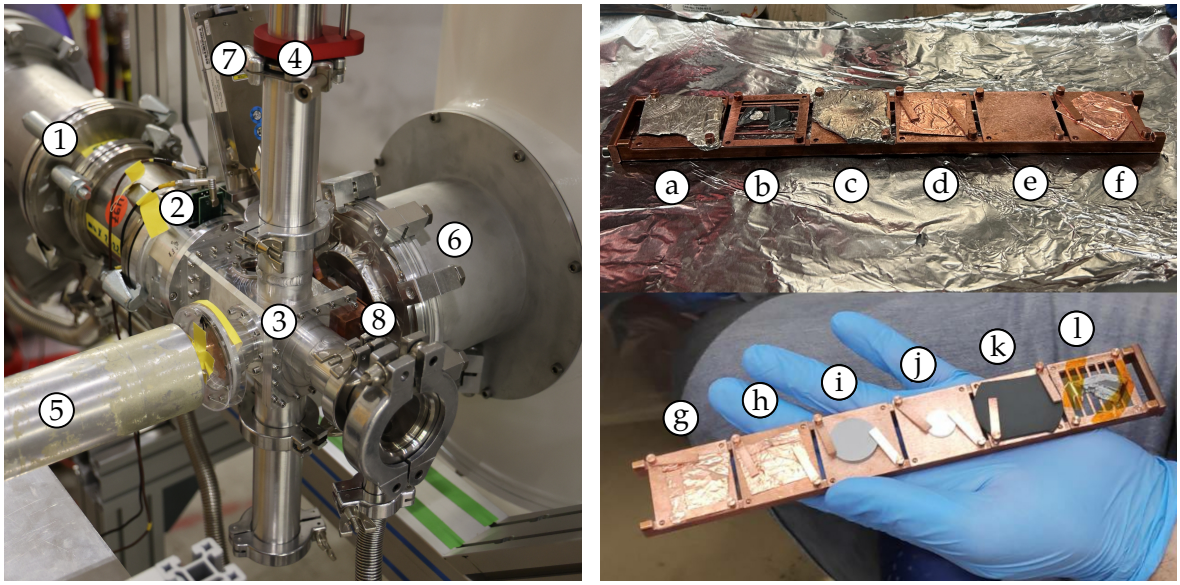

Figure 5.11.: Photographs of the target chamber during the data run (left) and the targets used during the test run (right) [7]. Muons from the ① muon beamline pass through the ② entrance scintillator and are stopped in the target located in the ③ target chamber. The target can be exchanged via the ④ target ladder. The resulting X-rays are detected by a ⑤ germanium detector for beam tuning and the MMC-based detector located in the ⑥ cryostat sidearm. An ⑦ X-ray tube and additional calibration sources, mounted on the ⑧ source holder in front of the detector, are used for energy calibration. The two target ladders used during the test run held the following targets: ⓐ–ⓕ ^{7}Li, Mo and Ag, ^{6}Li, ^{12}C, Cu, ^{13}C, and ⓖ–ⓛ ^{13}C, ^{12}C, Be, BeO, B, Mo.

Chapter 6.

Data Analysis

The triggered signals, acquired with *PAQS*, must be analysed to obtain energy spectra. The analysis typically begins with a data reduction, in which the signals are fitted and the volume of the raw data is reduced from several TB to a few GB of fit results and metadata. In a subsequent data selection, the processed data is filtered and selected based on the fit results, and the different pulse families are identified. Data selection relies on the well-defined, typically energy-independent pulse shape of an MMC, as well as on the relative timing between signals. Finally, a data correction is applied to account for temperature fluctuations and gain drifts, and to perform an energy calibration, yielding the final energy spectrum. This processing must be performed online, to some extent, for monitoring and preliminary evaluation during the QUARTET run, and in full detail offline to determine the exact energy positions of the muonic lines with the highest possible accuracy. The analysis must be energy independent, reliably distinguish different pulse shapes, correct gain and temperature drifts over time, apply the ADC calibration, and ensure both accurate energy calibration and high energy resolution.

An existing data reduction library is *DARQ*, a Python library, developed and optimised for the ECHo experiment [155]. This library ensures energy-independent data reduction and includes an initial filtering step based on the timestamps of signals [156]. The analysis assumes very high statistics per pixel, negligible timing jitter due to a fast signal rise time, and a small energy range. It enables a nearly automated data reduction of individual *PAQS* measurements into tabular data containing the fit results and metadata. However, *DARQ* cannot combine multiple measurements, does not apply an ADC calibration, and does not include subsequent analysis steps beyond data reduction. These steps are not part of a library and instead distributed across several independent scripts. *DARQ* and its analysis procedure are described in the corresponding work [155]. Despite these assumptions and limitations, the same library was also used for high-resolution X-ray spectroscopy, typically with relatively low statistics and non-negligible timing jitter. In addition to the original *template* fit without timing jitter correction used in *ECHo*, a fit based on the matched filter, called *opti* fit, was added [107, 157], and the *template* fit was modified to account for timing jitter [158]. Both implementations showed improvements compared to the original *template* fit but exhibit

amplitude-dependent artefacts. For QUARTET, a robust and amplitude-independent fit with timing jitter correction is required.

This chapter describes the development of *fitfiles*, an open-source Python library for data analysis [4]. As an example, the muonic Li measurement of the data run was analysed. This library provides a complete analysis chain for triggered signals, from raw data to calibrated energy spectra. Multiple low-statistics measurements can be combined and analysed iteratively, including during an ongoing measurement. It applies amplitude-independent fits, achieves significantly improved performance through *multiprocessing*, and applies the ADC calibration. In addition, we implemented a signal generator, capable of generating arbitrary signals and pile-up pulses, which can be analysed in the same way as measured data [15].

6.1. Data Reduction

The concept of *fitfiles* is to first index all raw data of multiple measurements and directly create a *pandas.DataFrame* object, which is a two-dimensional table. It is referred to as a *fitfile* once it contains fit results. Each row represents a measured signal, while each column stores a specific type of information. A unique index is defined by the data folder, measurement name, channel, polarity, and signal number, from which the raw data of any signal can be loaded. The *fitfiles* library provides a collection of functions that operate on a *fitfile*, typically returning a modified version with additional columns. A subset of the *fitfile* can be selected using a *pandas.Series* mask and passed to functions. For functions that can be parallelised, *multiprocessing* is employed to process signals in smaller batches and per pixel, which significantly accelerates computationally intensive operations, particularly during data reduction.

The *fitfile* library provides functions to load individual signals or to yield multiple signals. It also includes functions to extend and append to a *fitfile* while maintaining the dataset structure. Categorical data is stored efficiently using the *pandas* category data type. A *fitfile* is typically saved as a *Brotli*-compressed *parquet* file. Multiple files can be loaded and combined into a single *fitfile*, allowing the data to be split across several files and partially loaded when needed. To maintain unique column names, affixes such as prefixes or suffixes are applied in *snake_case*. This enables iterative data analysis while keeping datasets consistent, as the unique *fitfile* index preserves row integrity and issues warnings when files with identical column names but different content are combined.

Since the index of each *fitfile* entry contains all necessary information to access the corresponding measurement data, all functions can load raw data when required. When a pulse is loaded, an object of the *fitfiles.Signal* class is returned. This class represents either an individual signal or a template, the latter corresponding to the average of multiple signals. A *Signal* object contains the calibrated raw data, header information, ADC settings, various

methods, overloaded operators, and all metadata of the corresponding *fitfile* entry. Commonly used methods, for example, plot the signal in physical units, calculate its mean value, or compute the area relative to the pre-trigger offset. Another important method computes the PSD of the signal and returns an instance of the *fitfiles.Frequencyspectrum* class. This class is primarily used to extract the noise spectrum, defined as the average PSD of many randomly triggered signals without pulses. Similar to the *Signal* class, the *Frequencyspectrum* class contains data, header information, various methods, and overloaded operators. For example, commonly used methods plot the frequency spectrum or return a *Signal* object containing the corresponding noise with a random phase.

6.1.1. Indexing

The first step of the analysis is to index the raw data. The data can either be generated by *fitfiles.generator*, as described later, or recorded by *PAQS*. The *PulseReader* class from *fitfiles* handles both data types, using its own pulse reader for generated data or importing the *PulseReader* class from *darq.pulseprocessing* to read signals from *PAQS* measurements. When loading signals, it can also apply an ADC calibration. For *PAQS* measurements, *fitfiles.paqs* provides several functions to search for and open data. Data within folders can be searched recursively, returning a list of measurement paths that can be passed to another function to create the corresponding *fitfile*. Additional functions recover crashed measurements, summarise the measurements, combine and convert log entries, and list all ADC settings. In particular, it must be ensured that only measurements with identical ADC settings are evaluated together.

For preliminary online data reduction, *fitfiles* can fit only new signals, provided that the data is accessible during the measurement. Currently, *DARQ* cannot open a *PAQS* measurement with its *PulseReader* class during data acquisition, as this interrupts the measurement. For the two runs, the online analysis was therefore based on the downsampled online data reduction provided by *DARQ*, which could be loaded and converted during the measurement using the corresponding function from *fitfiles.paqs*. The result is a *fitfile* fully compatible with the data selection and correction functions provided by *fitfiles.analysis*, as described later. However, raw data should not be loaded of such a *fitfile*.

6.1.2. Templates

A template is an object of the *fitfiles.Signal* class, typically calculated as the average of many signals and ideally representing the noise-free, amplitude-independent pulse shape of a pixel. Nearly all fitting procedures require a template to accurately determine signal parameters. Templates for multiple pixels are stored in a *pandas.DataFrame* and managed by the functions in *fitfiles.templates*. They are generated by a function that creates a template for each pixel

present in the *fitfile* from all of its signals. Therefore, the *fitfile* should be masked to contain only the pulses selected for template generation. Once the *pandas.DataFrame* of templates has been generated, several implemented functions can plot, save, and load templates or evaluate specific properties, such as pulse height, FOM, or an exponential fit to the pulse shape of each template. A measured pulse and the corresponding template, calculated as the average of many such pulses, are shown in Figure 6.1. For a signal, the FOM is defined as the template amplitude divided by the mean standard deviation of its pre-trigger. While a single signal can be used as a template, a suitable template should be nearly noise-free, with an FOM of several thousand, typically around 10^4, requiring several thousand signals.

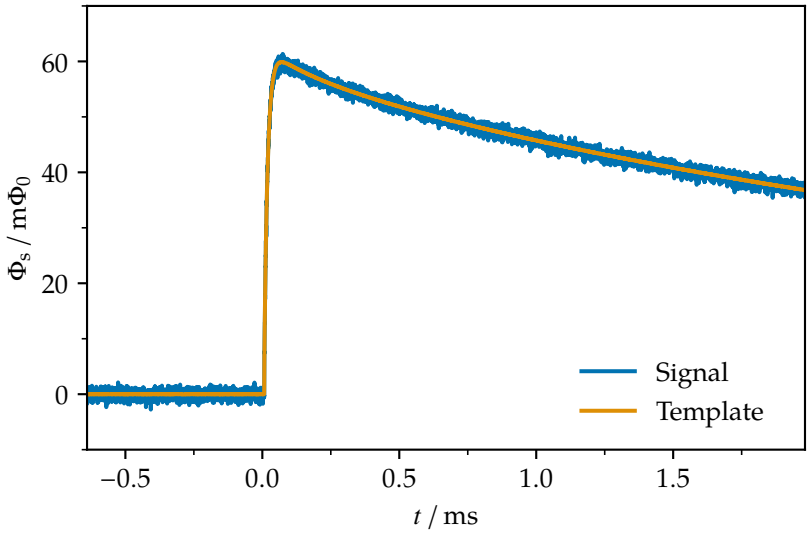

Figure 6.1.: A single signal and the corresponding template obtained as the average of many such signals. The data was recorded during the data run at an energy of $E \approx 5.9\,\mathrm{keV}$, corresponding to the ^{55}Mn K_α line of an ^{55}Fe source. The template has an FOM of about 10 000.

For the two runs, the test run and data run at PSI, templates were created by first performing a *general* fit, as described later. By selecting signals within a small parameter space around a specific line, defined by their pulse area and height, pile-ups were suppressed, as they generally deviate from the otherwise linear scaling in one of these parameters. These selected signals were then used to generate an initial template, which was subsequently applied to fit signals in the corresponding energy range, yielding the fit parameters χ_0^2 and timing jitter j. The selection was further refined using the χ_0^2 values, omitting for each pixel the signals with the largest values within a narrow amplitude range around the template amplitude. The timing jitter j was used to correct the relative timing jitter during template generation. The process was repeated iteratively five times, each time with a decreasing amplitude range. For

the Li measurement of the data run, the templates of the final iteration were generated from about 1×10^4 signals each and reached an FOM of about 9000.

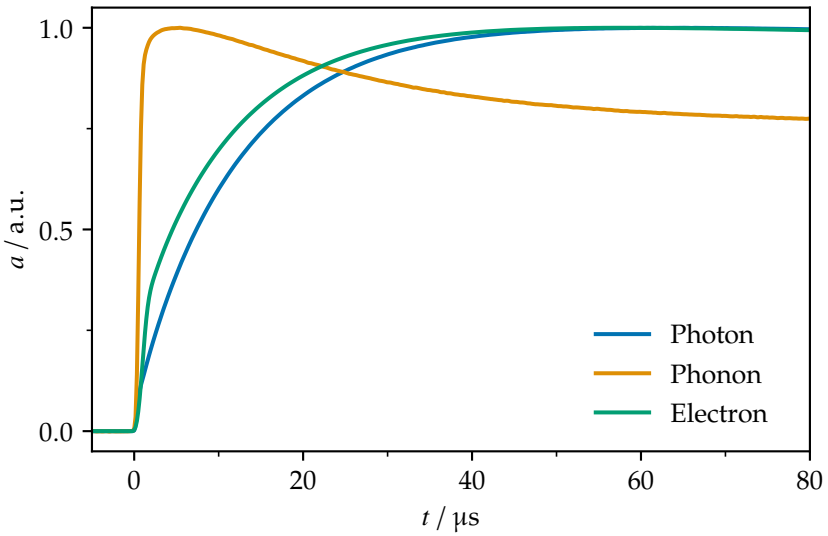

Figure 6.2.: Trigger region of three different templates, generated from distinct pulse families. The templates are aligned for timing jitter and normalized to an amplitude $a = 1$. The photon template originates from a photon stopped in the absorber, the phonon template from athermal phonons in the substrate induced by a Michel electron, and the electron template from a Michel electron depositing energy in absorber, sensor, and substrate.

After the template had been generated and applied in a subsequent fit, as described later, additional templates at other energies could be generated more easily. Signals with different pulse shapes could be identified from their χ_0^2 and timing jitter j values and these signals were then used to generated templates for other pulse families. The different pulse families, together with their normalized χ^2 and timing jitter j distributions, are shown later in Figure 6.11. The trigger region of three, timing jitter aligned templates, is shown in Figure 6.2. The χ_0^2 values were used to filter signals that were not sufficiently described by the template, and the selection was iteratively refined to obtain templates for other pulse shapes. The photon template was generated at the ^{55}Mn K_α line of an ^{55}Fe source, representing the pulse of a photon stopped in the absorber with the previously described well-defined, amplitude-independent pulse shape. Its rise time is determined by the thermal bottleneck between absorber and sensor, and its decay time by the bottleneck to the thermal bath, as described in Chapter 3.

The phonon template, as discussed later, originates from athermal phonons in the substrate, typically produced by a Michel electron. The athermal phonons thermalize in the sensor and the rise time is limited by the acoustic mismatch between substrate and sensor and the sensor thermalization. It exhibits an additional fast decay component caused by the thermalization

to the absorber, limited by the thermal bottleneck between sensor and absorber. This template is approximately amplitude independent.

The electron template originates from a Michel electron depositing energy in the absorber and substrate, and in some cases also directly in the sensor. Since most of the energy is deposited in the absorber, the resulting pulse shape is similar to that of a photon. However, energy deposited directly in the sensor, or transferred from the substrate into the sensor, introduces a fast rise time in the signal with a small relative fraction of the pulse height. The pulse shape is energy dependent, as it reflects the relative energy deposited in the sensor. Accurate amplitude-independent fits and timing-jitter corrected templates are required to identify these subtle changes in the pulse shape.

6.1.3. Noise Spectra

While a template is sufficient for some fits, fitting the signals in the time domain, more accurate fits require a noise spectrum, represented by an object of the *fitfiles.Frequencyspectrum* class. A noise spectrum is calculated as the average of many frequency spectra, each obtained from the PSD of a signal without a pulse, identified based on their standard deviation. The frequency range is thus defined by the number of samples and the effective sampling rate of a signal. Similar to templates, noise spectra are stored for each channel in a *pandas.DataFrame* and are managed by the functions in *fitfiles.noisespectra*. For example, implemented functions can generate noise spectra, plot them in physical units, save or load them. A frequency spectrum of a signal without a pulse, and the corresponding noise spectrum calculated as the average of many such spectra, are shown in Figure 6.3.

To obtain a representative noise spectrum of the time-independent noise, all signals without a pulse are typically included. For the two runs, signals were selected in a single iteration based on their standard deviation of the signal σ and pre-trigger σ_0 values after a *general* fit. Only a broad cut was applied, omitting the highest σ values to suppress outliers while avoiding artificial modifications of the resulting noise spectra. For the measurements of the data run, each noise spectrum was generated from about 3×10^4 signals.

6.1.4. Fitting

A fit is performed with a dedicated function from *fitfiles*, which loads each signal and applies a corresponding function for each selected fit to it. These functions return fit results, which are then stored as new columns in the *fitfile*. Consequently, any operation on a signal is typically implemented as a fit, even if it is not a conventional fitting procedure. This approach allows all operations requiring raw data to be applied at once. Currently, eight fits are implemented in *fitfiles*: *header*, *general*, *template*, *jtemplate*, *opti*, *matched*, *wmatched*, and *shape*.

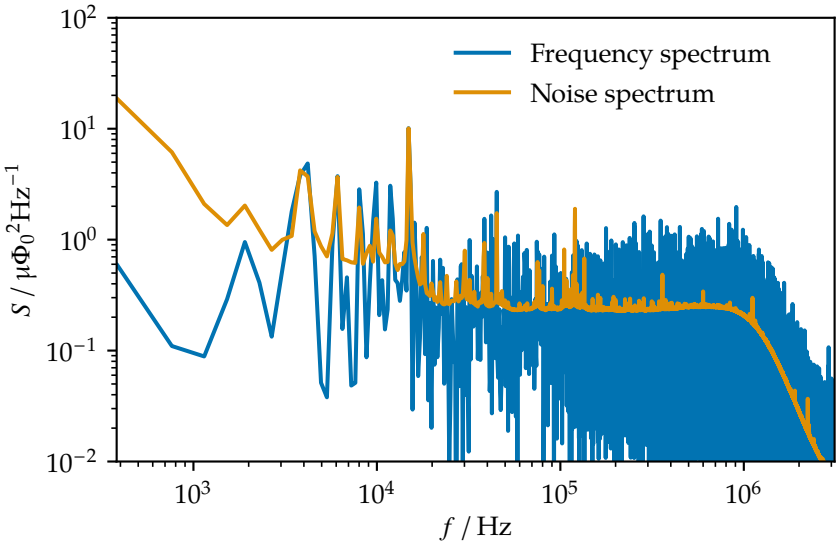

Figure 6.3.: Frequency spectrum of a signal without a pulse and the corresponding noise spectrum obtained as the average of many such spectra. The data was recorded during the data run.

For the two runs, the *header* and *general* fits were first applied to extract metadata and general signal properties. For template generation, noise spectra generation, and subsequent data reduction, only the *wmatched* fit was applied, with a maximum timing jitter of $j_{\max} = 64$ samples. This fit provides the best energy resolution while being fast and reliable, as demonstrated later. The *shape* fit was used for the pulse-shape analysis of the new *maXs 30-56-14* detector.

Header Fit

The *header* fit loads all metadata from the signal that is not yet present in the *fitfile* and adds it as new columns. This is required because *DARQ* stores the metadata together with the binary signal data for each signal. For a *DARQ* measurement, this includes: the timestamp, the timestamp of the previous signal, the CPU time, the ADC settings and ADC temperature, the signal offset, height, and area, its characteristic timescale, its relative onset to the trigger, the average count rate on the channel, the last comment number set during the measurement, the coincident temperature information and its uncertainty, and, for the two runs, also the last and previous time differences to events in the muon entrance scintillator as well as the lower absolute value of both. Some of this information may be estimated and therefore has reduced accuracy.

General Fit

The *general* fit applies several functions defined as methods of the *Signal* class. It depends only on the pre-trigger, defined as the number of samples before the trigger, typically the first 4000 samples. It does not require a template and is particularly useful for masking signals during the initial generation of templates or noise spectra. It calculates the mean, standard deviation, and linear slope of the signal, as well as the corresponding values only for the pre-trigger. In addition, it determines the minimum and maximum of the signal, the maximum absolute difference between two samples, the height and area relative to the pre-trigger, and whether the signal is clipped by the ADC code range or saved without binary data.

Template Fit

The *template* fit is a least-squares fit that estimates the amplitude a and offset o under the assumption that the offset-corrected pulse is proportional to the template, with the proportionality factor given by the amplitude. The pulse P with samples p_i is described as

$$p_i(t) = a\, t_i(t) + o \tag{6.1}$$

where T is the template with samples t_i. This fit assumes perfect time alignment between the pulse and the template, without any timing jitter. The unnormalised χ_0^2 is defined as

$$\chi_0^2 = \frac{1}{N} \sum_i [p_i - (a\, t_i + o)]^2 \tag{6.2}$$

where N is the number of samples. Minimisation with respect to a and o yields

$$a = \frac{\mathrm{cov}(P, T)}{\mathrm{var}(T)} \tag{6.3}$$

$$o = \bar{P} - a\, \bar{T} \tag{6.4}$$

where cov and var denote the covariance and variance, respectively, and $\bar{P}$ and $\bar{T}$ are the mean values of the pulse and the template. Since this fit does not account for timing jitter, it should not be used if the timing jitter is non-negligible. The output parameters of its *fitfiles* implementation are the amplitude a, offset o, and χ_0^2.

The *jtemplate* fit extends the *template* fit by including a timing jitter correction between the signal and the template, up to a maximum jitter value $\pm j_{\max}$. The template is trimmed by $j_{\max}$ samples at both ends, while the signal is shifted in time by an integer number of samples within the range $\pm j_{\max}$ and trimmed accordingly to match the template length. A *template* fit is then performed for each shifted signal, yielding fit parameters as a function of the jitter j.

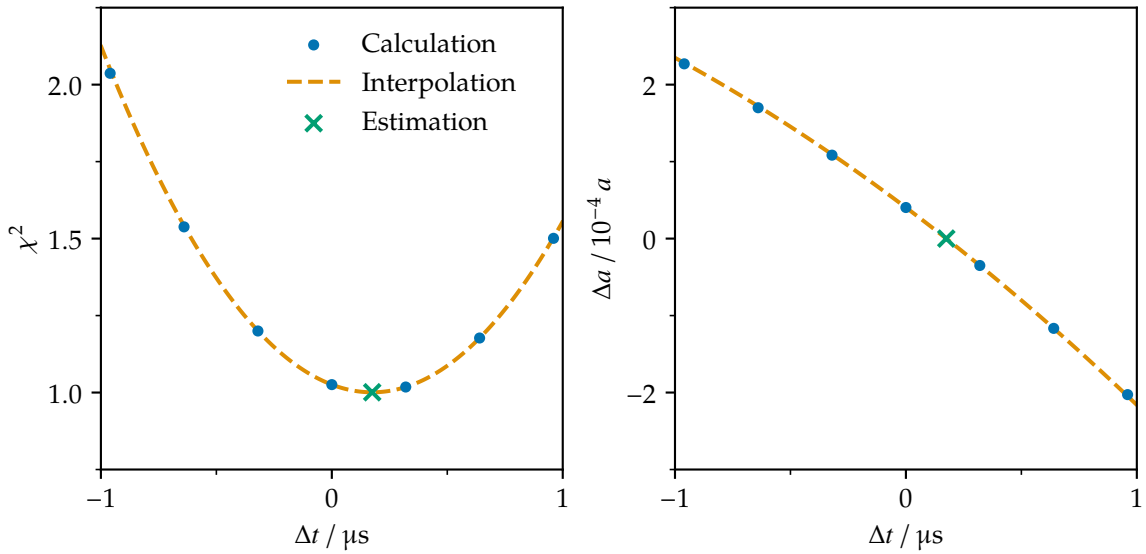

Figure 6.4.: Timing jitter correction of the *jtemplate* fit, evaluated for generated data. The *template* fit is calculated for the shifted and trimmed signal within a maximum jitter $\pm j_{\max}$. The jitter is estimated by interpolation around the minimum χ_0^2 (left), and the corresponding amplitude is determined from the interpolated value at this jitter (right).

The optimal parameters are determined by identifying the jitter value with the lowest χ_0^2 and its two neighbouring values, and calculating the corresponding quadratic function through these three points. The optimal jitter is then estimated with sub-sample precision as the minimum of this quadratic function. The amplitude is interpolated in the same way, using the amplitudes corresponding to the three χ_0^2 values to estimate the amplitude at the optimal jitter. This process is illustrated in Figure 6.4. The *jtemplate* fit is significantly more computationally expensive than the *template* fit, with runtime scaling linearly with the maximum jitter $j_{\max}$, which is typically $j_{\max} = 16$. It returns an amplitude a, offset o, and timing jitter j.

For the *jtemplate*, *opti*, *matched*, and *wmatched* fits, a χ_0^2 is calculated from the amplitude and jitter values. It is defined as the unnormalised mean-squared difference between the jitter-corrected template and the signal, evaluated for the full signal as well as separately for the pre-trigger, trigger, and post-trigger regions. The trigger region typically corresponds to samples 4000-4384. Sub-sample precision is achieved by shifting the signal relative to the template by integer jitter values, with the remaining fractional jitter accounted for by interpolating the template at sub-sample resolution.

Matched Filter

A matched filter is given by the correlation of the template with a signal. A whitened matched filter extends this by whitening the noise, thereby maximising the SNR in the frequency

domain. The whitened matched fit minimises the unnormalised χ_0^2 in the frequency domain, given by

$$\chi_0^2 = \sum_\nu \frac{\left|\tilde{P}(\nu) - a\,\tilde{T}(\nu)\right|^2}{S(\nu)} \tag{6.5}$$

where $\tilde{P}(\nu)$ and $\tilde{T}(\nu)$ are the Fourier transforms of the pulse and the template, and $S(\nu)$ is the PSD of the stationary noise [159]. Minimising χ_0^2 yields the amplitude

$$a = \sum_\nu \tilde{F}(\nu)\,\tilde{P}(\nu) \tag{6.6}$$

with the matched filter in the frequency domain

$$\tilde{F}(\nu) = \frac{\tilde{T}^*(\nu) \,/\, S(\nu)}{\sum_\nu \tilde{T}(\nu)\,\tilde{T}^*(\nu) \,/\, S(\nu)} \tag{6.7}$$

where $\tilde{T}^*(\nu)$ denotes the complex conjugate of $\tilde{T}(\nu)$. The filter $\tilde{F}(\nu)$ can be applied directly in the frequency domain or transformed into its time-domain representation $F(t)$. In practice, the filter is usually applied in the time domain by convolution with the conjugated, time-reversed filter, which is mathematically equivalent to a correlation.

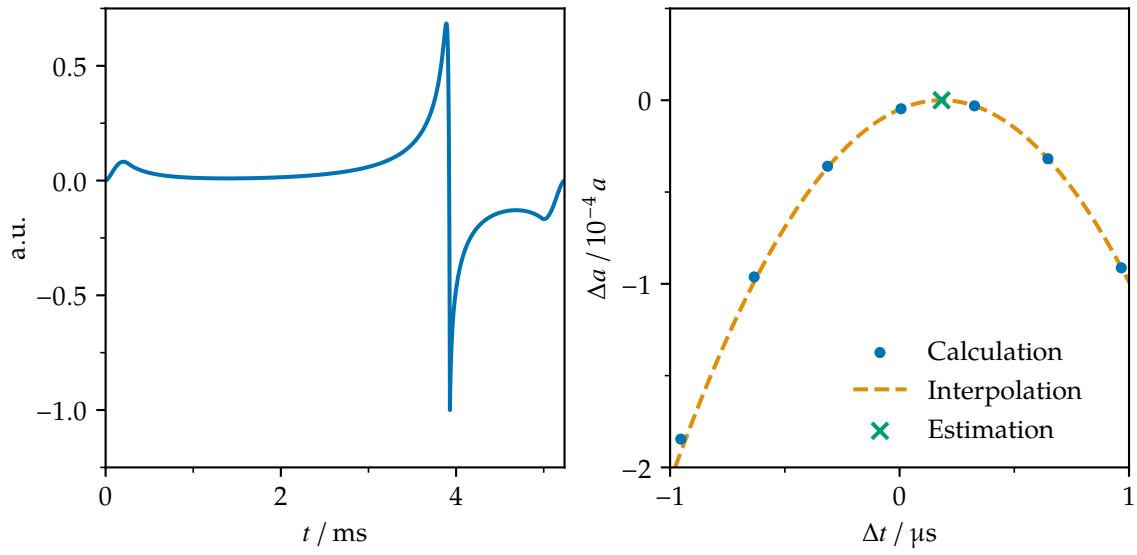

Figure 6.5.: The whitened matched fit *wmatched*, evaluated for generated data. The filter is calculated from the template and noise spectrum (left). Its convolution with a signal yields a peak, from which the amplitude and jitter are determined (right).

The *wmatched* fit applies the whitened matched filter as the convolution of the pulse $P(t)$ with $F(t)$. The time-domain filter $F(t)$ is obtained from the template $T(t)$ by trimming by the maximum jitter $j_{\max}$, whitening in the frequency domain after applying a window, time-

reversing, and finally applying the same window again. Similar to the *jtemplate* fit, the amplitude a and jitter j are determined with sub-sample precision by calculating the corresponding quadratic function through the maximum and its two neighbouring samples of the convolution. The amplitude is normalised by comparison with the convolution of the template $T(t)$ and the filter $F(t)$. This process is illustrated in Figure 6.5. The *wmatched* fit provides a jitter-corrected result and is typically significantly faster than the *jtemplate* fit. It returns an amplitude a, timing jitter j, along with the corresponding unnormalised χ^2_0 values.

The *matched* fit corresponds to the *wmatched* fit without noise whitening. It provides a fast, jitter-corrected result that does not require a noise spectrum, but generally yields a reduced resolution. The *opti* fit is a time-domain implementation of the *wmatched* fit, in which the convolution is evaluated only for jitter values within the maximum jitter $j_{\max}$ [107]. Only for very small maximum jitter $j_{\max}$, the time-domain convolution can be faster than its frequency-domain implementation.

Shape Fit

The *shape* fit determines the pulse shape by least-squares fitting a parametric pulse-shape model to the signal. The model consists of a sum of exponential rise and decay components, parameterised by the number of rise and decay times specified for the fit. The pulse model $P(t)$ is given by

$$P(t) = o + a\,\Theta(t)\left[\sum_r f_r\, e^{-t/\tau_r} - \sum_d f_d\, e^{-t/\tau_d}\right] \tag{6.8}$$

where o is a constant offset, a the amplitude, Θ the Heaviside step function, and t the timing-jitter corrected time defined as $t = t_0 - j$. The coefficients f_r and f_d are the relative fractions of the rise and decay components with time constants τ_r and τ_d, respectively, and fulfill $\sum_r f_r = 1$ and $\sum_d f_d = 1$. The initial parameters of the model are obtained by fitting it to a given template and are then used for fitting individual signals. The fit returns an amplitude a, offset o, timing jitter j, as well as the rise and decay times and their relative contributions. Although the fit provides an amplitude, it should not be used for its determination but rather to extract rise and decay times for characterising the overall pulse shape of individual signals. As the most computationally expensive fit, it should be restricted to a small subset of signals with a shape similar to the template, in order to ensure fast convergence.

6.2. Simulation

We implemented a signal generator in *fitfiles.generator* to simulate measurements and generate large datasets of signals having random noise, but all pulse shape parameters exactly known, in contrast to measured signals [15]. This allows direct comparison of fit results with the

expected values, assisting in the identification of artefacts and the investigation of correlations that may reveal biases in the analysis. It was used to verify the implemented fits and to study the identification of pile-up events. The simulated measurements are automatically indexed and processed in the same way as measured data. Each simulated signal consists of an arbitrary sum of exponential pulse models, noise with random phase generated from a noise model, and ADC digitisation with limited bandwidth.

6.2.1. Measurement Generation

Simulating a measurement requires three sets of settings: signal, noise, and ADC parameters. The ADC parameters define digitisation and readout, given by the number of samples per signal, the oversampling factor, subsampling factor, sampling rate, number of pre-trigger samples, code range, flux conversion in $\Phi_0\,\mathrm{bit}^{-1}$, and readout bandwidth. The subsampling factor is used to reduce the number of simulated samples and must be an integer divisible by two and smaller than half of the oversampling factor to satisfy the Nyquist criterion.

The signal parameters define up to an arbitrary number of pulses per signal, allowing the generation of pile-up events. Each pulse is identified by a prefix and can have an amplitude, timing jitter, and offset, as well as one or more rise and decay times. If multiple rise or decay times are defined, a factor specifies their relative contributions with respect to the pulse amplitude. All signal parameters are given in s and Φ_0. The settings can be tested together with the ADC parameters by generating a noise-free signal without bandwidth limitation, which returns an object of the *Signal* class and can also serve as an artificial template.

The noise parameters define the different noise components. Each component is identified by a prefix and may include suffixes specifying its type, which my be white noise, pink noise $1/f$ noise with the slope given by an exponent, and a cutoff frequency. These settings can reproduce the discussed MMC noise and are specified in Hz and $\Phi_0{}^2\,\mathrm{Hz}^{-1}$. They can be tested together with the ADC parameters by generating a noise spectrum, which returns an object of the *Frequencyspectrum* class and can also serve as an artificial noise spectrum.

Measurements may be simulated, generating the data and returning a *fitfile* of indexed signals. Signal and noise settings are specified per channel and polarity, together with the ADC parameters. Parameters may be fixed values, lists from which random elements are drawn, or functions representing random distributions evaluated for each signal. The generation of a measurement begins by creating the *fitfile* with the corresponding index and evaluating the settings for each signal. Each signal is constructed by summing its pulses, and the result is inverted if the pixel polarity is negative. Noise is generated from the channel noise spectrum with a random phase and added to the signal. A low-pass filter of the SQUID readout is then applied, followed by the addition of the offset and half of the ADC code range. Finally, the signal is digitised by rounding to the nearest integer, clipping to the maximum ADC code

range, and applying downsampling with averaging. The resulting signals are saved in batches as *Brotli*-compressed *parquet* files, which can be read by the *PulseReader* of *fitfiles*.

6.2.2. Fit Verification

To verify the fits implemented in *fitfiles* and compare them to those in *DARQ*, signals of a spectrum consisting of delta functions were generated. The pulse shape was based on the simulation results of the *maXs 30-56-14* detector, with the characteristics listed in Table 4.2 and the noise spectrum shown in Figure 4.2. For the measurement, ADC settings corresponding to a muonic Li measurement with a feedback resistance $R_{\mathrm{fb}} = 100\,\mathrm{k}\Omega$ were used, resulting in a conversion of $1.8 \times 10^{-5}\,\Phi_0\,\mathrm{bit}^{-1}$ and limiting the usable energy range by the ADC range to approximately 35 keV. A spectrum of delta functions at intervals of 1 keV over the range 0 keV-30 keV was generated, with 100×10^3 simulated signals at each energy. The signals included a small timing jitter with Gaussian width $\sigma_j = 0.5\,\mu\mathrm{s}$ and a small fluctuating constant offset with Gaussian width $\sigma_o = 0.5\,\mathrm{m}\Phi_0$, both estimated from measurements with a *maXs 30-56-14* detector.

After the generation, the corresponding noise spectrum and template were produced in the same way as for a real measurement. The noise spectrum was obtained from the simulated signals at $E = 0\,\mathrm{keV}$ without pulses. The initial template was generated at $E = 6\,\mathrm{keV}$, corresponding approximately to the energy of the ^{55}Mn K_α line from an ^{55}Fe source, which is typically used for template generation. Through multiple iterations, the template and noise spectrum were used to fit the signals, and the resulting jitter values were applied to correct the timing jitter of the template in the next iteration. The resulting jitter-corrected template had a FOM of about 1.2×10^5, more than an order of magnitude higher than typically achieved with measured data. Due to the jitter correction, the template was sharper at the trigger position compared to a non-corrected template and nearly identical to a noise-free, bandwidth-limited template generated by the *signal* function with the same signal and ADC settings as used for the simulated signals. It is important to emphasize that while the implementation allows arbitrary distributions, for this fit verification the pulses all had the same energy-independent pulse shape and the same time-independent noise, and only the timing jitter, offset and noise phase was varied randomly.

The simulated signals were then fitted using both the fits implemented in *fitfiles* and those imported from *DARQ*. For all fits, a maximum jitter of $j_{\mathrm{max}} = 16$ was used. The fastest fit was the *template* fit, which involves only vector operations in the time domain, followed by the *matched* and *wmatched* fits, which evaluate the convolution in the frequency domain. The *jtemplate* and *opti* fits are the slowest, with computation time scaling linearly with j_{max}. In *DARQ*, two fits are implemented: *template* and *opti*. The *template* fit in *DARQ* with $j_{\mathrm{max}} = 0$ corresponds to the original *template* fit without jitter correction used in the *ECHo*

experiment [155]. It is identical to the *template* fit in *fitfiles* and was therefore fitted only once. The *template* fit in *DARQ* with $j_{\max} > 0$ is similar to the *jtemplate* fit in *fitfiles* and is referred to here as the *jtemplate* fit from *DARQ* for simplicity. The *opti* fit in both *DARQ* and *fitfiles* is based on the same concept [107], but their implementations differ significantly. The *wmatched* fit and the *opti* implementation in *fitfiles* are mathematically equivalent, with the *wmatched* fit being the faster implementation, and the *opti* fit of *fitfiles* is therefore omitted from the comparison.

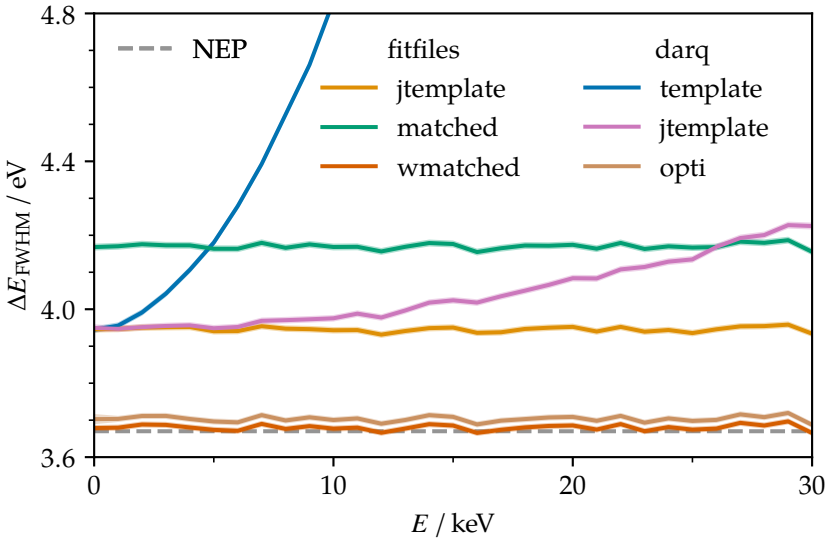

Figure 6.6.: The FWHM energy resolution ΔE_{FWHM} with its $\pm\sigma$ uncertainty as a function of energy E for the different fits, compared to the NEP limit. The resolution is estimated from the RMS energy resolution σ_E, assuming a Gaussian detector response. The results of the different fits at the same energy are correlated because they are applied to the same generated data, which includes statistical fluctuations.

After fitting, the amplitude of each fit was calibrated at the template energy $E = 6\,\mathrm{keV}$. The detector response at different energies is mostly Gaussian for the matched-filter based fits, while deviations occur for the jitter-corrected template fits and are significant for the *template* fit. The *template* and *opti* fits in *DARQ* exhibit a non-linear amplitude response, whereas the other fits scale linearly. For the *opti* fit in *DARQ*, this non-linearity reaches nearly 2 eV at 30 keV. The FWHM energy resolution ΔE_{FWHM}, based on the RMS energy resolution σ_E and assuming a Gaussian detector response, is shown in Figure 6.6. The *template* fit shows a pronounced energy dependence, reaching $\Delta E_{\mathrm{FWHM}} \approx 9\,\mathrm{eV}$ at 30 keV. The *jtemplate* fit from *DARQ* exhibits a slight amplitude dependence, since its implementation does not interpolate the amplitude, while the *jtemplate* fit from *fitfiles* maintains its resolution across the energy range. The *wmatched* fit in *fitfiles* nearly reaches the NEP limit and performs slightly better than the *opti* implementation in *DARQ*. The *matched* fit yields a worse energy resolution but is

faster than the jitter-corrected fits in *DARQ* and does not require a noise spectrum. All fits accurately determine the timing jitter, except for the *template* fit without jitter correction and the *opti* fit in *DARQ*, which deviates by more than one sample due to a missing normalisation in its implementation.

The resulting reduced χ^2 values can be used to compare both amplitude and jitter estimation for the different fits and evaluate the fit quality. Figure 6.7 shows the χ^2 values, normalised by the mean pre-trigger standard deviation σ_0, at the template energy $E = 6\,\mathrm{keV}$. All timing-jitter corrected fits of *fitfiles* yield similar reduced χ^2 values centred around one. The *template* fit reaches similar values for signals with near-zero timing jitter but deviates significantly when a timing jitter is present. The *jtemplate* and *opti* implementations in *DARQ* yield significantly higher χ^2 values due to a combination of insufficient amplitude and timing jitter determination. The reduced χ^2 values for the timing-jitter corrected fits in *fitfiles* show no amplitude dependence, whereas the fits implemented in *DARQ* exhibit significantly higher χ^2 values at higher energies. This clearly indicates issues in the *DARQ* implementations, as all timing-jitter corrected fits in *fitfiles* perform significantly better and without artefacts.

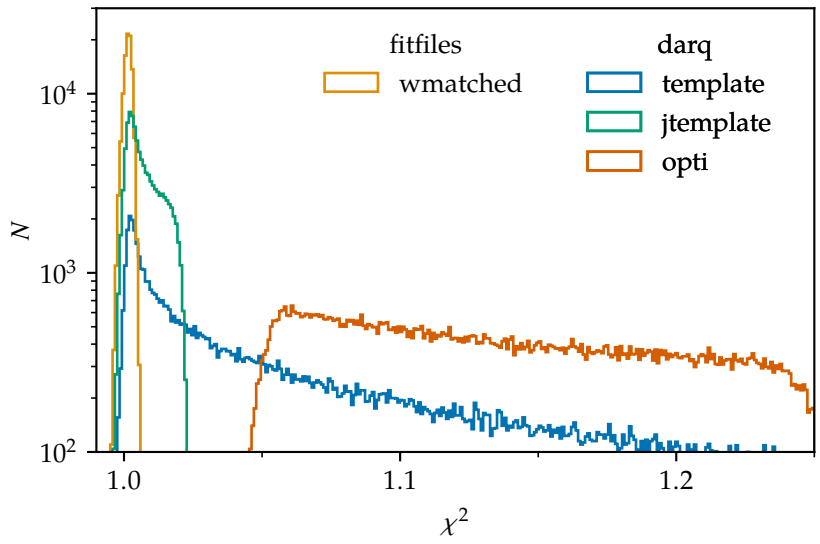

Figure 6.7.: Reduced χ^2 at the template energy $E = 6\,\mathrm{keV}$ for the different fits. The *jtemplate*, *matched*, and *opti* implementations in *fitfiles* yield nearly identical results to the *wmatched* fit at this scale and are therefore omitted. The jitter-corrected fits in *fitfiles* yield consistent results centred around one, whereas the fits implemented in *DARQ* show significantly worse χ^2 values.

In contrast to the fits implemented in *DARQ*, which show artefacts and energy dependence, all jitter-corrected fits in *fitfiles* yield energy-independent results. The *wmatched* fit achieves an energy resolution close to the NEP limit, is computationally efficient, energy independent,

and yields the expected reduced χ^2 values. Consequently, the *wmatched* fit of *fitfiles* is used for the data reduction of the two runs.

It is important to emphasise that only the fit implementations were compared, using the same jitter-corrected templates and noise spectra from *fitfiles*. The *DARQ* library does not allow the combination of multiple measurements, which typically results in a much lower FOM for the template due to the use of fewer signals. In addition, *DARQ* does not support iterative template generation and does not correct the template for the timing jitter of signals, both of which further degrade the template quality, and consequently leads to reduced energy resolution and systematically higher χ^2 values.

6.2.3. Pile-up Identification

The χ^2 distribution is directly relevant for identifying pile-up events by their χ^2 value. To investigate pile-up identification, pile-up events were simulated under the assumption that the pile-up pulse has the same shape as the underlying pulse. For pulses at 19 keV, approximately corresponding to the $2p$–$1s$ transition energy of muonic Li, about 10×10^6 pile-up pulses were generated, each consisting of an additional pile-up pulse with an energy in the range $E_\mathrm{p} = \pm 10\,\mathrm{keV}$ and a timing offset in the range $\Delta t_\mathrm{p} = \pm 20\,\mathrm{ms}$. The pile-up events were processed in the same way as pulses without pile-up. From the distribution of pile-up free pulses, an energy-dependent χ^2 cut was defined so that, at each energy, 99 % of pulses were accepted, while 1 % were falsely rejected as pile-ups. This cut was then applied to the pile-up events. The remaining pile-up fraction p_p for the *opti* fit in *DARQ* and the *wmatched* fit in *fitfiles* is shown in Figure 6.8 as a function of the energy of the pile-up pulse E_p and timing difference Δt_p.

Pile-up events cannot be identified if the energy of the pile-up pulse E_p is close to zero, in which case the overall signal shape remains nearly unchanged, or if the timing difference between the two pulses Δt_p is close to zero and the signal can be sufficiently described by a single pulse with a different amplitude. The *wmatched* fit fails to identify pile-up events with an energy E_p of $\pm 30\,\mathrm{eV}$ or a timing difference Δt_p of $\pm 0.6\,\mu\mathrm{s}$ for the same polarity, or $\pm 0.3\,\mu\mathrm{s}$ for opposite polarity. In comparison, one sample corresponds to $0.32\,\mu\mathrm{s}$, while the rise time $\tau_r = 15\,\mu\mathrm{s}$ is significantly longer. The results for all fits implemented in *DARQ* are significantly worse, with the *jtemplate* fit performing slightly better and the *template* fit slightly worse. The *opti* fit in *DARQ* fails to identify pile-ups with E_p of $\pm 600\,\mathrm{eV}$ and Δt_p of $\pm 4\,\mu\mathrm{s}$ for the same polarity, or $\pm 1\,\mu\mathrm{s}$ for opposite polarity. Consequently, the unresolved pile-up fraction improves by about a factor of 5, while overall changes in the pulse shape are detected with about a factor of 20 higher sensitivity. These values, however, represent only lower limits, as the comparison does not take into account the more accurate template generation in *fitfiles*, nor the χ^2 evaluation in the trigger region, which is particularly sensitive to pile-ups but is not

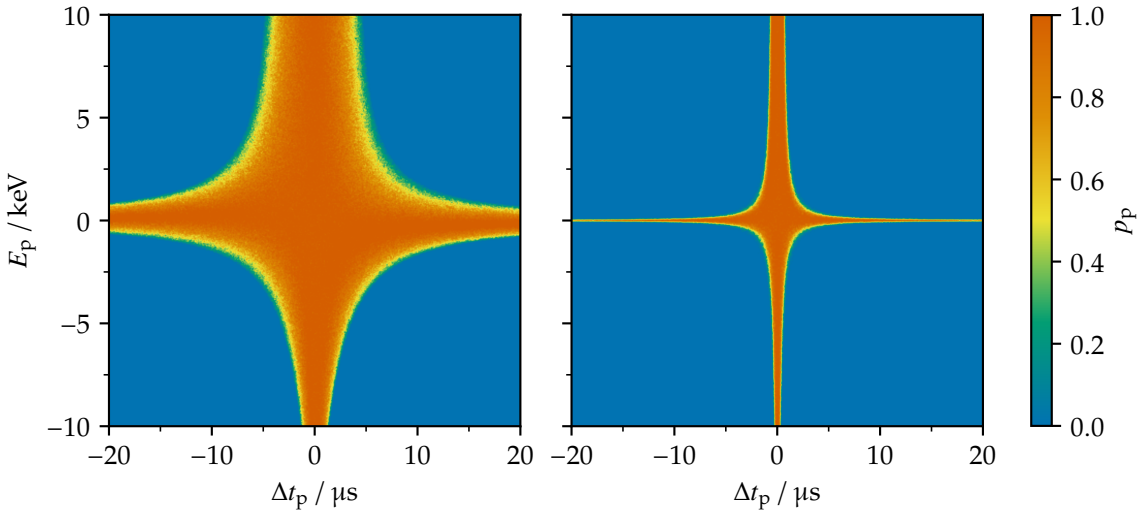

Figure 6.8.: Remaining pile-up fraction p_p for the *opti* fit in *DARQ* (left) and the *wmatched* fit in *fitfiles* (right) for signals at 19 keV, shown as a function of the pile-up energy E_p and timing difference Δt_p. All timing-jitter corrected fits in *fitfiles* perform similarly to the *wmatched* fit and significantly better than any fit implemented in *DARQ*.

calculated in *DARQ*. The fits in *fitfiles* are therefore much more sensitive to small pulse-shape changes. For QUARTET, this improved sensitivity is essential for identifying and suppressing events related to Michel electrons.

6.3. Data Selection

After the data reduction, the processed data must be masked and the different pulse families identified. This step is essential to prepare for the subsequent corrections applied to the pulse amplitudes in order to determine their energies. Typically, many masks are defined based on metadata and fit results, specifying the physical origin of the pulses and selecting those for which the energy can be determined with high accuracy.

For the two runs, masks defined from the general fit typically identified integrator resets of the SQUID readout as well as clipped signals. The unnormalised χ_0^2 values of the fits with different templates were used as an initial classification of pulse families. The pre-trigger was employed for a time-dependent normalisation of the χ_0^2. Subsequently, the families were refined and pile-up pulses identified by applying masks on the normalised χ^2 values of the signals and their trigger regions, as well as on the jitter j. Finally, the time differences relative to the last triggered pulse or to a pulse of a given family between signals of the same and of different channels were evaluated to determine the dead time and the influence of Michel-electron related events. Coincidences between different channels were identified, and

clusters of Michel-electron related events were assigned. The time difference to the muon entrance scintillator was used to identify muon-induced signals.

For the data selection, several functions were implemented in *fitfiles.analysis*. For example, a peak-like distribution can be iteratively fitted, and the corresponding σ values can be assigned. The distribution is typically Gaussian, and the iterative process efficiently suppresses outliers. A drifting distribution over time can be assigned a time-dependent centre by applying a non-uniform Gaussian filter with a given time width. A more stable alternative is a non-uniform median filter. The results can then be used to define masks. For instance, a time-varying distribution can first be corrected with the non-uniform Gaussian filter and then masked by a Gaussian fit applied to the corrected data, to define a mask based on a σ limit for a time-dependent Gaussian mask.

6.3.1. Time

For a *PAQS* measurement, each signal contains the ADC timestamp, which is reset at the start of every new measurement. The corresponding unambiguous time can be calculated with the ADC settings to determine the time of each signal. This time can optionally be correct for timing jitter using the jitter values obtained from a fit. The absolute accuracy is about 1 s, limited by the precision of the recorded measurement start time, while the drift of the ADC clock frequency is negligible for the typically 1 h-long measurements. The relative accuracy between signals is limited by onset differences, caused by the timing jitter of the constant-fraction trigger, which in turn arise from variations in pulse shapes between pixels and from differences between pulse families. For the two runs, these onset differences were not corrected in this work, as no improvement in the analysis was expected. The relative uncertainty of the trigger time between two signals is therefore up to 16 µs, limited by the differences in signal onsets.

6.3.2. General Masks

Based on the results of the *general* fit and the fits with different templates, several masks can be defined. Signals are distinguished between triggered and randomly triggered ones, the latter being used to acquire data for noise spectra. In addition, not all signals have raw data saved, and some are traceless and must therefore be omitted. Signals that exceed the ADC code range must also be rejected. These clipped signals typically arise from background pulses, pile-ups, or integrator resets of the SQUID readout. For the Li measurements during the data run with a feedback resistance $R_{\mathrm{fb}} = 100\,\mathrm{k\Omega}$, the voltage range of the ADC is smaller than one Φ_0, and all integrator resets result in clipped signals. For smaller feedback resistances, the maximum difference between two samples is used to identify the sharp rise of an integrator reset, which

cannot originate from any physical pulse in an MMC due to the limited thermalisation time of the sensor. Based on the unnormalised χ_0^2 values from different templates, a preliminary pulse family is assigned according to the lowest value. These masks significantly reduce the number of signals and suppress outliers in subsequent steps.

6.3.3. χ^2 Normalisation

The pre-trigger of a signal should represent a constant offset, with its standard deviation σ_0 determined by the noise of the channel. This noise level limits the unnormalised χ_0^2 of an ideal fit. The standard deviation of the pre-trigger σ_0 can therefore be used to normalise χ_0^2 given by

$$\chi^2 = \frac{\chi_0^2}{\sigma_0^2} \tag{6.9}$$

which should yield a χ^2 distribution centred around one. The normalisation must not be calculated per signal, since this would be sensitive to statistical fluctuations of individual pre-triggers, but instead from an average over many signals. The standard deviation σ_0 varies slightly with time and broadens the χ^2 distribution, such that a filter can be applied to correct for these slow variations.

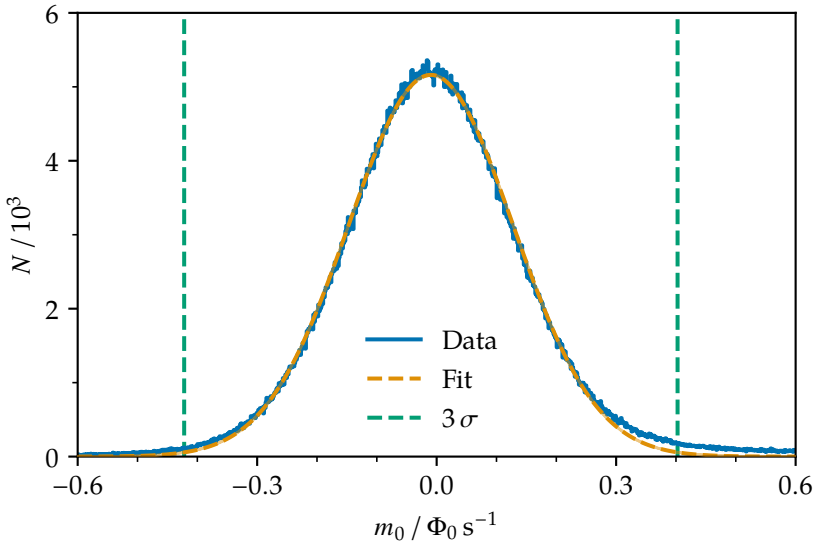

Figure 6.9.: Distribution of the pre-trigger slope m_0 with a Gaussian fit and the $\pm 3\,\sigma$ range. The distribution is not centred at zero, as this is a temperature-sensitive channel. For the runs, a σ limit of 5 was used to ommit outliers.

The slope of the pre-trigger m_0 in each channel was first fitted with a Gaussian distribution, as shown in Figure 6.9, and then masked with a σ limit of 5 to ommit outliers before applying

a filter. Subsequently, a non-uniform Gaussian filter with a width of 10 min was iteratively applied. In each iteration, the Gaussian filter was applied, the pre-trigger values were corrected based on the time-dependent centre value of the filter, and the corrected values were fitted with a Gaussian distribution to determine the corresponding σ difference. The σ values were then used to define a mask with a σ limit of 5 to reduce outliers for the next iteration. The Gaussian filter from the last iteration is shown in Figure 6.10 and its centre was used to obtain the normalised χ^2 values. The masks on the slope and standard deviation of the pre-trigger were used later for the calculation of the temperature information.

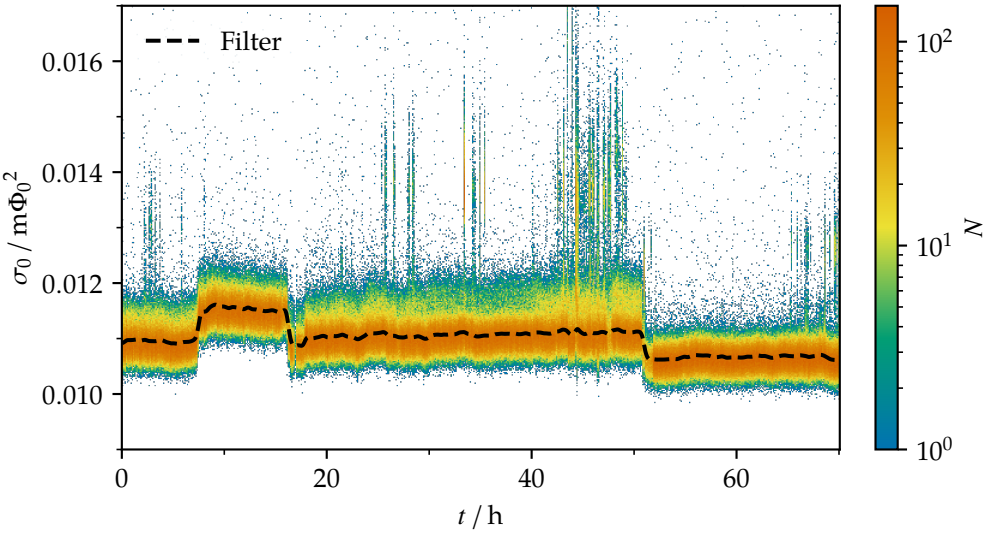

Figure 6.10.: The pre-trigger standard deviation σ_0 as a function of time with the applied non-uniform Gaussian filter. The distribution contains many outliers, which were filtered and omitted for the following analysis.

6.3.4. χ^2 Masks

The reduced χ^2 value characterises the quality of a fit and indicates whether a pulse can be described by the given template. Large χ^2 values typically correspond to pile-up pulses or to pulses belonging to a different family. By defining amplitude-dependent χ^2 and jitter masks based on the fits with different templates, the different pulse families can be distinguished. Pulses from photons that are presumably free of pile-up can thus be selected and masked for the subsequent energy spectrum.

To select photon pulses, non-uniform median filters with an amplitude width of 1/2, corresponding to about 3 keV, were applied iteratively to the χ^2, the χ^2 of the trigger region, and the timing jitter j, for signals with a lower χ^2 value for the photon template than for the templates generated for phonon or electron pulses. In each iteration, the values were

corrected, then fitted with a Gaussian distribution, and a mask with a σ limit of 5 was defined for the next iteration. The resulting χ^2 and jitter masks were then used to identify pile-up pulses, as shown for the different pulse families.

6.3.5. Pulse Families

Based on the previously defined masks, different pulse families were identified, as shown in Figure 6.11 for the χ^2 and jitter j of the photon template. The phonon and electron pulse families are used to study the effect of Michel electrons, while the photon pulses are selected for the energy spectrum.

Phonon pulses, originating from athermal phonons predominantly produced by the energy deposition of Michel electrons in the substrate and thermalising in the sensor, exhibit a sharp rise limited by the acoustic mismatch between substrate and sensor as well as the thermalisation time of the sensor. They were assigned solely based on their χ^2 value in the trigger region of the phonon template compared to the other templates. They appear at a low energy, up to about 10 keV, arising from the difference in deposited energy between the two pixels of a channel. The fast initial rise results in a well-defined jitter from the constant fraction trigger, while at low energies this distribution broadens due to the reduced jitter accuracy for low-amplitude pulses.

Electron pulses originate from energy deposition of Michel electrons in the absorber and substrate. Pulses that also include direct energy deposition in the sensor were assigned solely by their χ^2 value in the trigger region of the electron template compared to the other templates. Electron pulses without direct energy deposition in the sensor were identified by a combination of χ^2, χ^2 in the trigger region, and jitter values. Their energy is higher, with a minimum of about 20 keV and an average around 40 keV, predominantly determined by the energy deposition in the absorber. The pulse shape, and consequently the jitter value, depend on the fraction of the energy deposited directly or indirectly in the sensor.

Photon pulses are identified as those not classified as phonon or electron pulses and are masked based on their χ^2, χ^2 in the trigger region, and jitter. They exhibit a nearly energy-independent pulse shape, leading to χ^2 values close to one and an nearly energy-independent timing jitter. The remaining pulses are predominantly pile-up events, mostly photon pulses with a higher χ^2 value in the trigger region. Other unphysical pulse families, for example those caused by integrator resets of the SQUID readout or by external noise, are omitted for simplicity and have even higher χ^2.

6.3.6. Time Differences

After a pulse, the pixels thermalises back to their operating temperature. The time difference to the last triggered pulse in the same channel or in any other channel can be used to determine

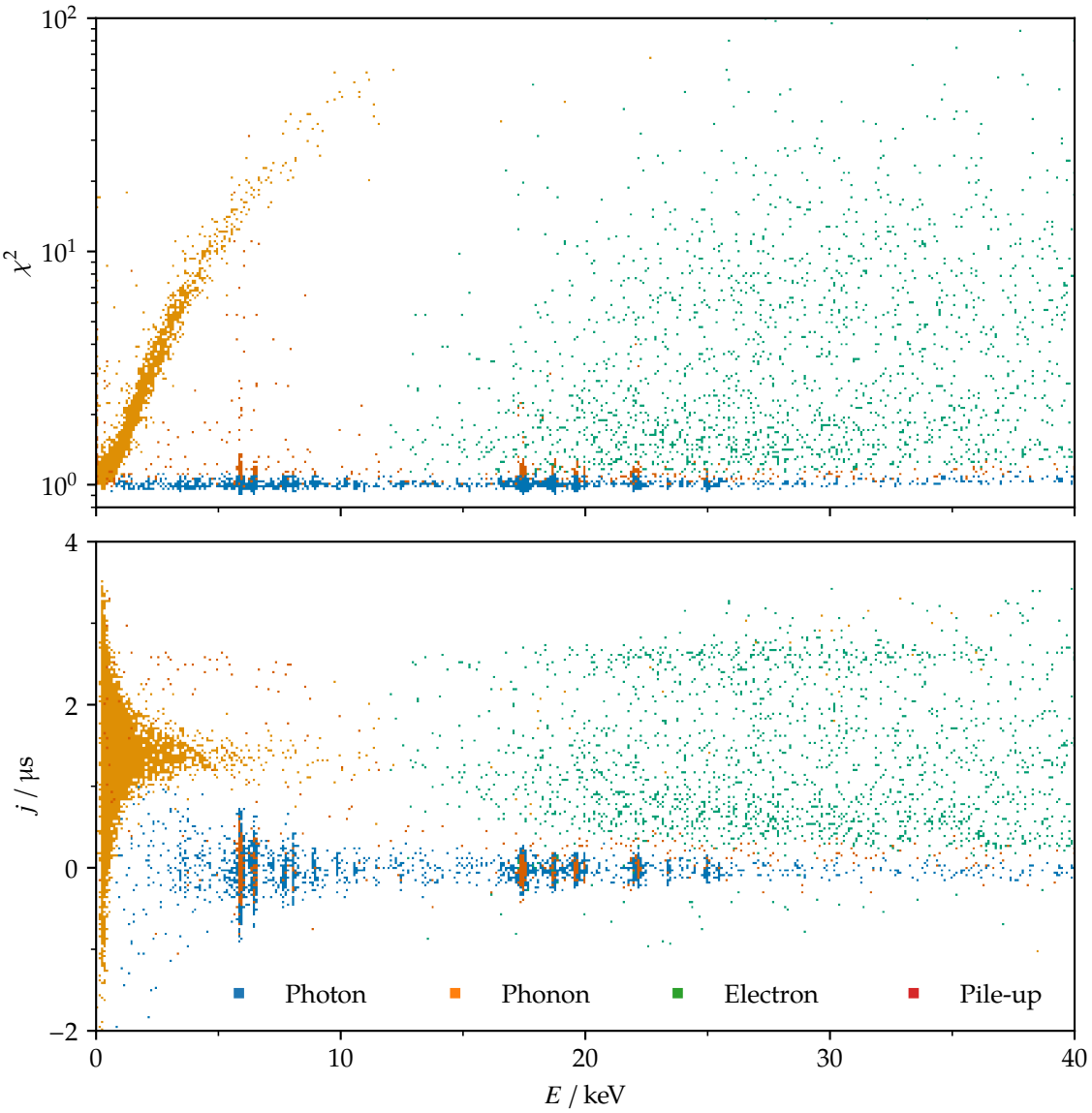

Figure 6.11.: Pulse families of photon, phonon, electron, and pile-up pulses for the χ^2 (top) and jitter j (bottom) of the photon template, shown here as an example for a single pixel. The families are identified by a combination of fit results from different templates based on χ^2 and jitter masks.

the dead time of a pixel and investigate their thermalisation behaviour. For each pulse, the time difference to the last pulse in the same pixel, in the same channel, and on the detector, both for all pulses and separately for each pulse family is calculated.

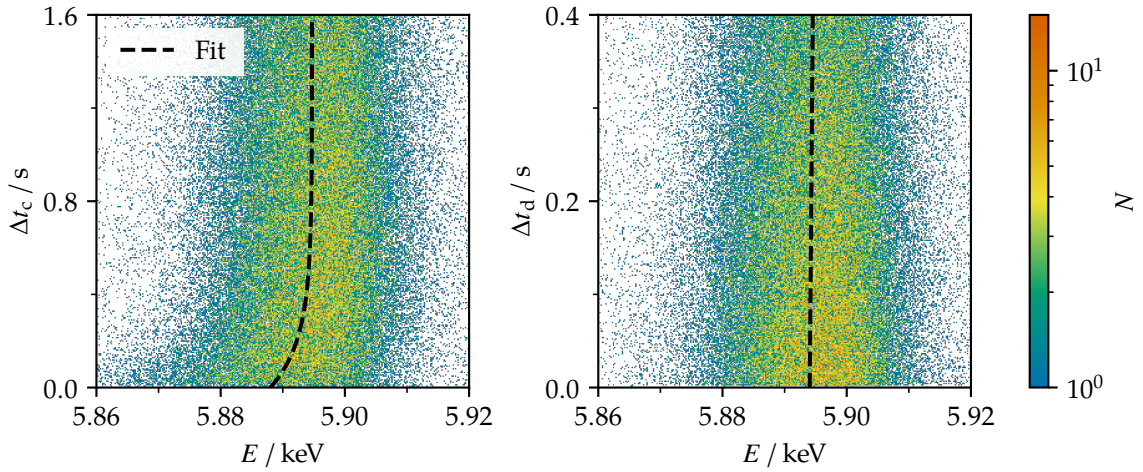

Figure 6.12.: Time difference to the last triggered pulse in the same channel Δt_c (left) and to the last phonon or electron pulse of the detector Δt_d (right) if it is smaller than the time difference to the last triggered pulse in the same channel, at the ^{55}Mn K_α line of an ^{55}Fe source for the Li measurements of the data run. The calibrated energy E is already used here for a sharper distribution.

The time difference to the last triggered pulse in the same channel Δt_c as well as to the last phonon or electron pulse in the detector Δt_d is shown in Figure 6.12. When the time since the last triggered pulse is short, the determined energy of subsequent pulses decreases, as the channel is slightly warmer and thus yields smaller pulse heights. An exponential fit yields an energy reduction of up to about 7 eV with a time constant of approximately 0.2 s. This agrees well with the slow thermalisation time constant of the *maXs 30-v2b* detector, limited by the thermal conductance to the silicon substrate, estimated to be about 0.3 s at 17 mK [146]. A channel-wise holdoff of 0.5 s was defined after each triggered pulse in both runs to reduce the effect of incomplete thermalisation while maintaining sufficient statistics.

The time difference to the last phonon or electron pulse in any channel Δt_d does not show an effect on the estimated pulse energy within the fit uncertainty. Michel electrons deposit a significant amount of energy, typically about 40 keV in the absorber, 2 keV in the sensor, and 110 keV in the substrate, according to *Geant4* simulations [160]. The effect of the deposited energy is clearly visible in the triggered channels, and the previously defined channel-wise holdoff must therefore be applied. The energy deposition of a Michel electron thus appears to be mostly local rather than detector-wide, and remaining effects seem negligible, assuming the trigger threshold is low enough. They may, to some extent, already be compensated

by the subsequent temperature correction, which accounts for homogeneous detector-wide temperature variations.

6.3.7. Coincidences

For each pulse, coincidences are assigned by evaluating whether it occurs within a given time difference of another pulse belonging to a specified mask, typically any triggered pulse or pulses of a specific family. For the coincidence threshold, the relative accuracy of 16 µs was used, corresponding to ten samples for the Li measurements of the data run. All coincidences of triggered pulses are omitted from the subsequent analysis, which for photon pulses are dominated by coincidences with phonon pulses.

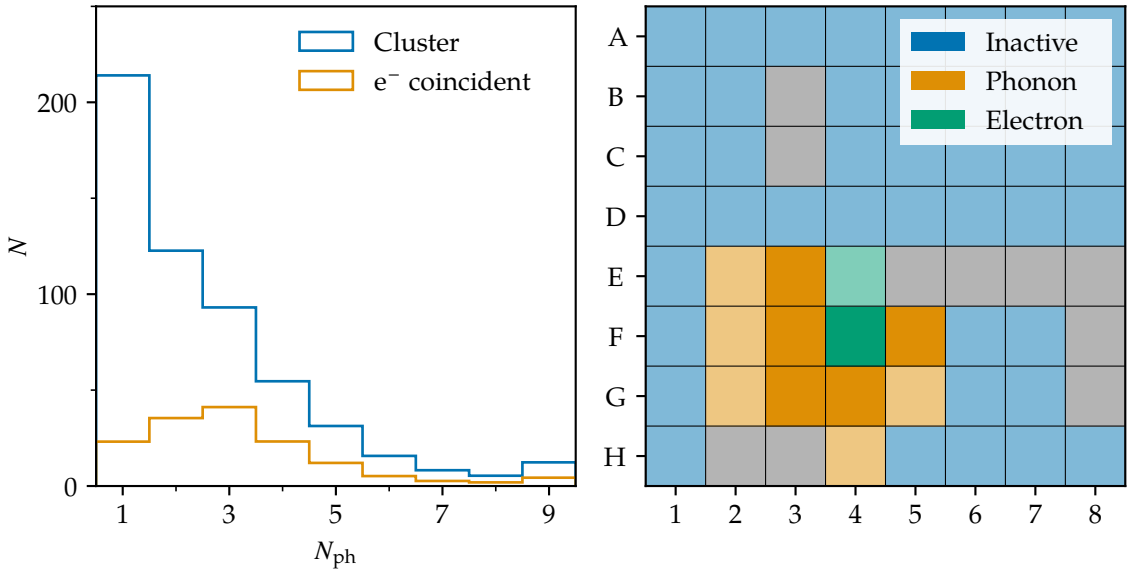

Figure 6.13.: The number of phonon clusters N for different number of phonon pulses per cluster N_{ph}, and those clusters coincident with an electron pulse (left), and the pixel positions of a large phonon cluster coincident with an electron pulse (right). The triggered pixels are shown with higher saturation. Only channels close to the electron event trigger, and each of the triggered pixels is the geometrically closest pixel of its channel to the electron hit.

Most phonon pulses, about 85 %, are coincident with other phonon pulses, and 34 % of phonon pulses are coincident with an electron pulse. Most electron pulses, about 84 %, are coincident with at least one phonon pulse, while only 2 % are coincident with another electron pulse. To further evaluate the coincidences, each phonon and electron pulse is assigned to a coincident cluster within a threshold of 16 µs. A cluster may therefore also consist of a single phonon pulse. The distribution of the number of phonon pulses per cluster, N_{ph}, and if they are coincident with an electron pulse, as well as the pixel positions of a large, phonon cluster coincident with an electron pulse, are shown in Figure 6.13. About 27 % of the clusters are

coincident with an electron pulse, which approximately matches the ratio of active area to chip area. While most phonon and electron pulses are coincident to other phonon pulses, many phonon or electron pulses cannot be assigned to a cluster and can only be identified by their pulse shape.

For a typical phonon cluster coincident with an electron pulse, the phonon signals originate from channels located directly adjacent to the channel of the electron pulse. Clusters without electron coincidence are typically found at the border of the active area or near a non-operational detector channel. This demonstrates the origin of phonon pulses from energy deposition in the substrate by a Michel electron and its predominantly local, position-dependent effect on the detector. Even though not the entire detector is affected by a Michel electron, many channels can still trigger, significantly increasing the dead time due to the required channel-wise holdoff, which is limited by the slowest thermalisation time of the detector.

6.3.8. Muon Coincidence

To identify muonic events, the signal from the muon entrance scintillator is digitized, processed with an energy threshold, and the resulting trigger signal is co-triggered with any other triggered signal. The online analysis of *DARQ* includes a preliminary analysis of these signals, but its accuracy is limited. The digital signals were not analysed as part of this work. Instead, the timing information of the digital signals as well as the onset correction of pulses were taken from the dedicated analysis of the muonic Li spectrum [160].

The time difference to the last signal in the muon entrance scintillator, Δt_μ, over a broad energy range around the muonic $2p$–$1s$ transition of Li, is shown in Figure 6.14. The transition is clearly visible as a coincidence with the muon entrance scintillator at a time difference between $-0.8\,\mu s$ and $0.0\,\mu s$. A mask in this range yields a 93 % efficiency for selecting muonic events. Additionally, an anti-coincidence mask can be defined in the time window between $10\,\mu s$ and $650\,\mu s$, which contains less than 0.4 % residual muon related signals. The accuracy of the coincidence mask is limited by unresolved coincidences from the muon entrance scintillator. The time window of the anti-coincidence mask is constrained by the pre-trigger length, the method of co-triggering the signals with the same ADC settings, the ADC dead time, and the efficiency of the entrance scintillator. Both masks were later used to identify the origin of different lines in the energy spectrum. The anti-coincidence mask was also applied for the calibration with the Ag K_α line, as this line overlaps with the muonic $3p$–$1s$ transition of Li within the energy resolution of the detector. Since the background is negligible and no other overlapping transitions are present, the masks were otherwise not applied to not reduce statistics.

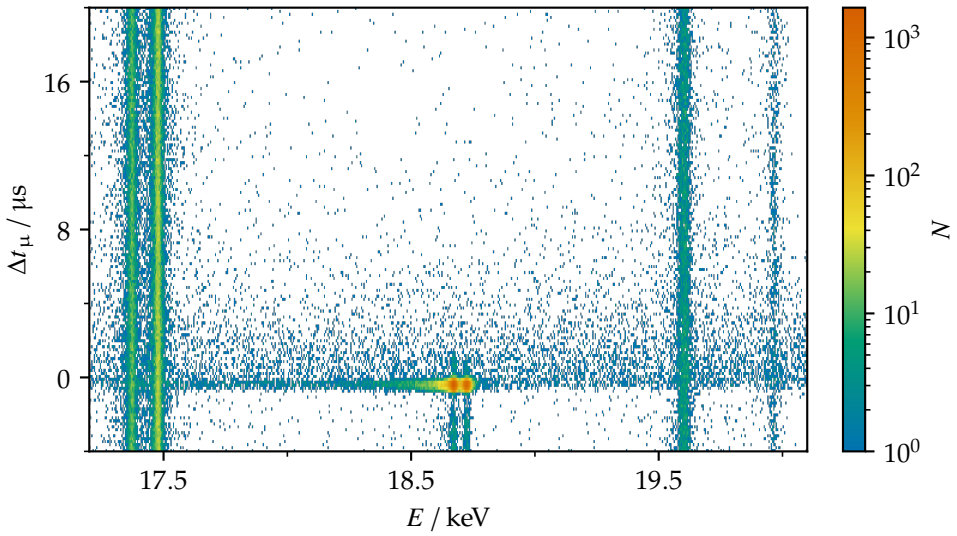

Figure 6.14.: Time difference to the last signal in the muon entrance scintillator Δt_μ at different energies E for the Li measurements of the data run. The onset-corrected time differences are taken from the dedicated analysis [160]. At 18.7 keV, the coincidence with the muonic $2p$–$1s$ transition of Li, at a time difference between −0.8 µs and 0.0 µs, is clearly visible.

6.4. Data Correction

Based on the previously defined masks, each pulse amplitude a, expressed in units of the template amplitude a_0, must be assigned its corresponding energy E. As a first step, the temperature-dependent pre-trigger offsets of the asymmetric channels are combined into a single temperature information. The temperature dependence of the amplitude is then corrected using this information. Remaining slow variations over time are corrected by applying a time-dependent gain-drift correction. On the corrected amplitude spectrum, a combined line-shape model is fitted to several calibration lines to determine their positions. A calibration function is then fitted to obtain an energy calibration, and the corrected amplitudes are subsequently converted into energies. These steps must be performed individually for each pixel, and after calibration the spectra of the different pixels can be superimposed to yield the overall energy spectrum for further analysis.

For this analysis, the required functions are implemented in *fitfiles.analysis*. They are designed such that they can be applied offline, as discussed here, but also online during a running measurement.

6.4.1. Temperature Information

The signal amplitude is highly sensitive to the channel temperature, and a reliable correction requires some knowledge of the detector temperature. A proportional measure of the temper-

ature can be extracted from the temperature-dependent pre-trigger offset of an asymmetric channel. However, the temperature information obtained from a single channel is limited by its dead time and is susceptible to flux losses as well as variations in the external magnetic field. In particular, high-energy particles can temporarily drive a small part of the superconducting meander of the temperature-sensitive channel into the normal-conducting state, resulting in the loss of one or more magnetic flux quanta Φ_0. While the corresponding gain change is typically negligible, this effect can introduce an offset corresponding to an integer multiple of Φ_0 in the meander flux Φ_m without an actual temperature change. Moreover, offset changes by fractions of a flux quantum have been observed. These are attributed to changes in the surrounding magnetic field experienced by the sensor and only partially shielded by screening currents in the underlying meander. The rate of such offset changes in a channel can vary from less than one per week to several per day, and is not yet fully understood. Consequently, pre-trigger offsets from multiple asymmetric channels are typically used to identify and correct such offset changes and to extract a corrected temperature information for the subsequent temperature correction.

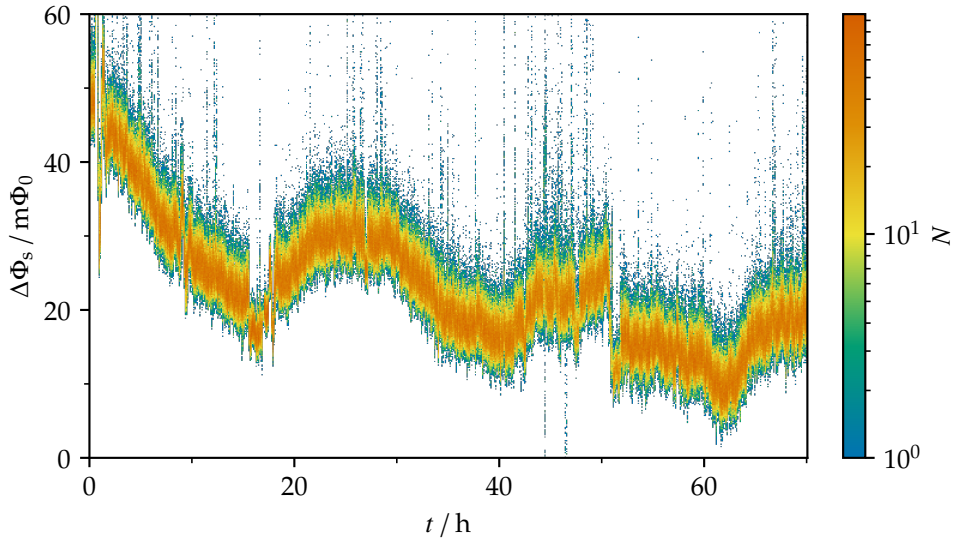

Figure 6.15.: Temperature-dependent pre-trigger offset of an asymmetric channel $\Delta\Phi_s$ during the Li measurements of the data run. The offset exhibits slow fluctuations over time due to detector temperature variations and shows rapid increases caused by events in this channel.

For the Li measurements of the data run, four channels with a temperature-dependent pre-trigger offset were co-triggered. The pre-trigger information of coincident signals from these four channels, after applying the previously defined masks, was analysed and combined. One channel was unstable and therefore excluded from the analysis. For each of the remaining

channels, outliers were iteratively masked with a non-uniform Gaussian filter with a width of 1 min, followed by a Gaussian fit with a σ limit of 3. From the three stable channels, the temperature-dependent pre-trigger offset of the first channel is shown in Figure 6.15. It exhibits a single flux change not correlated with temperature at about 51 h, coinciding with entering the experimental area and switching off the beam, while the other two channels showed several flux changes distributed over time. Consequently, the first channel was used as a reference, and the information from the other two channels were applied relative to it. For each of the other two channels, the relative pre-trigger offset $\Delta\Phi_{s1}\,\Delta\Phi_{si}{}^{-1}$ was calculated, as shown for the second channel in Figure 6.16. Again, a non-uniform Gaussian filter and Gaussian fit were iteratively applied to the relative pre-trigger offset with the same parameters. The resulting filters were then used to correct the relative pre-trigger offsets of the other two channels. A filter width of 1 min sufficiently corrects for slow gain changes between channels as well as for flux changes absent in the first channel, while remaining slow enough to preserve the fast relative temperature variations between channels.

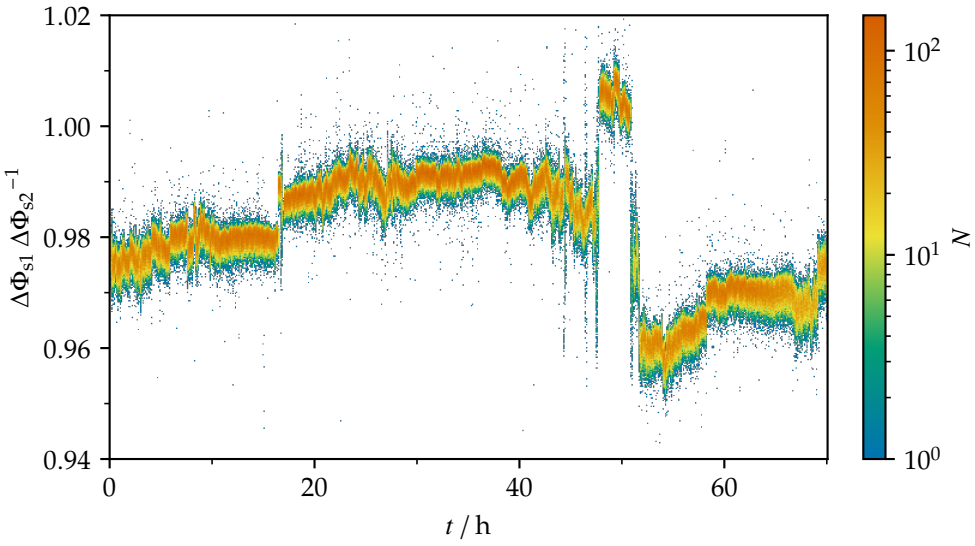

Figure 6.16.: Relative pre-trigger offset between two asymmetric channels. The gain between the two channels changes slowly over time, while several abrupt changes indicate flux changes that are not correlated with the detector temperature.

The up to three different pre-trigger offsets, converted into the frame of the first channel, were averaged after applying the defined masks to exclude outliers in the different channels. A final non-uniform Gaussian filter and Gaussian fit were then iteratively applied to the combined pre-trigger offsets using the same parameters. The remaining flux change at about 51 h in the first channel was manually corrected using the relative pre-trigger offset to the third channel, which did not exhibit a flux change in this time interval. The combined,

offset-corrected, and filtered temperature information, shown in Figure 6.17, describes the fast temperature fluctuations, while having reduced noise and strongly suppressed outliers, predominantly originating from events in the individual temperature-sensitive channels. The temperature information is then applied to all coincident signals within 16 µs for the temperature correction.

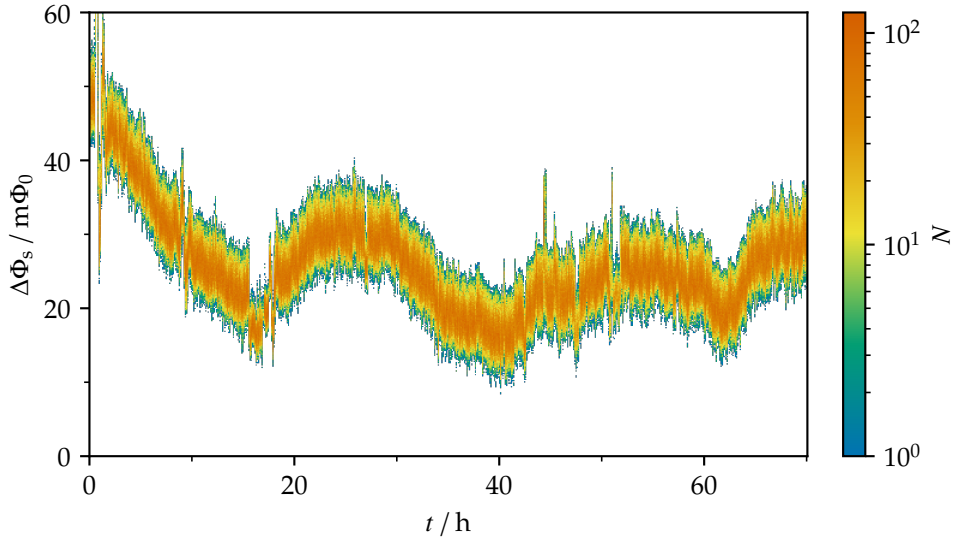

Figure 6.17.: Combined, offset-corrected, and filtered pre-trigger offset $\Delta\Phi_s$ describing the detector temperature as a function of time. The temperature fluctuations are significantly smaller during periods without muon beam.

The accuracy of the combined temperature information appears to be limited by temperature fluctuations introduced by Michel electrons. Based on the cluster analysis, the energy deposited in the substrate by Michel electrons is highly position dependent, while the rate was on the order of 1 Hz during the Li measurements of the data run. In combination with the slow thermalisation time of about 200 ms, this is expected to cause temperature fluctuations across all channels. The effect of Michel electrons is clearly visible in the temperature information between 16 h and 18 h, when no muon beam was present for an extended period of time. In the absence of Michel electrons, the temperature is slightly reduced and the fluctuations are significantly smaller. Consequently, larger temperature differences between channels are expected during measurements with muon beam, which can not be described by the combined and averaged temperature information. These temperature fluctuations cannot be corrected and therefore result in a degraded energy resolution.

6.4.2. Temperature Correction

The temperature correction accounts for the dependence of the signal amplitude on the operating temperature. Even for small temperature variations of several µK, the resulting amplitude change must be corrected to avoid a significant degradation of the energy resolution. Typically, the dependence is well described by a linear behaviour corresponding to the previously described leading-order term, while higher-order contributions can be neglected within the typical temperature fluctuations. A linear fit at a single calibration line then yields the temperature dependence, which can be used to rescale the amplitude of each signal of the corresponding pixel. Each amplitude is divided by the value of the temperature correction at the measured temperature, which corresponds to normalising the fit to unity.

For the data run, the temperature correction was calculated using the ^{55}Mn K_α line. A linear model was fitted iteratively to suppress outliers. The temperature correction was calculated, applied to the amplitude, followed by a Gaussian fit to the corrected amplitude with a $3\,\sigma$ limit for the next iteration. The resulting temperature correction for a single pixel is shown in Figure 6.18.

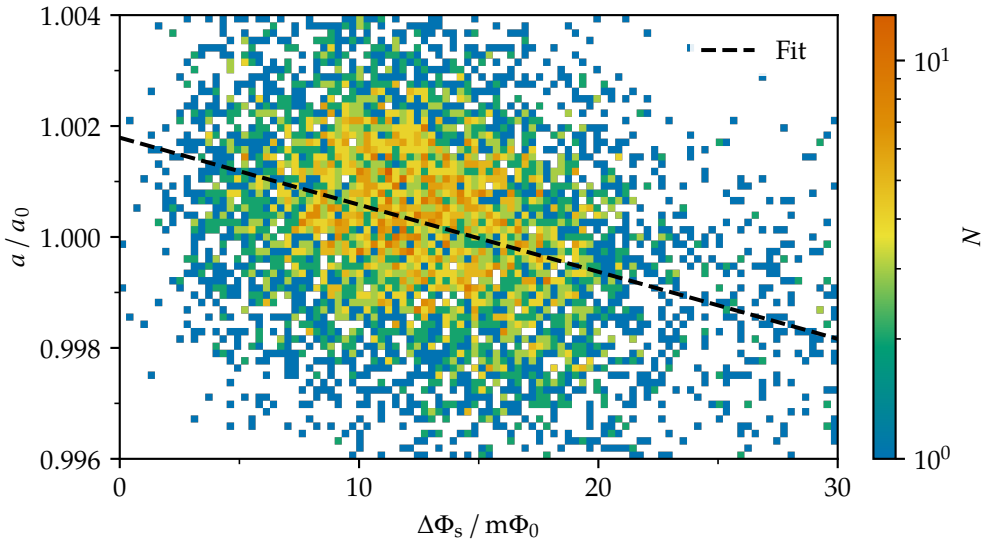

Figure 6.18.: The amplitude a as a function of the temperature information $\Delta\Phi_s$ with its temperature correction for a single pixel. The linear fit used for the temperature correction describes the leading-order amplitude dependence of the temperature.

The quality of the temperature correction is typically evaluated by the degradation in energy resolution, as determined for example from the NEP. At a low-energy calibration line, a substantial degradation in resolution usually indicates uncorrected flux changes, either in the pixel itself or in the temperature information. At higher energies, a significant decrease in resolution generally indicates increased uncertainty in the temperature information, for

example due to temperature differences between the channels providing the temperature signal and the pixel being corrected. However, a small decrease in resolution is also expected from non-linearity and partial energy loss. This may be caused by an insufficient holdoff and particle depositing energy in one of those channels or by changing temperature gradients over the detector.

6.4.3. Gain-Drift Correction

After the temperature correction, small and slow amplitude variations over time typically remain. While part of this may result from a non-optimal temperature correction, the majority is expected to originate from the temperature dependence of the room-temperature electronics. The SQUID electronics and the ADC are expected to exhibit a temperature-dependent gain. For the data run, the slow time drifts were corrected iteratively using a non-uniform Gaussian filter applied to the ^{55}Mn K_α line with a width of 100 min, as shown in Figure 6.19, and subsequent a Gaussian fit on the corrected amplitude with a $3\,\sigma$ limit to reduce outliers for the next iteration. Each signal of the corresponding pixel was then rescaled using the time-dependent filter.

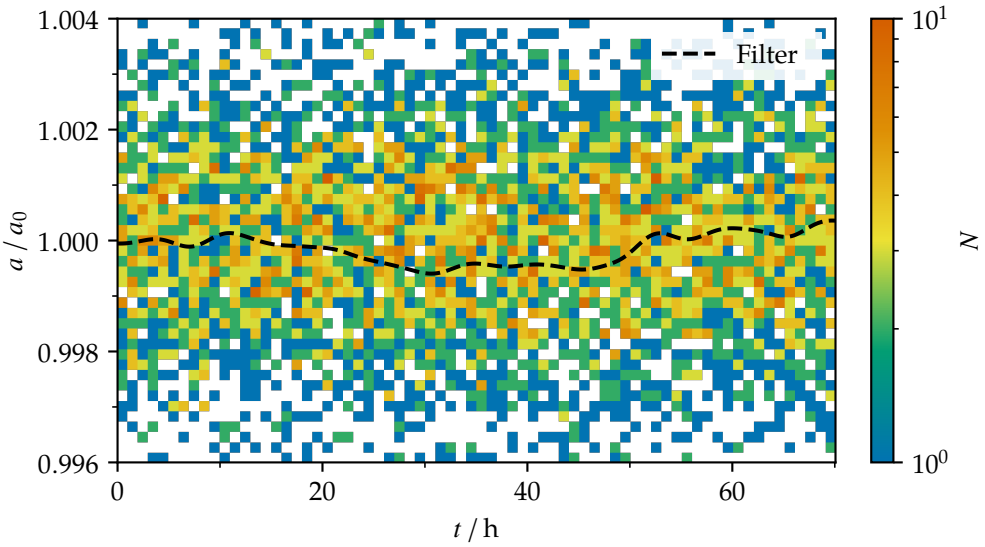

Figure 6.19.: Temperature-corrected amplitude a as a function of time for a single pixel. The applied non-uniform Gaussian filter is used to correct for slow amplitude drifts over time.

The quality of the gain-drift correction must be evaluated using a calibration line different from the one employed for the correction itself. If the filter width is chosen too small, the energy resolution at the reference line may appear artificially improved, while additional noise is introduced at other lines. If the filter width is too large, the amplitude variations are insufficiently corrected. The optimal filter width minimises the energy resolution across

all other calibration lines and can be determined by systematic scanning the filter width. Typically, a high-intensity line is selected to allow for smaller filter widths and thus a faster correction of drifts. In practice, the resolution minimum is often broad, such that the same filter width can be applied to all channels. A sudden amplitude change may indicate a flux change in the channel, which is otherwise not identifiable in symmetric channels.

6.4.4. Energy Calibration

As a final step, each temperature and gain corrected amplitude must be assigned their corresponding energy. Several calibration lines are usually measured, and their positions are determined with a line-shape model. The resulting amplitude values, together with the theoretical line energies and their respective uncertainties, are then used to derive an energy calibration. The calibration is typically well described by a quadratic function without an offset. If the ADC calibration is insufficient, a higher-order polynomial may be required to account for non-linearities.

For a precise calibration, the line shape must be accurately described by a suitable model. A detailed study of the line shape during the Li measurements is beyond the scope of this thesis, and only a general analysis for QUARTET is presented here. A comprehensive discussion can be found in the corresponding work, analysing the muonic Li spectrum [160]. To model the line shape, the same line-shape model is used, consisting of a Voigt core with a short tail toward higher energies and a short tail toward lower energies. This corresponds to the widely used hypermet function [161], a semi-empirical peak-shape function, except that in this case the Gaussian core is replaced, and steps are omitted. Each of the two short tails is described by an exponential function folded with a Gaussian. The resulting line model $M(E)$ is given by

$$M(E) = a\Big[L(E, E_0, \gamma) + a_\mathrm{l}\, e^{-\beta_\mathrm{l}(E_0 - E)}\, \Theta(E_0 - E) \tag{6.10}$$

$$+ a_\mathrm{r}\, e^{-\beta_\mathrm{r}(E - E_0)}\, \Theta(E - E_0)\Big] \otimes G(E, \sigma) \tag{6.11}$$

where L denotes the Lorentzian function, G the Gaussian function, and Θ the Heaviside step function. The degrees of freedom of this model are reduced compared to the hypermet function. For the tails, the origins of the exponentials are fixed to the Voigt position, and the Gaussian folding function is the same for all components. A single line is thus described by the free parameters given by the Voigt position E_0, the area a, the Lorentzian width γ, the Gaussian width σ, the relative amplitudes of the two tails with respect to the Voigt area a_l and a_r, and their logarithmic slopes β_l and β_r.

When applying the model, the Lorentzian width γ was fixed to the corresponding natural line width. The energy resolution was described by the Gaussian width σ, which was further constrained for all lines to follow

$$\sigma(E) = \sqrt{\sigma_E^2 + (E\,\zeta_T)^2} \tag{6.12}$$

with the energy-independent contribution σ_E and the relative temperature sensitivity ζ_T, as discussed previously. The tail parameters were determined from the combined spectrum of the Kα lines of Mn, Mo, and Ag and were then fixed for the individual calibration of all lines and pixels. The values $a_\mathrm{l} = 146(10) \times 10^{-3}$, $a_\mathrm{r} = 55.6(18) \times 10^{-3}$, $\beta_\mathrm{l} = 0.600(18) \times 10^{-3}\,\mathrm{eV}^{-1}$, and $\beta_\mathrm{r} = 1.29(13) \times 10^{-3}\,\mathrm{eV}^{-1}$ were found to describe the tails independently of the calibration line or pixel within their uncertainty. The left, lower-energy tail may originate from athermal phonon losses to the substrate, or from incomplete thermalisation of the pixel, while the right, higher-energy tail may result from inaccurate temperature information, or pile-up. The tail parameters are therefore expected to be influenced by the previous analysis and defined masks.

Table 6.1.: Reference X-ray lines used for the calibration [162–165]. The Li measurements of the data run were calibrated with the Kα lines of Mn, Mo, and Ag. The calibration lines are listed with their energies E and natural linewidths γ.

Element	Line	E / eV	γ / eV
Mn	Kα_1	5898.8010(84)	1.235
	Kα_2	5887.6859(84)	1.460
Mo	Kα_1	17 479.389(10)	3.195
	Kα_2	17 374.577(15)	3.194
Ag	Kα_1	22 163.06(3)	4.30
	Kα_2	21 990.44(10)	4.45

For the Li measurements of the data run, an ^{55}Fe source was used to provide the Kα X-rays of ^{55}Mn, together with an X-ray tube with Mo and Ag targets providing their respective Kα lines. The literature values of the reference lines are listed in Table 6.1. As the Mn Kα_1 and Kα_2 lines significantly overlap, they were fitted together with fixed relative amplitude and position, while the other lines were fitted individually. The corresponding Kβ lines were not used, as they have less statistics, their line shape differs significantly and cannot be described by the model, and they are expected to exhibit chemical energy shifts, making them sensitive to the chemical environment of the emitting atom.

The model defined above is iteratively fitted to the spectra of each pixel. To obtain suitable starting parameters, the fit is first performed for each line individually using a Voigt profile,

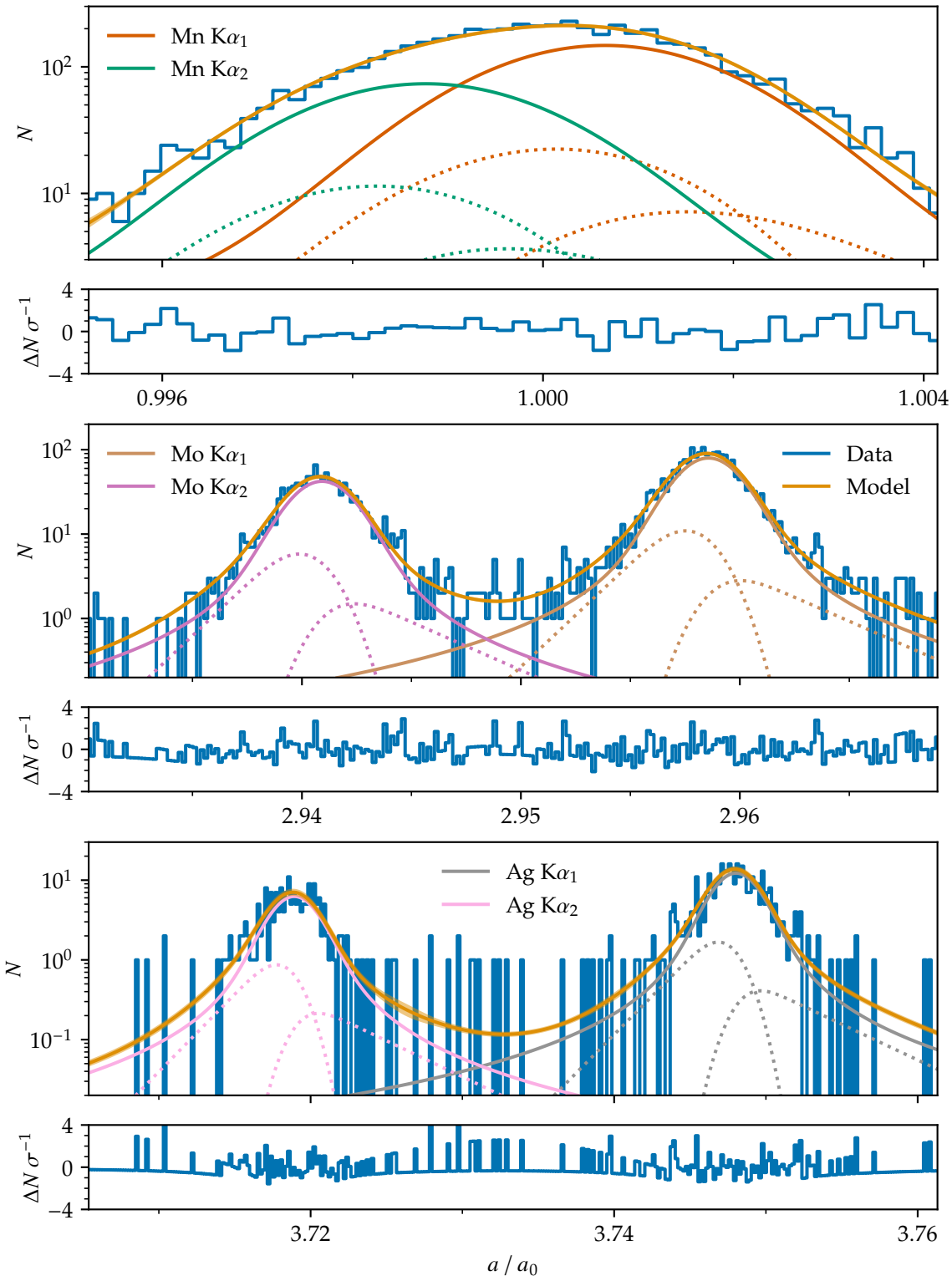

Figure 6.20.: Fit of the line-shape model to the Kα lines of Mn, Mo, and Ag of a single pixel. The model reproduces the line shape, including the tails, with sufficient accuracy.

then for all lines combined with a composite model, and finally with a composite model based on the described hypermet line shape. For the fits, the residuals are calculated as signed square roots of the Poisson deviance, which account for the likelihood ratio. As an example, the fit of the Kα lines of Mn, Mo, and Ag of a single pixel is shown in Figure 6.20.

The energy calibration is then obtained via orthogonal distance regression, based on the fit results and the corresponding literature values including their uncertainties. As the calibration model, a quadratic function without offset is used, with two free parameters, given by the slope and the quadratic non-linearity. This corresponds to the expected leading-order term of the non-linearity without ADC non-linearities. For the five calibration lines, four of which consist of two closely spaced line pairs, introducing additional free parameters would not yield a reliable fit or uncertainties. As an example, the energy calibration of a single pixel is shown in Figure 6.21.

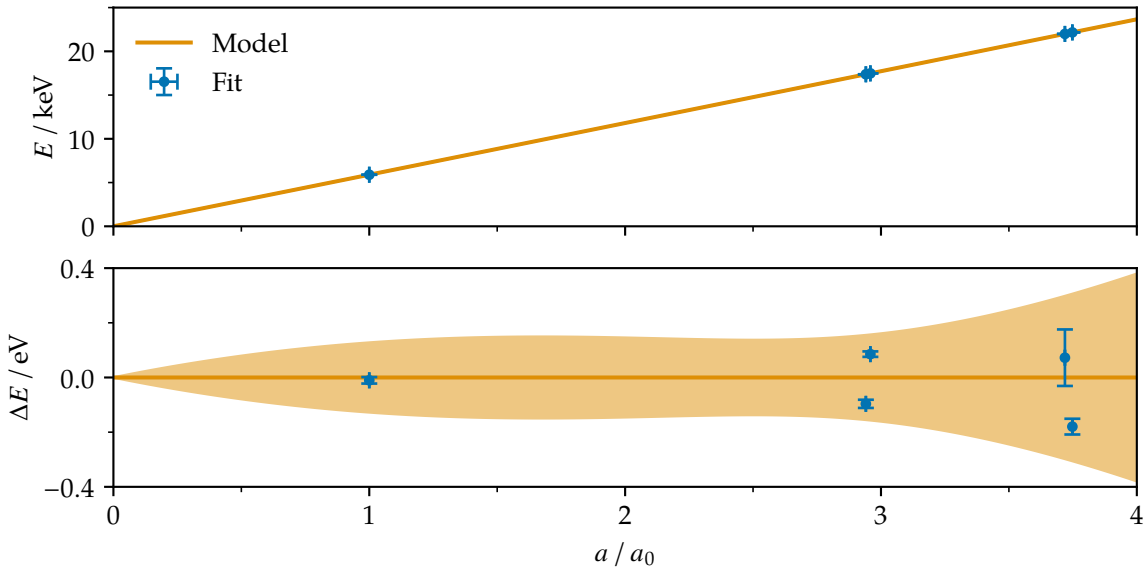

Figure 6.21.: Energy calibration of a single pixel with its 1 σ uncertainty, assigning each amplitude a to a corresponding energy E. The calibration uncertainty is dominated by the accuracy of the fitted line positions.

For the individual pixels, the calibration yields uncertainties of about 200 meV at 18.7 keV, corresponding to the $2p$–$1s$ transition of muonic Li. This uncertainty is limited by the accuracy of the fitted line positions, which is limited by the detector energy resolution, the limited number of calibration lines, and the relatively low statistics per line, in particular for the Kα lines of Ag. While the Kβ lines cannot be sufficiently described by the model, their line shape can be determined from the overlaid spectrum of all pixels. This can not yield absolute values for the calibration, but could assist in aligning the individual pixels relative to each other in

a combined, detector wide model. However, this approach is under discussion and is not considered in this thesis.

For the combined energy spectrum, the dc-measured temperature-sensitive channels are excluded, as they are more strongly affected by the remaining ADC non-linearity due to their varying offset. In addition, one channel was unstable with uncorrectable amplitude variations over time and was therefore excluded. Furthermore, two pixels with significantly worse energy resolution were omitted, as well as three pixels with calibration residuals larger by more than a factor of five. In addition, five pixels showing a weaker combination of both effects were excluded. Several of these also exhibited abrupt amplitude offsets during the gain-drift correction. It is expected that most of the omitted channels experienced uncorrectable flux changes in their meander.

Chapter 7.

Results

The successful letter of intent [6] led to a first test run in October 2023, carried out with the previously described experimental setup at the *πE1* beamline at PSI. This seven-day long test run, serving as a proof of principle and marking the first application of MMCs for high-precision X-ray spectroscopy of exotic atoms, is briefly discussed. Several limitations of the detector, the experimental setup, and the data analysis were identified and subsequently addressed in preparation for the data run, and the *maXs 30-56-14* detector for QUARTET was developed. Results of its first measurements before to the data run are presented. After the data run, we characterized the detector in more detail and at different temperatures, as described in the corresponding work [14]. A successful research proposal [7] allowed a data run in October 2024 at PSI. This eleven-day long run is discussed at the end of the chapter. Long and stable measurements of muonic Li, Be, and B allow for a precise determination of their muonic $2p$–$1s$ transition energy, and consequently their nuclear charge radii. As an example, the muonic Li measurement is analysed in more detail, following the analysis of the previous chapter, and the combined spectrum together with the estimated calibration accuracy is discussed. The dedicated analysis of the muonic Li measurements, including the determination of the nuclear charge radii and the isotope shift, is presented in the corresponding work [160], while the analyses of muonic Be and B are reported in their respective ongoing works.

These results demonstrate the feasibility of QUARTET for significantly improving the accuracy of nuclear charge radii of light nuclei with MMC-based detectors. Based on the measurements of muonic Li, Be, and B during the data run, an improvement in the accuracy of their nuclear charge radii by a factor of 3 to 5 is expected. Another beamtime request has been approved for 2025 with a *maXs 100-56-14* detector, which is based on the *maXs 30-56-14* design but employs 100 µm-thick absorbers, and will target muonic C and O [8].

7.1. Test Run 2023

At the *πE1* beamline at PSI, a test run was conducted in October 2023 with the previously described experimental setup, consisting of the *maXs 30-v2b* detector and the cryostat sidearm [2]. It was followed by nearly a month of preparations and optimizations at the staging area. The

run served both as a proof of principle for X-ray spectroscopy of exotic atoms and as preparation for the subsequent data run, and is therefore only briefly summarized here.

7.1.1. Measurement Schedule

During the test run, longer measurements were performed with the Li, Be, and B targets. In addition, measurements were carried out with the other targets shown in Figure 5.11, shorter calibration runs using different sources and rates, tests with the X-ray tube at various targets and rates, background measurements with and without the muon beam, and measurements at different muon beam momenta. An overview of the test run timeline is shown in Figure 7.1, where longer stable measurements are marked with their respective muon target.

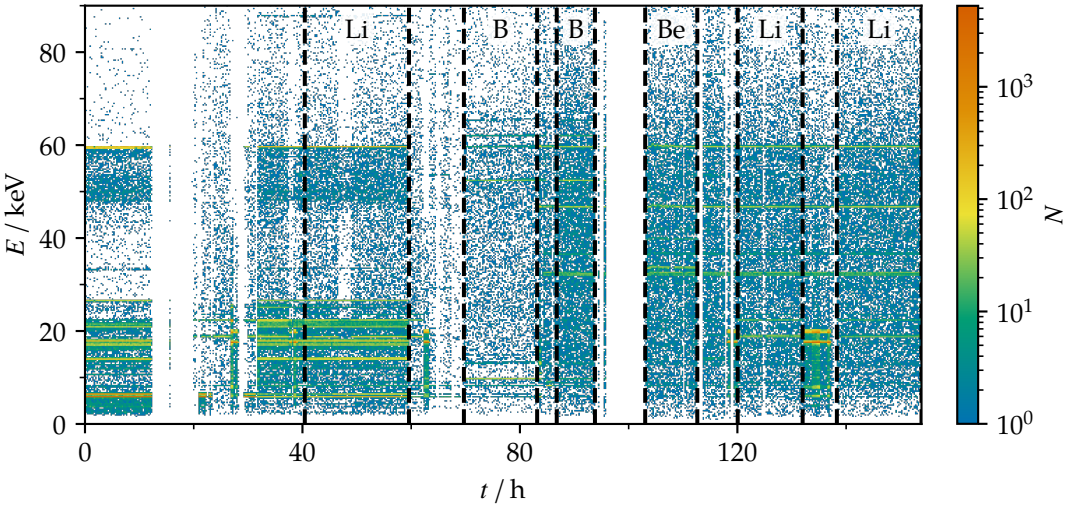

Figure 7.1.: Overview of the estimated energy E as a function of time t during the test run. Longer stable measurement periods are marked with their corresponding muon target. The energy values are derived from the uncorrected pulse amplitude.

During periods without muon beam, calibration source and rate tests were performed. The calibration sources were positioned between the X-ray windows of the target chamber and the cryostat sidearm, at a radial distance that did not cover the field of view of the target. For the calibration lines observed on the different pixels, significant shadowing across the detector was visible, with some pixels hardly detecting certain sources. This effect was caused by the relatively small opening angle of the outer X-ray window of the cryostat sidearm. The calibration sources were therefore later positioned closer to the center, partly overlapping with the detector field of view of the target.

During periods with muon beam, measurements with the different muon targets were performed. The effect of Michel electrons was studied at different muon momenta and corresponding rates. Phonon clusters from Michel electrons were identified, and the detector

performance at different cluster rates was investigated. The rates of the muonic $2p$–$1s$ transitions of the different targets were estimated and found later to be consistent with expectations from *Geant4* simulations [7]. Longer measurements were carried out for the Li, Be, and B targets. The analysis yielded an expected accuracy for the corresponding $2p$–$1s$ transitions comparable to the most precise existing measurements. However, the energy calibration of the individual pixels showed large residuals, and the individual spectra of most pixels could not be consistently superimposed with sufficient accuracy.

The data-taking efficiency of the detector during the measurements was about 84 %, limited mainly by template generation for the online analysis with *PAQS*, which does not allow parallel measurements, and by a temporary loss of cooling power of the cryostat. After about 100 hours, the dilution refrigerator lost significant cooling power and was subsequently warmed up to 4 K. The ^{3}He^{4}He mixture was pumped out, recondensed, and cooled down again to 12 mK. The cooling power loss was later attributed to unstable operation caused by increased ^{4}He circulation due to a high still temperature of the cryostat, as well as by a larger than usual amount of condensed ^{3}He^{4}He mixture. Measurements were resumed after about 6 hours.

7.1.2. Detector Performance

Of the 32 channels, 26 were operational during the test run. Among the six non-operational channels, one had a broken front-end SQUID, one had a broken electrical connection between the first- and second-stage SQUID readout, one temperature-sensitive channel was unstable and therefore not used, and three channels showed no pulses. The pulse height and energy resolution of the detector during the test run are shown in Figure 7.2. The median pulse height was $10\,\mathrm{m}\Phi_0\,\mathrm{keV}^{-1}$, and the median energy resolution was $\Delta E_{\mathrm{FWHM}} = 15\,\mathrm{eV}$.

Compared to previously reported values for the same detector module [146], the pulse heights were about one third smaller and the energy resolution was more than a factor of two worse. The detector temperature during the test run, about 25(1) mK, was significantly higher than the previously achieved value of down to 15(1) mK with this module [146]. This higher operating temperature resulted in reduced pulse heights and degraded energy resolution. The higher temperature was likely due to the glue underneath the detector and SQUID chips becoming brittle during repeated cooldowns of the module, caused by the different thermal contraction of the copper platform and the silicon chips.

7.1.3. Implications and Improvements

During the test run, the limitations of the detector, the experimental setup, and the data analysis were identified, and provided the basis for preparing the data run.

In addition to the significantly degraded energy resolution of the *maXs 30-v2b* detector, the slow thermalization of the individual thermal baths to the silicon substrate, about 200 ms,

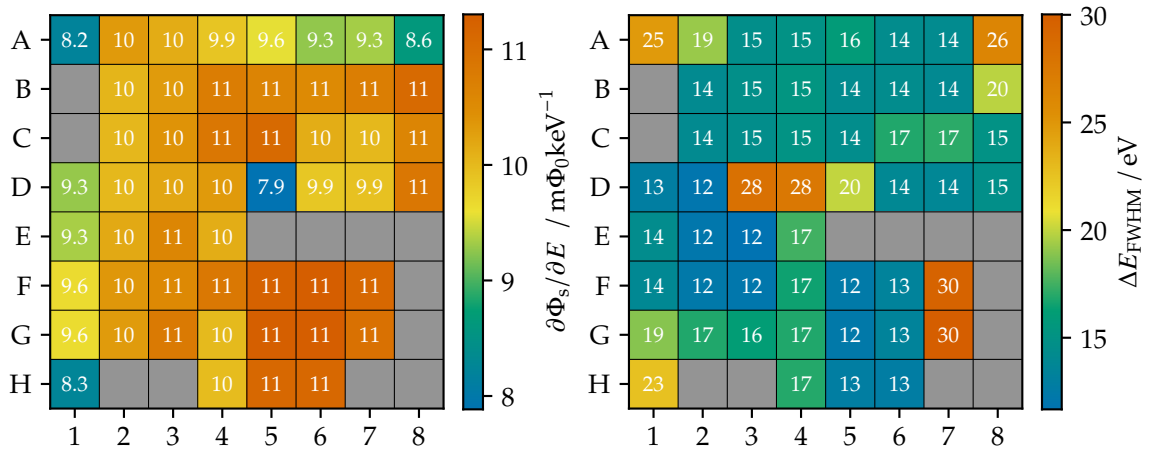

Figure 7.2.: Pulse height $\partial\Phi_s/\partial E$ (left) and energy resolution ΔE_{FWHM} of the individual pixels during the test run. The pulse height was estimated from the difference between the pre-trigger offset and the signal maximum or minimum, and the energy resolution was derived from the NEP.

limited the maximum rate due to the required long channel-wise holdoff time. This motivated the design and fabrication of the *maXs 30-56-14* detector. It was developed to achieve improved energy resolution, including at higher energies, by optimizing the general design, reducing temperature sensitivity, and introducing more sensitive asymmetric temperature channels. These channels are more strongly coupled to the detector substrate and therefore more responsive to energy deposited in the substrate by Michel electrons. The interconnected thermal baths reduce the thermalization time, allowing shorter channel-wise holdoff times and thus a higher maximum rate.

The experimental setup was further improved. For the cryostat sidearm, the diameter of the outer X-ray window was increased from 14 mm to 28 mm, together with larger diameters of the inner windows. This modification almost completely removed shadowing and allowed the distance between the detector and the muon target to be reduced from about 15 cm to about 13 cm for the data run. Furthermore, the large calibration residuals reported during the test run were addressed by developing the ADCs calibration, thereby reducing the effect of its non-linearity. Measurements with different calibration sources and rates, with the X-ray tube at various targets, and background measurements formed the basis for developing a calibration strategy for the data run. For each muon target, a set of calibration sources and lines was selected while avoiding overlapping lines.

The data analysis with *DARQ* was limited to individual measurements and yielded low-FOM templates for short, low-statistics measurements. Its amplitude dependence and not corrected timing jitter significantly reduced its usability for QUARTET. The results showed

artefacts, were strongly amplitude dependent, and pile-ups could not be reliably distinguished based on their χ^2 values. Phonon clusters were identified only by coincidence, which was insufficient to distinguish Michel-electron events or to study cluster properties. These limitations led to the development of *fitfiles*, which is not restricted to single *PAQS* measurements and provides amplitude-independent, timing-jitter corrected data reduction. It allows reliable identification of different pulse families and pile-ups with significantly higher sensitivity. While the online data reduction during the test run was limited to the downsampled *PAQS* analysis, the *fitfiles* library provides the same functionality online as in the offline analysis. Although it cannot read raw *PAQS* data during a running measurement, the implemented data selection and correction, in particularly the temperature correction and energy calibration, were applied during the data run.

7.2. maXs 30-56-14

After the fabrication of three *maXs 30-56-14* wafers, several detectors were tested at 4 K in liquid helium, of which three were selected and operated at mK temperatures in a dilution refrigerator. All tested detectors exhibited significantly reduced critical currents of the electrical vias, and the preparation of a persistent current proved unreliable. These issues were later related to fabrication issues caused by sharp corners after etching and by overetching of the first wiring layer, which led to nearly cut-off electrical lines in the second wiring layer at line crossings and electrical vias. Of the three detectors operated in a dilution refrigerator, the *v1w1c16* detector was identified as the best-performing one. Based on these measurements, it was decided to use the *maXs 30-v2b* detector, which had already been used for the test run, also for the data run. The *v1w1c16* detector had too few working channels and an unreliable preparation of a persistent current. The first measurements with this detector before to the data run are discussed here, focusing on the properties most relevant for QUARTET, in particular the energy resolution and thermalization. After the data run, we characterized this detector at different temperatures in the cryostat sidearm, and the results are reported in the corresponding work [14].

As the cryostat sidearm was still being optimized and modified for the data run, it was not yet available. The measurements were therefore conducted with a setup previously adapted for a detector implanted with ^{193}Pt [20], itself based on an earlier setup [166]. This setup was mounted downwards on the mixing chamber of the cryostat, placing the detector at a large distance from the outer X-ray window at the bottom of the cryostat, which significantly limited the solid angle seen by the detector of external radioactive sources. In addition, radioactive safety regulations at KIP, part of Heidelberg University, permit the use of radioactive sources only in the permanent presence and under the constant supervision of an authorized person,

regardless of their activity. Consequently, only short measurements with low count rates were possible.

7.2.1. Detector Performance

While all 32 SQUID readout channels were functional, most MMC channels were not operational and showed no signals. At 4 K, the bonding wires between the detector and the input coil of the front-end SQUID are normal conducting and generate Johnson-Nyquist noise, which is large compared to the intrinsic SQUID noise. This characteristic noise is measured as flux noise in the SQUID if its input coil is part of a closed electrical circuit, and from the noise spectrum the inductance of the circuit can be determined. Several channels did not exhibit this characteristic noise and therefore had a disconnected electrical line, presumably in the connection of the second wiring layer linking the central bond pad to the persistent current switch.

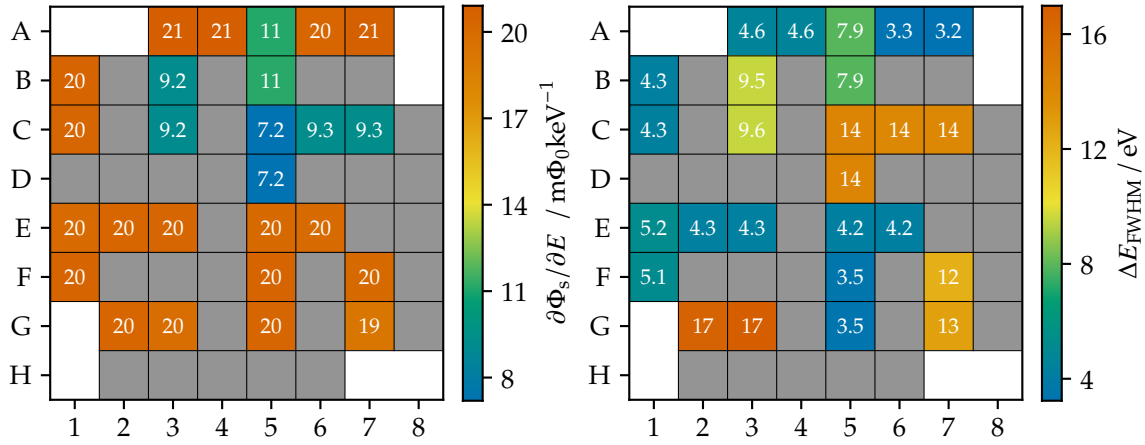

Figure 7.3.: Pulse height $\partial\Phi_s/\partial E$ (left) and energy resolution ΔE_{FWHM} (right) for the symmetric channels of the *maXs 30-56-14 v1w1c16* detector. A field current I_f of 40 mA was used. The pulse height was estimated from the difference between the pre-trigger offset and the signal maximum or minimum, and the energy resolution was derived from the NEP.

The detector was operated at the base temperature of the dilution refrigerator, with the mixing chamber reaching below 7 mK. A persistent current was prepared over a wide range of field currents I_f and heater currents I_h, but its preparation was generally unreliable. Pulses were observed only for field currents up to 50 mA in some channels, while a field current of 40 mA yielded pulses in most operable channels, presumably with the largest pulse heights. The pulse height $\partial\Phi_s/\partial E$ and the energy resolution ΔE_{FWHM} for the different symmetric channels are shown in Figure 7.3.

Out of the 28 symmetric channels, only 13 were operational. Among these, four exhibited significantly lower pulse heights, indicating that the preparation of the persistent current was not successful for them. Of the remaining nine channels with large pulse heights, three showed higher noise levels, and only six channels performed as expected for the relatively low persistent current, with an energy resolution of about $\Delta E_{\mathrm{FWHM}} = 4\,\mathrm{eV}$. These pixels had pulse heights of about $20\,\mathrm{m}\Phi_0\,\mathrm{keV}^{-1}$, which, according to detector simulations, corresponds to a detector temperature of about 14(1) mK and an energy resolution of up to $\Delta E_{\mathrm{FWHM}} = 3.1\,\mathrm{eV}$ for a channel with very low SQUID noise. This detector temperature is among the lowest reported operating temperatures of an MMC array.

All asymmetric temperature-sensitive channels were operational but covered by the collimator. The *v1w1c16* detector is a version with two temperature-sensitive channels directly coupled to the thermal bath, while the other two are thermally coupled only to the silicon substrate.

7.2.2. Pulse Shape

The pulse shape can be described by the exponential pulse model, previously introduced in equation (6.8). A model with two rise and two decay time constants reproduces the observed pulse shape with sufficient accuracy. The corresponding model and its components are shown in Figure 7.4. After the data run, we investigated the signal shape also at different temperatures [14].

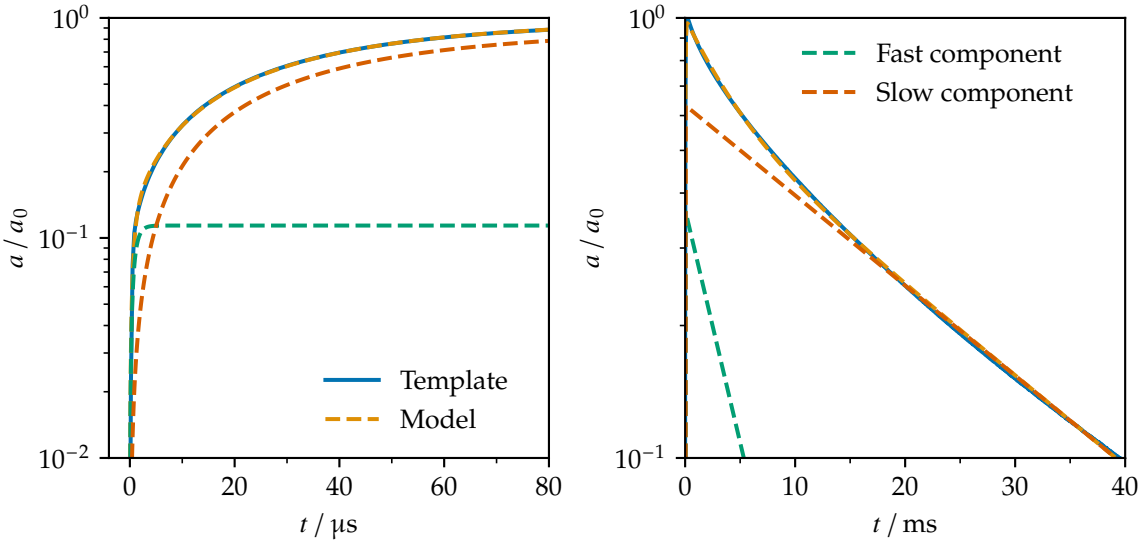

Figure 7.4.: Fast and slow components of the pulse rise (left) and decay (right) from the exponential pulse model fitted to the template of a pixel. The pulses exhibit two rise and two decay components.

The pulse rise consists of a fast component with a time constant $\tau_{r1} = 0.8\,\mu s$ and a slower, dominant component with $\tau_{r2} = 37\,\mu s$ and a relative amplitude fraction of $r_{r2} = 0.89$. The fast component originates from the sensor region beneath the stems, before the thermal bottleneck in the sensor. This region directly responds to the temperature increase and the thermalization of the absorber. It accounts for about 14 % of the total sensor area and matches reasonably well the corresponding relative fraction $r_{r1} = 0.11$. The slower rise time constant, expected to be about 20 µs at a temperature of 14 mK, is limited by four thermal links, each estimated to be about 2/3 square. The larger measured value may be explained by a thermal gradient extending from the wide thermal links into the main sensor area, effectively increasing the geometrical resistance compared to the estimated value.

The decay also exhibits two components, a fast time constant $\tau_{d1} = 4.1\,ms$ and a slower, dominant component with $\tau_{d2} = 21\,ms$ and a relative amplitude fraction of $r_{d1} = 0.63$. The fast component agrees, within fabrication uncertainties, with the expected time constant of about 6 ms, whereas the significantly slower component can only be explained by the thermalization of a non-ideal thermal bath. The thermal bath stretches across the full detector, with its heat capacity distributed over the entire structure. The part of the bath directly connected to the thermal link of the MMC has a small heat capacity compared to that of the MMC itself and therefore relies on thermalization to other regions with larger heat capacities. These include the backside via a thermal via, the large front-side gold pads, and the heat capacities of other MMCs. Measurements of the signal shape at different temperatures show that this slow component appears only at low temperatures [14], most likely due to faster thermalization at higher temperatures. The slowest decay component, with a time constant of 21 ms, is more than one order of magnitude faster than the roughly 300 ms time constant of the *maXs 30-v2b* detector at low temperatures [146], which should allow for a significantly shorter holdoff and a higher signal rate.

7.2.3. Thermalization

For the QUARTET measurements, the holdoff time is expected to limit the maximum achievable rate, while the accuracy of the temperature information is expected to constrain the energy resolution at higher energies. To investigate these effects, both properties are further inversitaged for the new detector. The time difference to the last triggered pulse in the same pixel Δt_p, and the absolute flux difference between the asymmetric temperature-sensitive channels $|\Delta\Phi_{s1} - \Delta\Phi_{s2}|$, are shown in Figure 7.5.

For short time differences Δt_p to the last triggered pulse in the same pixel, the determined energy of subsequent pulses decreases significantly. An exponential fit yields an energy reduction of up to about 270 eV with a time constant of approximately 27 ms. This effect cannot be explained by the amplitude reduction of a slightly warmer pixel. Based on the

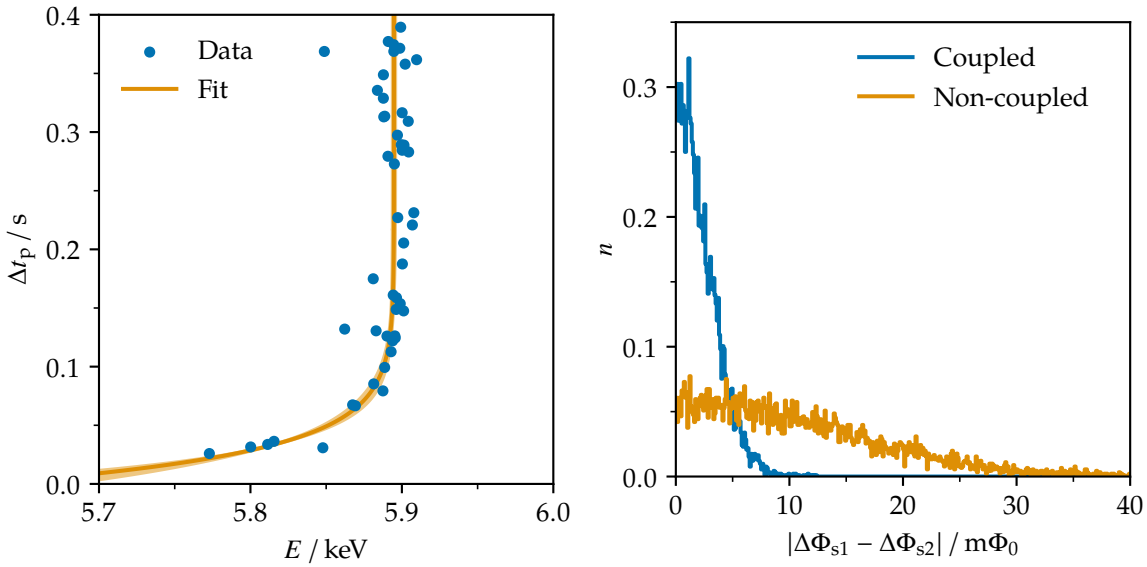

Figure 7.5.: Energy E as a function of the time difference to the last triggered pulse in the same pixel Δt_p at the ^{55}Mn K_α line of an ^{55}Fe source (left), and the gain- and offset-corrected absolute flux difference between the two asymmetric temperature-sensitive channels $|\Delta\Phi_{s1} - \Delta\Phi_{s2}|$, directly coupled to the thermal bath, and the two non-coupled channels (right).

temperature sensitivity $\zeta_T/T \approx -6.6 \times 10^{-2}\,\mathrm{mK}^{-1}$ from detector simulations, the expected energy reduction of a pile-up at the ^{55}Mn K_α line is only about 24 eV. The much larger observed reduction instead originates from pre-trigger distortion caused by the slow decay of the previous pulse. This residual exponential decay shifts the pre-trigger offset, resulting in an incorrect normalization and thus an artificially reduced amplitude. The required holdoff time is therefore limited by the pre-trigger distortion associated with the longest decay component of the pulse shape. In comparison to the previously used 500 ms holdoff for the *maXs 30-v2b* detector, which corresponds to a maximum energy reduction of up to 0.5 eV, the required holdoff for the same maximum reduction of the observed distortion is about 170 ms, an improvement by roughly a factor of three. However, with ac-measured signals, the energy reduction caused by the pre-trigger distortion can be significantly suppressed, such that an overall reduction of the holdoff time by about an order of magnitude should be achievable. A correction of the pre-trigger distortion in the data reduction might even further reduce the holdoff time and should be investigated in a higher-statistics measurement.

To evaluate the accuracy of the temperature information obtained from the pre-trigger offsets of the different asymmetric channels, the differences between their pre-trigger offsets were analyzed. The absolute flux difference $|\Delta\Phi_{s1} - \Delta\Phi_{s2}|$ between the gain- and offset-corrected coincident pre-trigger offsets of the two types of asymmetric temperature-sensitive channels was calculated. The distribution of the uncoupled asymmetric channels, not directly

thermally connected to the thermal bath, follows a Gaussian with a FWHM of 33 mΦ_0, which corresponds, based on the pulse height, to temperature fluctuations of $\sigma_T = 6.8\,\mu$K. In contrast, the channels directly coupled to the thermal bath exhibit a FWHM of 6.4 mΦ_0, corresponding to $\sigma_T = 1.3\,\mu$K, about five times smaller. In addition, the coupled channels reach a lower effective temperature [14]. These channels are therefore significantly more precise and may be used to extract more accurate temperature information, which is expected to reduce the degradation of the energy resolution at higher energies. The achieved mean energy resolution of $\Delta E_{\mathrm{FWHM}} = 4\,$eV, combined with the temperature sensitivity ζ_T/T from simulations, even at its higher value for low field currents I_{f}, and even at the base temperature of the cryostat with expected higher temperature fluctuations, corresponds at the muonic $2p$–$1s$ transition energy of 18.7 keV to an energy resolution of $\Delta E_{\mathrm{FWHM}} = 5.5\,$eV when applying the temperature information from the coupled channels. In contrast, the uncoupled channels yield an expected energy resolution of only 20 eV, limited solely by temperature fluctuations. In addition, stabilizing the cryostat slightly above the base temperature is expected to reduce temperature fluctuations for both coupled and uncoupled channels, further improving the energy resolution.

7.3. Data Run 2024

The data run was carried out in October 2024, one year after the test run, at the same $\pi E1$ beamline at PSI. As the fabrication of the developed *maXs 30-56-14* detector did not succeed, the run was performed with the same *maXs 30-v2b* detector that had been used for the test run. Several optimizations were implemented for the detector setup as previously described. Among these, the ADC calibration, the increased opening angle of the X-ray windows, and the reduced distance between the detector and the target significantly improved the overall performance of the measurements compared to the test run. The detector setup was prepared and optimized for nearly a month at the staging area. During these preparations, a measurement of ^{225}Ac for medical research was also conducted [3], which is not discussed here. In the following, the beamtime schedule and detector performance are described, while the muonic Li measurement is discussed as an example in more detail.

7.3.1. Measurement Schedule

During the data run, nearly all of the measurement time was dedicated to long measurements with Li, Be, and B targets. In addition, a short measurement with Mn was performed to evaluate the possibility of resolving the isotope shift of the muonic $2s$–$2p$ transition. An overview of the data run timeline is shown in Figure 7.1. For the lower-energy Li and Mn measurements, a feedback resistance of $R_{\mathrm{f}} = 100\,\mathrm{k}\Omega$ was used for the SQUID readout in order

to probe a larger range of the ADC code. This reduced the effect of the remaining ADC non-linearity, but also limited the energy range to about 50 keV. For the Be and B measurements, calibration lines at higher energy were required, and a feedback resistance of 30 kΩ was chosen, increasing the energy range by about a factor of three. The change in feedback resistance changed the measured pulse shape and noise, such that the two measurement series had to be evaluated separately, of which the data analysis of the Li and Mn measurements was described as an example in the previous chapter.

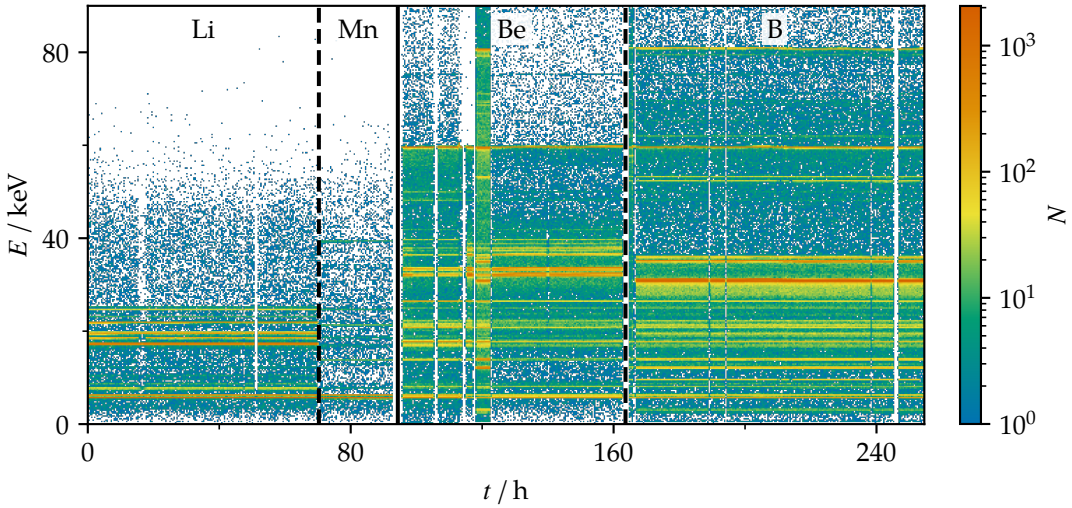

Figure 7.6.: Overview of the estimated energy E as a function of time t during the data run. The energy is estimated from the uncorrected amplitude. The corresponding $2p$–$1s$ transitions of Li, Be, and B are visible at their respective energies of 18.7 keV, 33.4 keV, and 52.3 keV, together with the calibration lines.

Based on the experience from the test run, the individual measurements could be prepared within a short time, and the available muon beam time was used significantly more efficiently. The data-taking efficiency of the detector during the measurements was about 95 % and was mainly limited by target and calibration source changes, as well as by interruptions of the *PAQS* acquisition. In addition, the measurements were continuously calibrated to allow easier identification of flux changes during the analysis. Whenever possible, they were neither interrupted nor was the experimental area entered, in order to maintain stable and unchanged measurement conditions.

7.3.2. Detector Performance

The pulse height and energy resolution of the individual pixels are shown in Figure 7.2. During the data run, 27 out of 32 channels were operational. Among the 5 non-operational channels, one channel was unstable and therefore not used, while the remaining channels

were already non-operational during the test run, showing no pulses or having a broken front-end SQUID. The median pulse height of 10 $m\Phi_0$ keV^{-1} was nearly unchanged compared to the test run, and thus also indicates a similar detector temperature. In contrast, the median energy resolution was ΔE_{FWHM} = 21 eV, significantly worse than the previously reached median of 15 eV. This is related to a higher readout noise, mainly due to lower bias parameters of the front-end SQUIDs, which were necessary to maintain a sufficiently low detector temperature comparable to that of the test run. While a higher front-end bias would have resulted in lower noise, it would also have reduced the pulse height due to a higher detector temperature, leading to an even worse energy resolution.

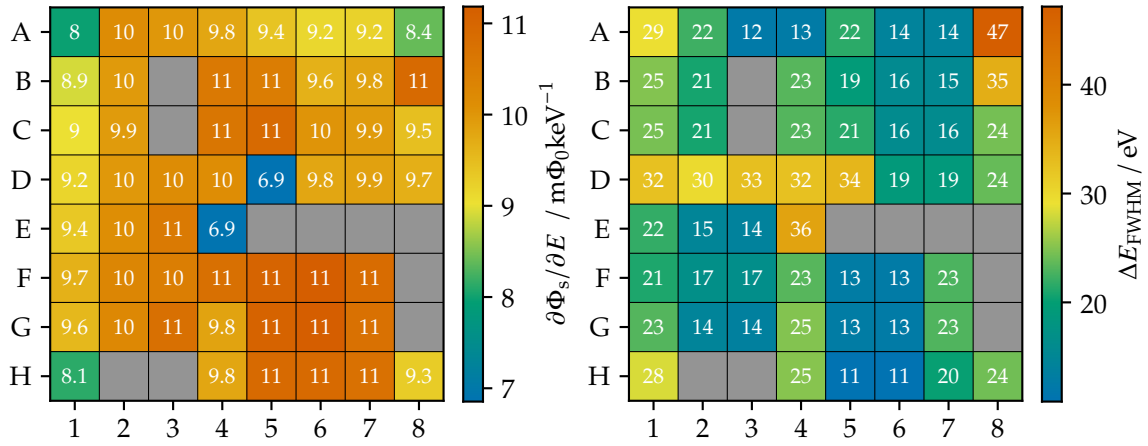

Figure 7.7.: Pulse height $\partial\Phi_s/\partial E$ (left) and energy resolution ΔE_{FWHM} during the data run. The pulse height was estimated from the difference between the pre-trigger offset and the signal maximum or minimum, and the energy resolution was derived from the NEP.

7.3.3. Muonic Lithium

As an example, the measurement of muonic Li, using a split ^{6}Li and ^{7}Li target, is discussed in more detail, following the exemplary analysis presented in the previous chapter. Up to the stage of the energy calibration, the statistics of the Li and Mn measurements were combined. The following demonstrates the successful ADC calibration and the feasibility of QUARTET to precisely determine $2p$–$1s$ transition energies, using muonic Li as an example of the developed general analysis for QUARTET. The precise determination of the $2p$–$1s$ transition energies and the isotope shift with their corresponding uncertainties is beyond the scope of this thesis and is presented in detail in the dedicated analysis [160].

Combined Spectrum

An overview of the calibrated energy as a function of time for the Li measurement is shown in Figure 7.1. The approximately 70-hour long measurement was continuously calibrated with ^{55}Mn Kα X-rays from an ^{55}Fe source, as well as with an X-ray tube operated with Mo and Ag targets. The X-ray tube and the muon beam, however, had to be turned off whenever the experimental area was entered, for example to refill the cooling trap of the dilution refrigerator. The measurement remained stable throughout the entire period, and the muon beam was available for nearly the whole time.

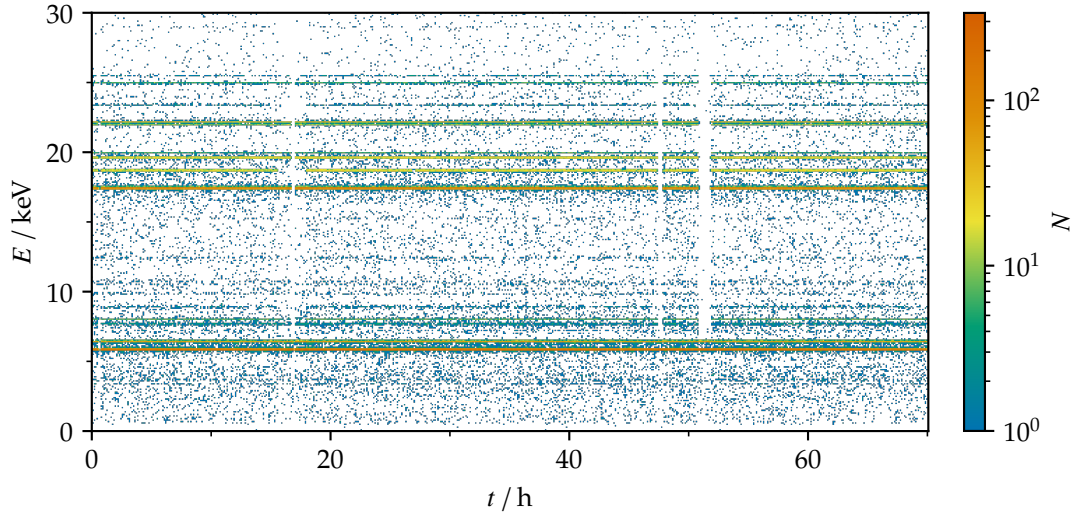

Figure 7.8.: Overview of the measured energy E as a function of time t during the muonic Li measurement. The energy is given as the calibrated energy.

The mean rate of triggered pulses per pixel was about 190 mHz, of which 71 mHz were identified as photons, 88 mHz as phonons, 10 mHz as electrons, and 10 mHz as pile-ups. The efficiency of the data analysis for as photon identified pulses was about 72 %, limited by the required holdoff time of 0.5 s, resulting in a remaining rate of 51 mHz per pixel of accepted pulses. The average remaining rate per pixel r at different calibration lines, as well as at the resolvable muonic Li transitions, is summarised in Table 7.1.

The combined spectrum of the 34 pixels is shown in Figure 7.9. The muonic lines can be identified by their coincidence with the muon entrance window, while non-muon induced lines are identified by their anti-coincidence. However, both have a relatively high false-positive fraction, and their relative contributions must be taken into account. Several muonic Li lines are resolved, whereas other muonic lines originate from copper, the material of the inner wall of the target chamber. In addition to the Kα and Kβ lines of Mn, Mo, and Ag,

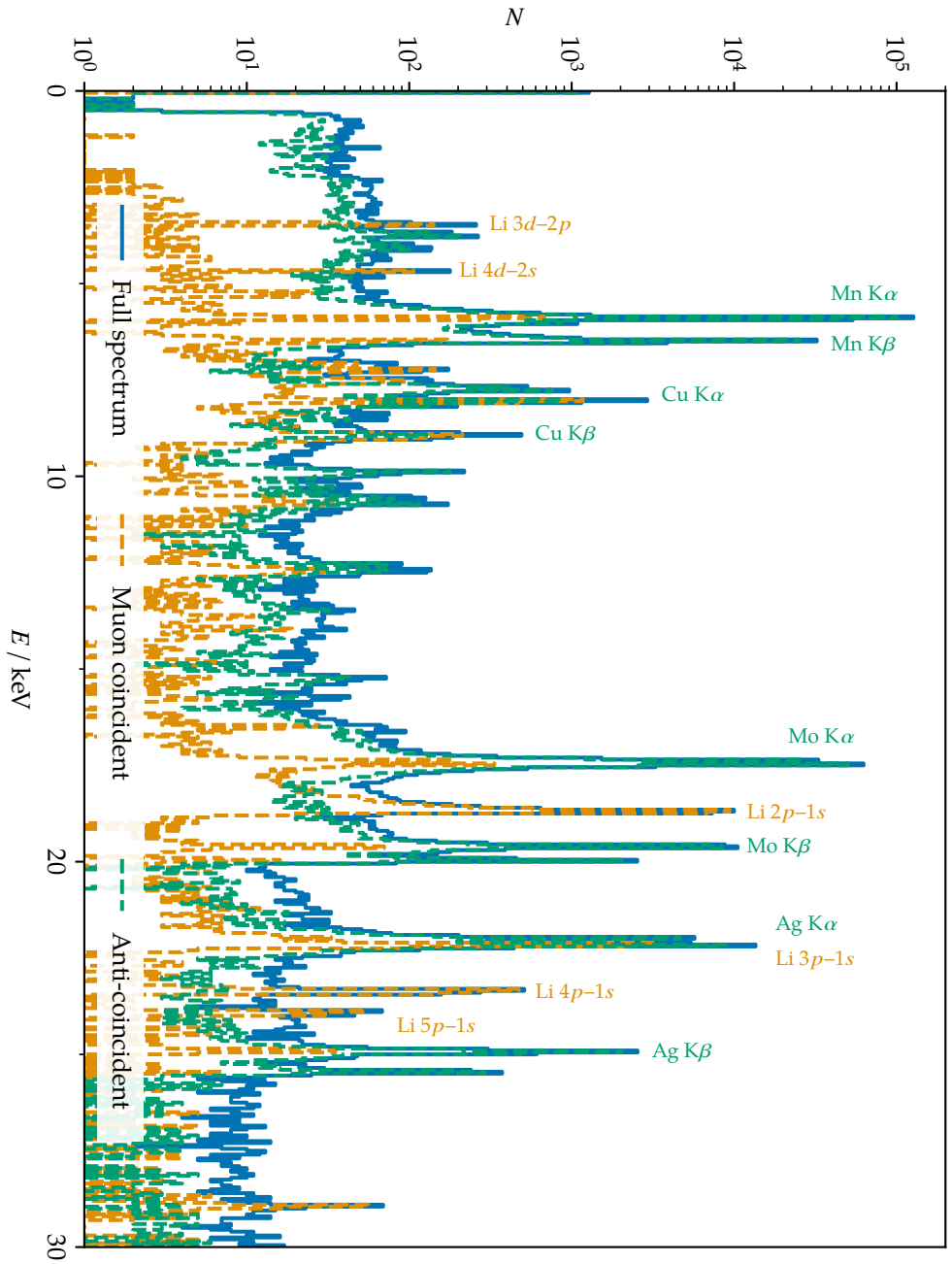

Figure 7.9.: Combined energy spectrum of the muonic Li measurement. The calibration and muonic Li lines are marked. Several other lines, for example from muonic Cu or escape lines from the characteristic energy loss of the Au absorber, are also visible.

Table 7.1.: Remaining rate per pixel r after data analysis at different lines with energy E. In addition to the calibration lines, several muonic Li lines were observed. The rates are not corrected for the energy-dependent absorber efficiency.

Element	Line	E / keV	r / mHz	Element	Line	E / keV	r / mHz
Mn	Kα	5.9	20	μLi	$3d$–$2p$	3.5	0.021
	Kβ	6.5	4.3		$4d$–$2s$	4.7	0.014
Mo	Kα	17.4	12		$2p$–$1s$	18.7	2.1
	Kβ	19.6	2.3		$3p$–$1s$	22.2	0.65
Ag	Kα	22.1	2.5		$4p$–$1s$	23.4	0.10
	Kβ	24.9	0.41		$5p$–$1s$	24.4	0.012

further lines can be identified as escape lines, originating from high-intensity lines and partial energy loss in the Au absorber due to the emission of characteristic X-rays.

Energy Calibration

To estimate the accuracy of the energy calibration, the previously defined line-shape model was fitted to the combined spectrum of all pixels. Figure 7.10 shows the fit of the Kα lines of Mn, Mo, and Ag to the combined spectrum, analogous to Figure 6.20 for a single pixel. The residuals between the fitted line positions of the calibrated spectrum and the literature energies are shown in Figure 7.11.

The calibration uncertainty is obtained as the weighted combination of the calibration uncertainties of the individual pixels, assuming independent Gaussian distributions. This yields an uncertainty of about $\sigma \approx 30\,\text{meV}$ at 18.7 keV, corresponding to the $2p$–$1s$ transition of muonic Li. This statistics-limited calibration corresponds to an accuracy better than 2 ppm, exceeding previously reported calibrations by more than an order of magnitude and meeting the calibration accuracy goal of QUARTET, provided it can be proven to be reliable. A χ^2 test of the residuals yields a reduced χ^2 of 0.75, corresponding to a probability of $p = 0.59$. Thus, the residuals scatter less than statistically expected, and the individual pixels appear to overlay consistently. Additional tests, such as refitting the residuals or excluding individual pixels from the combined spectrum, yields consistent results with similar uncertainties or negligible effects. While the stated uncertainty provides a reasonable estimate, it was not possible to prove its reliability.

Verification of the calibration would require additional calibration lines that can be described by the line-shape model, have sufficiently well-known energies, and provide high enough statistics. The other lines present in the spectrum either cannot be adequately described by the line-shape model, suffer from low statistics, or have insufficiently well-known energies. For example, the Kβ lines provide sufficient statistics, but are affected by chemical shifts

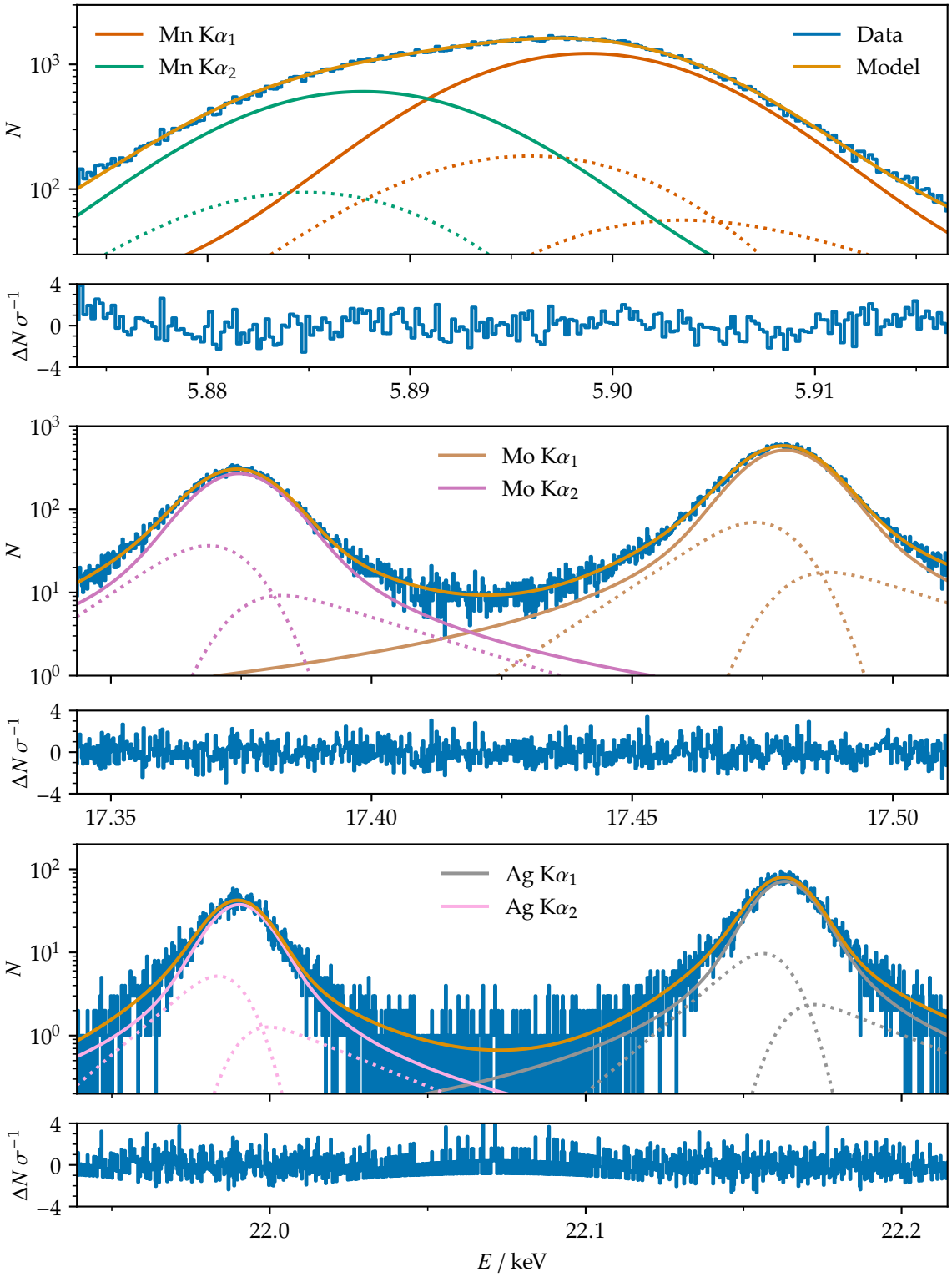

Figure 7.10.: Fit of the line-shape model to the Kα lines of Mn, Mo, and Ag in the combined spectrum.

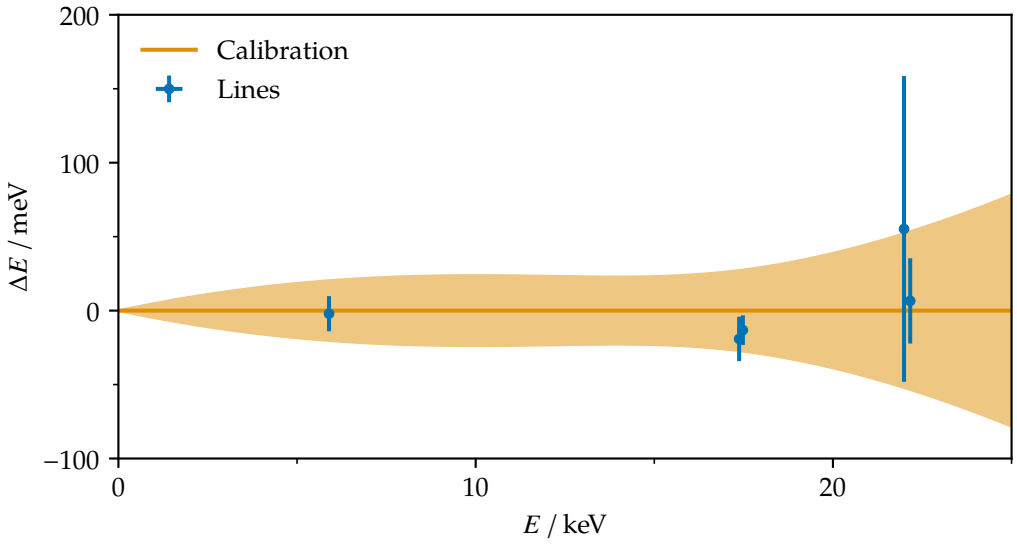

Figure 7.11.: Calibration residuals ΔE of the combined spectrum. The one σ calibration uncertainty is estimated as the weighted combination of the calibration uncertainties of the individual pixels.

and cannot be described by the line-shape model. A new study with a long-term, stable, high-statistics measurement including several calibration lines over a wide energy range could provide proof that an accuracy of 2 ppm, or even better, is feasible. Such a study is, however, not possible due to radiation safety regulations at KIP.

The identical data analysis was repeated without applying the ADC calibration in order to evaluate its effect. The pixel-wise calibration yields on average relative residuals about three times larger. A further pixel-wise comparison would require additional calibration lines with sufficient statistics, as a quadratic calibration function without offset, having two free parameters, can be fitted reasonably well through the five calibration lines, four of which are part of two closely spaced line pairs, even with distinct bit jumps in the ADC response. However, the combined spectrum showed significantly larger residuals, with $\chi^2 = 5.6$ and a corresponding probability of $p = 4.0 \times 10^{-5}$, clearly demonstrating the improvement in energy calibration achieved with the ADC calibration.

Muonic Transition

The muonic Li lines of the $2p$–$1s$ transitions of ^{6}Li and ^{7}Li are shown in Figure 7.12. Fitting the previously defined line-shape model, with only the amplitudes and positions as free parameters, yields uncertainties of about 60 meV for the line positions and an expected improvement in the accuracy of the nuclear charge radii by about one order of magnitude. However, the measured line shape deviates significantly from the model. The observed line

shape exhibits a pronounced low-energy tail, whereas the high-energy tail appears to be suppressed.

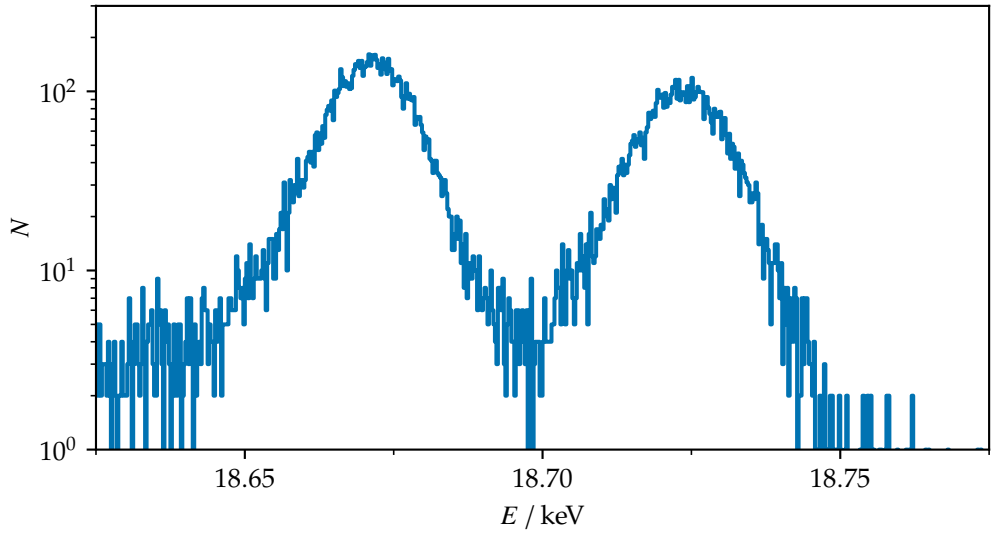

Figure 7.12.: The muonic $2p$–$1s$ lines of ^{6}Li below and ^{7}Li above 18.7 keV. The measured lines deviate significantly from the line-shape model.

The line shape of the $2p$–$1s$ transition of muonic Li is not yet understood. Other muonic lines do not provide sufficient statistics to evaluate if the line shape of muonic lines differ from the line shape of the calibration lines. A possible mechanism that could introduce such a difference would be the origin of the muonic X-rays, which always occur in coincidence with a decaying muon, producing a Michel electron if the muon is not captured by the nucleus. If, in a coincident event, the muonic X-ray is detected and the Michel electron deposits energy in the detector substrate, this could generate a low-energy tail present only in muonic lines. However, the probability of such an event is several orders of magnitude too small, given the limited solid angle covered by the detector, and coincidence events are, if triggered, excluded.

Given the results of the data run with muonic Li, Be, and B, and their ongoing analyses, an improvement in the accuracy of their nuclear charge radii by a factor of 3 to 5 is expected. These expected results, together with those presented in this thesis, demonstrate the feasibility of QUARTET for significantly improving the accuracy of nuclear charge radii of light nuclei with MMC-based detectors. For the data run, the sensitivity was primarily limited by the energy resolution of the detector, which operated at a significantly higher temperature, and by the exclusion of several pixels presumably affected by uncorrectable flux changes. While the fabrication of the developed *maXs 30-56-14* detector did not succeed, such a detector is expected to provide, for example, an energy resolution better than $\Delta E_{\mathrm{FWHM}} = 6\,\mathrm{eV}$ at 18.7 keV, corresponding to the $2p$–$1s$ transition of muonic Li, while also allowing for a higher

maximum rate. A successful fabrication could yield a detector with a significantly improved FOM, estimated to be a factor of five, for a revised measurement.

Chapter 8.

Conclusions

Muonic atoms are particularly well suited for studying nuclear properties. Their low-lying energy levels are highly sensitive to nuclear structure due to the strong overlap of the muon wavefunction with the nucleus. In particular, the muonic $2p$–$1s$ transition exhibits a measurable energy shift caused by the finite nuclear size, which is significantly larger in muonic atoms than in electronic atoms. A fundamental nuclear quantity that can be extracted from accurate measurements of such transitions is the nuclear charge radius [5]. Precise knowledge of this quantity is essential for establishing reliable nuclear models. However, existing methods have left a precision gap for light nuclei [27].

The QUARTET collaboration aims to close this gap by performing high-resolution X-ray spectroscopy of light muonic atoms from Li to Ne [6]. At PSI, the $\pi E1$ beamline provides a continuous low-energy muon beam with a rate of approximately 10 kHz, of which about 60 % are stopped in a muon target. Approximately 80 % of the stopped muons undergo the muonic $2p$–$1s$ transition, emitting characteristic X-rays in the energy range from 19 keV to 207 keV. By employing low-temperature MMC-based detectors, the collaboration aims to achieve a relative accuracy of the muonic $2p$–$1s$ transition energies of up to 2 ppm. This accuracy, combined with refined theoretical models, corresponds to an improvement in the precision of nuclear charge radii by about a factor of 20.

This thesis, carried out within the QUARTET collaboration, focuses on the development and application of MMC-based detectors for high-resolution X-ray spectroscopy of light muonic atoms. It describes the optimization of MMC-based detectors for QUARTET, the preparation of the experimental setup, the development of a general-purpose open-source analysis package, and both the proof of principle test run and the first dedicated data run at PSI, using Li, Be, and B as target materials. The detector, with an active area of 16 mm^2, is positioned approximately 135 mm from the target, covering a fraction of about 7×10^{-5} of the full solid angle and yielding a rate of up to 0.3 Hz for muonic $2p$–$1s$ X-rays. The results represent the first successful application of MMCs to high-precision X-ray spectroscopy of exotic atoms and demonstrate that QUARTET can significantly improve the accuracy of nuclear charge radii for light nuclei by employing MMC-based detectors.

A new MMC-based detector design was optimized for QUARTET. With an active area of $14\,\mathrm{mm}^2$, the design parameters were chosen to achieve high energy resolution while minimizing degradation at higher energies by reducing its sensitivity to temperature fluctuations. The design features interconnected thermal baths to ensure fast thermalization, allowing for a higher event rate and shorter holdoff time. Highly temperature-sensitive asymmetric channels provide precise determination of the relative detector temperature for correcting temperature fluctuations. Based on an FOM that combines the energy-dependent resolution and absorption efficiency, the performance of the detector design was evaluated for the different nuclei targeted by QUARTET.

For the data run, three *maXs 30-56-14* detector wafers of the new design with 25 µm-thick absorbers were fabricated, optimized for the muonic $2p$–$1s$ transitions of Li, Be, and B at 18.7 keV, 33.4 keV, and 52.3 keV, respectively. During production, severe problems occurred in the microfabrication of the wiring layers, resulting in a very low yield of functional channels. Nevertheless, the functional channels of the different detector chips performed as expected. These channels achieved an excellent energy resolution of about $\Delta E_{\mathrm{FWHM}} = 4\,\mathrm{eV}$, faster thermalization with the slowest time constant of about 37 µs, and a more accurate relative detector temperature accuracy of $\sigma_T = 1.3\,\mu\mathrm{K}$. For a fully functional detector, these results would correspond to an improvement of the FOM by approximately a factor of five compared to the *maXs 30-v2b* detector used.

To integrate the detector efficiently with the target chamber and muon beamline, a dedicated experimental setup was prepared, featuring a custom-built cryostat sidearm. The newly developed sidearm reliably reaches low temperatures while positioning the detector approximately 135 mm from the target and providing a large opening angle of about 30°. A fully operational two-stage SQUID readout was implemented, together with an automated system for SQUID tuning and characterization, enabling reliable and rapid preparation of the detector readout. In addition, an ADC calibration procedure was developed to minimize non-linearities. This calibration corrects for discontinuities in the ADC response and is estimated to improve the non-linearity by more than an order of magnitude. Applying the ADC calibration resulted in a significant reduction of residuals in the combined, pixel-wise energy-calibrated spectrum, lowering the reduced χ^2 by more than an order of magnitude and allowing the spectra of individual pixels to be overlaid consistently.

To obtain high-resolution energy spectra, a general-purpose open-source analysis library called *fitfiles* was developed for online processing, data reduction, and offline analysis [4]. The library provides a complete analysis chain for triggered signals, from raw data to calibrated energy spectra. It allows multiple low-statistics measurements to be combined and analyzed iteratively, improves performance through *multiprocessing*, and applies the ADC calibration. The library provides amplitude-independent, timing-jitter corrected fits that yield reliable

results. The data reduction was validated using a signal generator capable of producing arbitrary pulses and pile-up events. The fit based on the whitened matched filter achieves the expected energy resolution limited by the NEP. Compared to the *DARQ* library and for pulses with non-negligible timing jitter, unresolved pile-ups are reduced by about a factor of 5, while overall changes in the pulse shape are detected with approximately a factor of 20 higher sensitivity. As an example, the muonic Li measurements from the data run were analyzed. With the newly developed library, it was possible to identify individual pulse families and to successfully address Michel-electron related events.

Using the developed detector setup, two successful beamtime measurements were conducted at PSI with an existing *maXs 30-v2b* detector module [2]. For both runs, the detector setup was transported, reassembled, and optimized at a staging area. The first test run served as a proof of principle for X-ray spectroscopy of exotic atoms and as preparation for the subsequent data run. The dedicated data run consisted of long and stable measurements of muonic Li, Be, and B [7]. The measurements were primarily limited by the energy resolution of the detector, which operated at a significantly higher temperature, and by several pixels presumably affected by uncorrectable flux changes. For muonic Li, the estimated sensitivity based on the statistics, was about 4 ppm, while the energy calibration reached an accuracy of approximately 30 meV. However, it was not possible to independently verify the energy calibration and the line shape of the muonic $2p$–$1s$ transition is currently not understood, further limiting the expected accuracy. Due to these limitations, the results indicate that the nuclear charge radii of Li, Be, and B can be determined with an accuracy improved by a factor of 3 to 5 [160].

Another beamtime request has been approved for 2025 with a *maXs 100-56-14* detector [8]. This detector is based on the *maXs 30-56-14* design but employs 100 µm-thick absorbers to enhance its efficiency at higher energies, and will target muonic C and O [148, 167]. A follow-up measurement with Li and Be is under consideration with a *maXs 30-56-14* detector for 2026.

Appendix

Appendix A.

SQUID Characteristics

A large number of front-end SQUIDs and SQUID array chips from HDSQ wafer *14w1* were automatically characterized for the QUARTET experiment. The most relevant measured characteristics are summarised in Tables A.1–A.3. Table A.1 lists the front-end SQUIDs used in the first detector module, Table A.2 those used in the second detector module, and Table A.3 the SQUID arrays of the amplifier module. These measurements were conducted at mK temperatures in a dilution refrigerator during many cooldowns.

Table A.1.: Measured characteristics of the front-end SQUIDs from HDSQ wafer *14w1* used in the first detector module.

Chip		I_b / µA	M_{fb}^{-1} / µA $\Phi_0{}^{-1}$	M_{in}^{-1} / µA $\Phi_0{}^{-1}$	ΔU / µV
3A-06	1	17.7	43.8	9.0	31.8
	2	17.9	43.2	8.9	31.8
	3	17.5	43.5	9.0	31.5
	4	18.0	43.2	8.9	41.4
4B-02	1	18.2	44.0	9.1	35.9
	2	18.2	43.6	9.0	35.7
	3	18.4	43.4	9.0	35.9
	4	18.9	43.5	8.7	31.9
3C-06	1	17.6	43.1	9.0	33.4
	2	17.7	43.0	8.9	33.9
	3	17.6	42.9	8.9	33.3
	4	17.7	42.6	8.9	33.6
4B-20	1	18.2	43.4	9.0	33.5
	2	18.2	43.8	9.0	33.6
	3	17.9	43.5	8.9	32.7
	4	18.0	43.5	9.0	32.8
3B-14	1	17.9	43.5	8.9	33.4
	2	17.9	42.8	8.9	33.0
	3	17.7	43.3	8.9	33.0
	4	17.5	43.0	8.9	32.8
4A-16	1	18.2	44.0	9.1	32.4
	2	18.2	43.8	9.0	32.4
	3	18.2	44.0	9.0	32.5
	4	18.2	43.8	9.0	31.9
3B-18	1	18.0	43.1	8.9	34.5
	2	17.7	42.6	8.8	34.6
	3	17.7	43.2	8.9	34.9
	4	17.8	42.7	8.9	35.7
3B-20	1	17.5	43.6	9.0	32.4
	2	17.7	43.4	8.9	32.9
	3	17.6	42.7	8.9	33.1
	4	17.6	43.3	8.9	32.4

Table A.2.: Measured characteristics of the front-end SQUIDs from HDSQ wafer *14w1* used in the second detector module. The second channel of chip *3B-22* exhibits a large critical current, and the chip was subsequently replaced by chip *4B-22*, tested at 4 K in liquid helium.

Chip		I_b / µA	M_{fb}^{-1} / µA $\Phi_0{}^{-1}$	M_{in}^{-1} / µA $\Phi_0{}^{-1}$	ΔU / µV
4C-12	1	18.5	43.8	9.0	36.1
	2	18.6	43.9	9.1	36.6
	3	18.6	44.1	9.1	36.6
	4	18.5	43.6	9.0	31.5
3B-22	1	16.7	42.5	8.9	35.6
	2	27.9	42.8	8.9	48.1
	3	16.9	42.8	8.9	34.3
	4	16.7	43.3	8.9	34.9
4B-12	1	17.6	43.2	8.9	35.1
	2	17.8	43.2	9.0	36.3
	3	17.9	43.2	9.0	35.5
	4	18.1	43.3	9.0	36.4
4A-06	1	18.3	44.1	9.0	32.9
	2	18.4	43.7	9.1	33.0
	3	18.3	43.0	9.0	33.4
	4	18.3	43.3	9.0	33.1
4B-16	1	17.0	43.2	8.9	35.9
	2	17.5	42.9	8.8	36.8
	3	17.5	43.0	8.4	38.3
	4	17.3	42.9	8.9	36.6
3B-02	1	18.0	43.0	8.4	34.7
	2	18.0	42.9	8.9	34.7
	3	18.0	42.8	8.9	34.9
	4	18.0	43.1	9.0	34.6
4B-10	1	18.5	43.8	9.0	34.3
	2	18.3	43.6	9.0	34.4
	3	18.3	43.7	9.0	33.1
	4	18.2	43.5	8.9	33.0
3C-22	1	16.9	42.4	8.9	33.7
	2	16.8	42.1	8.9	33.8
	3	16.6	42.6	8.8	32.7
	4	16.7	43.2	8.8	34.0

Table A.3.: Measured characteristics of the SQUIDs arrays from HDSQ wafer *14w1* used in the amplifier module. The chips are listed in the order in which they appear in modules α–γ and connectors A–D.

Chip		I_b / µA	M_x^{-1} / µA $\Phi_0{}^{-1}$	M_{in}^{-1} / µA $\Phi_0{}^{-1}$	ΔU / µV
3D-05	1	13.6	11.7	11.7	488
	2	13.4	11.7	11.7	485
2A-17	1	12.7	11.9	11.9	386
	2	13.1	11.8	11.8	425
1A-05	1	13.8	11.9	11.9	483
	2	13.5	11.9	11.8	476
2A-09	1	13.2	11.9	11.8	451
	2	13.3	11.9	11.9	465
1A-15	1	13.6	11.9	11.9	452
	2	13.4	11.8	11.8	423
2A-11	1	13.6	11.8	11.8	464
	2	13.8	11.8	11.8	437
1D-11	1	15.5	11.8	11.8	631
	2	15.6	11.9	11.9	635
2A-23	1	12.5	11.8	11.8	376
	2	12.0	11.8	11.8	368
2D-11	1	13.1	11.7	11.7	514
	2	13.4	11.7	11.7	511
1C-15	1	14.7	11.9	11.8	560
	2	14.6	11.9	11.9	598
4C-05	1	14.9	11.7	11.7	621
	2	14.3	11.7	11.7	489
4C-11	1	15.7	11.8	11.8	594
	2	15.6	11.9	11.9	636
2B-11	1	12.3	11.8	11.8	410
	2	12.6	11.8	11.8	418
2A-05	1	13.0	11.8	11.9	449
	2	13.1	11.8	11.8	437
3B-23	1	13.8	11.7	11.7	551
	2	13.9	11.7	11.7	543
2B-23	1	13.0	11.7	11.7	450
	2	12.8	11.7	11.7	412
2B-05	1	13.0	11.7	11.7	462
	2	13.2	11.7	11.7	512
2B-09	1	13.0	11.7	11.7	470
	2	13.1	11.8	11.7	465

Bibliography

[1] D. Unger et al., "High-resolution for IAXO: MMC-based X-ray detectors", J. Instrum. **16**, P06006 (2021) 10.1088/1748-0221/16/06/P06006.

[2] D. Unger et al., "MMC array to study X-ray transitions in muonic atoms", J. Low Temp. Phys. **216**, 344–351 (2024) 10.1007/s10909-024-03141-x.

[3] K. Maurer et al., "Towards cancer theragnostic–probing the ^{225}Ac decay chain with ultra-high-resolution MMC-based detectors", under review.

[4] D. Unger et al., "fitfiles", https://github.com/unger-daniel/fitfiles.

[5] B. Ohayon et al., "Towards precision muonic X-ray measurements of charge radii of light nuclei", Physics **6**, 206–215 (2024) 10.3390/physics6010015.

[6] A. Fleischmann et al. (QUARTET Collaboration), "Quantum interactions with exotic atoms", Letter of Intent, 2023.

[7] A. Abeln et al. (QUARTET Collaboration), "Measurement of charge radii from lithium to neon", Quartet Reasearch Proposal for BVR 55, 2024.

[8] A. Abeln et al. (QUARTET Collaboration), "Measurement of charge radii from lithium to neon", Quartet Progress Report and Beamtime Request for BVR 56, 2025.

[9] F. Mantegazzini et al., "Multichannel read-out for arrays of metallic magnetic calorimeters", J. Instrum. **16**, P08003 (2021) 10.1088/1748-0221/16/08/P08003.

[10] A. P. Jadhav et al., "Large area photon detector for the search of $0\nu\beta\beta$ using scintillators", in preparation.

[11] A. Abeln et al. (IAXO Collaboration), "Conceptual design of BabyIAXO, the intermediate stage towards the international axion observatory", J. High Energy Phys. **2021**, 137 (2021) 10.1007/JHEP05(2021)137.

[12] L. Gastaldo, D. Hengstler, and D. Unger, "High energy resolution x-ray detectors for IAXO: advantages in pre- and post-discovery phases", PoS **COSMICWISPers**, 038 (2024) 10.22323/1.454.0038.

[13] C. Ständer and D. Unger, "F98: SQUIDs and noise thermometers", https://physi.uni-heidelberg.de/Einrichtungen/FP/anleitungen/F98.pdf, Advanced Physics Lab for Physicists, Mar. 2022.

[14]P. L. Wiedemann, "Characterisation of thermal properties of an MMC array designed for X-ray spectroscopy of muonic atoms", Master's thesis (Heidelberg University, 2025).

[15]I. G. N. W. Saor, „Simulationsbasierter Vergleich von Algorithmen zur Datenreduzierung für die hochauflösende Röntgenspektroskopie", Bachelor's Thesis (Heidelberg University, 2025).

[16]A. P. Jadhav, "Design and fabrication of a large area photon detector for the search of $0\nu\beta\beta$ using scintillators", Master's thesis (Heidelberg University, 2024).

[17]D. Behrend-Uriarte, "Assembly and characterization of a SQUID amplifier module for IAXO and automation of SQUID tuning", Bachelor's Thesis (Heidelberg University, 2021).

[18]S. Hilscher, "Addressing noise in SQUID-based MMC-readout: investigating lossy input coils and automated SQUID-tuning", Bachelor's Thesis (Heidelberg University, 2024).

[19]D. L. Klumpp, "Spectral shape analysis with the kernal density estimation for the ECHo-experiment", Bachelor's Thesis (Heidelberg University, 2022).

[20]I.-A. Nitu, "Calorimetric measurement of the ^{193}Pt electron capture spectrum", Bachelor's Thesis (Heidelberg University, 2022).

[21]P. J. Mohr et al., "CODATA recommended values of the fundamental physical constants: 2022", Rev. Mod. Phys. **97**, 025002 (2025) 10.1103/RevModPhys.97.025002.

[22]M. S. Safronova et al., "Search for new physics with atoms and molecules", Rev. Mod. Phys. **90**, 025008 (2018) 10.1103/RevModPhys.90.025008.

[23]R. Pohl et al., "The size of the proton", Nature **466**, 213–216 (2010) 10.1038/nature09250.

[24]A. Antognini et al., "Proton structure from the measurement of 2s-2p transition frequencies of muonic hydrogen", Science **339**, 417–420 (2013) 10.1126/science.1230016.

[25]J. Friar, "Nuclear finite-size effects in light muonic atoms", Ann. Phys. **122**, 151–196 (1979) 10.1016/0003-4916(79)90300-2.

[26]A. Antognini et al., *Muonic-atom spectroscopy and impact on nuclear structure and precision QED theory*, 2022, https://arxiv.org/abs/2210.16929.

[27]B. Ohayon, "Critical evaluation of reference charge radii and applications in mirror nuclei", At. Data Nucl. Data Tables, 101732 (2025) 10.1016/j.adt.2025.101732.

[28]R. Pohl et al. (CREMA Collaboration), "Laser spectroscopy of muonic deuterium", Science **353**, 669–673 (2016) 10.1126/science.aaf2468.

[29]J. J. Krauth et al., "Measuring the α-particle charge radius with muonic helium-4 ions", Nature **589**, 527–531 (2021) 10.1038/s41586-021-03183-1.

[30]G. Fricke et al., "Behavior of the nuclear charge radii systematics in the s-d shell from muonic atom measurements", Phys. Rev. C **45**, 80–89 (1992) 10.1103/PhysRevC.45.80.

[31]G. Fricke et al., "Nuclear ground state charge radii from electromagnetic interactions", At. Data Nucl. Data Tables **60**, 177–285 (1995) 10.1006/adnd.1995.1007.

[32]W. Ruckstuhl et al., "High-precision muonic x-ray measurement of the rms charge radius of ^{12}C with a crystal spectrometer", Phys. Rev. Lett. **49**, 859–862 (1982) 10.1103/PhysRevLett.49.859.

[33]W. Ruckstuhl et al., "Precision measurement of the 2p-1s transition in muonic ^{12}C: search for new muon-nucleon interactions or accurate determination of the rms nuclear charge radius", Nucl. Phys. A **430**, 685–712 (1984) 10.1016/0375-9474(84)90101-5.

[34]H. Hergert, "A guided tour of ab initio nuclear many-body theory", Front. Phys. **8** (2020) 10.3389/fphy.2020.00379.

[35]X.-X. Sun et al., "Radii of light nuclei from the jacobi no-core shell model", Phys. Rev. C **112**, 024317 (2025) 10.1103/j4ky-tn1j.

[36]S. Devons and I. Duerdoth, "Muonic atoms", in *Advances in nuclear physics: volume 2*, edited by M. Baranger and E. Vogt (Springer US, New York, NY, 1969), pp. 295–423, 10.1007/978-1-4684-8343-7_5.

[37]D. Measday, "The nuclear physics of muon capture", Physics Reports **354**, 243–409 (2001) 10.1016/S0370-1573(01)00012-6.

[38]Paul Scherrer Institut, *High intensity proton accelerator facility*, https://psi.ch/en/cas/hipa, 2025.

[39]Paul Scherrer Institut, *πE1 beam line*, https://psi.ch/en/smus/pie1, 2025.

[40]S. Sturniolo and A. Hillier, "Mudirac: a Dirac equation solver for elemental analysis with muonic X-rays", X-Ray Spectrom. **50**, 180–196 (2021) 10.1002/xrs.3212.

[41]S. Sturniolo et al., *MuDirac: a muonic atom Dirac equation solver*, https://github.com/muon-spectroscopy-computational-project/mudirac, 2025.

[42]L. Michel, "Interaction between four half-spin particles and the decay of the μ-meson", Proc. Phys. Soc. A **63**, 514 (1950) 10.1088/0370-1298/63/5/311.

[43]National Nuclear Data Center, *NuDat 3.0 Database*, https://nndc.bnl.gov/nudat3/, 2025.

[44]J. Zatorski, V. Patkóš, and K. Pachucki, "Quantum electrodynamics of two-body systems with arbitrary masses up to α^6 order", Phys. Rev. A **106**, 042804 (2022) 10.1103/PhysRevA.106.042804.

[45]E. A. Uehling, "Polarization effects in the positron theory", Phys. Rev. **48**, 55–63 (1935) 10.1103/PhysRev.48.55.

[46]F. de Boer et al., "Precision measurement of the 2p-1s transition wavelength in muonic ^{13}C", Nucl. Phys. A **444**, 589–596 (1985) 10.1016/0375-9474(85)90106-X.

[47]W. Geithner et al., "Masses and charge radii of $^{17-22}$Ne and the two-proton-halo candidate ^{17}Ne", Phys. Rev. Lett. **101**, 252502 (2008) 10.1103/PhysRevLett.101.252502.

[48]P. Müller et al., "The nuclear charge radius of ^{13}C", Nat. Commun. **16**, 6234 (2025) 10.1038/s41467-025-60280-9.

[49]M. Gorchtein, *A hitchhiker's guide to nuclear polarization in muonic atoms*, 2025, https://arxiv.org/abs/2501.15274.

[50]C. Enss et al., "Metallic magnetic calorimeters for particle detection", J. Low Temp. Phys. **121**, 137–176 (2000) 10.1023/A:1004863823166.

[51]A. Fleischmann, C. Enss, and G. Seidel, "Metallic magnetic calorimeters", in *Cryogenic particle detection*, edited by C. Enss (Springer Berlin, Heidelberg, 2005), pp. 151–216, 10.1007/10933596_4.

[52]S. Kempf et al., "Physics and applications of metallic magnetic calorimeters", J. Low Temp. Phys. **193**, 365–379 (2018) 10.1007/s10909-018-1891-6.

[53]M. Linck, „Entwicklung eines metallischen magnetischen Kalorimeters für die hochauflösende Röntgenspektroskopie", Dissertation (Heidelberg University, 2007), 10.11588/heidok.00007356.

[54]L. Fleischmann et al., "Metallic magnetic calorimeters for X-ray spectroscopy", IEEE Trans. Appl. Supercond. **19**, 63–68 (2009) 10.1109/TASC.2009.2012724.

[55]S. Schäfer, „Entwicklung einer Detektorzeile aus metallischen magnetischen Kalorimetern zur hochauflösenden Röntgenspektroskopie an hochgeladenen Ionen", Dissertation (Heidelberg University, 2012), 10.11588/heidok.00013348.

[56]T. Sikorsky et al., "Measurement of the ^{229}Th isomer energy with a magnetic microcalorimeter", Phys. Rev. Lett. **125**, 142503 (2020) 10.1103/PhysRevLett.125.142503.

[57]C. Pies et al., "maXs: microcalorimeter arrays for high-resolution X-ray spectroscopy at GSI/FAIR", J. Low Temp. Phys. **167**, 269–279 (2012) 10.1007/s10909-012-0557-z.

[58]D. Hengstler et al., "Towards FAIR: first measurements of metallic magnetic calorimeters for high-resolution X-ray spectroscopy at GSI", Phys. Scr. **2015**, 014054 (2015) 10.1088/0031-8949/2015/T166/014054.

[59]L. Gastaldo et al., "Characterization of low temperature metallic magnetic calorimeters having gold absorbers with implanted ^{163}Ho ions", Nucl. Instrum. Methods Phys. Res. A **711**, 150–159 (2013) 10.1016/j.nima.2013.01.027.

[60]A. Göggelmann et al., "Study of muon-induced background in MMC detector arrays for the ECHo experiment", Eur. Phys. J. C **81**, 363 (2021) 10.1140/epjc/s10052-021-09148-y.

[61]S. R. Bandler et al., "Metallic magnetic bolometers for particle detection", J. Low Temp. Phys. **93**, 709–714 (1993) 10.1007/BF00693500.

[62]J. S. Adams et al., "Particle detection using cryogenic magnetic calorimeters", Phys. B: Condens. Matter **263-264**, 604–606 (1999) 10.1016/S0921-4526(98)01432-X.

[63]A. Fleischmann et al., "Metallic magnetic calorimeters", AIP Conf. Proc. **1185**, 571–578 (2009) 10.1063/1.3292407.

[64]L. Gastaldo et al., "The electron capture ^{163}Ho experiment ECHo", J. Low Temp. Phys. **176**, 876–884 (2014) 10.1007/s10909-014-1187-4.

[65]L. Gastaldo et al., "The electron capture in ^{163}Ho experiment – ECHo", Eur. Phys. J. Spec. Top. **226**, 1623–1694 (2017) 10.1140/epjst/e2017-70071-y.

[66]C. Velte, "Measurement of a high energy resolution and high statistics ^{163}Ho electron capture spectrum for the ECHo experiment", Dissertation (Heidelberg University, 2019), 10.11588/heidok.00027340.

[67]F. Mantegazzini, "Development and characterisation of high-resolution metallic magnetic calorimeter arrays for the ECHo neutrino mass experiment", Dissertation (Heidelberg University, 2021), 10.11588/heidok.00030250.

[68]H. Bhang et al., "AMoRE experiment: a search for neutrinoless double beta decay of ^{100}Mo isotope with $^{40}Ca^{100}MoO_4$ cryogenic scintillation detector", J. Phys. Conf. Ser. **375**, 042023 (2012) 10.1088/1742-6596/375/1/042023.

[69]A. Agrawal et al. (AMoRE Collaboration), "Projected background and sensitivity of AMoRE-II", Eur. Phys. J. C **85**, 9 (2025) 10.1140/epjc/s10052-024-13516-9.

[70]A. Agrawal et al. (AMoRE Collaboration), "Improved limit on neutrinoless double beta decay of ^{100}Mo from AMoRE-I", Phys. Rev. Lett. **134**, 082501 (2025) 10.1103/PhysRevLett.134.082501.

[71]B. von Krosigk et al., "DELight: a direct search experiment for light dark matter with superfluid helium", SciPost Phys. Proc., 016 (2023) 10.21468/SciPostPhysProc.12.016.

[72]E. Armengaud et al. (IAXO Collaboration), "Physics potential of the international axion observatory (IAXO)", J. Cosmol. Astropart. Phys. **2019**, 047 (2019) 10.1088/1475-7516/2019/06/047.

[73]S. Allgeier, „Entwicklung und Charakterisierung des metallischen magnetischen Kalorimeterarrays maXs100 zur Röntgenspektroskopie von heliumartigen U^{90+}-Ionen", Dissertation (Heidelberg University, 2024), 10.11588/heidok.00035586.

[74]M. O. Herdrich et al., "Application of a metallic-magnetic calorimeter for high-resolution x-ray spectroscopy of Fe at an EBIT", J. Phys. B **57**, 085001 (2024) 10.1088/1361-6455/ad34a2.

[75]L. E. Gamer, „Entwicklung und Charakterisierung des 4 k-Pixel Detektorarrays MOCCA für die energie- und ortsaufgelöste Detektion neutraler Molekülfragmente“, Dissertation (Heidelberg University, 2019), 10.11588/heidok.00027343.

[76]L. Gamer et al., “MOCCA: a 4k-pixel molecule camera for the position- and energy-resolving detection of neutral molecule fragments at CSR”, J. Low Temp. Phys. **184**, 839–844 (2016) 10.1007/s10909-015-1453-0.

[77]D. P. Schulz, “Development and characterization of MOCCA, a 4k-pixel molecule camera for the energy-resolved detection of neutral molecule fragments”, Dissertation (Heidelberg University, 2021), 10.11588/heidok.00029810.

[78]A.-D. Brown et al., “Absorber materials for transition-edge sensor X-ray microcalorimeters”, J. Low Temp. Phys. **151**, 413–417 (2008) 10.1007/s10909-007-9669-2.

[79]E. Cosulich, F. Gatti, and S. Vitale, “Further results on μ-calorimeters with superconducting absorber”, J. Low Temp. Phys. **93**, 263–268 (1993) 10.1007/BF00693430.

[80]A. G. Kozorezov et al., “Quasiparticle-phonon downconversion in nonequilibrium superconductors”, Phys. Rev. B **61**, 11807–11819 (2000) 10.1103/PhysRevB.61.11807.

[81]D. McCammon et al., “Thermal calorimeters for high resolution X-ray spectroscopy”, Nucl. Instrum. Methods Phys. Res. A **326**, 157–165 (1993) 10.1016/0168-9002(93)90346-J.

[82]P. C.-O. Ranitzsch, “Low temperature calorimeter with superconducting particle absorbers”, Diploma thesis (Heidelberg University, 2009).

[83]D. Hengstler, „Untersuchung der Eigenschaften von supraleitenden Re-, Zn- und Zn:Mn-Absorbern für magnetische Mikrokalorimeter“, Diploma thesis (Heidelberg University, 2012).

[84]P. C.-O. Ranitzsch, “Development and characterization of metallic magnetic calorimeters for the calorimetric measurement of the electron capture spectrum of ^{163}Ho for the purpose of neutrino mass determination”, Dissertation (Heidelberg University, 2014), 10.11588/heidok.00017462.

[85]M. A. Herbst, “High resolution magnetic micro-calorimeters: thermodynamics, cooling requirements, and noise”, Dissertation (Heidelberg University, 2023), 10.11588/heidok.00033590.

[86]A. Agrawal et al. (AMoRE Collaboration), “Development of MMC-based lithium molybdate cryogenic calorimeters for AMoRE-II”, Eur. Phys. J. C **85**, 172 (2025) 10.1140/epjc/s10052-024-13498-8.

[87]L. L. Isaacs, “Low-temperature specific heat of gold, silver, and copper”, J. Chem. Phys. **43**, 307–308 (1965) 10.1063/1.1696473.

[88]M. J. Berger et al., *XCOM: photon cross sections database*, NIST, Mar. 1998, 10.18434/T48G6X.

[89]J. H. Hubbell and S. M. Seltzer, *Tables of X-ray mass attenuation coefficients and mass energy-absorption coefficients*, NIST, July 2004, 10.18434/T4D01F.

[90]G. Weber et al., "Simulation of the photopeak efficiency of microcalorimeters equipped with small volume gold absorbers", in (Annual Report 2022, Helmholtz Institute Jena, 2022), p. 46, 10.15120/GSI-2023-00687.

[91]D. D. E. Martin et al., "Resolution limitation due to phonon losses in superconducting tunnel junctions", Appl. Phys. Lett. **88**, 123510 (2006) 10.1063/1.2187444.

[92]A. G. Kozorezov et al., "Electron energy down-conversion in thin superconducting films", Phys. Rev. B **75**, 094513 (2007) 10.1103/PhysRevB.75.094513.

[93]A. Kozorezov, "Energy down-conversion and thermalization in metal absorbers", J. Low Temp. Phys. **167**, 473–484 (2012) 10.1007/s10909-011-0426-1.

[94]A. G. Kozorezov et al., "Athermal energy loss from x-rays deposited in thin superconducting films on solid substrates", Phys. Rev. B **87**, 104504 (2013) 10.1103/PhysRevB.87.104504.

[95]R. Franz und G. Wiedemann, „Über die Wärme-Leitungsfähigkeit der Metalle", Ann. Phys. **165**, 497–531 (1853).

[96]A. Sommerfeld, „Zur Elektronentheorie der Metalle auf Grund der Fermischen Statistik", Z. Phys. **47**, 1–32 (1928) 10.1007/BF01391052.

[97]J. Korringa, "Nuclear magnetic relaxation and resonnance line shift in metals", Physica **16**, 601–610 (1950) 10.1016/0031-8914(50)90105-4.

[98]H. Rotzinger et al., "Performance of micro-fabricated magnetic calorimeters arrays for X-ray spectroscopy", J. Low Temp. Phys. **151**, 351–356 (2008) 10.1007/s10909-007-9658-5.

[99]P. E. Rider, K. A. Gschneidner Jr, and O. D. McMasters, "Gold-rich rare-earth-gold solid solutions", Trans. Met. Soc. AIME **Vol: 233** (1965).

[100]A. Abragam and B. Bleaney, *Electron paramagnetic resonance of transition ions*, International series of monographs on physics (Claredon Press, Oxford, 1970).

[101]S. Fraga, J. Karwowski, and K. M. S. Saxena, *Handbook of atomic data* (Elsevier, 1976).

[102]G. Williams and L. L. Hirst, "Crystal-field effects in solid solutions of rare earths in noble metals", Phys. Rev. **185**, 407–415 (1969) 10.1103/PhysRev.185.407.

[103]W. Hahn, M. Loewenhaupt, and B. Frick, "Crystal field excitations in dilute rare earth noble metal alloys", Physica B **180-181**, 176–178 (1992) 10.1016/0921-4526(92)90698-R.

[104]L. J. Tao et al., "Hyperfine splitting of Er and Yb resonances in Au: a separation between the atomic and covalent contributions to the exchange integral", Phys. Rev. B **4**, 5–9 (1971) 10.1103/PhysRevB.4.5.

[105] A. Fleischmann et al., "Low temperature properties of erbium in gold", J. Low Temp. Phys. **118**, 7–21 (2000) 10.1023/A:1004654401827.

[106] J. Schönefeld, „Entwicklung eines mikrostrukturierten magnetischen Tieftempertatur-Kalorimeters zum hochauflösenden Nachweis von einzelnen Röntgenquanten", Dissertation (Heidelberg University, 2000).

[107] A. Fleischmann, „Magnetische Mikrokalorimeter: Hochauflösende Röntgenspektroskopie mit energiedispersiven Detektoren", Dissertation (Heidelberg University, 2003), 10.11588/heidok.00012877.

[108] M. Herbst et al., "Numerical calculation of the thermodynamic properties of silver erbium alloys for use in metallic magnetic calorimeters", J. Low Temp. Phys. **209**, 1119–1127 (2022) 10.1007/s10909-022-02739-3.

[109] M. A. Ruderman and C. Kittel, "Indirect exchange coupling of nuclear magnetic moments by conduction electrons", Phys. Rev. **96**, 99–102 (1954) 10.1103/PhysRev.96.99.

[110] T. Kasuya, "A theory of metallic ferro- and antiferromagnetism on Zener's model", Progress of Theoretical Physics **16**, 45–57 (1956) 10.1143/PTP.16.45.

[111] K. Yosida, "Magnetic properties of Cu-Mn alloys", Phys. Rev. **106**, 893–898 (1957) 10.1103/PhysRev.106.893.

[112] A. Burck, „Entwicklung großflächiger mikrostrukturierter magnetischer Kalorimeter mit Au:Er- und Ag:Er-Sensoren für den energieaufgelösten Nachweis von Röntgenquanten und hochenergetischen Teilchen", Dissertation (Heidelberg University, 2008), 10.11588/heidok.00008832.

[113] T. Herrmannsdörfer, R. König, and C. Enss, "Properties of Er-doped Au at ultralow temperatures", Physica B **284-288**, 1698–1699 (2000) 10.1016/S0921-4526(99)02942-7.

[114] M. E. Sjöstrand and G. Seidel, "Hyperfine resonance properties of Er^{3+} in Au", Phys. Rev. B **11**, 3292–3297 (1975) 10.1103/PhysRevB.11.3292.

[115] D. L. Martin, "Specific heat of copper, silver, and gold below 30°K", Phys. Rev. B **8**, 5357–5360 (1973) 10.1103/PhysRevB.8.5357.

[116] C. Foiles, "Transport anomalies in dilute silver-rare earth alloys", J. Phys. Chem. Solids **32**, 1205–1209 (1971) 10.1016/S0022-3697(71)80178-6.

[117] A. Fleischmann et al., "Metallic magnetic calorimeters (MMC): detectors for high-resolution X-ray spectroscopy", Nucl. Instrum. Methods Phys. Res. A **520**, 27–31 (2004) 10.1016/j.nima.2003.11.212.

[118] T. Daniyarov, „Metallische magnetische Kalorimeter zum hochauflösenden Nachweis von Röntgenquanten und hochenergetischen Molekülen", Dissertation (Heidelberg University, 2005), 10.11588/heidok.00005231.

[119]V. Hoffmann, „Messung der AC-Suszeptibilität von paramagnetischem Au:Er bei Temperaturen oberhalb des Spinglas-Übergangs“, Bachelor's Thesis (Heidelberg University, 2012).

[120]V. Wißdorf, „Magnetisches 1/f-Rauschen und Imaginärteil der magnetischen Suszeptibilität von Erbium dotiertem Gold bei Millikelvin Temperaturen“, Bachelor's Thesis (Heidelberg University, 2012).

[121]R. Yang, "Magnetic noise of erbium-doped silver at millikelvin temperatures", Bachelor's Thesis (Heidelberg University, 2023).

[122]S. Kempf et al., "Direct-current superconducting quantum interference devices for the readout of metallic magnetic calorimeters", Supercond. Sci. Technol. **28**, 045008 (2015) 10.1088/0953-2048/28/4/045008.

[123]D. McCammon, "Thermal equilibrium calorimeters – an introduction", in *Cryogenic particle detection*, edited by C. Enss (Springer Berlin, Heidelberg, 2005), pp. 1–34, 10.1007/10933596_1.

[124]B. Zink et al., "Lithographically patterned magnetic calorimeter X-ray detectors with integrated SQUID readout", Nucl. Instrum. Methods Phys. Res. A **520**, 52–55 (2004) 10.1016/j.nima.2003.11.218.

[125]M. Krantz, "Development of a metallic magnetic calorimeter with integrated SQUID readout", Dissertation (Heidelberg University, 2020), 10.11588/heidok.00027340.

[126]M. Krantz et al., "Magnetic microcalorimeter with paramagnetic temperature sensors and integrated dc-SQUID readout for high-resolution x-ray emission spectroscopy", Appl. Phys. Lett. **124**, 032601 (2024) 10.1063/5.0180903.

[127]F. Ahrens, "Development and microfabrication of an integrated photon and phonon detector for the search of $0\nu\beta\beta$ decay using scintillating bolometers", Master's thesis (Heidelberg University, 2016).

[128]F. Forndran, "Optimization of Si deep etching and fabrication of the first P2 detector with trenches", Master's thesis (Heidelberg University, 2019).

[129]C. Pies, „maXs-200: Entwicklung und Charakterisierung eines Röntgendetektors basierend auf magnetischen Kalorimetern für die hochauflösende Spektroskopie hochgeladener Ionen“, Dissertation (Heidelberg University, 2012), 10.11588/heidok.00014182.

[130]D. Drung et al., "Highly sensitive and easy-to-use SQUID sensors", IEEE Trans. Appl. Supercond. **17**, 699–704 (2007) 10.1109/TASC.2007.897403.

[131]B. Josephson, "Possible new effects in superconductive tunnelling", Phys. Lett. **1**, 251–253 (1962) 10.1016/0031-9163(62)91369-0.

[132]M. Wegner, „Entwicklung, Herstellung und Charakterisierung eines auf metallischen magnetischen Kalorimetern basierenden Detektorarrays mit 64 Pixeln und integriertem Mikrowellen-SQUID-Multiplexer“, Dissertation (Heidelberg University, 2018), 10.11588/heidok.00025741.

[133]D. P. Richter, „Multikanal-Auslesung von metallischen magnetischen Kalorimetern mittels eines vollständigen Mikrowellen-SQUID-Multiplexer-Systems“, Dissertation (Heidelberg University, 2021), 10.11588/heidok.00030266.

[134]F. K. Ahrens, “Cryogenic read-out system and resonator optimisation for the microwave SQUID multiplexer within the ECHo experiment”, Dissertation (Heidelberg University, 2022), 10.11588/heidok.00032038.

[135]D. Richter et al., “Simultaneous MMC readout using a tailored μMUX based readout system”, IEEE Trans. Appl. Supercond. **33**, 1–5 (2023) 10.1109/TASC.2023.3264200.

[136]J. Clarke and A. I. Braginski, *The SQUID handbook: fundamentals and technology of SQUIDs and SQUID systems* (Wiley, 2004).

[137]J. Clarke and A. I. Braginski, *The SQUID handbook: applications of SQUIDs and SQUID systems* (Wiley, 2006).

[138]W. C. Stewart, “Current-voltage characteristics of josephson junctions”, Appl. Phys. Lett. **12**, 277–280 (1968) 10.1063/1.1651991.

[139]D. E. McCumber, “Effect of ac impedance on dc voltage-current characteristics of superconductor weak-link junctions”, J. Appl. Phys. **39**, 3113–3118 (1968) 10.1063/1.1656743.

[140]A. Ferring, „Entwicklung von dc-SQUIDs zur Auslesung von metallischen magnetischen Kalorimetern“, Master’s thesis (Heidelberg University, 2015).

[141]D. P. Richter, „Auslesung von SQUIDs mittels Flussrampenmodulation“, Master’s thesis (Heidelberg University, 2017).

[142]F. Bauer, „Rauscharme Stromsensor-dc-SQUIDs mit Impedanzanpassung für metallische magnetische Kalorimeter“, Dissertation (Heidelberg University, 2022), 10.11588/heidok.00032001.

[143]A. Ferring-Siebert, „Untersuchung des niederfrequenten Flussrauschens in dc-SQUIDs bei Temperaturen unter 1K“, Dissertation (Heidelberg University, 2024), 10.11588/heidok.00034757.

[144]D. Hengstler, “Development and characterization of two-dimensional metallic magnetic calorimeter arrays for the high-resolution X-ray spectroscopy”, Dissertation (Heidelberg University, 2017), 10.11588/heidok.00023815.

[145]J. Geist, „Bestimmung der Isomerenergie von ^{229}Th mit dem hochauflösenden Mikrokalorimeter-Array maXs30“, Dissertation (Heidelberg University, 2020), 10.11588/heidok.00027340.

[146]D. Unger, “Development and characterization of a high energy resolution and low background detector module for the IAXO experiment”, Master’s Thesis (Heidelberg University, 2020).

[147]S. Allgeier, „Entwicklung einer modularen 36-Kanal-Auslesekette mit rauscharmen SQUID-basierten Vorverstärkern für die 4k-Pixel-Molekülkamera MOCCA“, Master’s thesis (Heidelberg University, 2017).

[148]D. Kreuzberger, Dissertation (Heidelberg University).

[149]B. Henke, E. Gullikson, and J. Davis, “X-ray interactions: photoabsorption, scattering, transmission, and reflection at E = 50–30000 eV, Z = 1–92”, At. Data Nucl. Data Tables **54**, 181–342 (1993) 10.1006/adnd.1993.1013.

[150]Magnicon GmbH, *XXF-1 Manual: High Performance dc SQUID Electronics* (2012).

[151]M. Friedrich, „Aufbau und Charakterisierung eines maXs30-Detektors zur hochaufgelösten Röntgenspektroskopie an Elektronenstrahl-Ionenfallen (EBITs)“, Bachelor’s Thesis (Heidelberg University, 2019).

[152]J. Wendel, „Bestimmung der Nichtlinearität des Analog-Digital-Wandlers SIS3316 für die hochpräzise Energiekalibrierung im QUARTET-Experiment“, Bachelor’s Thesis (Heidelberg University, 2024).

[153]A. A. Striebel, “Characterization of a maxs100 metallic magnetic microcalorimeter array with 100 μm thick absorbers and improvement of the non-linearity of the readout system”, Master’s thesis (Heidelberg University, 2025).

[154]MIDAS, *Wiki*, https://midas.triumf.ca/, 2025.

[155]A. Barth, “High resolution MMC arrays for low energy electron capture spectrum studies”, Dissertation (Heidelberg University, 2024), 10.11588/heidok.00034457.

[156]R. Hammann et al., “Data reduction for a calorimetrically measured ^{163}Ho spectrum of the ECHo-1k experiment”, Eur. Phys. J. C **81**, 963 (2021) 10.1140/epjc/s10052-021-09763-9.

[157]L. Eisenmann, „Aufbau und Charakterisierung eines maXs30-Detektor-Moduls zur hochaufgelösten Röntgenspektroskopie“, Bachelor’s thesis (Heidelberg University, 2023).

[158]E. Biedert, „Charakterisierung und Optimierung von Methoden zur Auswertung digitalisierter Pulssignale aus magnetischen Mikrokalorimetern“, Bachelor’s Thesis (Heidelberg University, 2024).

[159]J. Wilson et al., "The level-1 trigger for the SuperCDMS experiment at SNOLAB", J. Instrum. **17**, P07010 (2022) 10.1088/1748-0221/17/07/P07010.

[160]K. von Schoeler, Dissertation (ETH Zürich, 2026).

[161]G. W. Phillips and K. W. Marlow, "Automatic analysis of gamma-ray spectra from germanium detectors", Nucl. Instrum. Methods Phys. Res. **137**, 525–536 (1976) 10.1016/0029-554X(76)90472-9.

[162]E. G. Kessler et al., "Mid-to-high-Z precision x-ray measurements", Phys. Rev. A **26**, 2696–2706 (1982) 10.1103/PhysRevA.26.2696.

[163]G. Hölzer et al., "$K\alpha_{1,2}$ and $K\beta_{1,3}$ x-ray emission lines of the $3d$ transition metals", Phys. Rev. A **56**, 4554–4568 (1997) 10.1103/PhysRevA.56.4554.

[164]R. D. Deslattes et al., *X-ray transition energies database*, https://doi.org/10.18434/T4859Z, 2005.

[165]M. H. Mendenhall et al., "The molybdenum K-shell x-ray emission spectrum", J. Phys. B **52**, 215004 (2019) 10.1088/1361-6455/ab45d6.

[166]T. Schmitt, "Calorimetric measurement of the ^{193}Pt electron capture spectrum", Master's thesis (Heidelberg University, 2019).

[167]A. Abeln, Dissertation (Heidelberg University).